

University of Southern Queensland

**RBF-BASED MESHLESS MODELING OF
STRAIN LOCALIZATION AND FRACTURE**

A dissertation submitted by

Le Bui Hong Phong

B.Eng., HoChiMinh City University of Technology, Vietnam, 2003

For the award of the degree of

Doctor of Philosophy

February 2010

Dedication

To my parents, my wife and my daughter.

Certification of Dissertation

I certify that the idea, experimental work, results and analyses, software and conclusions reported in this dissertation are entirely my own effort, except where otherwise acknowledged. I also certify that the work is original and has not been previously submitted for any other award.

Phong Hong Bui Le, Candidate

Date

ENDORSEMENT

Prof. Thanh Tran-Cong, Principal supervisor

Date

Dr. Nam Mai-Duy, co-supervisor

Date

Acknowledgments

The research reported in this thesis was carried out at the Computational Engineering and Science Research Centre, Faculty of Engineering and Surveying, USQ.

I would like to express my deepest gratitude and appreciation to Prof. Thanh Tran-Cong for his encouragement and comprehensive guidance throughout this research. Without his continuous support this thesis would not have been possible.

I would like to express my sincere thanks to Dr. Nam Mai-Duy for acting his role as the co-supervisor. I wish to record thanks to Prof. Graham Baker, Associate Prof. David Buttsworth, Ms. Ruth Hilton and Ms. Juanita Ryan for their kind supports. My special thanks go to Ms. Dang Thi Hoang Dung for her beautiful friendship and valuable support.

I also would like to express my gratitude and appreciation to Prof. Timon Rabczuk at the Institute of Structural Mechanics, Bauhaus-University Weimar, Germany, for his invaluable collaboration and fruitful discussion as well as his beautiful friendship.

The financial support provided by the Australian Research Council and a PhD Scholarship from USQ are gratefully acknowledged.

Finally, I dedicate this work to my parents, my wife and my daughter.

Notes to Readers

For ease of reading of this thesis, a number of files are included on the attached CD-ROM to provide colour presentation as well as animation of some numerical results in this thesis. The contents of the CD-ROM include:

1. thesis.pdf: An electronic version of this thesis with colour figures;
2. Chapter-5-Displacement-Local.avi: An animation showing the evolution of displacement using local continuum model (Section 5.4.2, Chapter 5);
3. Chapter-5-Strain-Local.avi: an animation showing the evolution of strain using local continuum model (Section 5.4.2, Chapter 5);
4. Chapter-5-Velocity-Local.avi: an animation showing the evolution of velocity using local continuum model (Section 5.4.2, Chapter 5);
5. Chapter-5-Displacement-Nonlocal.avi: An animation showing the evolution of displacement using nonlocal continuum model (Section 5.4.3 , Chapter 5);
6. Chapter-5-Strain-Nonlocal.avi: an animation showing the evolution of strain using nonlocal continuum model (Section 5.4.3, Chapter 5);
7. Chapter-5-Velocity-Nonlocal.avi: an animation showing the evolution of velocity using nonlocal continuum model (Section 5.4.3, Chapter 5).

Abstract

This work attempts to contribute further knowledge and understanding in the discipline of computational science in general and numerical modeling of discontinuity problems in particular. Of particular interest is numerical simulation of dynamic strain localization and fracture problems. The distinguishing feature in this study is the employment of neural-networks-(RBF)-based meshfree methods, which differentiates the present approach from many other computational approaches for numerical simulation of strain localization and fracture mechanics.

As a result, new meshfree methods based on RBF networks, namely moving RBF-based meshless methods, have been devised and developed for solving PDEs. Unlike the conventional RBF methods, the present moving RBF is locally supported and yields sparse, banded resultant matrices, and better condition numbers. The shape functions of the new method satisfy the Kronecker-delta property, which facilitates the imposition of the essential boundary conditions. In addition, the method is applicable to arbitrary domain and scattered nodes. To capture the characteristics of discontinuous problems, the method is further improved by special techniques including coordinate mapping and local partition of unity enrichment. Results of simulation of strain localization and fracture, presented in the latter chapters of the thesis, indicate that the proposed meshless methods have been successfully applied to model such problems.

Papers resulting from the research

Journal papers

1. P. Le, N. Mai-Duy, T. Tran-Cong and G. Baker, (2007). A numerical study of strain localization in elasto-thermo-viscoplastic materials using radial basis function networks, *CMC: Computers, Materials & Continua*, **5**: 129–150.
2. S. Bordas, M. Dufflot and P. Le, (2008). A simple error estimator for extended finite elements, *Communications In Numerical Methods In Engineering*, **24**: 961–971.
3. P. Le, N. Mai-Duy, T. Tran-Cong and G. Baker, (2008). A meshless modeling of dynamic strain localization in quasi-brittle materials using radial basis function networks, *CMES: Computer Modeling in Engineering & Sciences*, **25**(1): 43–66.
4. P. Le, N. Mai-Duy, T. Tran-Cong and G. Baker, (2010). A Cartesian-grid Collocation Technique with Integrated Radial Basis Functions for mixed boundary value problems, *International Journal for Numerical Methods in Engineering*, **82**(4): 435-463.
5. P. Le, T. Rabczuk, N. Mai-Duy, and T. Tran-Cong (2010). A Moving

- IRBFN-based integration-free meshless method, *CMES: Computer Modeling in Engineering & Sciences*, under review.
6. P. Le, T. Rabczuk, N. Mai-Duy, and T. Tran-Cong (2010). A Moving IRBFN-based Galerkin meshless method, *CMES: Computer Modeling in Engineering & Sciences*, under review.
 7. P. Le, T. Rabczuk, N. Mai-Duy, T. Tran-Cong and S. Bordas (2010). An eXtended Moving IRBFN-based meshless method for elasto-static crack analysis, *International Journal for Numerical Methods in Engineering*, special issue of XFEM, under review.
 8. P. Le, T. Rabczuk, N. Mai-Duy, and T. Tran-Cong (2010). A Moving IRBFN meshless approach for simulation of elasto-plasticity in two dimensions, *in preparation*.
 9. P. Le, T. Rabczuk, N. Mai-Duy, and T. Tran-Cong (2010). A Moving IRBFN meshless approach for simulation of visco-plasticity in two dimensions, *in preparation*.
 10. P. Le, T. Rabczuk, N. Mai-Duy, and T. Tran-Cong (2010). A Moving IRBFN meshless approach for simulation of strain localization in two dimensions, *in preparation*.

Conference papers

1. P. Le, N. Mai-Duy, T. Tran-Cong and G. Baker, (2006). A meshless IRBF-based numerical simulation of adiabatic shear band formation in one dimension. In *Conference on Nonlinear Analysis & Engineering Mechanics Today*, Nguyen Quoc Son and Nguyen Dung (eds), HoChiMinh City, Vietnam, CD paper No 28 (10 pages).
2. P. Le, N. Mai-Duy, T. Tran-Cong and G. Baker, (2007). Meshless IRBF-based numerical simulation of dynamic strain localization in quasi-brittle

materials. In *9th U.S. National Congress on Computation Mechanics*, july, San Francisco, USA, CD page 63.

3. P. Le, N. Mai-Duy, T. Tran-Cong and G. Baker, (2008). An IRBFN Cartesian Grid Method Based on Displacement-Stress Formulation for 2D Elasticity Problems. In *8th World Congress on Computational Mechanics (WCCM8)*, June-July, Venice, Italy.

Contents

Dedication	ii
Certification of Dissertation	i
Acknowledgments	ii
Notes to Readers	iii
Abstract	iv
Published Papers Resulting from the Research	v
Acronyms & Abbreviations	xv
List of Tables	xvi
List of Figures	xix
Chapter 1 Introduction	1

1.1	Motivation	1
1.2	Review of strong discontinuities simulation	4
1.2.1	Boundary element methods	5
1.2.2	Finite element methods	5
1.2.3	Meshfree/meshless methods	9
1.3	The global IRBFN approximation	13
1.4	Outline of the Thesis	16

**Chapter 2 An IRBFN-based Cartesian-grid collocation technique
for mixed boundary value problems 18**

2.1	Introduction	19
2.2	Problem formulations	22
2.2.1	First-order systems	22
2.2.2	Two-dimensional Poisson equation	23
2.2.3	Linear elasticity problems	24
2.3	Numerical formulations	25
2.3.1	1D-IRBFN approximation	26
2.3.2	Irregular boundary interpolation technique	31
2.4	Numerical examples	32
2.4.1	Poisson equation in a regular domain	33

2.4.2	Poisson equation in a multiply-connected domain	36
2.4.3	Poisson equation in an irregular domain	38
2.4.4	Linear elastic cantilever beam	40
2.4.5	Linear elastic infinite plate with a circular hole	44
2.5	Conclusion	49

Chapter 3 A Moving IRBFN-based integration-free meshless method 54

3.1	Introduction	55
3.2	Construction of Moving IRBFN	57
3.2.1	Moving least-square approximants	57
3.2.2	Moving IRBFN interpolation	59
3.2.3	Selection of RBF centers and support radius	62
3.3	Numerical examples	63
3.3.1	Poisson equation	65
3.3.2	Linear elasticity problems	73
3.4	Concluding remarks	92

Chapter 4 A Moving IRBFN-based Galerkin meshless method 93

4.1	Introduction	94
4.2	Variational form of two dimensional elasticity problems	95

4.3	Numerical examples	97
4.3.1	One dimensional example	98
4.3.2	Cantilever Beam	100
4.3.3	Infinite plate with a circular hole	104
4.3.4	Mode I crack problem	108
4.4	Concluding remarks	111

Chapter 5 Modeling dynamic strain localization in quasi-brittle materials with IRBFN collocation technique 114

5.1	Introduction	115
5.2	Problem definition	117
5.3	Numerical formulation	120
5.3.1	Spatial discretisation	120
5.3.2	Regularization of IRBFNs and capturing of discontinuous strains	124
5.4	Numerical examples	129
5.4.1	Wave propagation in fully elastic bars	129
5.4.2	Wave propagation and strain localization in strain-softening bars: local continuum model	134
5.4.3	Wave propagation and strain localization in strain-softening bars: non-local continuum model	141

5.5	Conclusion	150
Chapter 6 Modeling strain localization in elasto- thermo-viscoplastic materials with IRBFN collocation technique		154
6.1	Introduction	155
6.2	Problem definition	157
6.3	Resolution of very large spatial gradients	159
6.4	Numerical examples	163
6.4.1	Example 1: A model of thermal imperfection	163
6.4.2	Example 2: A model of strength imperfection	170
6.4.3	Convergence characteristics	181
6.5	Conclusion	182
Chapter 7 Modeling elasto-plastic and strain localization problems in two dimensions with MIRBFN meshless method		185
7.1	Introduction	185
7.2	Constitutive models	186
7.2.1	Rate-independent elasto-plastic materials	186
7.2.2	Rate-dependent elasto-visco-plastic materials	188
7.3	Numerical algorithms	188
7.3.1	Weak form of MIRBFN meshless method	188

7.3.2	Radial return mapping scheme	189
7.3.3	Orthogonal residual solver	193
7.4	Preliminary results	195
7.4.1	Elasto-plastic constitutive model with linear strain hardening	195
7.4.2	Elasto-visco-plastic constitutive model with linear strain softening	197
7.5	Conclusion	198

Chapter 8 Modeling elasto-static crack problems with an extended MIRBFN (XMIRBFN) meshless method 203

8.1	Introduction	204
8.2	Extended Moving IRBFN procedure	206
8.2.1	Local PU enrichment	206
8.2.2	Variational form of 2D elasticity crack problems	208
8.2.3	Numerical Integration	210
8.3	Numerical examples	211
8.3.1	Infinite plate with a straight crack	213
8.3.2	Edge-cracked plate under tension	218
8.3.3	Edge-cracked plate under shear loading	220

8.3.4	Center crack in a finite plate	222
8.3.5	Double edge crack plate	224
8.4	Conclusion	226
Chapter 9 Conclusion		231
Appendix A Near crack tip asymptotic enrichment functions and computation of stress intensity factor		234
A.1	Derivatives of near crack tip enrichment functions	234
A.2	Contour integrals and their domain representations in two-dimensions	237

Acronyms & Abbreviations

BEM	Boundary Element Method
DRBFN	Direct Radial Basis Function Network
EFG	Element Free Galerkin
FDM	Finite Difference Method
FEM	Finite Element Method
FVM	Finite Volume Method
GFEM	General Finite Element Method
IRBFN	Indirect/Integrated Radial Basis Function Network
MLPG	Meshless Local Petrov-Galerkin
MLS	Moving Least Square
MRBFN	Moving Radial Basis Function Network
MRBFG	Moving Radial Basis Function Galerkin
PDEs	Partial Differential Equations
PU	Partition of Unity
RBFN	Radial Basis Function Network
RBF	Radial Basis Function
SVD	Singular Value Decomposition
XFEM	eXtended Finite Element Method
XMIRBFN	eXtended Moving Indirect Radial Basis Function Network

List of Tables

3.1	Poisson equation in a regular domain: uniform discretisations with MIRBFN	66
3.2	Poisson equation in a regular domain: uniform discretisations with global IRBFN	66
3.3	Poisson equation in a regular domain: unstructured nodes with MIRBFN	67
3.4	Poisson equation in an irregular domain: structured discretizations with MIRBFN	71
3.5	Poisson equation in an irregular domain: structured discretizations with global IRBFN	72
3.6	Poisson equation in an irregular domain: unstructured discretisation with MIRBFN	74
3.7	Cantilever beam: uniform discretizations with MIRBFN ($\mu = 0.3$).	75
3.8	Cantilever beam: uniform discretizations with MIRBFN ($\mu = 0.5$).	77
3.9	Cantilever beam: uniform discretizations with global IRBFN ($\mu = 0.3$).	78

3.10	Cantilever beam: unstructured nodes with MIRBFN ($\mu = 0.3$).	79
3.11	Cantilever beam: structured FEM mesh with four-node quadrilateral element (Q4) ($\mu = 0.3$).	80
3.12	Infinite plate with a circular hole: structured discretisation with MIRBFN ($\mu = 0.3$).	83
3.13	Infinite plate with a circular hole: structured discretisation with MIRBFN ($\mu = 0.5$).	83
3.14	Infinite plate with a circular hole: structured discretisation with global IRBFN ($\mu = 0.3$).	85
3.15	Infinite plate with a circular hole: unstructured node distribution with MIRBFN ($\mu = 0.3$).	86
3.16	Center crack problem: uniform discretisations with MIRBFN ($\mu = 0.3$).	88
3.17	Center crack problem: uniform discretizations with MIRBFN ($\mu = 0.5$).	91
6.1	Comparison of the results between methods: The results obtained by the present IRBFN method are generally between those by the MSPH and the CPS methods, except for the case of Θ_{min} and γ_{t_1}	181
6.2	Comparison of the time lags between methods: agreement is generally excellent, except that the CPS results show an earlier occurrence of the local temperature minimum.	181

8.1	Edge-cracked plate in tension: normalised $\frac{K_I}{K_I^{ref}}$ computed by the present method compared to that of XFEM and EFG	219
8.2	Edge-cracked plate under shearing: K_I and K_{II} computed by the present method	220
8.3	Edge-cracked plate under shearing: SIFs by EFG (Fleming et al., 1997)	221
8.4	Center crack in a finite plate: K_I computed by the present method	223
8.5	Double edge crack plate: K_I computed by the present method .	225

List of Figures

2.1	Domain discretization by Cartesian grid: the boundary and interior points used for constructing the IRBFN approximations at point \mathbf{x} are highlighted. The intersections of the grid lines and the boundary (e.g. points 1, N) are referred to as irregular if they do not coincide with grid points.	28
2.2	1D interpolation scheme for irregular boundary	32
2.3	Poisson equation in a regular domain: domain discretisation with 11×11 points.	34
2.4	Poisson equation in a regular domain: solution of $\phi(x, y)$ obtained by the proposed method in comparison with exact solution along $y = 1$	35
2.5	Poisson equation in a regular domain: solution of $\phi(x, y)$ obtained by the proposed method in comparison with exact solution along $y = 0$	36
2.6	Poisson equation in a regular domain: solution of $\phi(x, y)$ obtained by the proposed method in comparison with exact solution along $x = 1$	37

2.7	Poisson equation in a regular domain: solution of $\xi(x, y)$ obtained by the proposed method in comparison with exact solution (a) along $y = 1$, (b) along $y = 0$	38
2.8	Poisson equation in a regular domain: solution of $\eta(x, y)$ obtained by the proposed method in comparison with exact solution (a) along $x = 0$, (b) along $x = 1$	38
2.9	Poisson equation in a regular domain: relative error norms L_2^ϕ and $L_2^{\xi\eta}$	39
2.10	Poisson problem in a multiply-connected domain: domain discretisation with 512 nodes.	40
2.11	Poisson equation in a multiply-connected domain: solutions along curved boundary of $\phi(x, y)$ with 512 nodes.	41
2.12	Poisson equation in a multiply-connected domain: solutions along curved boundary $\xi(x, y)$ with 512 nodes.	41
2.13	Poisson equation in a multiply-connected domain: solutions along curved boundary $\eta(x, y)$ with 512 nodes.	42
2.14	Poisson equation in a multiply-connected domain: relative error norms L_2^ϕ and $L_2^{\xi\eta}$, and convergence rates.	43
2.15	Poisson problem in an irregular domain: domain discretisation with 77 points.	44
2.16	Poisson equation in an irregular domain: relative error norms L_2^ϕ and $L_2^{\xi\eta}$, and convergence rates.	45
2.17	Cantilever beam: a mathematical model.	45

2.18 Cantilever beam: discretisation model with 20×5 CPs.	46
2.19 Cantilever beam: $u_y(x, y)$ along $y = 0$ with 20×5 CPs ($\mu = 0.3$).	46
2.20 Cantilever beam: s_{xy} along Dirichlet boundary $x = L$ with 20×5 CPs ($\mu = 0.3$).	47
2.21 Cantilever Beam ($\mu = 0.3$): s_x solution with 20×5 CPs (a) along $y = D/2$, (b) along $y = -D/2$	47
2.22 Cantilever beam ($\mu = 0.3$): relative error norms L_2^u and L_2^σ , and convergence rates.	48
2.23 Cantilever beam ($\mu = 0.5$): relative error norms L_2^u and L_2^σ , and convergence rates.	49
2.24 Cantilever beam ($\mu = 0.3$): comparison of efficiency between the proposed method and FEM. Computational cost (second) versus L2 relative error norm in displacement.	50
2.25 Cantilever beam ($\mu = 0.3$): comparison of efficiency between the proposed method and the most efficient ES-PIM and ES-RPIM. Differential computational cost (DCC) of different methods in comparison with FEM (CPU time of FEM – CPU time of the reference method) at the same level of relative error in displacement norm.	50
2.26 Infinite plate with a circular hole.	51
2.27 Infinite plate with a circular hole: domain discretisation with 493 CPs.	51
2.28 Infinite plate with a circular hole: $u_x(x, y)$ along $y = 0$ with 493 CPs ($\mu = 0.3$).	52

2.29	Infinite plate with a circular hole: s_x along $x = 0$ with 493 CPs ($\mu = 0.3$).	52
2.30	Infinite plate with a circular hole ($\mu = 0.3$): relative error norms L_2^u and L_2^σ , and convergence rates.	53
2.31	Infinite plate with a circular hole ($\mu = 0.5$): relative error norms L_2^u and L_2^σ , and convergence rates.	53
3.1	Schematic representation of a moving IRBFN: Ω is the domain of interest which is subdivided into N overlapping subdomains Ω_I centered at \mathbf{x}_I	61
3.2	Moving IRBFN yields symmetric, sparse and banded interpola- tion matrices.	62
3.3	Example of MIRBFN shape functions: (a) $\phi_I(x)$ in one dimension and (b) $\phi_I(x, y)$ in two dimensions.	63
3.4	Poisson equation in a regular domain: discretisation with uniform distribution of (a) 11×11 nodes, (b) 21×21 nodes. The small circles are RBF centers and the big one is subdomain Ω_I	66
3.5	Poisson equation in a regular domain with uniform distribution of 21×21 nodes: influence of the local support radius on the accuracy of the solution.	67
3.6	Poisson equation in a regular domain with uniform distribution of 21×21 nodes: influence of the RBF width β on the accuracy of the solution.	68

3.7	Poisson equation in a regular domain with uniform distribution of nodes: relative error norms L_2^ϕ and $L_2^{\xi\eta}$, and associated convergence rates.	69
3.8	Poisson equation in a regular domain: discretisation with unstructured distribution of (a) 327 nodes, (b) 691 nodes, (c) 1723 nodes and (d) 2248 nodes.	70
3.9	Poisson equation in a regular domain: relative error norms L_2^ϕ and $L_2^{\xi\eta}$, and associated convergence rates obtained by MIRBFN method with unstructured nodes.	71
3.10	Poisson equation in a regular domain with uniform distribution of nodes: CPU times of MIRBFN method versus that of global IRBFN method.	72
3.11	Poisson equation in an irregular domain: structured discretisation with 266 nodes.	72
3.12	Poisson equation in an irregular domain: discretisation with unstructured distribution of (a) 51 nodes, (b) 338 nodes, (c) 1046 nodes and (d) 1711 nodes.	73
3.13	Poisson equation in an irregular domain with regular distribution of nodes: relative error norms L_2^ϕ and $L_2^{\xi\eta}$, and associated convergence rates.	74
3.14	Poisson equation in an irregular domain with unstructured distribution of nodes: relative error norms L_2^ϕ and $L_2^{\xi\eta}$, and associated convergence rates.	75

3.15 Poisson equation in an irregular domain with structured points: CPU times of MIRBFN method versus that of global IRBFN method.	76
3.16 Cantilever beam: a mathematical model.	76
3.17 Cantilever beam: discretisation with 20×5 nodes.	77
3.18 Cantilever beam: a FEM mesh with 8×32 Q4 elements.	77
3.19 Cantilever beam: discretisation with unstructured distribution of (a) 43 nodes, (b) 170 nodes, (c) 616 nodes, and (d) 1112 nodes.	78
3.20 Cantilever beam: s_{xy} at $x = 2.4686$ with 36×9 nodes ($\mu = 0.3$).	79
3.21 Cantilever beam: L_2 relative error norms for displacement and stress for $\mu = 0.3$ and $\mu = 0.5$, with associated convergence rates.	80
3.22 Cantilever beam: L_2 relative error norms for displacement and stress, and associated convergence rates for $\mu = 0.3$ with different unstructured nodal configurations.	81
3.23 Cantilever beam: CPU times of MIRBFN method versus that of FEM and global IRBFN method.	82
3.24 Infinite plate with a circular hole.	82
3.25 Infinite plate with a circular hole: computational domain with 119 nodes.	83
3.26 Infinite plate with a circular hole: discretisation with unstruc- tured distribution of (a) 68 nodes, (b) 156 nodes, (c) 1024 nodes, and (d) 2439 nodes.	84

3.27	Infinite plate with a circular hole: s_x along $x = 0$ with 409 nodes ($\mu = 0.3$).	85
3.28	Infinite plate with a circular hole: L_2 relative error norms for displacement and stress for $\mu = 0.3$ and $\mu = 0.5$. Convergence rates are also shown.	86
3.29	Infinite plate with a circular hole: L_2 relative error norms for displacement and stress for $\mu = 0.3$ with unstructured nodes. Convergence rates are also shown.	87
3.30	Infinite plate with a circular hole: CPU times of MIRBFN method versus that of global IRBFN method.	88
3.31	Infinite cracked plate under remote tension.	89
3.32	Infinite cracked plate: analyzed portion.	89
3.33	Infinite cracked plate: u_x obtained by (a) exact solution and (b) MIRBFN method with 24×24 nodes ($\mu = 0.3$).	90
3.34	Infinite cracked plate: u_y obtained by (a) exact solution and (b) MIRBFN method with 24×24 nodes ($\mu = 0.3$).	90
3.35	Infinite cracked plate - stress ahead of the crack-tip ($\theta = 0, r > 0$): (a) s_x and (b) s_y obtained by MIRBFN method and exact solutions with 24×24 nodes ($\mu = 0.3$).	90
3.36	Infinite cracked plate: L_2 relative error norms for displacement and stress, and associated convergence rates for $\mu = 0.3$ and $\mu = 0.5$	91
4.1	One dimensional example: a mathematical model.	98

4.2	One dimensional example: the results obtained by present method with 9 nodes are interpolated with 50 nodes, (a) displacement and (b) stress.	99
4.3	One dimensional example: the results obtained by the EFG method with 9 nodes are interpolated with 50 nodes, (a) displacement and (b) stress.	99
4.4	One dimensional example: L_2 error norm for displacement.	99
4.5	One dimensional example: L_2 error norm for energy.	100
4.6	Cantilever beam: a mathematical model.	101
4.7	Cantilever beam: discretisation model with 20×5 nodes.	101
4.8	Cantilever beam: σ_x given by (a) MIRBFNG with 20×5 nodes and (b) Exact solution.	102
4.9	Cantilever beam: L_2 error norm for displacement.	103
4.10	Cantilever beam: L_2 error norm for energy.	104
4.11	Cantilever beam: unstructured discretisations.	104
4.12	Cantilever beam: convergence of τ_{xy} at $x = 2.40$ with unstructured nodal refinement.	105
4.13	Cantilever beam: L_2 error norm for displacement with unstructured nodes.	105
4.14	Cantilever beam: L_2 error norm for energy with unstructured nodes.	106
4.15	Infinite plate with a circular hole.	106

4.16	Infinite plate with a circular hole: computational domain discretization with 315 nodes.	107
4.17	Infinite plate with a circular hole: L_2 error norm for displacement.	108
4.18	Infinite plate with a circular hole: L_2 error norm for energy. . .	109
4.19	Infinite cracked plate under remote tension.	110
4.20	Infinite cracked plate: analyzed portion.	110
4.21	Infinite cracked plate: (a) MIRBFNG solution and (b) exact solution of u_x with 20×10 nodes ($\mu = 0.3$).	111
4.22	Infinite cracked plate: (a) MIRBFNG solution and (b) exact solution of u_y with 20×10 nodes ($\mu = 0.3$).	111
4.23	Infinite cracked plate: (a) MIRBFNG solution and (b) exact solution of σ_x with 20×10 nodes ($\mu = 0.3$).	112
4.24	Infinite cracked plate: L_2 error norm for displacement.	112
4.25	Infinite cracked plate: L_2 error norm for energy.	113
5.1	A model of uniform bars.	118
5.2	A constitutive relation for quasi-brittle materials.	118
5.3	Regularization of IRBFNs.	125
5.4	Noisy input, exact solution, DRBFN regularization and IRBFN regularization.	128

5.5	Fully elastic bars: the evolution of displacement, the continuous curves denote the IRBFN solutions and the dash ones the exact solution.	132
5.6	Fully elastic bars: the propagation of step function waves of strain: the continuous curves denote the IRBFN solutions, the dashed ones exact solutions and the dot-dashed curves indicate the IRBFN regularized results on the left column. On the right column, the non-regularized results are removed for clarity. . . .	133
5.7	Fully elastic bars: the propagation of step function waves of strain: the continuous curves denote the IRBFN solutions, the dashed ones exact solutions and the dot-dashed curves indicate the IRBFN regularized results on the left column. On the right column, the non-regularized results are removed for clarity. . . .	134
5.8	Fully elastic bars: the displacement and strain waves propagations.	135
5.9	Local continuum model: the evolution of: (a) displacement, (b) strain, (c) velocity and (d) stress at $x = -0.6329$ with 80 uniform collocation points.	137
5.10	Local continuum model: the evolution of displacement with a uniform discretisation of 80 points.	138
5.11	Local continuum model: the evolution of velocity with a uniform discretisation of 80 points.	139
5.12	Local continuum model: the evolution of strain with a uniform discretisation of 80 points.	140

5.13	Local continuum model: the curve labels represent time levels: 1($t = 60.0$) ; 2($t = 70.0$) ; 3($t = 80.0$) ; 4($t = 90.0$) ; 5($t = 100.0$) (a) the evolution of velocity, (b) stress obtained with a uniform discretisation of 80 points.	140
5.14	Local continuum model: the evolution of displacement at time levels: 1($t = 60.0$) ; 2($t = 70.0$) ; 3($t = 80.0$) ; 4($t = 90.0$) ; 5($t =$ 100.0) (the curve labels indicate time levels) (a) 20 points, (b) 40 points, (c) 60 points and (d) 80 points (uniformly discretised).	141
5.15	Local continuum model: the evolution of strain at time levels: 1($t = 60.0$) ; 2($t = 70.0$) ; 3($t = 80.0$) ; 4($t = 90.0$) ; 5($t = 100.0$) (a) 20 points, (b) 40 points, (c) 60 points and (d) 80 points (uniformly discretised).	142
5.16	Example of IRBFN regularization.	146
5.17	Non-local continuum model: the evolution of velocity with a uni- form distribution of 161 collocation points.	147
5.18	Non-local continuum model: the evolution of displacement with a uniform distribution of 161 collocation points.	148
5.19	Non-local continuum model: the evolution of non-local strain with a uniform distribution of 161 collocation points.	149
5.20	Non-local continuum model: the curve labels represent time lev- els: 1($t = 60.0$) ; 2($t = 70.0$) ; 3($t = 80.0$) ; 4($t = 90.0$) ; 5($t = 100.0$) (a) the evolution of velocity obtained ,(b) stress obtained with a uniform distribution of 161 collocation points .	150

- 5.21 Non-local continuum model: the evolution of displacement at time levels: 1($t = 60.0$) ; 2($t = 70.0$) ; 3($t = 80.0$) ; 4($t = 90.0$) ; 5($t = 100.0$) (the curve labels indicate time levels) (a) 41 points, (b) 81 points, (c) 121 points and (d) 161 points uniformly discretised. 151
- 5.22 Non-local continuum model: the evolution of non-local strain at time levels: 1($t = 60.0$) ; 2($t = 70.0$) ; 3($t = 80.0$) ; 4($t = 90.0$) ; 5($t = 100.0$) (the curve labels indicate time levels) (a) 41 points, (b) 81 points, (c) 121 points and (d) 161 points uniformly discretised. 152
- 5.23 Non-local continuum model: convergence of the solution, the curve labels indicate number of collocation points (CP) as follows. 1(41 CPs, $\lambda = 3.39150$); 2(81 CPs, $\lambda = 3.39150$); 3(121 CPs, $\lambda = 3.39150$); 4(161 CPs, $\lambda = 3.391895$); 5(201 CPs, $\lambda = 6.2267131$); 6(241 CPs, $\lambda = 7.8271318$) at the time $t = 70.0$. 153
- 6.1 (a) Coordinate mapping with 61 collocation points, uniformly spaced in the computational space y , (b) IRBFN solution $v(x)$ and exact solution $u(x)$ of (6.18) with $\epsilon = 10^{-6}$, $\alpha = 13$, on the physical space x 161
- 6.2 The curve labels indicate time levels (μs): 1(59.489); 2(60.257); 3(60.433); 4(60.477); 5(60.507); 6(60.602); 7(60.702); 8(60.804); 9(60.903); 10(60.934); 11(60.975); 12(60.992); 13(61.003); 14(61.019). (a) Evolution of temperature, (b) the temperature in the neighbourhood of $y = 0$ showing that the solution is highly consistent with the boundary conditions at $y = 0$, (c) evolution of Ψ , (d) evolution of plastic train. 164

6.3	The evolution of plastic strain rate $\dot{\gamma}$. The curve labels indicate time levels (μs): 1(59.489); 2(60.257); 3(60.433); 4(60.477); 5(60.507); 6(60.602); 7(60.702); 8(60.804); 9(60.903); 10(60.934); 11(60.975); 12(60.992); 13(61.003); 14(61.019).	165
6.4	The curve labels indicate time levels (μs): 1(59.489); 2(60.257); 3(60.433); 4(60.477); 5(60.507); 6(60.602); 7(60.702); 8(60.804); 9(60.903); 10(60.934); 11(60.975); 12(60.992); 13(61.003); 14(61.019). (a) Spatial structure of shear stress at different times, (b) the shear stress in the neighbourhood of $y = 0$ showing that the solution is highly consistent with the boundary conditions at $y = 0$, (c) spatial structure of particles velocity at different times of localization, (d) the structure of the velocity boundary layer. . . .	166
6.5	(a) and (b) evolution of shear stress at $y = 0$, (c) and (d) evolution of temperature at $y = 0$	167
6.6	(a) Evolution of plastic strain rate $\dot{\gamma}$ at $y = 0$, (b) evolution of plastic strain at $y = 0$	168
6.7	The behaviour of the shear stress at $y = 0$ around the onset of localisation. P is defined by (6.23).	169
6.8	More detailed evolutions at $y = 0$	170
6.9	Evolution of the spatial profile of the plastic strain rate.	171

- 6.10 The spatial structure of particle velocity at selected points of time: (a) full linear scale, (c) semi-log scale $0 < y \leq 1$, (b) behaviour in the neighbourhood of $y = 0$, linear scale, (d) behaviour in the neighbourhood of $y = 0$, semi-log scale $y > 0$. The band narrowing stage (the solid curves) includes instants of $t = 0.76963(1)$, $0.77020(2)$, $0.77056(3)$, $0.77091(4)$, $0.77116(5)$, $0.77145(6)$ and the band widening or post-localization stage (the dash curves) includes instants $t = 0.77254(7)$, $0.78364(8)$, $0.78815(9)$, $0.79408(10)$, $0.79763(11)$, $0.80000(12)$ 173
- 6.11 The spatial structure of field variables at selected points of time (a) plastic strain, (b) plastic strain rate, (c) temperature, (d) shear stress. The band narrowing stage (the solid curves) includes instants of $t = 0.76963(1)$, $0.77020(2)$, $0.77056(3)$, $0.77091(4)$, $0.77116(5)$, $0.77145(6)$ and the band widening or post-localization stage (the dash curves) includes instants $t = 0.77254(7)$, $0.78364(8)$, $0.78815(9)$, $0.79408(10)$, $0.79763(11)$, $0.80000(12)$ 174
- 6.12 Evolution of bandwidths shows the band narrowing stage followed by the band widening stage, and the bandwidth based on the plastic strain rate is the narrowest while the one based on temperature is the widest. 175
- 6.13 The evolution of (a) shear stress, (b) temperature, (c) plastic strain, (d) plastic strain rate at $y = 0$. A peak value of the plastic strain rate of 10606.778 occurs at $t_1 = 0.77154$, the temperature of 10.9490 at $t_2 = 0.77250$, the stress of 0.84238 at $t_3 = 0.77440$, and a second peak (local minimum of 7.4781) of temperature at $t_4 = 0.77759$. Thus $t_1 < t_2 < t_3 < t_4$ 176

6.14	The interaction between thermal diffusion and plastic heating at $y = 0$: the dash curve depicts the evolution of the effect of thermal diffusion, $k\Theta_{,yy}$, dash-dot curve the effect of plastic heating $s\dot{\gamma}$, and the solid curve the combined effect $\frac{d\Theta}{dt} = k\Theta_{,yy} + s\dot{\gamma}$ of thermal diffusion and plastic heating. The onset of strain localisation occurs at $t = 0.76976$. Some key events occur at $t_1 = 0.77154 < t_2 = 0.77250 < t_3 = 0.77440 < t_4 = 0.77759$, as identified in the previous figure.	177
6.15	The evolution of plastic strain rate $\dot{\gamma}$	178
6.16	The evolution of temperature.	179
6.17	The evolution of shear stress.	180
6.18	Convergence characteristics: (a) thermal imperfection model, (b) strength imperfection model.	184
7.1	Schematic representation of orthogonal residual method.	193
7.2	A holed plate in uniaxial tension: a mathematical model.	196
7.3	A holed plate in uniaxial tension: discretization.	196
7.4	A holed plate in uniaxial tension with elasto-plastic constitutive model: load versus displacement.	197
7.5	A holed plate in uniaxial tension with elasto-plastic constitutive model: equivalent plastic strain at load-step 15.	198
7.6	A holed plate in uniaxial tension with elasto-plastic constitutive model: equivalent plastic strain at load-step 25.	199

7.7	A holed plate in uniaxial tension with elasto-plastic constitutive model: equivalent plastic strain at load-step 45	199
7.8	A holed plate in uniaxial tension with elasto-plastic constitutive model: von Mises stress at load-step 45.	200
7.9	A holed plate in uniaxial tension with elasto-visco-plastic constitutive model with linear strain softenig: load versus displacement.	200
7.10	A holed plate in uniaxial tension with elasto-visco-plastic constitutive model with linear strain softenig: strain localization at load-step 10.	201
7.11	A holed plate in uniaxial tension with elasto-visco-plastic constitutive model with linear strain softenig: strain localization at load-step 15.	201
7.12	A holed plate in uniaxial tension with elasto-visco-plastic constitutive model with linear strain softenig: von Mises stress at load-step 15.	202
8.1	Domain of influence of nodes partially and completely cut by a crack	206
8.2	A body with internal discontinuous surface subjected to loads.	208
8.3	Schematic representation of sub-triangulation of integration cells.	211
8.4	Mapping transformation of integration on a rectangle into integration on a unit triangle for near singular enrichment functions.	212
8.5	Infinite cracked plate under remote tension	213
8.6	Infinite cracked plate: discretised with 50×50 nodes.	214

8.7	Infinite cracked plate: energy error norm versus different values of β with 30×30 nodes ($\alpha = 2.1$).	215
8.8	Infinite cracked plate: (a) XMIRBFN solution and (b) exact solution to u_x with 50×50 nodes.	215
8.9	Infinite cracked plate: (a) XMIRBFN solution and (b) exact solution to u_y with 50×50 nodes.	215
8.10	Infinite cracked plate: (a) XMIRBFN solution and (b) exact solution to σ_x with 50×50 nodes.	216
8.11	Infinite cracked plate: (a) XMIRBFN solution and (b) exact solution to σ_y with 50×50 nodes.	216
8.12	Infinite cracked plate: (a) XMIRBFN solution and (b) exact solution to σ_{xy} with 50×50 nodes.	217
8.13	Infinite cracked plate: L_2 error norm for displacement.	217
8.14	Infinite cracked plate: L_2 error norm for energy.	218
8.15	Infinite cracked plate: convergence of K_I	219
8.16	Infinite cracked plate: relative error of K_I	220
8.17	Edge-cracked plate under tension	221
8.18	Edge-cracked plate under tension: discretization with 12×24 nodes	221
8.19	Edge-cracked plate under tension: deformed configuration with 12×24 nodes.	222
8.20	Edge-cracked plate under shearing	223

8.21	Edge-cracked plate under shearing: XMIRBFN solution to $u_y(x, y)$ with 12×26 nodes	224
8.22	Center crack in a finite plate under tension	225
8.23	Center crack in a finite plate: XMIRBFN solution to $u_y(x, y)$ with 21×62 nodes.	226
8.24	Center crack in a finite plate: deformed configuration with 21×62 nodes.	227
8.25	Double edge crack plate	228
8.26	Double edge crack plate: XMIRBFN solution to $u_x(x, y)$ with 15×44 nodes.	228
8.27	Double edge crack plate: XMIRBFN solution to $u_y(x, y)$ with 15×44 nodes.	229
8.28	Double edge crack plate: deformed configuration with 15×44 nodes.	230
A.1	Global and local coordinate systems	236
A.2	Domain used for computation of mixed mode stress intensity factors in two dimensional space	240

Chapter 1

Introduction

This chapter gives a general description of the overall picture of the present research. In this chapter, we present an overview of numerical simulation of strong discontinuity including crack and shear bands. In addition, global Indirect/Integrated/Integral Radial Basis Function Network (IRBFN) approximation is briefly reviewed and the plan of this research is outlined at the end of the chapter.

1.1 Motivation

In classical solid mechanics, analyses are generally carried out in the context of the strict continuum assumption where the displacement field is postulated to be continuous. However, jumps in the displacement field have necessarily to be regarded (in macroscopic scale) in phenomena such as shear bands (strain localization), cracks and slip lines. These behaviours are observed on a wide range of engineering materials including metals, concrete and geological materials, and are characteristics of inelastic deformations. From now on the jumps in the displacement field are termed *strong discontinuities*. They need to be dis-

tinguished from *weak discontinuities* corresponding to the jumps in the strain field (the displacement remains C^0 continuous). Typically, strain localization may occur within a very narrow zone (e.g. in a $1m$ structure the width of a shear band might be $10^{-5}m$) while the remaining part of the structure experiences unloading. Such strain localization usually can be induced by geometrical nonlinearities (e.g. necking of metallic bars) or by material instabilities (e.g. micro-cracking). The formation of shear bands often precedes the formation and development of cracks, leading to fracture and rupture in the structure. Furthermore, stress and strain fields are singular at crack tip in a linear elastic fracture mechanics theory or a highly localized strain region (i.e. the nonlinear zone around the crack tip is often referred to as the fracture process zone) exists in the vicinity of the crack tip in a nonlinear elastic fracture mechanics scope (Tada et al., 2000).

Mathematically, the onset of strain localization in the context of a rate-independent local continuum model leads to loss of hyperbolicity of the governing partial differential equations, i.e. when the matrix of tangent modulus ceases to be positive-definite. At the critical point, the fundamental path may bifurcate into several equilibrium paths and the solution starts losing its uniqueness. From a physical point of view, the loss of hyperbolicity results in ill-posed mathematical model since the region undergoing strain softening was restricted to a volume of (Lebesgue) measure zero (Bazant and Belytschko, 1985). Thus the conventional theory of solid mechanics is proved inadequate for simulation of strain localization and fracture.

It is well-known that there are two types of mesh sensitivities in numerical simulation of shear bands in inelastic solids. The first appears in phenomenological rate-independent plasticity as stated above. It is due to the fact that the rate-independent plasticity theories admit the singular solutions exhibiting a zero volume of strain localization. Hence, the discrete Galerkin formulations with finite mesh size are unable to capture this discontinuous surface precisely. The

second is mesh-alignment sensitivity. It is often referred to as the inability of a finite element mesh to resolve shear bands at angles oblique to the elements boundaries, which happens in mesh-based numerical computations regardless of whether a continuum model is regularized or not (Sluys, 1992).

To regularize the ill-posed problems (the first type of mesh sensitivities), there are presently two large families of methodologies for numerical simulation of strong discontinuities which can be categorized into continuum and discrete approaches (Oliver, 1996a). In continuum approaches, standard stress-strain constitutive equations can be considered everywhere. In order to model the discontinuities, the following two basic ingredients have been resorted to: (i) an implicit regularization employs the so-called *characteristic length* which is taken as a material property or as a numerical parameter (Oliver, 1996b; Wells and Sluys, 2000; Jirásek, 2000), and (ii) regularized constitutive models lead to well-posed mathematical models and allow strain localization to occur, for example, non-local models (Patzák and Jirásek, 2003; Le et al., 2007b, 2008a), rate-dependent models (Le et al., 2006, 2007a), gradient-dependent models, viscoplastic models (Wang et al., 1997), damage-based models (de Borst, 2002), and Cosserat continuum model (Sluys, 1992; Alsaleh, 2004). In contrast to continuum approaches, discrete approaches such as smeared crack and cohesive crack models (Elices et al., 2002; Kubair and Geubelle, 2003) are based on nonlinear fracture mechanics theory to characterize cohesive behaviour at the discontinuous surfaces, whereas standard stress-strain constitutive relations are utilized for the remaining continuous parts of the domain. Furthermore, appropriate criteria have to be chosen (Rudnicki and Rice, 1975; Belytschko et al., 2003a) to determine the initiation and propagation of the discontinuity.

1.2 Review of strong discontinuities simulation

The equations governing the evolution of strain localization (in the context of a rate-independent local continuum model) are fully coupled, highly nonlinear and stiff, and it is not simple, even for one-dimensional problems, to obtain closed form solutions that could describe a range of constitutive behaviours and boundary and initial conditions. For a number of special cases, closed form exact and approximate solutions have been developed by several authors to capture some of the fundamental characteristics of strain localization. For example, evolution of adiabatic shear bands in elasto-thermo-viscoplastic materials was studied by Rice and Rudnicki (1980); Molinari and Clifton (1987); Wright (1990); Bai and Dodd (1992); Wright (2002); Sherif and Shawki (1992) and isothermal shear bands in quasi-brittle materials by Bazant and Belytschko (1985); Sluys (1992); Xin and Chen (2000); Armero and Park (2003) for one-dimensional problems. For two- (three-) dimensional problems, Hill (1962) investigated general characteristics of wave propagation in solids. Bardet (1991) presented the analytical solutions for localized bifurcation of compressible solids subjected to plane strain loadings. Loret and Prevost (1990a,b) introduced viscosity as a means to regularize the ill-posed problems and devised general formulations of strain localization in elasto-visco-plastic solids.

Generally, numerical solutions are helpful in a parametric study to cover a range of possible behaviours. However, it could be costly to resolve shear bands fully in a large scale computation since the morphology of a shear band exhibits very fine transverse scales, with aspect ratios of the high shear region usually in the hundreds or even thousands or more (Bai and Dodd, 1992; Wright, 2002). Thus it is highly desirable to have effective and efficient numerical methods for the analysis of strain localization and fracture problems.

1.2.1 Boundary element methods

Among the conventional numerical methods, Boundary Element method (BEM) has been successfully applied to model crack propagation. However, to the author's best knowledge a majority of works has been developed in the context of linear elastic fracture mechanics, BEM is not yet well-developed for non-linear materials and multiple-cracks (Beballal et al., 2006). See also the studies by Mackerle (2000); Wu and Stern (1989); Yan and Nguyen-Dang (1995); Liang and Li (1991); Silveira et al. (2005); Tan et al. (2005); García-Sánchez et al. (2006); Rungamornrat (2006); Beballal et al. (2006), for example.

1.2.2 Finite element methods

The conventional FEM (Belytschko et al., 2003b) based on the piecewise continuous polynomial function space is sufficient to yield very good results for smooth problems and enrichment does not offer any significant improvement. However, when the solutions are not smooth or possess high/steep gradients (i.e. crack, shear-band, boundary layer, singularity), standard FEMs seem unable to lead to good results. In these cases, attempts have been made to capture the discontinuities by techniques such as remeshing, element deletion methods, cohesive element methods and enriched FEM.

Finite elements integrated with adaptive remeshing have been used (Pastor et al., 1991; Potyondy et al., 1995; Askes, 2000; Schollmann et al., 2003; Patzák and Jirásek, 2004; Li et al., 2005). However, for multiple cracks, the FEM may be very burdensome due to the requirement of remeshing. Furthermore, remeshing requires mapping the internal variables between different meshes, which decreases accuracy for nonlinear problems.

The simplest way to treat cracks are the so-called element deletion methods (Fan and Fish, 2008), where the elements containing discontinuities in the underlying

coarse mesh are deleted and replaced by a local finer mesh, and the discontinuities are treated explicitly by double nodes in the superimposed mesh. To avoid mesh-dependence, the dissipative energy in the softening region is scaled to the fracture energy.

In the cohesive elements approaches (Xu and Needleman, 1994; Camacho and Ortiz, 1996; Ortiz and Pandoli, 1999; Zhou and Molinari, 2004; Yang et al., 2005; Molinari et al., 2006), cracks or shear bands are only allowed to develop along existing inter-element edges. This provides the method with comparative simplicity. However, the disadvantage is that the crack/shear band propagation depends on the geometry and the topology of the mesh. Furthermore, the dissipated energy is over-estimated when the actual discontinuity path is not coincident with element edges. Remeshing and refinement could overcome this shortcoming but these approaches are computationally expensive. Mesh-dependence has been reported in the work of Falk et al. (2001). This can be lessened by adding randomness to the strength as in Zhou and Molinari (2004).

Finite elements with embedded discontinuities (EFEM) (Oliver, 1996a,b; Wells and Sluys, 2000; Jirásek, 2000; Oliver et al., 2003; Spencer and Shing, 2003; Oliver and Huespe, 2004a,b; Oliver et al., 2006b,a; Linder and Armero, 2007; Oliver et al., 2008) are based on an enrichment at element level. Thus EFEM can be incorporated into commercial FEM packages with relatively small effort. This method can handle arbitrary discontinuities without remeshing. Crack opening is mostly assumed constant although more realistic piecewise linear crack opening was reported by Linder and Armero (2007). EFEM can be classified into three different groups: KOS, SOS and KSON. In kinematically optimal symmetric formulation (KOS), the kinematics is introduced in a way that does not restrict the rigid body relative motion of the two portions of the element. However, traction continuity across the discontinuous interface is not guaranteed. For statically optimal symmetric formulation (SOS), in contrast to KOS, the traction continuity across the discontinuous interface is satisfied but

the rigid body relative motion of the two portions of the element is not guaranteed and stress locking phenomenon is encountered in many cases (Oliver et al., 2003). Hence, mixed and assumed enhanced strain techniques are envisaged as appropriate remedies. Both traction continuity across the discontinuous interface and rigid body relative motion of the two portions of the element are guaranteed in statically and kinematically optimal non-symmetric formulation (SKON). However, this formulation results in an unsymmetric stiffness matrix. Since the enrichment can be reduced at element level in EFEM, the computational cost does not increase for multiple cracks/shear bands (Oliver et al., 2006b). A comprehensive review of EFEM has been presented by Jirásek (2000).

A very accurate method to capture discontinuities is the extended finite element method (XFEM) (Belytschko and Black, 1999; Moës et al., 1999a), in which the solution space is enriched by a priori knowledge about the behaviour of the solution near any discontinuity (Dolbow, 1999; Chessa, 2002) with the use of the partition of unity method (Melenk and Babuška, 1996; Babuška and Melenk, 1997). Recently developed XFEM has been proven to be an efficient tool for computational fracture mechanics, including multiple-cracks simulation (Budyn, 2004). This method can also deal with arbitrary crack or shear band propagation without adaptive remeshing. Unlike EFEM, XFEM enriches the nodes whose support (i.e. the elements surrounding a specific node) is intersected by the discontinuity surfaces, hence additional degrees of freedom inherent to the nodes are introduced in the variational formulation and have to be solved for (Bordas, Dufloot, and Le, 2008a). Recent studies (Fries and Belytschko, 2006) show that no additional unknowns are introduced at the enriched nodes, which makes the method very flexible, e.g. higher order crack openings can be incorporated quite easily. However, as a result, it is more complicated to implement XFEM into commercial FEM packages. A shortcoming of XFEM is the blending region (Chessa et al., 2003), which is introduced to the neighboring elements of the crack tip element. Those elements in the blending region are partially enriched where the local partition of unity does not hold,

thus the solution becomes inaccurate in this region. Nevertheless difficulties in the blending region can be overcome by shifting in Partition of Unity method. On the other hand, XFEM requires an explicit representation of discontinuity surface, which usually has been provided by the Level Sets method (Moës et al., 2002; Gravouil et al., 2002). Therefore, the treatment of phenomena such as branching and fragmentation is more difficult, since additional level sets need to be introduced whenever a new branch emerges. A complete review on recent development of XFEM is presented in the works of Karihaloo and Xiao (2003); Xiao and Karihaloo (2005). A very interesting comparative study between element deletion, cohesive elements and XFEM is presented by Song et al. (2008). Another exciting comparison of XFEM versus EFEM is presented by Oliver et al. (2006b).

The generalized finite element method (GFEM), which is very similar to XFEM in methodology, was first introduced by Strouboulis et al. (2000a,b) and Duarte et al. (2000), and has been proven to be a promising technique for complex geometries (including multiple voids and cracks) and fracture mechanics problems in some recent works (Rüegg, 2002; Duarte and Babuška, 2002; Tian et al., 2006; Babuška et al., 2007; Strouboulis et al., 2007; Babuška et al., 2008). This method allows an incorporation of analytically known or numerically computed handbook functions within some range of their applicability into the standard FE shape functions with the partition of unity method to enhance the local and global accuracy of the computed solution. GFEM can model arbitrary dynamic crack propagation without any remeshing of the domain, and has been also successful at modeling 3D cracks (Duarte et al., 2001; Pereira and Duarte, 2005; Duarte et al., 2006, 2007; Duarte and Kim, 2008).

1.2.3 Meshfree/meshless methods

In contrast to the FEM, meshless methods (Atluri and Zhu, 1998; Li and Liu, 2000; Batra and Zhang, 2004; Atluri and Shen, 2002; Han and Atluri, 2003, 2004; Han et al., 2005, 2006) offer some advantages, including (i) shape functions are constructed by using a highly smooth window function, (ii) a purely displacement-based formulation does not exhibit volumetric locking within a range of support size of the window functions (Li and Liu, 2000), and (iii) approximations are non-local. Thus, meshless methods provide more continuous solutions than the piece-wise continuous ones obtained by the FEM. These properties not only provide an effective remedy for the mesh alignment sensitivity in the computation of strain localization but also are able to model arbitrary crack path propagation without refinement.

Meshless methods can be largely classified into two major categories: weak form approaches such as element free Galerkin method (Belytschko et al., 1994), meshless local Petrov-Galerkin method (Atluri and Zhu, 1998), natural element method (Sukumar et al., 2001), and strong form approaches such as the meshless collocation methods. Meshfree weak form methods possess the following attractive advantages (Liu and Gu, 2003; Gu and Liu, 2005): They exhibit very good stability and excellent accuracy (The reason is that the weak form can spread the error over the integral domain and control the error level); Traction (Neumann or derivative) boundary conditions can be naturally and conveniently incorporated into the same weak form equation. However, a major drawback of weak form methods is high computational cost due to numerical integration. See, for example, Li and Liu (2002); Liu (2003); Li and Liu (2004); Liu and Gu (2005) for an overview of meshfree weak-form methods.

The element free Galerkin method (EFG), which is based on moving least square approximation, was first introduced by Belytschko et al. (1994) and has been intensively developed in recent years (Krongauz and Belytschko, 1998; Rao

and Rahman, 2000; Belytschko et al., 2000; Duflo and Nguyen-Dang, 2002a,b; Liu, 2003; Li and Liu, 2004; Liu and Gu, 2005). Reviews of EFG method are presented in the works of Belytschko et al. (1996b); Fries and Matthies (2004a); Nguyen et al. (2008a). For crack problems, a crack is considered to be opaque and techniques to describe the crack include the visibility method, transparency and diffraction method (Fleming et al., 1997). To capture the singular stress/strain field near crack tip without refinement, Fleming et al. (1997) introduced methods to enrich the trial and the basis functions with the near-crack-tip asymptotic fields; Duflo and Nguyen-Dang (2004) and Duflo (2006) proposed to enrich the weight functions for 2D and 3D crack propagation problems. Fleming et al. also presented a mapping algorithm to align the discontinuity with the crack geometry for multiple-crack segment problems. However, these enrichment techniques may not be appropriate for solving nonlinear fracture mechanics problem. Therefore, Rao and Rahman (2004) suggested a new enriched basis functions technique based on elastic-plastic fracture mechanics for nonlinear fracture analysis. Based on the idea of XFEM, the partition-of-unity-based meshfree method, which uses a jump function to account for the displacement discontinuity along the crack surfaces and level set method to track arbitrary crack path propagation, was offered by Ventura et al. (2002), and successfully developed for cohesive crack problems by Rabczuk and Zi (2007) afterwards. Since the work of Ventura et al. (2002), level set method has been an effective tool for the description of the evolution of failure surfaces (crack or shear band) in EFG methods (Sethian, 1999; Duflo, 2008). To simplify representation of crack, Rabczuk and Belytschko (2004b) introduced the cracked particle method where a crack is modeled by unconnected piecewise segments passing through cracked particles, displacement discontinuity across crack surface is described by mean of the sign enrichment function and no crack topology representation is needed. This approach is simple and able to treat the nucleation of cracks and complex pattern involving cohesive crack branching and crossing in 2D and 3D (Rabczuk and Belytschko, 2007b). However, the accuracy of this method is limited. Recently, Zi et al. (2007) proposed a

new approach, which does not need any crack tip enrichment to ensure that the crack closes at the tip and was successfully applied to static and dynamic cohesive crack problems. Three-dimensional crack problems have been successfully modeled by EFG method, for example, linear fracture mechanics problems with static and elasto-dynamic crack growth are analyzed in the studies of Sukumar et al. (1997); Duffot (2006) and Krysl and Belytschko (1999), respectively; nonlinear problems with crack growth are examined by Rabczuk and Belytschko (2005b); Rabczuk et al. (2008b); nonlinear problems with multiple-crack initiation, propagation and junction are studied in Rabczuk et al. (2007d); Rabczuk and Belytschko (2007b). A very interesting overview on three-dimensional crack growth was presented in the work of Rabczuk et al. (2008a). For shear band problems, EFG has also been demonstrated to be an efficient method to model complicated patterns of shear band in full-scale engineering models. Li and Liu (2000); Li et al. (2000) simulated the shear band propagation in 2D and 3D without any special treatment except the refinement around the expected paths. Based on the idea of cracked particles in the previous works (Rabczuk and Belytschko, 2004b, 2007b), Rabczuk et al. (2007a); Rabczuk and Samaniego (2008) recently developed the so-called sheared particles method, which is able to simulate the evolution of multiple cohesive shear bands in 2D and 3D. However, the accuracy of this method is also limited.

Some other meshfree weak form methods such as meshless local Petrov-Galerkin (MLPG) method (Atluri and Zhu, 1998; Atluri and Shen, 2002; Han and Atluri, 2003, 2004; Atluri et al., 2004; Fries and Matthies, 2004b; Han et al., 2005, 2006), and natural neighbour Galerkin (NNG) method (Sukumar et al., 1998, 2001; Idelsohn et al., 2003; Cueto et al., 2003; Hehua et al., 2007), are able to model cracks in linear elastic fracture mechanics context, for example, see Batra and Ching (2002); Sladek et al. (2004); Gao et al. (2006); Kaiyuan et al. (2006); Sladek et al. (2006) for MLPG method, and Sukumar et al. (1998) for NNG method. However, to the best knowledge of the author they have not yet been applied for simulation of strong discontinuities such as shear bands and cracks

in nonlinear fracture mechanics framework.

In contrast to meshfree weak form methods, meshfree strong form methods have the following attractive advantages (Liu and Gu, 2003; Gu and Liu, 2005): (i) they are simple to implement; (ii) they are computationally efficient since no numerical integration is required; (iii) they are truly meshless. However meshfree strong form methods result in typically poorer accuracy for problems governed by partial differential equations with Neumann-type boundary conditions such as solid mechanics problems with traction (natural) boundary conditions. Therefore, many efforts have been made to develop techniques for handling the Neumann-type boundary conditions such as direct collocation, fictitious points (Liu and Gu, 2005); Hermite-type collocation (Zhang et al., 2000; Li et al., 2003); meshfree weak-strong-form method (Liu and Gu, 2003; Gu and Liu, 2005). Recently, Libre et al. (2008) proposed a stabilized collocation scheme for radial basis functions (RBF) by increasing the shape parameter of RBF and the number of collocation points around the Neumann boundaries, Le et al. (2008b, 2010a) introduced a new approach based on first-order system formulation where both displacements and stresses are considered as primary variables to treat the Neumann-type boundary conditions. There has been just a few meshfree strong form methods developed for problems involving discontinuities so far. For example, Kim et al. recently developed meshfree point collocation methods for weak discontinuity problems in two-dimension, which use the moving least square (MLS) procedure and both intrinsic (Kim et al., 2007a) and extrinsic enrichments (Kim et al., 2007b). Lee and Yoon (2004a) incorporated diffuse derivatives into MLS approximation and used discontinuous weight functions to model two-dimensional linear elastic cracks without any enrichment, and later on this method was enriched with the near tip field for general two-dimensional linear elasto-static crack problems (Yoon et al., 2006). For strain localization simulation, meshfree strong-form methods are mostly developed for one-dimensional problems such as the meshfree collocation methods based on pseudo-spectral method (Bayliss et al., 1994), smooth-particle hydro-

dynamics (Batra and Zhang, 2004) and RBF interpolation (Le et al., 2006, 2007b,a, 2008a).

The present review of literature shows a need for further development of numerical methods for simulation of strain localization (shear bands) and fracture phenomena, especially in three-dimensional problems, and meshfree methods are more suitable for such problems.

1.3 The global IRBFN approximation

The global IRBFN for approximating functions and solving PDEs is presented in this section. In the IRBF method (Mai-Duy and Tran-Cong, 2001, 2003, 2005; Mai-Duy and Tanner, 2005; Le et al., 2007a, 2008a), the formulation of the problem starts with the decomposition of the highest order derivatives under consideration into RBFs. The derivative expression obtained is then integrated to yield expressions for lower order derivatives and finally for the original function itself. The present work is illustrated with the approximation of a function and its derivatives of order up to 2, the formulation can be thus described as follows.

$$u_{,jj}(\mathbf{x}) = \sum_{i=1}^m w^{(i)} g^{(i)}(\mathbf{x}), \quad (1.1)$$

$$u_{,j}(\mathbf{x}) = \int \sum_{i=1}^m w^{(i)} g^{(i)}(\mathbf{x}) dx_j + C_1(x_l; l \neq j) = \sum_{i=1}^{m+p_1} w^{(i)} H_{[x_j]}^{(i)}(\mathbf{x}), \quad (1.2)$$

$$u(\mathbf{x}) = \int \sum_{i=1}^{m+p_1} w^{(i)} H^{(i)}(\mathbf{x}) dx_j + C_2(x_l; l \neq j) = \sum_{i=1}^{m+p_2} w^{(i)} \overline{H}_{[x_j]}^{(i)}(\mathbf{x}), \quad (1.3)$$

or in compact form

$$u_{,jj}(\mathbf{x}) = \mathbf{G}(\mathbf{x})\mathbf{w}_{[x_j]}, \quad (1.4)$$

$$u_{,j}(\mathbf{x}) = \mathbf{H}_{[x_j]}(\mathbf{x})\mathbf{w}_{[x_j]}, \quad (1.5)$$

$$u(\mathbf{x}) = \bar{\mathbf{H}}_{[x_j]}(\mathbf{x})\mathbf{w}_{[x_j]}, \quad (1.6)$$

where, the comma denotes partial differentiation, m is the number of RBFs, $\{g^{(i)}(\mathbf{x})\}_{i=1}^m$ is the set of RBFs, $\{w^{(i)}\}_{i=1}^{m+p_2}$ is the set of corresponding network weights to be found, $\{H^{(i)}(\mathbf{x})\}_{i=1}^m$ and $\{\bar{H}^{(i)}(\mathbf{x})\}_{i=1}^m$ are new basis functions obtained by integrating the radial basis function $g^{(i)}(\mathbf{x})$, p_1 and p_2 are the number of centers used to represent integration constants in the first and second derivatives, (1.2) and (1.3), respectively ($p_2 = 2p_1$). For the multiquadric function

$$g^{(i)}(\mathbf{x}) = \sqrt{\|\mathbf{x} - \mathbf{c}^{(i)}\|^2 + (a^{(i)})^2}, \quad (1.7)$$

where $\mathbf{c}^{(i)}$ is the RBF center and $a^{(i)}$ is the RBF width. The width of the i^{th} RBF can be determined according to the following simple relation

$$a^{(i)} = \beta d^{(i)}, \quad (1.8)$$

where β is a factor, $\beta > 0$, and $d^{(i)}$ is the distance from the i^{th} center to its nearest neighbour.

Now, the ‘‘constants’’ of integration $C_1(x_l; l \neq j)$ and $C_2(x_l; l \neq j)$ on the right hand side of (1.2) and (1.3) can also be interpolated using the IRBFN method as follows.

$$C_1''(x_l; l \neq j) = \sum_{i=1}^M \bar{w}^{(i)} g^{(i)}(x_l; l \neq j), \quad (1.9)$$

$$C_1'(x_l; l \neq j) = \sum_{i=1}^M \bar{w}^{(i)} H^{(i)}(x_l; l \neq j) + \hat{C}_1, \quad (1.10)$$

$$C_1(x_l; l \neq j) = \sum_{i=1}^M \bar{w}^{(i)} \bar{H}^{(i)}(x_l; l \neq j) + \hat{C}_1 x_{k; k \neq j} + \hat{C}_2, \quad (1.11)$$

where $\{\bar{w}^{(i)}\}_{i=1}^M$ are the corresponding weights; M is the number of distinct centers. The unknowns to be found are the sets of weights in (1.1) and (1.9), which can be determined by the SVD (singular value decomposition) procedure, for example.

Mai-Duy and Tran-Cong (2005) performed a prior conversion of the unknowns from network weights, i.e. $\{w^{(i)}\}_{i=1}^{m+p_2}$, to nodal function value \mathbf{u} in order to form a square system of equations of smaller size as follows.

Without loss of generality, a two-dimensional system is considered. The set of network weights are expressed in terms of nodal function value as

$$\mathbf{w}_{[x]} = [\bar{\mathbf{H}}_{[x]}]^{-1} \mathbf{u}, \quad (1.12)$$

$$\mathbf{w}_{[y]} = [\bar{\mathbf{H}}_{[y]}]^{-1} \mathbf{u}, \quad (1.13)$$

and the substitution of (1.12) and (1.13) into the system (1.4)-(1.6) yields

$$u_{,xx}(\mathbf{x}) = \mathbf{G}(\mathbf{x}) [\bar{\mathbf{H}}_{[x]}]^{-1} \mathbf{u}, \quad (1.14)$$

$$u_{,x}(\mathbf{x}) = \mathbf{H}_{[x]}(\mathbf{x}) [\bar{\mathbf{H}}_{[x]}]^{-1} \mathbf{u}, \quad (1.15)$$

$$u(\mathbf{x}) = \bar{\mathbf{H}}_{[x]}(\mathbf{x}) [\bar{\mathbf{H}}_{[x]}]^{-1} \mathbf{u} = \mathbf{I}\mathbf{u}, \quad (1.16)$$

$$u_{,yy}(\mathbf{x}) = \mathbf{G}(\mathbf{x}) [\bar{\mathbf{H}}_{[y]}]^{-1} \mathbf{u}, \quad (1.17)$$

$$u_{,y}(\mathbf{x}) = \mathbf{H}_{[y]}(\mathbf{x}) [\bar{\mathbf{H}}_{[y]}]^{-1} \mathbf{u}, \quad (1.18)$$

$$u(\mathbf{x}) = \bar{\mathbf{H}}_{[y]}(\mathbf{x}) [\bar{\mathbf{H}}_{[y]}]^{-1} \mathbf{u} = \mathbf{I}\mathbf{u}, \quad (1.19)$$

where \mathbf{I} is the identity matrix. It can be seen from (1.14)-(1.19) that the function and its derivatives are all expressed in terms of the function values rather than network weights. Consequently, the system of equations obtained is normally smaller, square and the unknowns to be solved for are the nodal function values instead of the network weights.

1.4 Outline of the Thesis

The rest of the thesis is organized as follows.

- Chapter 2 devises and implements numerical schemes (Le et al., 2010a) that enhance the performance of strong form meshless methods based on the IRBFN for irregular domain problems with traction (derivative or Neumann) boundary conditions in solid mechanics.
- Chapter 3 proposes a novel approximation method based on RBF for generally complicated geometries and random data point distribution, namely Moving IRBFN (MIRBFN) interpolation (Le et al., 2010c). The MIRBFN method is implemented in the collocation of first-order system formulation in chapter 2 (section 2.3.1) to solve PDEs governing various problems including heat transfer, elasticity and linear static crack problems.
- Chapter 4 presents a weak form approach to formulate a new Galerkin meshfree method based on the MIRBFN interpolation introduced in chapter 3. The new method has successfully been verified by various test examples including elasticity and crack problems.
- Chapter 5 describes an IRBFN meshless method for the numerical modeling of the dynamics of strain localization due to strain softening in quasi-brittle materials (Le et al., 2008a). Also, we introduce a new and effective regularization method to enhance the performance of the IRBFN method and alleviate the numerical oscillations associated with weak discontinuity at the elastic wave front. The dynamic response of a one dimensional bar is investigated using both local and non-local continuum models.
- Chapter 6 reports a numerical simulation of the formation and evolution of strain localization in elasto-thermo-viscoplastic materials (adiabatic shear band) by the IRBFN meshless method (Le et al., 2007a). The effects of strain and strain rate hardening, plastic heating, and thermal softening

are considered. The IRBFN method is enhanced by a new coordinate mapping which helps capture the steep spatial structure of the resultant band.

- Chapter 7 reports a further development of the MIRBFN Galerkin mesh-free method for numerical simulation of elasto-plastic materials with linear strain hardening and strain localization of elasto-visco-plastic materials with strain softening in two dimensions as well as some preliminary results.
- Chapter 8 is to develop further the MIRBFN meshfree method in chapter 4 for fracture problems (Le et al., 2010d). The present method is enhanced by a local partition of unity enrichment technique to capture the discontinuity across the crack and the extremely sharp gradient in the vicinity of the crack tip.
- Chapter 9 draws some conclusions from the research and discusses some future works.

Chapter 2

An IRBFN-based Cartesian-grid collocation technique for mixed boundary value problems

This chapter reports a meshless method based on Cartesian discretisation with 1D-integrated radial basis function networks (1D-IRBFN) as approximants. In this method, high order systems are reformulated as first order systems which are then numerically solved by a collocation method. The present method is enhanced by a new boundary interpolation technique based on 1D-IRBFN which is introduced to obtain function approximation at irregular points in irregular domains. The proposed method is well suited to problems with mixed boundary conditions on both regular and irregular domains. The main results obtained are (a) the boundary conditions for the reformulated problem are of Dirichlet type only; (b) the integrated RBFN approximation avoids the well known reduction of convergence rate associated with differential formulations; (c) the primary variable (e.g. displacement, temperature) and the dual variable (e.g. stress, temperature gradient) have similar convergence order; (d) the volumetric locking effects associated with incompressible materials in solid mechanics

are alleviated. Numerical experiments show that the proposed method achieves very good accuracy and high convergence rates.

2.1 Introduction

Traditional finite element methods (FEM) (Belytschko et al., 2003b; Bordas et al., 2008a) and boundary element methods (BEM) (Mackerle, 2000; Bebalal et al., 2006) have been based on weak form formulations. Recently, weak form meshless (meshfree) methods are being developed as an alternative approach. Weak form methods have the following advantages (Liu, 2003) (a) they have good stability and reasonable accuracy for many problems; (b) Neumann boundary conditions can be naturally and conveniently incorporated into the same weak form equation. However, elements have to be used for the integration of a weak form over the global problem domain (Belytschko et al., 1994) and the numerical integration is still computationally expensive for these weak form methods. On the other hand, collocation methods are based on strong form governing equations and have been found to possess the following attractive advantages (Liu, 2003; Le et al., 2006, 2007b, 2008b) (a) they are computationally efficient since there is no need for numerical integration of the governing equations; (b) the implementation is simple; (c) implementation of Dirichlet boundary conditions is very straightforward. However, the strong form approach is less stable due to the pointwise nature of error minimisation and results in typically poorer accuracy for problems governed by partial differential equations with Neumann-type boundary conditions such as solid mechanics problems with traction (natural) boundary conditions. Furthermore, some strong form methods such as finite difference and pseudo spectral methods are restricted to rectangular domains.

Therefore, many efforts have been made to develop techniques for handling the Neumann-type boundary conditions such as direct collocation, fictitious points,

regular grids, dense nodes in the derivative boundaries (Liu and Gu, 2005), and Hermite-type collocation (Zhang et al., 2000; Li et al., 2003). Recently, Zhang et al. (2001) suggested a least-squares collocation meshless method which can improve the accuracy of the solution in comparison with that of standard collocation method. Onate et al. (2001) introduced a stabilization technique by adding artificial terms in both governing equations and Neumann boundary conditions, however, these terms only serve the stabilization purpose and their suitability is restricted to some special problems. Liu and Gu (Liu and Gu, 2003; Gu and Liu, 2005) proposed a meshfree weak-strong-form method, in which the weak form is applied to the subdomain concerned with Neumann boundary conditions and strong form to the one with Dirichlet boundary conditions. Pan et al. (2005) presented meshless Galerkin least-squares method by making use of Galerkin method in the boundary domain and least-squares method in the interior domain. Hu et al. (2006) and Chen et al. (2008a) introduced the weighted radial basis collocation method in which the residual error on the Neumann boundary is treated by a proper scaling weight. Atluri et al. (2004, 2006) proposed a “mixed” collocation technique, however, stable solutions are obtained with resort to the local weak form at nodal points for stress and the penalty method for Neumann boundary conditions. Libre et al. (2008) proposed a stabilized collocation scheme for RBF by increasing the shape parameter of RBF and the number of collocation points around the Neumann boundaries, however, increasing the shape parameter leads to increased ill-conditioning. Lee and Yoon (2004b) introduced generalized diffuse derivative in a collocation method.

In recent years, increased attention has been given to the development of first-order system formulation. In earlier works of Cai et al. (1994, 1997b), they developed the theory of first-order system formulation for general second-order elliptic PDEs. This methodology has been then extended to the Stokes equations (Cai et al., 1997a) in two and three dimensions, elasticity problems (Cai et al., 1998, 2000; Cai and Starke, 2003), and boundary value problems with Robin boundary conditions (Lee, 1999). However, the efforts have been mainly

concentrated in using weak form Galerkin or weak form least-squares formulation. For example, Jiang and Wu (2002) presented the least-squares finite element method; Park and Youn (2001) introduced the least-squares meshless method and Kwon et al. (2003) subsequently extended this method to elasticity problems. Relatively few works have been reported with first-order system formulation based on strong form method.

Following a strong form approach, this chapter describes a new efficient collocation method using integrated radial basis function network (IRBFN) and Cartesian grid (Mai-Duy and Tran-Cong, 2007) for the numerical modeling of certain problems governed by second order PDEs in both regular and irregular domains. Firstly, the governing equations are written or re-written as a first order system “mixed” formulation where both primary (e.g. displacement, temperature) and dual (e.g. stress, temperature gradient) variables are approximated independently. Secondly, a new technique based on 1D-IRBFN is introduced to easily interpolate variables along curved boundaries. The mixed boundary conditions are easily and directly accommodated as a result of the first-order formulation while the new boundary interpolation technique overcomes the challenge traditionally posed by Cartesian-grid discretisation of irregular domains (Roache, 1980). In the present approach (a) the mixed boundary conditions for the original second-order system are of Dirichlet type only for the reformulated first-order problem; (b) the integrated RBFN approximation is able to capture very sharp gradient (or boundary layer) (Le et al., 2007a, 2008a) and avoid the well known reduction of convergence rate associated with differential formulations; (c) the primary variable (e.g. displacement, temperature) and the dual variable (e.g. stress, temperature gradient) have similar convergence order; (d) the volumetric locking effects associated with incompressible materials in solid mechanics are alleviated without any extra effort. (In contrast, in meshless weak form approaches, special treatments need to be done in the case of incompressible materials, for instance, Dolbow and Belytschko (1999) introduced reduced integration procedure, Chen et al. (2000) proposed the pressure projection tech-

nique for the purpose of alleviating the incompressible locking.) Moreover, the generation of a Cartesian grid is a straightforward task and therefore the cost associated with spatial discretisation is greatly reduced in comparison with that associated with FE generation. Numerical experiments show that the proposed method achieves very good accuracy and high convergence rates.

The remainder of the chapter is organized as follows. The physical problem and its mathematical model are defined in section 2.2. The numerical formulation for the mathematical model is presented in section 2.3. The proposed method is illustrated by numerical examples in section 2.4. Section 2.5 draws some conclusions.

2.2 Problem formulations

2.2.1 First-order systems

It is noticed that in general higher-order differential equations can be transformed into first-order differential equations (Cai et al., 1994; Lee, 1999). The higher-order differential equations are transformed into first-order differential equations by introducing new dual variables. Both primary and dual variables are independently interpolated and have shape functions of the same order. Cai and co-workers (Cai et al., 1994, 1997b,a, 1998, 2000; Cai and Starke, 2003) studied the behaviour of equivalent first-order formulations of second-order systems and found that FE implementation of such first-order systems yields uniform optimal performance. The resultant first-order system of governing equations can be written as follows.

$$\mathcal{L}\mathbf{u} = \mathbf{f}, \quad \text{in } \Omega \quad (2.1)$$

$$\mathbf{B}\mathbf{u} = \mathbf{g}, \quad \text{on } \Gamma \quad (2.2)$$

where Ω is a bounded domain in \mathbb{R}^d , $d = 1, 2$ or 3 , Γ the boundary of Ω , $\mathbf{u}^T = [u_1, u_2, \dots, u_m]$ is a vector of m unknown functions (including primary and dual variables) of $\mathbf{x}^T = [x_1, x_2, \dots, x_d]$, \mathbf{f} a given function in the domain, \mathbf{B} a boundary algebraic operator, and \mathbf{g} a given function on the boundary, \mathcal{L} is a first-order linear differential operator

$$\mathcal{L}\mathbf{u} = \mathcal{L}_0\mathbf{u} + \sum_{i=1}^d \mathcal{L}_i \frac{\partial \mathbf{u}}{\partial x_i}, \quad (2.3)$$

in which \mathcal{L}_i are the coefficient matrices which characterize the differential operator \mathcal{L} . Examples of problems formulated as first-order systems are given in the following sections.

2.2.2 Two-dimensional Poisson equation

Consider the following two-dimensional Poisson equation

$$\frac{\partial^2 \phi(x, y)}{\partial x^2} + \frac{\partial^2 \phi(x, y)}{\partial y^2} = f(x, y) \quad \text{in } \Omega, \quad (2.4a)$$

$$\phi(x, y) = g(x, y) \quad \text{on } \Gamma_D, \quad (2.4b)$$

$$\frac{\partial \phi(x, y)}{\partial n} = h(x, y) \quad \text{on } \Gamma_N, \quad (2.4c)$$

where Ω is a bounded domain in \mathbb{R}^2 , Γ_D and Γ_N the boundary of Ω on which the Dirichlet and Neumann boundary conditions are imposed, respectively, $\mathbf{n} = (n_x, n_y)^T$ the outward unit normal to Γ_N , and f , g and h given functions on Ω , Γ_D and Γ_N , respectively.

A first-order formulation is obtained by introducing the dual variables in (2.4)

as follows

$$\frac{\partial \phi(x, y)}{\partial x} - \xi(x, y) = 0 \quad \text{in } \Omega \quad \text{and on } \Gamma_D \cup \Gamma_N, \quad (2.5a)$$

$$\frac{\partial \phi(x, y)}{\partial y} - \eta(x, y) = 0 \quad \text{in } \Omega \quad \text{and on } \Gamma_D \cup \Gamma_N, \quad (2.5b)$$

$$\frac{\partial \xi(x, y)}{\partial x} + \frac{\partial \eta(x, y)}{\partial y} = f(x, y) \quad \text{in } \Omega \quad \text{and on } \Gamma_D \cup \Gamma_N, \quad (2.5c)$$

$$\phi(x, y) = g(x, y) \quad \text{on } \Gamma_D, \quad (2.5d)$$

$$n_x \xi + n_y \eta = h(x, y) \quad \text{on } \Gamma_N. \quad (2.5e)$$

2.2.3 Linear elasticity problems

Consider the following two-dimensional problem on a domain Ω bounded by $\Gamma = \Gamma_u \cup \Gamma_t$

$$\nabla \cdot \boldsymbol{\sigma} = \mathbf{b} \quad \text{in } \Omega, \quad (2.6a)$$

$$\mathbf{u} = \bar{\mathbf{u}} \quad \text{on } \Gamma_u, \quad (2.6b)$$

$$\boldsymbol{\sigma} \cdot \mathbf{n} = \bar{\mathbf{t}} \quad \text{on } \Gamma_t, \quad (2.6c)$$

in which $\boldsymbol{\sigma}$ is the stress tensor, which corresponds to the displacement field \mathbf{u} and \mathbf{b} is the body force, \mathbf{n} the outward unit normal to Γ_t . The superposed bar denotes prescribed value on the boundary.

The governing equations (2.6) are closed when a constitutive relation is specified for $\boldsymbol{\sigma}$. Here the linear Hooke's law is used to describe the $\boldsymbol{\sigma} - \mathbf{u}$ relation. By choosing displacement \mathbf{u} as primary variable and stress $\boldsymbol{\sigma}$ as dual variable, the governing equations remain first-order, which are written for plane stress case

as follows

$$\frac{\partial u}{\partial x} - \frac{1}{E}\sigma_x + \frac{\mu}{E}\sigma_y = 0, \quad (2.7a)$$

$$\frac{\partial v}{\partial y} + \frac{\mu}{E}\sigma_x - \frac{1}{E}\sigma_y = 0, \quad (2.7b)$$

$$\frac{\partial u}{\partial y} + \frac{\partial v}{\partial x} - \frac{2(1+\mu)}{E}\tau_{xy} = 0, \quad (2.7c)$$

$$\frac{\partial \sigma_x}{\partial x} + \frac{\partial \tau_{xy}}{\partial y} = b_x, \quad (2.7d)$$

$$\frac{\partial \tau_{xy}}{\partial x} + \frac{\partial \sigma_y}{\partial y} = b_y, \quad (2.7e)$$

$$\mathbf{u} = \bar{\mathbf{u}} \quad \text{on } \Gamma_u, \quad (2.7f)$$

$$\boldsymbol{\sigma} \cdot \mathbf{n} = \bar{\mathbf{t}} \quad \text{on } \Gamma_t, \quad (2.7g)$$

where μ is Poisson ratio and E Young's modulus. By introducing the dimensionless stress tensor $\mathbf{s} = \boldsymbol{\sigma}/E$, the above first-order system can be rewritten as follows

$$\frac{\partial u}{\partial x} - s_x + \mu s_y = 0, \quad (2.8a)$$

$$\frac{\partial v}{\partial y} + \mu s_x - s_y = 0, \quad (2.8b)$$

$$\frac{\partial u}{\partial y} + \frac{\partial v}{\partial x} - 2(1+\mu)s_{xy} = 0, \quad (2.8c)$$

$$\frac{\partial s_x}{\partial x} + \frac{\partial s_{xy}}{\partial y} = b_x, \quad (2.8d)$$

$$\frac{\partial s_{xy}}{\partial x} + \frac{\partial s_y}{\partial y} = b_y, \quad (2.8e)$$

$$\mathbf{u} = \bar{\mathbf{u}} \quad \text{on } \Gamma_u, \quad (2.8f)$$

$$\mathbf{s} \cdot \mathbf{n} = \bar{\mathbf{t}} \quad \text{on } \Gamma_t. \quad (2.8g)$$

2.3 Numerical formulations

In a number of methods, approximations of spatial derivatives are less accurate because differentiation magnifies errors. Madych (1992) estimated that MQ-

RBF enjoys spectral convergence of order $O(\lambda^{\frac{a}{h}})$, where $0 < \lambda < 1$, a is the shape parameter and h is the maximum mesh size. A differential formulation with spatial derivatives of order δ reduces convergence rate of MQ to $O(\lambda^{\frac{a}{h}-\delta})$. To increase the accuracy and the convergence rate of MQ, several approaches have been proposed such as (a) increasing a or decreasing h or both (Libre et al., 2008), (b) integrated methods of Mai-Duy and Tran-Cong (2001, 2003, 2005, 2007) and (c) using higher order MQ, e.g. $\varphi_i = (r_i^2 + a_i^2)^\beta$, where $\beta > \frac{1}{2}$ (Wertz et al., 2006).

To avoid the reduction of convergence rates due to differentiation and enhance the stability of the collocation-based numerical schemes in the case of Neumann type boundary value problems, in the present work we use Cartesian grid technique to discretise governing equations obtained by first-order formulation as follows.

2.3.1 1D-IRBFN approximation

For the sake of completeness, the 1D-IRBFN approximation for 2D problems in Mai-Duy and Tran-Cong (2007) is reproduced as follows. Consider a grid point/regular point \mathbf{x} ($\mathbf{x} = (x, y)^T$) (Figure 2.1). Along the horizontal line passing through this point, one can use IRBFNs to construct the expressions for the function u and its derivatives with respect to x . The construction process can be described as follows. The second-order derivative of u is first decomposed into RBFs; the RBF network is then integrated twice to obtain the expressions

for the first-order derivative and the function itself

$$\frac{\partial^2 u(x)}{\partial x^2} = \sum_{i=1}^N w^{(i)} g^{(i)}(x) = \sum_{i=1}^N w^{(i)} H_{[2]}^{(i)}(x), \quad (2.9)$$

$$\frac{\partial u(x)}{\partial x} = \sum_{i=1}^N w^{(i)} H_{[1]}^{(i)}(x) + c_1, \quad (2.10)$$

$$u(x) = \sum_{i=1}^N w^{(i)} H_{[0]}^{(i)}(x) + c_1 x + c_2, \quad (2.11)$$

where N is the number of nodal points (interior and boundary points) on the line, $\{w^{(i)}\}_{i=1}^N$ are RBF weights to be determined, $\{g^{(i)}(x)\}_{i=1}^N$ are known RBFs, $H_{[1]}(x) = \int H_{[2]}(x) dx$, $H_{[0]}(x) = \int H_{[1]}(x) dx$, and c_1 and c_2 are integration constants. Here, it is referred to as a second-order 1D-IRBFN scheme, denoted by IRBFN-2. The present study employs multiquadrics (MQ) whose form is

$$g^{(i)}(x) = \sqrt{(x - c^{(i)})^2 + a^{(i)2}}, \quad (2.12)$$

where $c^{(i)}$ and $a^{(i)}$ are the center and the RBF width/shape parameter of the i th RBF. The width of the i th RBF can be determined according to the following simple relation

$$a_i = \beta d_i, \quad (2.13)$$

where β is a factor, $\beta > 0$, and d_i is the distance from the i^{th} center to its nearest neighbour. The set of centers is chosen to be the same as the set of the collocation points. It is more convenient to work in the physical space than in the network-weight space. The values of the variable u at the N nodal points

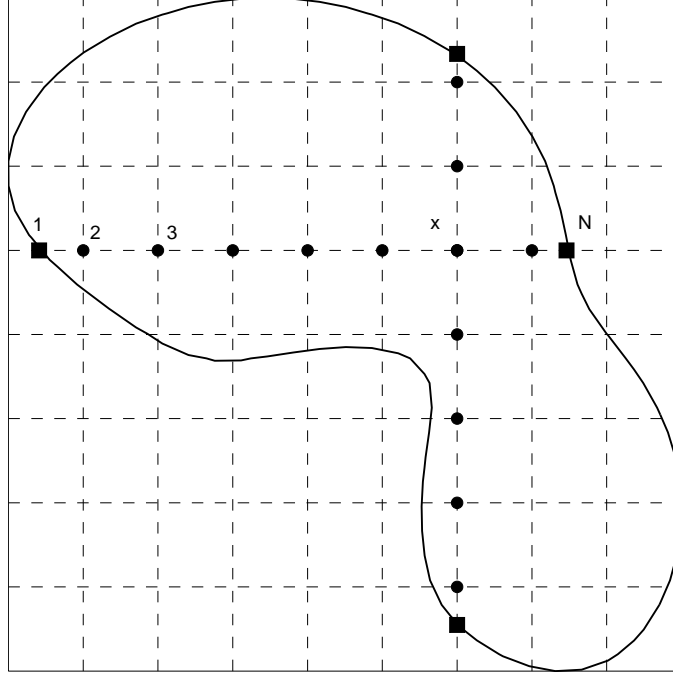


Figure 2.1: Domain discretization by Cartesian grid: the boundary and interior points used for constructing the IRBFN approximations at point \mathbf{x} are highlighted. The intersections of the grid lines and the boundary (e.g. points 1, N) are referred to as irregular if they do not coincide with grid points.

can be expressed as

$$u(x^{(1)}) = \sum_{i=1}^N w^{(i)} H_{[0]}^{(i)}(x^{(1)}) + c_1 x^{(1)} + c_2, \quad (2.14)$$

$$u(x^{(2)}) = \sum_{i=1}^N w^{(i)} H_{[0]}^{(i)}(x^{(2)}) + c_1 x^{(2)} + c_2, \quad (2.15)$$

... ..

$$u(x^{(N)}) = \sum_{i=1}^N w^{(i)} H_{[0]}^{(i)}(x^{(N)}) + c_1 x^{(N)} + c_2, \quad (2.16)$$

or in a matrix form

$$\hat{u} = \mathcal{H} \begin{pmatrix} \hat{w} \\ \hat{c} \end{pmatrix}, \quad (2.17)$$

where $\hat{u} = (u^{(1)}, u^{(2)}, \dots, u^{(N)})^T$, $\hat{w} = (w^{(1)}, w^{(2)}, \dots, w^{(N)})^T$, $\hat{c} = (c_1, c_2)^T$, and \mathcal{H} is a known matrix of dimension $N \times (N + 2)$ defined as

$$\mathcal{H} = \begin{bmatrix} H_{[0]}^{(1)}(x^{(1)}) & H_{[0]}^{(2)}(x^{(1)}) & \cdots & H_{[0]}^{(N)}(x^{(1)}) & x^{(1)} & 1 \\ H_{[0]}^{(1)}(x^{(2)}) & H_{[0]}^{(2)}(x^{(2)}) & \cdots & H_{[0]}^{(N)}(x^{(2)}) & x^{(2)} & 1 \\ \cdots & \cdots & \cdots & \cdots & \cdots & \cdots \\ H_{[0]}^{(1)}(x^{(N)}) & H_{[0]}^{(2)}(x^{(N)}) & \cdots & H_{[0]}^{(N)}(x^{(N)}) & x^{(N)} & 1 \end{bmatrix}.$$

Using the singular value decomposition (SVD) technique, one can write the RBF coefficients including two integration constants in terms of the physically meaningful nodal variable values

$$\begin{pmatrix} \hat{w} \\ \hat{c} \end{pmatrix} = \mathcal{H}^{-1} \hat{u}. \quad (2.18)$$

It is noted that the purpose of using SVD here is to provide a solution whose norm is the smallest in the least-squares sense. By substituting (2.18) into (2.9)-(2.11), the values of u and its derivatives with respect to x at point \mathbf{x} can now be computed by

$$\frac{\partial^2 u(x)}{\partial x^2} = \left(H_{[2]}^{(1)}(x), H_{[2]}^{(2)}(x), \dots, H_{[2]}^{(N)}(x), 0, 0 \right) \mathcal{H}^{-1} \hat{u}, \quad (2.19)$$

$$\frac{\partial u(x)}{\partial x} = \left(H_{[1]}^{(1)}(x), H_{[1]}^{(2)}(x), \dots, H_{[1]}^{(N)}(x), 1, 0 \right) \mathcal{H}^{-1} \hat{u}, \quad (2.20)$$

$$u(x) = \left(H_{[0]}^{(1)}(x), H_{[0]}^{(2)}(x), \dots, H_{[0]}^{(N)}(x), x, 1 \right) \mathcal{H}^{-1} \hat{u}. \quad (2.21)$$

Substituting a discrete approximation of \mathbf{u} and its first-order derivatives as given in (2.21) and (2.20) into (2.1) and (2.2) and using the collocation method at all the nodes of Ω and Γ , one obtains the linear algebraic system as presented below.

Let N_Ω denote the number of interior nodes, N_D the number of nodes on the Dirichlet boundary, N_N the number of nodes on the Neumann boundary, m_p the number of primary unknowns and m_d the number of dual un-

knowns associated with a node, the number of nodal unknowns is generally $(N_\Omega + N_D + N_N)(m_p + m_d)$. If one collocates the governing equations (2.1) at N_Ω interior nodes and the boundary conditions (2.2) at $(N_D + N_N)$ boundary nodes, the number of obtained equations is $(N_\Omega(m_p + m_d) + N_D k_D + N_N k_N)$, where k_D and k_N are the number of equations from the boundary conditions per node on the Dirichlet and Neumann boundaries, respectively. Consequently, the number of equations is less than the number of unknowns on the boundaries since k_D and k_N are usually less than $m_p + m_d$, respectively. To overcome this deficiency, we propose a new scheme for the treatment of boundary conditions of the first-order collocated system as follows. The governing equations (2.1) is collocated at all the interior and boundary nodes, yielding $(N_\Omega + N_D + N_N)(m_p + m_d)$ equations. The boundary conditions are imposed by collocating equation (2.2) at all the boundary nodes, i.e. the obtained system has $(N_\Omega + N_D + N_N)(m_p + m_d) + N_D k_D + N_N k_N$ equations. The final system is obtained by removing $N_D k_D + N_N k_N$ appropriate equations corresponding to the governing equations collocated at the boundary nodes. Consequently, the number of equations of the resultant system is equal to the number of nodal unknowns and it can be rewritten in a compact form

$$\mathbf{A}\mathbf{u} = \bar{\mathbf{f}}. \quad (2.22)$$

Another possible treatment of the boundary conditions in this case is that both governing equations (2.1) and boundary conditions (2.2) are imposed at all the boundary nodes. As a result, the number of equations is greater than the number of unknowns, and the resultant system can be solved in the least-square sense. However, our numerical study indicates that the least-squares scheme provides poorer accuracy than the proposed scheme.

2.3.2 Irregular boundary interpolation technique

Consider a representative irregular boundary as shown in Figure 2.2, Cartesian grid based methods generally are not able to represent irregular nodes (e.g. points 1, N in Figure 2.2) on this boundary and the 1D-IRBFN is no exception. To interpolate variables at irregular points, a new boundary interpolation technique based on 1D-IRBFN is introduced as follows.

If the curve (irregular boundary) is a function of x and y , i.e. $\zeta = \zeta(x, y)$, and $x = x(\zeta)$ and $y = y(\zeta)$, a function value $f = f(x, y)$ is invariant with respect to ζ coordinate system (i.e. the natural coordinate system)

$$f = f(x, y) = f[x(\zeta), y(\zeta)] = f(\zeta). \quad (2.23)$$

From (2.23), we have the following relation

$$\frac{\partial f}{\partial \zeta} = \frac{\partial f}{\partial x} \frac{\partial x}{\partial \zeta} + \frac{\partial f}{\partial y} \frac{\partial y}{\partial \zeta}, \quad (2.24)$$

which can be used for determining $\frac{\partial f}{\partial x}$ (or $\frac{\partial f}{\partial y}$) at the irregular nodes if $\frac{\partial x}{\partial \zeta}$, $\frac{\partial y}{\partial \zeta}$ and $\frac{\partial f}{\partial \zeta}$ (or $\frac{\partial f}{\partial x}$) are known. In general, $f(\zeta)$, $x(\zeta)$, $y(\zeta)$ and their corresponding derivatives can be approximated by 1D-IRBFN. To illustrate the proposed scheme, let the irregular boundary be a circular arc, we need to determine $\frac{\partial f}{\partial x}$ at the “square” nodes on the circular arc (Figure 2.2). We have the relations

$$\zeta(x, y) \equiv \theta(x, y) = \arctan(y/x), \quad (2.25)$$

$$x = r \cos(\theta), \quad y = r \sin(\theta), \quad (2.26)$$

$$f(\theta) = f[x(\theta), y(\theta)] = f, \quad (2.27)$$

$$\frac{\partial f}{\partial \theta} = \frac{\partial f}{\partial x} \frac{\partial x}{\partial \theta} + \frac{\partial f}{\partial y} \frac{\partial y}{\partial \theta}, \quad (2.28)$$

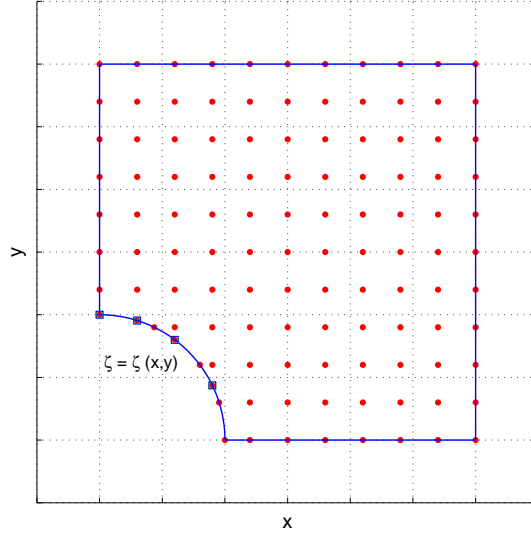


Figure 2.2: 1D interpolation scheme for irregular boundary

where r is the radius of the circular arc. In general, if $f(\theta)$ is not available analytically, it can be approximated by a 1D-IRBFN, $\frac{\partial f}{\partial y}$ ($\frac{\partial f}{\partial x}$) of these nodes can be approximated along the vertical (horizontal) lines. Therefore, $\frac{\partial f}{\partial x}$ ($\frac{\partial f}{\partial y}$) can be easily obtained by using (2.28).

2.4 Numerical examples

For an error estimation and convergence study, the discrete relative L_2 norm of errors of primary and dual variables are defined as

$$L_2^\phi = \frac{\sqrt{\sum_{i=1}^M (\phi_e^{(i)} - \phi^{(i)})^2}}{\sqrt{\sum_{i=1}^M (\phi_e^{(i)})^2}}, \quad (2.29)$$

$$L_2^{\xi\eta} = \frac{\sqrt{\sum_{i=1}^M [(\xi_e^{(i)} - \xi^{(i)})^2 + (\eta_e^{(i)} - \eta^{(i)})^2]}}{\sqrt{\sum_{i=1}^M [(\xi_e^{(i)})^2 + (\eta_e^{(i)})^2]}}, \quad (2.30)$$

for Poisson equation and

$$L_2^u = \frac{\sqrt{\sum_{i=1}^N \left((u_x)_e^{(i)} - (u_x)^{(i)} \right)^2 \left((u_y)_e^{(i)} - (u_y)^{(i)} \right)^2}}{\sqrt{\sum_{i=1}^N \left[\left((u_x)_e^{(i)} \right)^2 + \left((u_y)_e^{(i)} \right)^2 \right]}}, \quad (2.31)$$

$$L_2^\sigma = \frac{\sqrt{\sum_{i=1}^M \left[\left((s_x)_e^{(i)} - s_x^{(i)} \right)^2 + \left((s_y)_e^{(i)} - s_y^{(i)} \right)^2 + \left((s_{xy})_e^{(i)} - s_{xy}^{(i)} \right)^2 \right]}}{\sqrt{\sum_{i=1}^M \left[\left((s_x)_e^{(i)} \right)^2 + \left((s_y)_e^{(i)} \right)^2 + \left((s_{xy})_e^{(i)} \right)^2 \right]}}, \quad (2.32)$$

for elasticity problems, where M is the number of unknown nodal values and the subscript “e” denotes the exact solution. The convergence order of the solution with respect to the refinement of spatial discretization is assumed to behave as

$$L_2(h) \approx \zeta h^\lambda = O(h^\lambda), \quad (2.33)$$

where h is the maximum grid spacing in either x or y direction, ζ and λ are the parameters of the exponential model, which are found by general linear least square formula. It is noted that the value of the shape parameter β in (2.13) is 1 for all the following numerical examples.

2.4.1 Poisson equation in a regular domain

Consider the following Poisson equation

$$\frac{\partial^2 \phi(x, y)}{\partial x^2} + \frac{\partial^2 \phi(x, y)}{\partial y^2} = -2\pi^2 \cos(\pi x) \cos(\pi y), \quad (2.34)$$

defined in $\Omega = [0, 1] \times [0, 1]$, subject to the Dirichlet boundary condition

$$\phi(0, y) = \cos(\pi y), \quad \text{on } x = 0, \quad (2.35)$$

and the following Neumann boundary conditions

$$\frac{\partial \phi(1, y)}{\partial x} = 0, \quad \text{on } x = 1, \quad (2.36a)$$

$$\frac{\partial \phi(x, 0)}{\partial y} = 0, \quad \text{on } y = 0, \quad (2.36b)$$

$$\frac{\partial \phi(x, 1)}{\partial y} = 0, \quad \text{on } y = 1. \quad (2.36c)$$

$$(2.36d)$$

The corresponding exact solution is given by

$$\phi(x, y) = \cos(\pi x) \cos(\pi y). \quad (2.37)$$

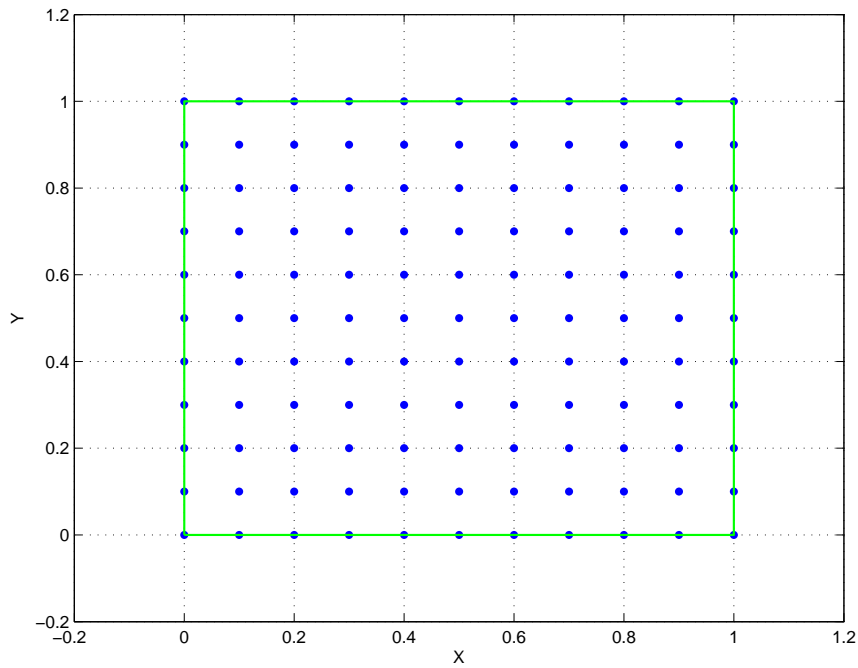


Figure 2.3: Poisson equation in a regular domain: domain discretisation with 11×11 points.

Figure 2.3 shows the geometry of the problem and the domain discretisation based on a uniform Cartesian grid with 11×11 collocation points (CPs). The obtained results with 11×11 CPs are presented in Figures 2.4-2.8. The solution

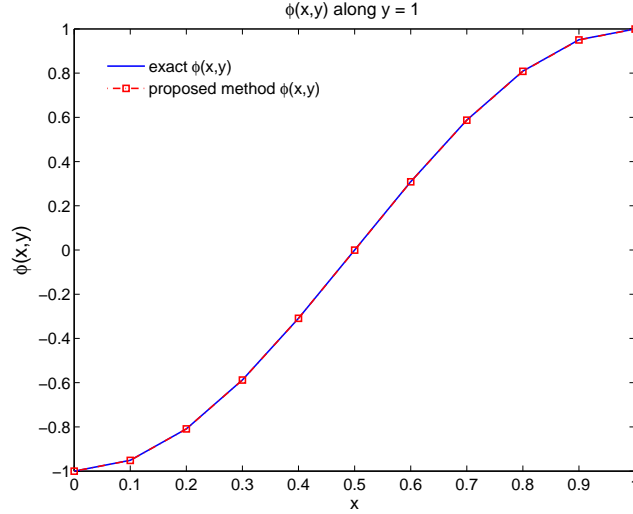


Figure 2.4: Poisson equation in a regular domain: solution of $\phi(x, y)$ obtained by the proposed method in comparison with exact solution along $y = 1$.

for the primary unknown $\phi(x, y)$ on three Neumann boundaries obtained by the present method and the exact solution are plotted in Figures 2.4-2.6, the solution for the dual unknowns $\xi(x, y)$ (on $y = 0$ and $y = 1$) and $\eta(x, y)$ (on $x = 0$ and $x = 1$) are shown in Figure 2.7 and Figure 2.8, respectively. From these figures, it can be seen that both the Dirichlet and Neumann boundary conditions are imposed exactly by the present method and the present solutions excellently agree with the exact solutions.

To study the convergence behaviour of the solution, a number of uniform grids, namely 11×11 , 21×21 , 31×31 , 41×41 , 51×51 , 71×71 , 81×81 , 121×121 and 141×141 CPs is employed in computation. The h is equivalent to the maximum grid space (in x direction) for all numerical examples. The convergence behaviours for $\phi(x, y)$ (L_2^ϕ) and its derivatives ($L_2^{\xi\eta}$) are shown in Figure 2.9. It can be observed that the error norm L_2^ϕ is slightly lower than $L_2^{\xi\eta}$, the convergence rates for $\phi(x, y)$ and $(\xi(x, y), \eta(x, y))$ are $O(h^{3.26})$ and $O(h^{3.5})$, respectively. At the finest grid, the relative error L_2^ϕ and $L_2^{\xi\eta}$ are 1.0458×10^{-7} and 1.1958×10^{-7} , respectively.

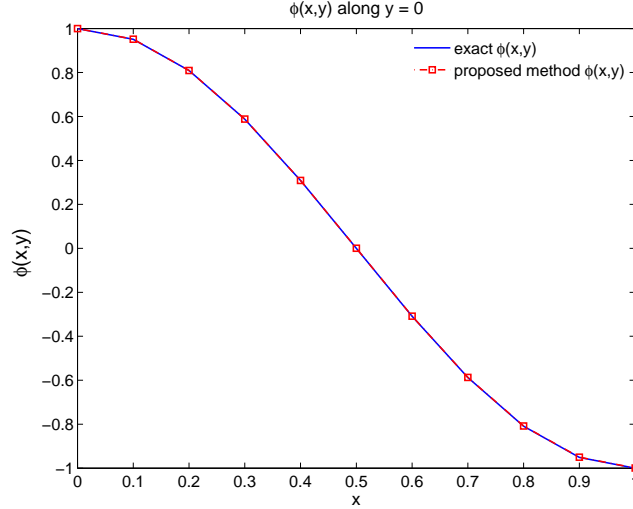


Figure 2.5: Poisson equation in a regular domain: solution of $\phi(x, y)$ obtained by the proposed method in comparison with exact solution along $y = 0$.

2.4.2 Poisson equation in a multiply-connected domain

To illustrate the proposed interpolation technique for irregular boundaries, we consider the Poisson equation in example 2.4.1 with a multiply-connected domain as shown in Figure 2.10, where the Dirichlet boundary condition is prescribed on the left edge and right edge as

$$\phi(-2, y) = \cos(\pi y), \quad (2.38a)$$

$$\phi(2, y) = \cos(\pi y), \quad (2.38b)$$

and the Neumann boundary condition is given on the other edges: upper edge, lower edge and curve edge as follows

$$\frac{\partial \phi(x, 2)}{\partial x} = 0, \quad (2.39a)$$

$$\frac{\partial \phi(x, -2)}{\partial y} = 0, \quad (2.39b)$$

$$n_x \frac{\partial \phi(x, y)}{\partial x} + n_y \frac{\partial \phi(x, y)}{\partial y} = q(x, y), \quad \text{on } x^2 + y^2 = 1, \quad (2.39c)$$

where $\mathbf{n} = (n_x, n_y)^T$ is the outward unit normal to the boundary, $q(x, y) = -n_x \pi \sin(\pi x) \cos(\pi y) - n_y \pi \cos(\pi x) \sin(\pi y)$. With the above boundary condi-

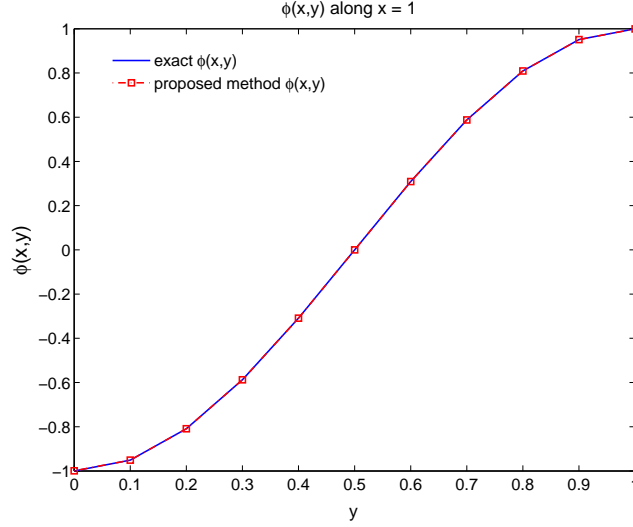


Figure 2.6: Poisson equation in a regular domain: solution of $\phi(x, y)$ obtained by the proposed method in comparison with exact solution along $x = 1$.

tions, the exact solution is given as in example 2.4.1.

In the case of irregular domains, the irregular boundary interpolation technique in section 2.3.2 is employed to improve the performance of 1D-IRBFN approximation. Figures 2.11-2.13 show the numerical results by the present method along the curved boundary (Neumann boundary condition). It can be seen that the obtained results are in good agreement with the exact solution.

The convergence of the method is investigated with 120, 512, 3232, 4688, 6716, 9984 and 16084 nodes (which are based on uniform grids of 11×11 , 24×24 , 62×62 , 75×75 , 90×90 , 110×110 and 140×140) as plotted in Figure 2.14. The convergence rates for $\phi(x, y)$ and its derivatives are $O(h^{2.57})$ and $O(h^{2.40})$, respectively. At the finest grid, the relative error norms L_2^ϕ and $L_2^{\xi\eta}$ are 9.455×10^{-4} and 1.345×10^{-3} , respectively. The obtained results indicate that the proposed boundary interpolation technique greatly improves performance of 1D-IRBFN in irregular domains.

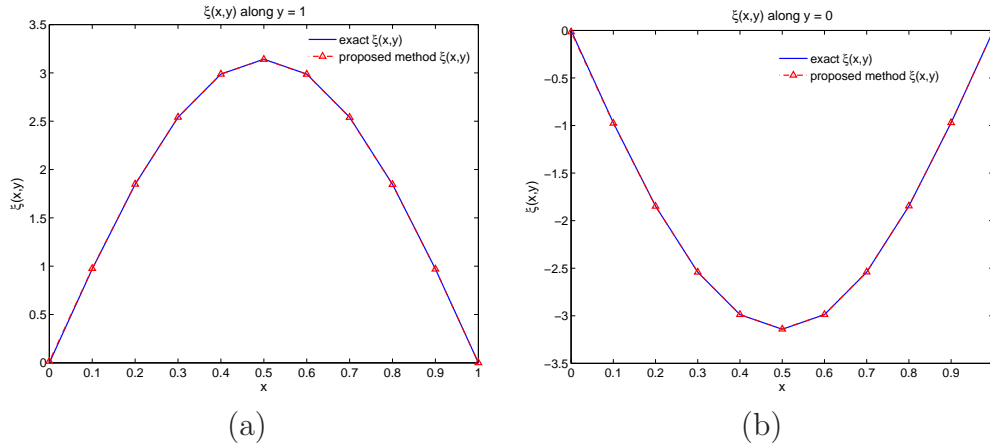


Figure 2.7: Poisson equation in a regular domain: solution of $\xi(x, y)$ obtained by the proposed method in comparison with exact solution (a) along $y = 1$, (b) along $y = 0$.

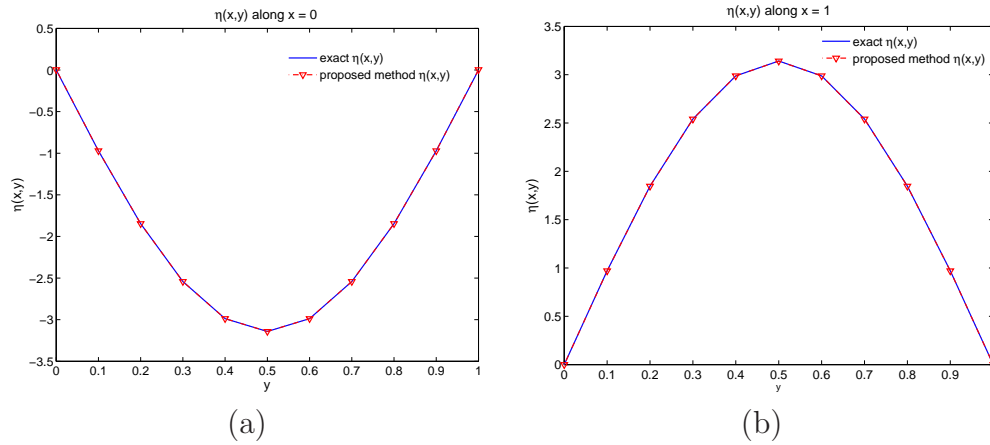


Figure 2.8: Poisson equation in a regular domain: solution of $\eta(x, y)$ obtained by the proposed method in comparison with exact solution (a) along $x = 0$, (b) along $x = 1$.

2.4.3 Poisson equation in an irregular domain

The Poisson equation in example 2.4.1 is examined in a more complicated irregular domain as shown in Figure 2.15. The Dirichlet boundary conditions on the upper edge and the left edge are given as follows.

$$\phi(0, y) = \cos(\pi y), \quad \text{on } x = 0, \quad (2.40a)$$

$$\phi(x, 0) = \cos(\pi x), \quad \text{on } y = 0. \quad (2.40b)$$

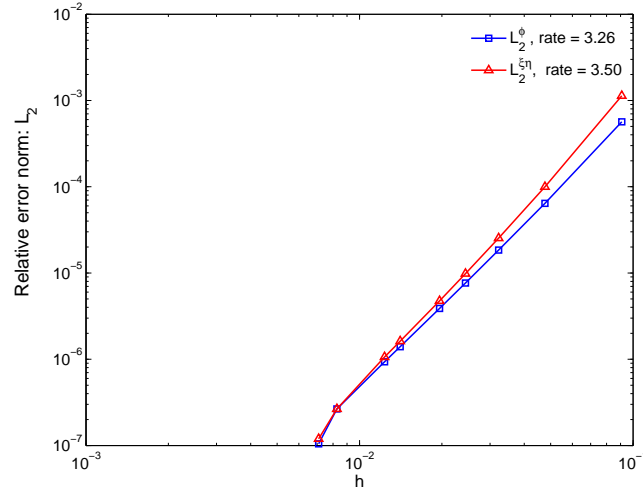


Figure 2.9: Poisson equation in a regular domain: relative error norms L_2^ϕ and $L_2^{\xi\eta}$.

The Neumann boundary conditions on the inner arc and the outer arc are, respectively

$$n_x \frac{\partial \phi(x, y)}{\partial x} + n_y \frac{\partial \phi(x, y)}{\partial y} = q(x, y), \quad \text{on } x^2 + y^2 = 1, \quad (2.41a)$$

$$n_x \frac{\partial \phi(x, y)}{\partial x} + n_y \frac{\partial \phi(x, y)}{\partial y} = q(x, y), \quad \text{on } x^2 + y^2 = 4, \quad (2.41b)$$

where $q(x, y) = -n_x \pi \sin(\pi x) \cos(\pi y) - n_y \pi \cos(\pi x) \sin(\pi y)$.

The complexity is increased with the Neumann boundary conditions on two curved boundaries. Making use of the proposed boundary interpolation scheme, the irregular boundaries can be accurately represented as in the following obtained results. A number of grids of 77, 275, 1459 and 2872 CPs is used for computation. Figure 2.16 numerically shows the convergence behaviour of the method. The convergence rates of the present method for primary variable ϕ and dual variables (ξ, η) are $O(h^{3.88})$ and $O(h^{3.43})$, respectively. At the finest grid, the relative error norm L_2^ϕ and $L_2^{\xi\eta}$ are 1.375×10^{-5} and 1.016×10^{-4} , respectively.

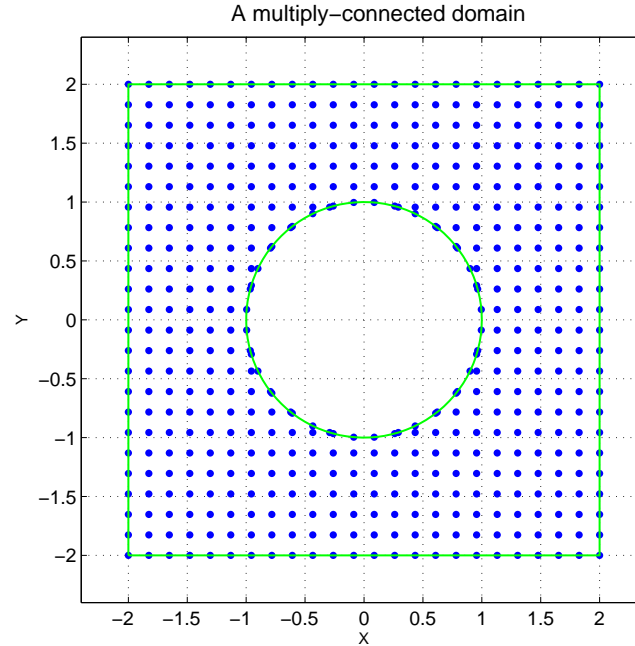


Figure 2.10: Poisson problem in a multiply-connected domain: domain discretisation with 512 nodes.

2.4.4 Linear elastic cantilever beam

The performance of the present method is now further evaluated, using the problem of a cantilever beam subject to parabolic shear load at the end $x = 0$ as shown in Figure 2.17.

The following parameters are used for the problem: $L = 4.8$ and $D = 1.2$. The beam has a unit thickness. Young's modulus is $E = 3 \times 10^6$, Poisson's ratio is $\mu = 0.3$ (also $\mu = 0.5$) and the integrated parabolic shear force is $P = 100$. Plane stress condition is assumed and there is no body force.

The exact solution for this problem was given by Timoshenko and Goodier (1970) as

$$\sigma_{xx}(x, y) = \frac{P(L-x)y}{I} \quad (2.42a)$$

$$\sigma_{yy}(x, y) = 0 \quad (2.42b)$$

$$\tau_{xy}(x, y) = \frac{-P}{2I} \left(\frac{D^2}{4} - y^2 \right) \quad (2.42c)$$

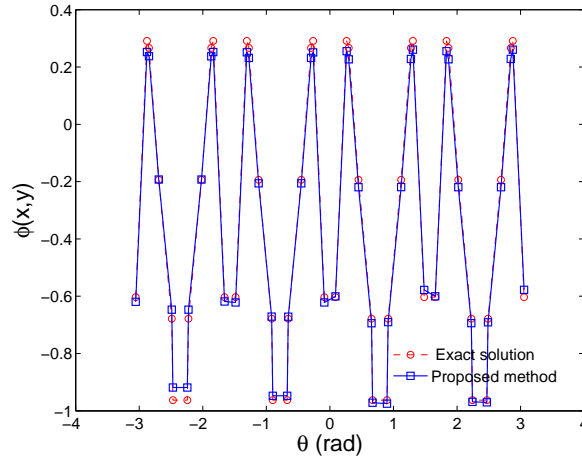


Figure 2.11: Poisson equation in a multiply-connected domain: solutions along curved boundary of $\phi(x, y)$ with 512 nodes.

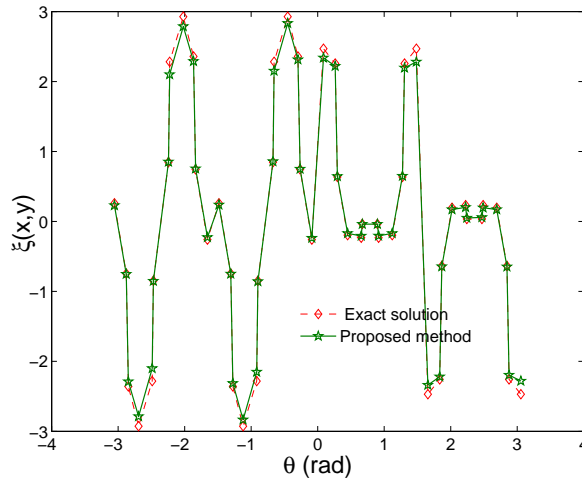


Figure 2.12: Poisson equation in a multiply-connected domain: solutions along curved boundary $\xi(x, y)$ with 512 nodes.

The displacements are given by

$$u_x = \frac{Py}{6EI} \left[(6L - 3x)x + (2 + \nu) \left(y^2 - \frac{D^2}{4} \right) \right] \quad (2.43)$$

$$u_y = \frac{-P}{6EI} \left[3\nu y^2(L - x) + (4 + 5\nu) \frac{Dx^2}{4} + (3L - x)x^2 \right] \quad (2.44)$$

The exact displacement (2.43) and (2.44) are applied on the Dirichlet boundary $x = L$. In the Galerkin formulation, the traction-free boundary condition is automatically met but in a collocation scheme, the the traction-free condition

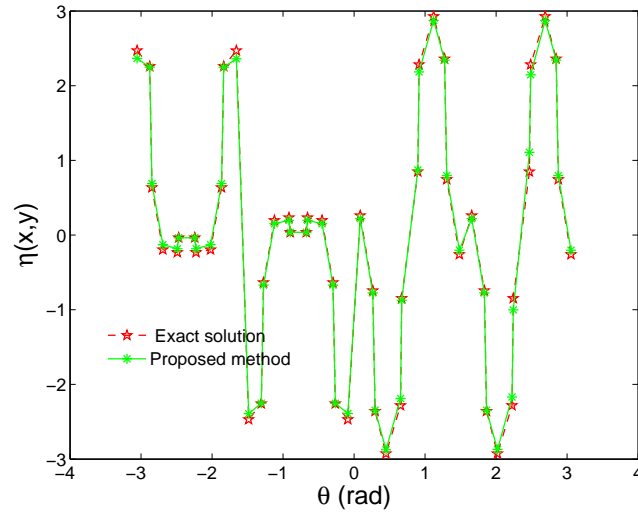


Figure 2.13: Poisson equation in a multiply-connected domain: solutions along curved boundary $\eta(x, y)$ with 512 nodes.

must be explicitly enforced.

Figure 2.19 shows a comparison of the exact solution and that of the present method (with a regular grid of 5×20 CPs as shown in Figure 2.18) for the beam deflection $u_y(x, y)$ along the x -axis. An excellent agreement between the analytical and numerical results is observed. Figure 2.20 and Figure 2.21 illustrate the comparison between analytically calculated solutions and the numerical results for s_{xy} along $x = L$ and s_x along upper and lower edges. Again, the plots show that numerical solution and exact solution are in excellent agreement, which is confirmed by the error measures as shown in Figure 2.22. The present results compare very favourably with those by direct and least-squares collocation meshless methods using moving least square approximation of Zhang et al. (2001) and Pan et al. (2005). Thus, compared with the standard collocation method, the present method has a good accuracy and stability for this problem.

For convergence study, a number of regularly distributed grids of 20×5 , 36×9 , 52×13 , 68×17 , 84×21 , 124×31 and 164×41 CPs is employed for both compressible material ($\mu = 0.3$) and incompressible material ($\mu = 0.5$) cases. The convergence behaviour in the case of $\mu = 0.3$ is shown in Figure 2.22, which

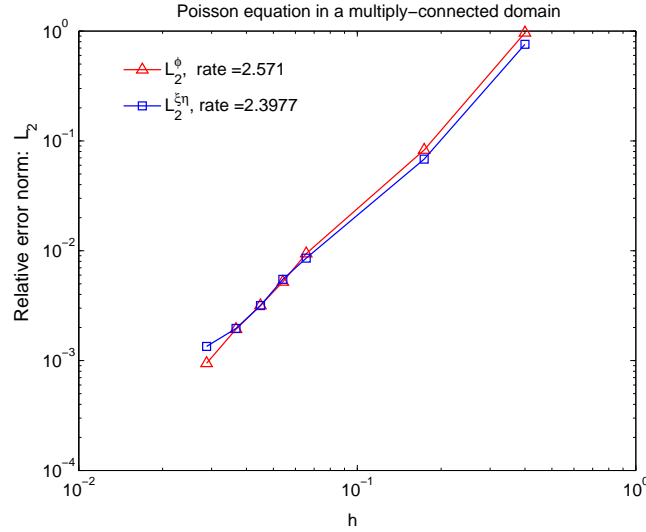


Figure 2.14: Poisson equation in a multiply-connected domain: relative error norms L_2^ϕ and $L_2^{\xi\eta}$, and convergence rates.

indicates that the present method has very good stability and accuracy with a convergence rate of 3.1265 and 3.0557 for displacement and stress, respectively. At the finest grid, the relative error norms L_2^u and L_2^σ are 5.102×10^{-6} and 4.802×10^{-6} , respectively. Moreover, unlike the displacement-based formulation, in which the accuracy for stress variables is much lower than that for the displacement variables, the proposed method obtained a higher accuracy and convergence rate for the stress field as well.

The robustness of the proposed method in the incompressible limit is also examined. The cantilever beam problem is analyzed with different values of Poisson ratio: $\mu = 0.499$, $\mu = 0.49999$, and $\mu = 0.5$. Our numerical experiments indicate that the volumetric locking can be alleviated by the present approach without any extra effort even in the case of $\mu = 0.5$, for which the convergence behaviour is presented in Figure 2.23, showing good stability and high accuracy. The convergence rates for displacement and stress variables are $O(h^{3.215})$ and $O(h^{3.0})$, respectively. At the finest grid, the relative error norms L_2^u and L_2^σ are 4.818×10^{-6} and 4.869×10^{-6} , respectively.

In term of efficiency, the computational costs versus error in displacement norm

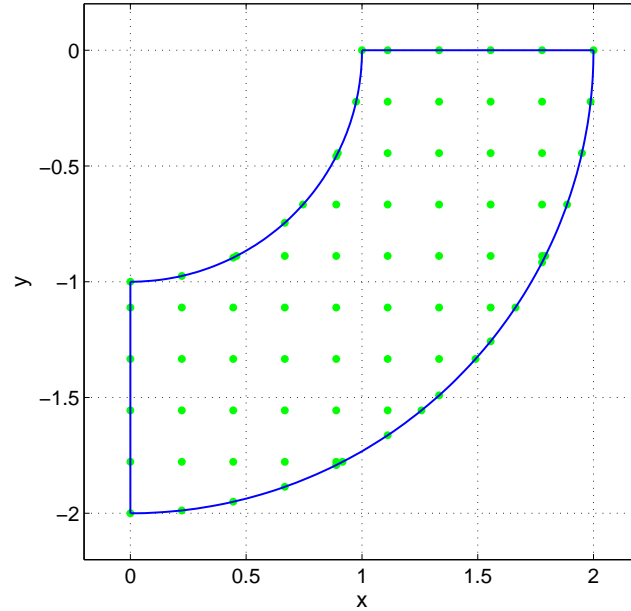


Figure 2.15: Poisson problem in an irregular domain: domain discretisation with 77 points.

of the proposed method and FEM (using Q4 element) are plotted in Figure 2.24. The comparisons in Figure 2.22 and 2.24 demonstrate that not only the accuracy and order of convergence but also the efficiency of the former exceed those of the latter. Furthermore, the efficiency of the proposed method is compared with that of the latest meshfree method, namely the edge based smooth point interpolation methods (ES-PIM and ES-RPIM) (Liu and Zhang, 2008), by plotting the differential computational cost (DCC) of the methods in comparison with the FEM ($\text{DCC} = \text{CPU time of FEM} - \text{CPU time of the reference method}$) at the same level of relative error in displacement norm (Figure 2.25). It can be observed that the proposed method is less efficient than ES-PIM(T3) (the most efficient one among the ES-PIM family) but more efficient than ES-RPIM(T6) (the most efficient one among the ES-RPIM family).

2.4.5 Linear elastic infinite plate with a circular hole

In this example, an infinite plate with a circular hole subjected to unidirectional tensile load of 1.0 in the x direction as shown in Figure 2.26 is analyzed. The

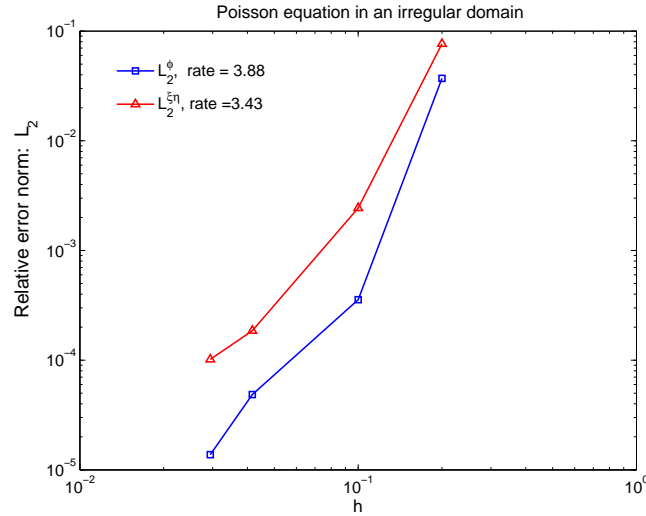


Figure 2.16: Poisson equation in an irregular domain: relative error norms L_2^ϕ and $L_2^{\xi\eta}$, and convergence rates.

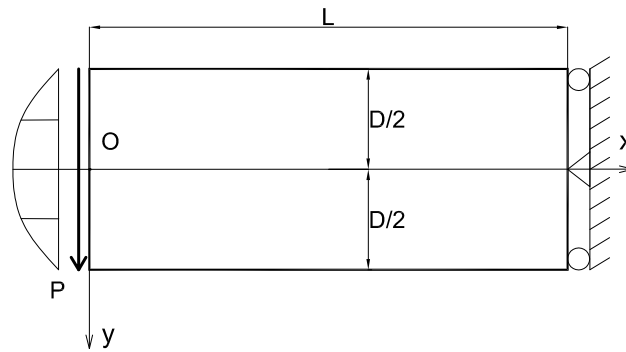


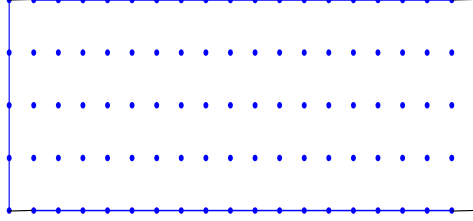
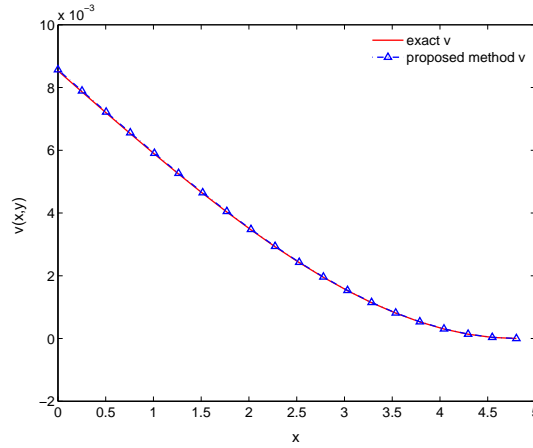
Figure 2.17: Cantilever beam: a mathematical model.

radius of the hole is taken as 1 unit. Owing to symmetry, only the upper right quadrant $[0, 3] \times [0, 3]$ of the plate is modeled (Figure 2.27).

In this problem, plane stress conditions are assumed with elastic isotropic properties $E = 10^3$, $\mu = 0.3$ (also $\mu = 0.5$). The exact solution to this problem was given by Timoshenko and Goodier (1970) as follows

$$\sigma_x(x, y) = \sigma \left[1 - \frac{a^2}{r^2} \left[\frac{3}{2} \cos(2\theta) + \cos(4\theta) \right] + \frac{3a^4}{2r^4} \cos(4\theta) \right], \quad (2.45a)$$

$$\sigma_y(x, y) = -\sigma \left[\frac{a^2}{r^2} \left[\frac{1}{2} \cos(2\theta) - \cos(4\theta) \right] + \frac{3a^4}{2r^4} \cos(4\theta) \right], \quad (2.45b)$$

Figure 2.18: Cantilever beam: discretisation model with 20×5 CPs.Figure 2.19: Cantilever beam: $u_y(x, y)$ along $y = 0$ with 20×5 CPs ($\mu = 0.3$).

$$\tau_{xy}(x, y) = -\sigma \left[\frac{a^2}{r^2} \left[\frac{1}{2} \sin(2\theta) + \sin(4\theta) \right] - \frac{3a^4}{2r^4} \sin(4\theta) \right], \quad (2.45c)$$

where (r, θ) are the polar coordinates, a the radius of the hole.

The corresponding displacements are given by

$$u_x(x, y) = \sigma \frac{(1 + \mu)}{E} \left[\frac{1}{1 + \mu} r \cos(\theta) + \frac{2}{1 + \mu} \frac{a^2}{r} \cos(\theta) + \frac{1}{2} \frac{a^2}{r} \cos(3\theta) - \frac{1}{2} \frac{a^4}{r^3} \cos(3\theta) \right] \quad (2.46a)$$

$$u_y(x, y) = \sigma \frac{(1 + \mu)}{E} \left[\frac{-\mu}{1 + \mu} r \sin(\theta) + \frac{1 - \mu}{1 + \mu} \frac{a^2}{r} \sin(\theta) + \frac{1}{2} \frac{a^2}{r} \sin(3\theta) - \frac{1}{2} \frac{a^4}{r^3} \sin(3\theta) \right] \quad (2.46b)$$

The boundary conditions of the problem are as follows. The tractions which

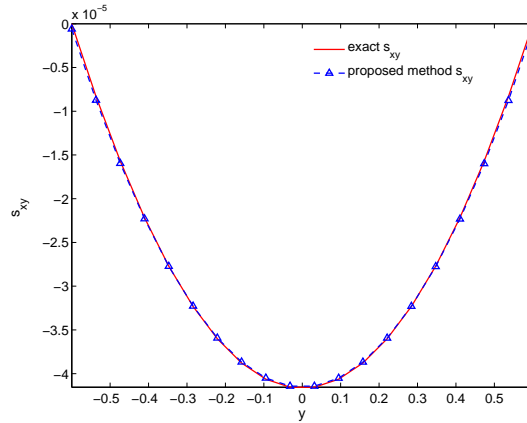


Figure 2.20: Cantilever beam: s_{xy} along Dirichlet boundary $x = L$ with 20×5 CPs ($\mu = 0.3$).

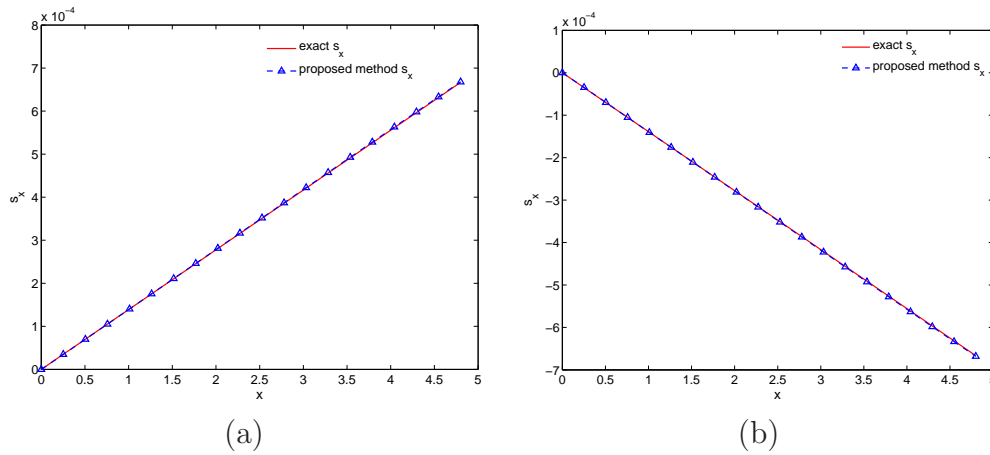


Figure 2.21: Cantilever Beam ($\mu = 0.3$): s_x solution with 20×5 CPs (a) along $y = D/2$, (b) along $y = -D/2$.

correspond to the exact solution for the infinite plate are applied on the top and right edges, the symmetric conditions are applied on the left and bottom edges, and the edge of the hole is traction free.

The obtained results with 493 CPs are plotted in the Figures 2.28-2.29. Figure 2.28 expresses a comparison of displacement $u_x(x, y)$ along $y = 0$ by the numerical method and the exact solution. This figure shows that the obtained result is in good agreement with the analytical solution. Figure 2.29 demonstrates a comparison of stress $s_x(x, y)$ along $x = 0$ by the proposed method and the exact solution. An excellent agreement of the numerical stress and the exact one can be observed in this figure.

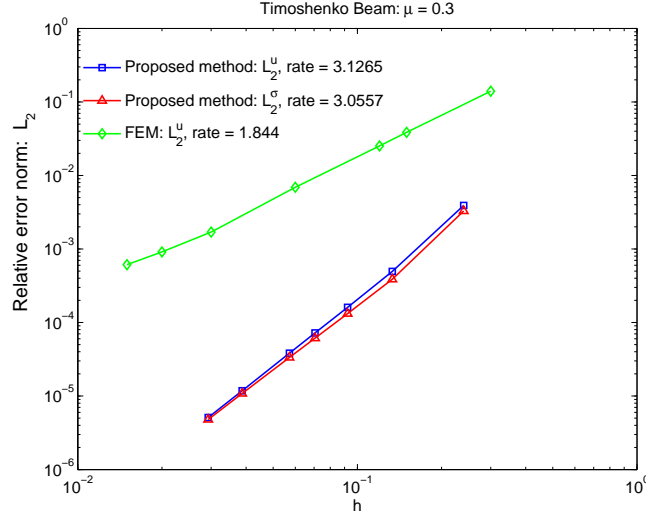


Figure 2.22: Cantilever beam ($\mu = 0.3$): relative error norms L_2^u and L_2^σ , and convergence rates.

The convergence behaviour of the proposed method in this example is studied with 116, 213, 493, 1136, 1872 and 2691 CPs, which are based on uniformly distributed grids. The convergence curves for a compressible case ($\mu = 0.3$) are presented in Figure 2.30. Good stability and high accuracy are obtained in this problem as shown in the figure. The same rates of convergence are observed for displacement and stress. The convergence rates for displacement and stress variables are $O(h^{4.141})$ and $O(h^{4.028})$, respectively. At the finest grid, the relative error norms L_2^u and L_2^σ are 8.687×10^{-4} and 6.221×10^{-4} , respectively.

The above configurations of collocation points are also employed to examine the performance of the present method in the case of incompressible materials ($\mu = 0.5$). The convergence behaviour is presented in Figure 2.31. Like the cantilever beam example, the obtained results indicate that the volumetric locking due to incompressibility is alleviated. Good accuracy and high convergence rate are obtained even in the case of $\mu = 0.5$ as shown in Figure 2.31. The convergence rates for displacement and stress variables are $O(h^{4.183})$ and $O(h^{4.118})$, respectively. At the finest grid, the relative error norms L_2^u and L_2^σ are 1.147×10^{-3} and 8.086×10^{-4} , respectively. Unlike standard collocation method, which is very unstable for elasticity problems with traction boundary

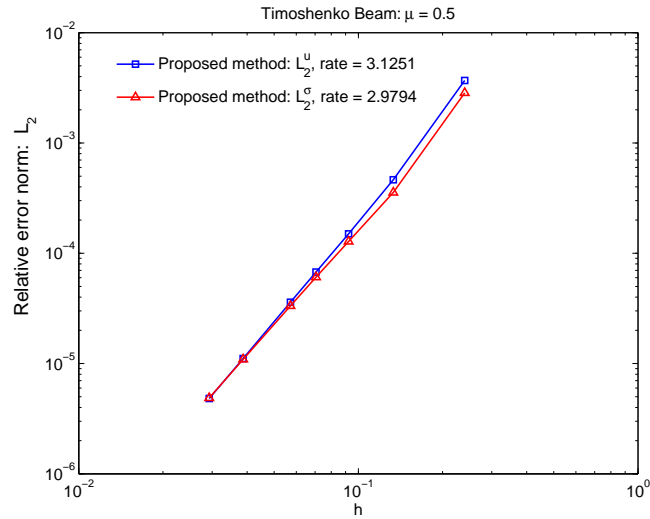


Figure 2.23: Cantilever beam ($\mu = 0.5$): relative error norms L_2^u and L_2^σ , and convergence rates.

conditions (Zhang et al., 2001; Pan et al., 2005), the present method shows superior accuracy and stable convergence.

2.5 Conclusion

This chapter reports a successful solution approach for problems governed by high order PDEs where the governing equations are reformulated as first-order systems. Such first-order systems are then numerically modeled with Cartesian grid discretisation and 1D-IRBFN, which is efficient (Cartesian grid) and yields high order accuracy (IRBFN), as illustrated by a variety of test problems with regular as well as irregular domains.

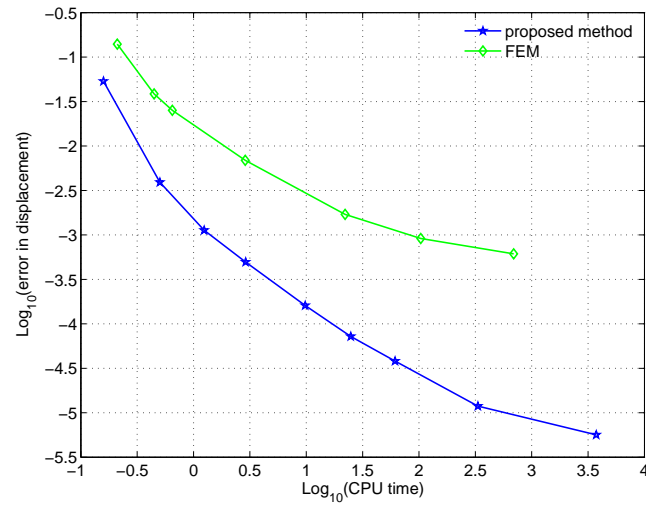


Figure 2.24: Cantilever beam ($\mu = 0.3$): comparison of efficiency between the proposed method and FEM. Computational cost (second) versus L2 relative error norm in displacement.

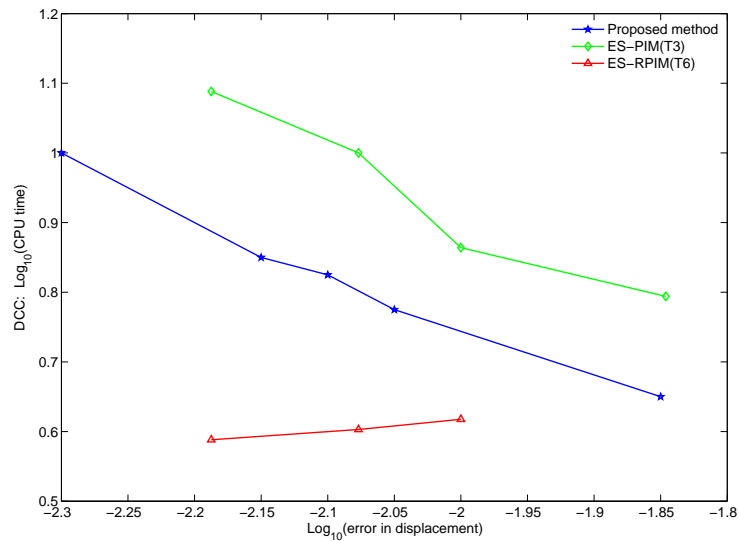


Figure 2.25: Cantilever beam ($\mu = 0.3$): comparison of efficiency between the proposed method and the most efficient ES-PIM and ES-RPIM. Differential computational cost (DCC) of different methods in comparison with FEM (CPU time of FEM – CPU time of the reference method) at the same level of relative error in displacement norm.

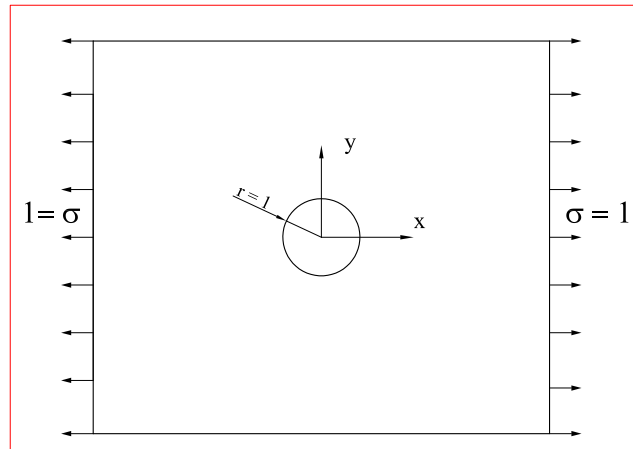


Figure 2.26: Infinite plate with a circular hole.

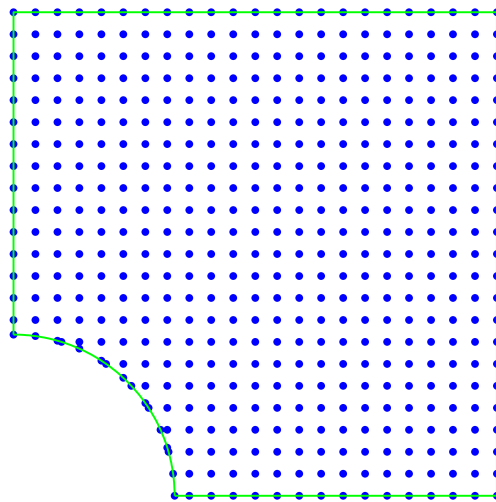


Figure 2.27: Infinite plate with a circular hole: domain discretisation with 493 CPs.

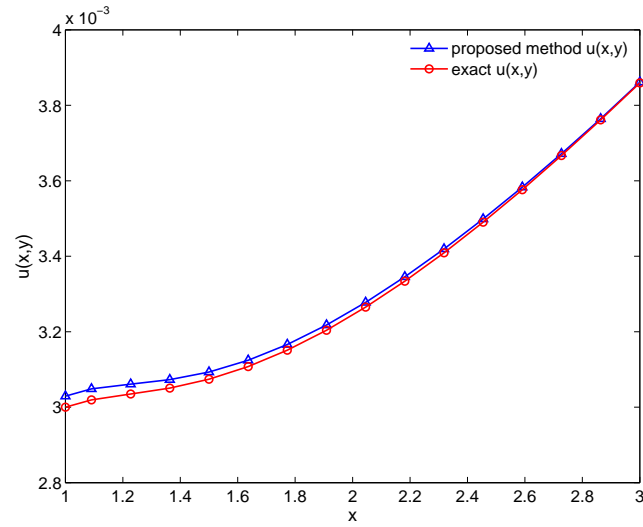


Figure 2.28: Infinite plate with a circular hole: $u_x(x, y)$ along $y = 0$ with 493 CPs ($\mu = 0.3$).

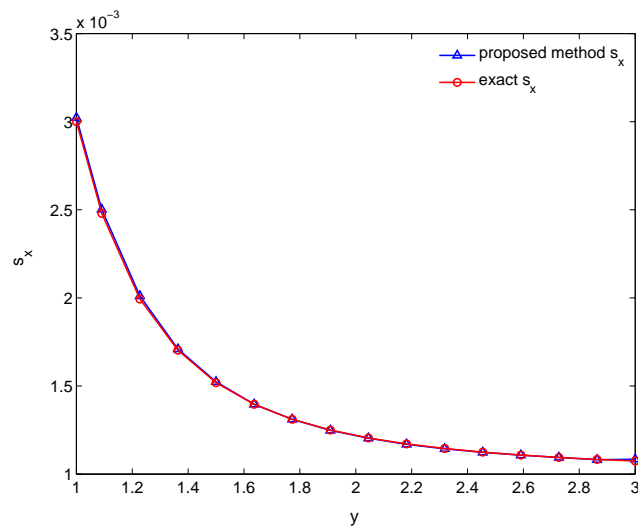


Figure 2.29: Infinite plate with a circular hole: s_x along $x = 0$ with 493 CPs ($\mu = 0.3$).

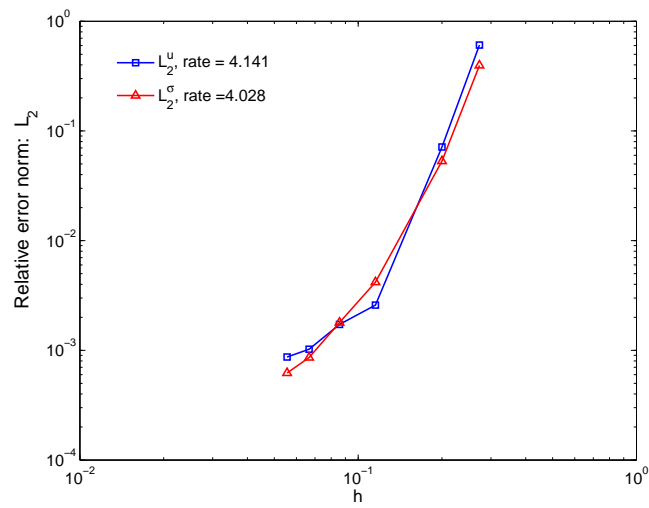


Figure 2.30: Infinite plate with a circular hole ($\mu = 0.3$): relative error norms L_2^u and L_2^σ , and convergence rates.

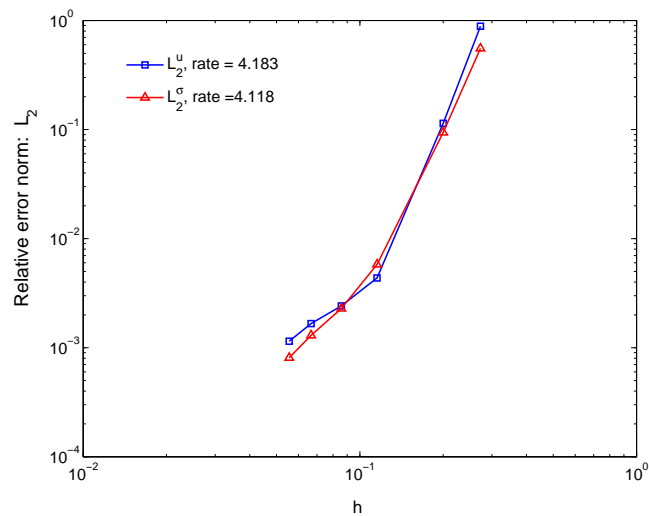


Figure 2.31: Infinite plate with a circular hole ($\mu = 0.5$): relative error norms L_2^u and L_2^σ , and convergence rates.

Chapter 3

A Moving IRBFN-based integration-free meshless method

A novel approximation method using integrated radial basis function networks (IRBFN) coupled with moving least square (MLS) approximants, namely moving integrated radial basis function networks (MIRBFN), is proposed in this chapter. In this method, the computational domain Ω is divided into finite sub-domains Ω_I which satisfy point-wise overlap condition. The local function interpolation is constructed by using IRBFN supported by all nodes in subdomain Ω_I . The global function is then constructed by using Partition of Unity Method (PUM), where MLS functions play the role of partition of unity. As a result, the proposed method is locally supported and yields sparse and banded interpolation matrices. The computational efficiency are excellently improved in comparison with that of the original global IRBFN method. In addition, the present method possesses the Kronecker- δ property, which makes it easy to impose the essential boundary conditions. The proposed method is applicable to randomly distributed datasets and arbitrary domains. In this work, the MIRBFN method is implemented in the collocation of first-order system formulation (Le et al., 2010a) to solve PDEs governing various problems includ-

ing heat transfer, elasticity of both compressible and incompressible materials, and linear static crack problems. The numerical results show that the present method offers high order of convergence and accuracy.

3.1 Introduction

In recent years, RBF-based meshless methods have received increasing interest from the research community since the associated discretisation of the governing PDEs is very simple for random point distribution and arbitrary domain. Furthermore, global RBFN/IRBFN enjoys spectral accuracy and exponential convergence (Madych, 1992; Cheng et al., 2003). However, the main drawback of the globally supported RBFN/IRBFN is that the resultant interpolation matrix is dense and highly ill-conditioned due to the nature of global approximation. For example, the condition number of such a matrix is about 6×10^{19} with only 20×20 collocation points (Fasshauer, 1997). Therefore, globally supported RBFN/IRBFN methods are less effective in large-scale computation and in problems concerning with small-scale features such as cracks/strain localization. Attempts to deal with this deficiency include domain decomposition method (Ling and Kansa, 2004), block partitioning and multizone methods (Kansa and Hon, 2000), and preconditioned methods (Baxter, 2002; Brown et al., 2005).

Recently, local RBFN methods have been developed as an alternative approach. Compactly supported RBF truncated from polynomials can improve the condition number, yet a large support is required to obtain a reasonable accuracy (Wendland, 1995). It is thus considered not a robust method against non-uniform datasets (Tobor et al., 2004). Moreover, some new local methods that exchange spectral accuracy for a sparse and better-conditioned system, have been proposed, including explicit local RBF (Šaler and Vertnik, 2006), finite difference based local RBF (Wright and Fornberg, 2006; Liu et al., 2006), dif-

ferential quadrature based local RBF (Shu et al., 2003; Shu and Wu, 2007), and radial point interpolation method (Liu et al., 2005b,a).

Another approach to local RBF is one based on the partition of unity (PU) method. The PU concept was first introduced by Shepard and known as Shepard's method. However, Shepard's method is not widely applied since it is only of constant precision. Since the works of Babuška and Melenk (1997), this method has received more attention and may be considered an underlying concept for many other methods such as, PUFEM (Melenk and Babuška, 1996), XFEM (Moës et al., 1999a; Bordas et al., 2006, 2008a), GFEM (Strouboulis et al., 2000a,b) and certain meshfree methods (Rabczuk and Belytschko, 2004a, 2007a; Rabczuk et al., 2007b; Ventura et al., 2002). For RBF methods, locally supported RBF based on the PU concept was first introduced in data fitting by Wendland (2002) and has been further expanded by several researchers (Tobor et al., 2004, 2006; Ohtake et al., 2006). In recent times, the idea of local RBF based on the PU concept was extended by Chen et al. (2008b) for solving PDEs. In their method, the reproducing kernel function is employed as PU function to achieve a higher precision than that of Shepard method.

Motivated by the former works, this chapter proposes a new locally supported MIRBFN method, in which the standard globally supported IRBFN is coupled with the moving least square (MLS) approximants via the PU concept to formulate a locally supported MIRBFN interpolation method. Moreover, the present interpolation method is implemented in the collocation of first-order system formulation, resulting in an integration-free meshless method for solving PDEs. The proposed method is verified by various numerical examples, including heat transfer, elasticity of compressible and incompressible materials, and linear static crack problems. The remaining of this chapter is organized as follows. The construction of the present MIRBFN is presented in section 3.2. Section 3.3 reports the numerical experiments and section 3.4 draws some conclusions.

3.2 Construction of Moving IRBFN

3.2.1 Moving least-square approximants

The moving least-square (MLS) procedure presented in Belytschko et al. (1994) is briefly reproduced in this section as follows. The interpolant $u^h(\mathbf{x})$ of the function $u(\mathbf{x})$ is defined in the domain Ω by

$$u^h(\mathbf{x}) = \sum_{j=1}^{\mathcal{M}} a_j(\mathbf{x}) p_j(\mathbf{x}) \equiv \mathbf{p}^T(\mathbf{x}) \mathbf{a}(\mathbf{x}), \quad (3.1)$$

where $\mathbf{x}^T = [x, y]$, $\mathbf{p}^T = [1, x, y]$ is a linear basis, $\mathcal{M} = 3$ in \mathbb{R}^2 .

$\mathbf{a}(\mathbf{x})$ is obtained at any point \mathbf{x} by minimizing the following weighted, discrete L_2 norm

$$J = \sum_{I=1}^n w(\mathbf{x} - \mathbf{x}_I) [\mathbf{p}^T(\mathbf{x}_I) \mathbf{a}(\mathbf{x}) - u_I]^2, \quad (3.2)$$

where n is the number of points in the neighbourhood of \mathbf{x} for which the weight function $w(\mathbf{x} - \mathbf{x}_I) \neq 0$, and u_I is the nodal value of u at $\mathbf{x} = \mathbf{x}_I$.

The minimization of J in equation (3.2) with respect to $\mathbf{a}(\mathbf{x})$ leads to the following linear relation between $\mathbf{a}(\mathbf{x})$ and the vector of local nodal values \mathbf{u}

$$\mathbf{A}(\mathbf{x}) \mathbf{a}(\mathbf{x}) = \mathbf{B}(\mathbf{x}) \mathbf{u}, \quad (3.3)$$

or

$$\mathbf{a}(\mathbf{x}) = \mathbf{A}^{-1}(\mathbf{x}) \mathbf{B}(\mathbf{x}) \mathbf{u}, \quad (3.4)$$

where $\mathbf{A}(\mathbf{x})$ and $\mathbf{B}(\mathbf{x})$ are defined by

$$\mathbf{A}(\mathbf{x}) = \sum_{I=1}^n w(\mathbf{x} - \mathbf{x}_I) \mathbf{p}(\mathbf{x}_I) \mathbf{p}^T(\mathbf{x}_I) \quad (3.5)$$

$$\mathbf{B}(\mathbf{x}) = \left[w(\mathbf{x} - \mathbf{x}_1) \begin{pmatrix} 1 \\ x_1 \\ y_1 \end{pmatrix}, w(\mathbf{x} - \mathbf{x}_2) \begin{pmatrix} 1 \\ x_2 \\ y_2 \end{pmatrix}, \dots, w(\mathbf{x} - \mathbf{x}_n) \begin{pmatrix} 1 \\ x_n \\ y_n \end{pmatrix} \right] \quad (3.6)$$

$$\mathbf{u}^T = [u_1, u_2, \dots, u_n]. \quad (3.7)$$

Substitution of equation (3.4) into equation (3.1) yields

$$u^h(\mathbf{x}) = \sum_{I=1}^n \sum_{j=1}^{\mathcal{M}} p_j(\mathbf{x}) (\mathbf{A}^{-1}(\mathbf{x}) \mathbf{B}(\mathbf{x}))_{jI} u_I \equiv \sum_{I=1}^n \varphi_I(\mathbf{x}) u_I, \quad (3.8)$$

where the shape function $\varphi_I(\mathbf{x})$ is defined by

$$\varphi_I(\mathbf{x}) = \sum_{j=1}^{\mathcal{M}} p_j(\mathbf{x}) (\mathbf{A}^{-1}(\mathbf{x}) \mathbf{B}(\mathbf{x}))_{jI}, \quad (3.9)$$

or in compact form

$$\varphi_I(\mathbf{x}) = \mathbf{c}^T(\mathbf{x}) w(\mathbf{x} - \mathbf{x}_I) \mathbf{p}(\mathbf{x}_I), \quad (3.10)$$

where $\mathbf{A}(\mathbf{x}) \mathbf{c}(\mathbf{x}) = \mathbf{p}(\mathbf{x})$ defines vector $\mathbf{c}(\mathbf{x})$.

$\mathbf{c}(\mathbf{x})$ can efficiently be computed by the LU factorization of $\mathbf{A}(\mathbf{x})$ with backward substitution (Belytschko et al., 1996a; Nguyen et al., 2008b) as follows.

$$\mathbf{L} \mathbf{U} \mathbf{c}(\mathbf{x}) = \mathbf{p}(\mathbf{x}), \quad \mathbf{U} \mathbf{c}(\mathbf{x}) = \mathbf{L}^{-1} \mathbf{p}(\mathbf{x}), \quad \mathbf{c}(\mathbf{x}) = \mathbf{U}^{-1} \mathbf{L}^{-1} \mathbf{p}(\mathbf{x}). \quad (3.11)$$

The partial derivatives of $\varphi_I(\mathbf{x})$ can be obtained by

$$\varphi_{I,i}(\mathbf{x}) = \mathbf{c}_{,i}^T(\mathbf{x})w(\mathbf{x} - \mathbf{x}_I)\mathbf{p}(\mathbf{x}_I) + \mathbf{c}^T(\mathbf{x})w_{,i}(\mathbf{x} - \mathbf{x}_I)\mathbf{p}(\mathbf{x}_I), \quad (3.12)$$

where $(\cdot)_{,i} = \frac{\partial(\cdot)}{\partial x_i}$ and

$$\mathbf{c}_{,i}(\mathbf{x}) = \mathbf{A}_{,i}^{-1}(\mathbf{x})\mathbf{p}(\mathbf{x}) + \mathbf{A}^{-1}(\mathbf{x})\mathbf{p}_{,i}(\mathbf{x}), \quad (3.13)$$

with

$$\mathbf{A}_{,i}(\mathbf{x}) = \sum_{I=1}^n w_{,i}(\mathbf{x} - \mathbf{x}_I)\mathbf{p}(\mathbf{x}_I)\mathbf{p}^T(\mathbf{x}_I). \quad (3.14)$$

It is noted that the following circular kernel function (Schilling et al., 2001) is used to compute MLS shape function in this chapter

$$w(r) = \begin{cases} [1 + \cos(\pi \frac{r}{R_s})]/2, & \frac{r}{R_s} \leq 1; \\ 0, & \frac{r}{R_s} > 1, \end{cases} \quad (3.15)$$

where R_s is the radius of the support domain of the weight function $w(r)$, $r = \|\mathbf{x} - \mathbf{x}_I\|$ and $\|\cdot\|$ denotes the Euclidean norm.

3.2.2 Moving IRBFN interpolation

We propose a locally supported IRBFN, constructed by using the partition of unity concept (Melenk and Babuška, 1996; Babuška and Melenk, 1997) as follows.

Let the open and bounded domain of interest $\Omega \subseteq \mathbb{R}^d$ be discretised by a set of N points \mathcal{X}

$$\mathcal{X} = \{\mathbf{x}_1, \mathbf{x}_2, \dots, \mathbf{x}_N\}, \quad \mathbf{x}_I \in \Omega, \quad I = 1, 2, \dots, N, \quad (3.16)$$

\mathcal{X} is used to define an open cover of Ω , i.e. $\{\Omega_I\}$ such that $\Omega \subseteq \bigcup_{I=1}^N \Omega_I$ and

$\{\Omega_I\}$ satisfies a point-wise overlap condition

$$\forall \mathbf{x} \in \Omega \quad \exists k \in \mathbb{N} \quad : \quad \text{card}\{I | \mathbf{x} \in \Omega_I\} \leq k. \quad (3.17)$$

We choose a family of compactly supported, non-negative, continuous functions ψ_I supported on the closure of Ω_I , such that at every point \mathbf{x} we have the following property

$$\sum_{I=1}^N \psi_I(\mathbf{x}) = 1, \quad \forall \mathbf{x} \in \Omega, \quad (3.18)$$

where $\{\psi_I\}$ is called a partition of unity subordinate to the cover $\{\Omega_I\}$.

For every subdomain Ω_I , a local approximation u_I is constructed by using IRBFN supported by all nodes in Ω_I as presented in section 1.3, i.e.

$$u_I^h(\mathbf{x}) \in V_I, \quad V_I = \text{span}\{\overline{H}_I^{(1)}(\mathbf{x}), \overline{H}_I^{(2)}(\mathbf{x}), \dots, \overline{H}_I^{(M)}(\mathbf{x})\}, \quad (3.19)$$

where $\{V_I\}$ are referred to as the local approximation spaces.

The global approximation of $u(\mathbf{x})$, $u^h(\mathbf{x})$ is obtained via

$$u^h(\mathbf{x}) = \sum_{I=1}^N \psi_I(\mathbf{x}) u_I^h(\mathbf{x}), \quad u^h(\mathbf{x}) \in V, \quad (3.20)$$

where $\psi_I(\mathbf{x})$ and $u_I^h(\mathbf{x})$ are associated with the subdomain Ω_I , and V is called PU method space and defined by

$$V := \sum_{I=1}^N \psi_I V_I. \quad (3.21)$$

In the present work, the partition of unity function ψ_I is chosen to be identical to the MLS shape function φ_I in equation (3.8), the subdomain Ω_I is centered at \mathbf{x}_I as shown in Figure 3.1.

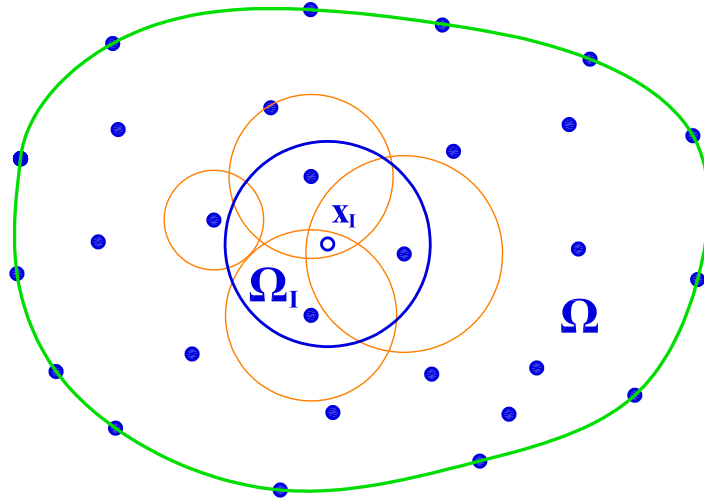


Figure 3.1: Schematic representation of a moving IRBFN: Ω is the domain of interest which is subdivided into N overlapping subdomains Ω_I centered at \mathbf{x}_I .

Replacing ψ_I with MLS shape function φ_I , equation (3.20) can be rewritten as follows

$$u^h(\mathbf{x}) = \sum_{I=1}^N \varphi_I(\mathbf{x}) u_I^h(\mathbf{x}), \quad (3.22)$$

and the associated derivatives of $u^h(\mathbf{x})$ are given by

$$u_{,x}^h(\mathbf{x}) = \sum_{I=1}^N [\varphi_{I,x}(\mathbf{x}) u_I^h(\mathbf{x}) + \varphi_I(\mathbf{x}) u_{I,x}^h(\mathbf{x})], \quad (3.23)$$

$$u_{,y}^h(\mathbf{x}) = \sum_{I=1}^N [\varphi_{I,y}(\mathbf{x}) u_I^h(\mathbf{x}) + \varphi_I(\mathbf{x}) u_{I,y}^h(\mathbf{x})], \quad (3.24)$$

where $u_{I,x}^h(\mathbf{x})$ and $u_{I,y}^h(\mathbf{x})$, are derived in equations (1.15) and (1.18).

$u^h(\mathbf{x})$ and its derivatives can be rewritten in a compact form as

$$u^h(\mathbf{x}) = \sum_{I=1}^N \varphi_I(\mathbf{x}) u_I^h(\mathbf{x}) = \Phi^T(\mathbf{x}) \mathbf{u}, \quad (3.25)$$

$$u_{,x}^h(\mathbf{x}) = \Phi_x^T(\mathbf{x}) \mathbf{u}, \quad (3.26)$$

$$u_{,y}^h(\mathbf{x}) = \Phi_y^T(\mathbf{x}) \mathbf{u}, \quad (3.27)$$

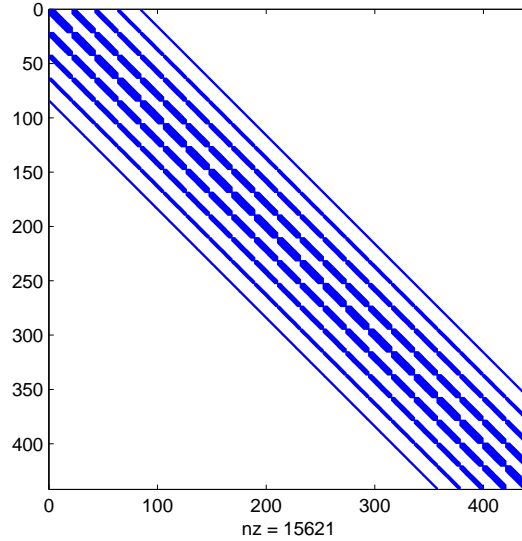


Figure 3.2: Moving IRBFN yields symmetric, sparse and banded interpolation matrices.

where $\mathbf{u} = \{u_1, u_2, \dots, u_N\}$, $\Phi(\mathbf{x})$ is the vector of shape functions.

It is noted that $\Phi_I(\mathbf{x}_J) = \delta_{IJ}$ as shown in Figures 3.3. Consequently, this MIRBFN method possesses the Kronecker- δ property which makes it easy to impose the essential boundary conditions. Owing to the locally supported property, MIRBFN yields symmetric, sparse and banded interpolation matrices as shown in Figure 3.2. This feature makes the method very efficient in storage and computation.

3.2.3 Selection of RBF centers and support radius

In the present MIRBFN method, the selection of local RBF centers $\{\mathbf{c}_i\}_I$ is very flexible. Generally, they can be different from the set of local data points $\{\mathbf{x}_i\}_I$ associated with subdomain Ω_I . For example, if a two-dimensional IRBFN is used, the size of the matrices to be inverted $\overline{\mathbf{H}}_{[x]}$ and $\overline{\mathbf{H}}_{[y]}$ in equations (1.12) and (1.13), respectively, will be $n_I \times (m_I + p_{2I})$, where n_I is the number of data points, m_I the number of RBF centers $\{\mathbf{c}_i\}_I$ and p_{2I} the number of centers used to represent integration constants in the second derivatives. Therefore,

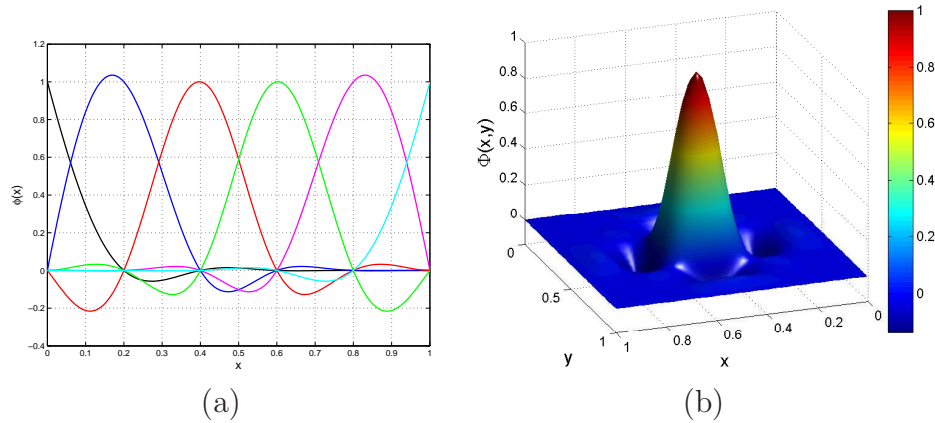


Figure 3.3: Example of MIRBFN shape functions: (a) $\phi_I(x)$ in one dimension and (b) $\phi_I(x, y)$ in two dimensions.

the number of columns of the matrices will be p_{2I} larger than the number of rows when $\{\mathbf{c}_i\}_I$ is the same as $\{\mathbf{x}_i\}_I$. To obtain square matrices, we choose the number of centers to be less than the number of data points ($m_I < n_I$) and p_{2I} to be appropriately small.

On the other hand, the selection of support radius for each subdomain Ω_I also affects the numerical results significantly. The larger support radius is, the higher accuracy and convergence rate are. However, the higher cost of storage and computation, and the deterioration of the condition number of the matrices are consequential trade-offs. Hence, to make the method more local and efficient, smaller values of support radius are preferred in this work.

3.3 Numerical examples

Several PDEs are recast as first-order system (see section 2.2) which are numerically solved in this chapter. The proposed MIRBFN method is implemented in the collocation of such first-order systems. As a result, an integration-free meshless method is formulated and has successfully been tested as reported in this section.

For an error estimation and convergence study, the discrete relative L_2 norm of errors of primary and dual variables are defined as

$$L_2^\phi = \frac{\sqrt{\sum_{i=1}^N \left(\phi_e^{(i)} - \phi^{(i)} \right)^2}}{\sqrt{\sum_{i=1}^N \left(\phi_e^{(i)} \right)^2}}, \quad (3.28)$$

$$L_2^{\xi\eta} = \frac{\sqrt{\sum_{i=1}^N \left[\left(\xi_e^{(i)} - \xi^{(i)} \right)^2 + \left(\eta_e^{(i)} - \eta^{(i)} \right)^2 \right]}}{\sqrt{\sum_{i=1}^N \left[\left(\xi_e^{(i)} \right)^2 + \left(\eta_e^{(i)} \right)^2 \right]}}, \quad (3.29)$$

for Poisson equation and

$$L_2^u = \frac{\sqrt{\sum_{i=1}^N \left((u_x)_e^{(i)} - (u_x)^{(i)} \right)^2 \left((u_y)_e^{(i)} - (u_y)^{(i)} \right)^2}}{\sqrt{\sum_{i=1}^N \left[\left((u_x)_e^{(i)} \right)^2 + \left((u_y)_e^{(i)} \right)^2 \right]}}, \quad (3.30)$$

$$L_2^\sigma = \frac{\sqrt{\sum_{i=1}^N \left[\left((s_x)_e^{(i)} - s_x^{(i)} \right)^2 + \left((s_y)_e^{(i)} - s_y^{(i)} \right)^2 + \left((s_{xy})_e^{(i)} - s_{xy}^{(i)} \right)^2 \right]}}{\sqrt{\sum_{i=1}^N \left[\left((s_x)_e^{(i)} \right)^2 + \left((s_y)_e^{(i)} \right)^2 + \left((s_{xy})_e^{(i)} \right)^2 \right]}}, \quad (3.31)$$

for elasticity problems, where N is the number of unknown nodal values and the subscript “e” denotes the exact solution. The convergence order of the solution with respect to the refinement of spatial discretization is assumed to be in the form of

$$L_2(h) \approx \zeta h^\lambda = O(h^\lambda), \quad (3.32)$$

where h is the maximum nodal spacing, ζ and λ are the parameters of the exponential model, which are found by general linear least square formula in this work.

It is noted that the CPU time in the following sections is associated with a computer which has 8.0 GB of RAM and two Intel(R) Xeon(R) CPUs of 3.0

GHz each. The code is written in MATLAB[®] language.

3.3.1 Poisson equation

Poisson equation in a regular domain

Consider the following Poisson equation

$$\frac{\partial^2 \phi(x, y)}{\partial x^2} + \frac{\partial^2 \phi(x, y)}{\partial y^2} = -2\pi^2 \cos(\pi x) \cos(\pi y), \quad (3.33)$$

defined in $\Omega = [0, 1] \times [0, 1]$, subjected to the Dirichlet boundary condition

$$\phi(0, y) = \cos(\pi y), \quad \text{on } x = 0, \quad (3.34)$$

and the following Neumann boundary conditions

$$\frac{\partial \phi(1, y)}{\partial x} = 0, \quad \text{on } x = 1, \quad (3.35a)$$

$$\frac{\partial \phi(x, 0)}{\partial y} = 0, \quad \text{on } y = 0, \quad (3.35b)$$

$$\frac{\partial \phi(x, 1)}{\partial y} = 0, \quad \text{on } y = 1. \quad (3.35c)$$

$$(3.35d)$$

The corresponding exact solution is given by

$$\phi(x, y) = \cos(\pi x) \cos(\pi y). \quad (3.36)$$

Two discretisations are considered for this problem: uniform and nonuniform distributions of nodes/collocation points (CPs) as shown in Figures 3.4 and 3.8, respectively. For both cases, the radius of support domains is set at $\frac{R_s}{h} = 2.1$, where h is the maximum spacing between two nearest nodes in x or y direction. The maximum number of uniformly distributed RBF centers m_I in

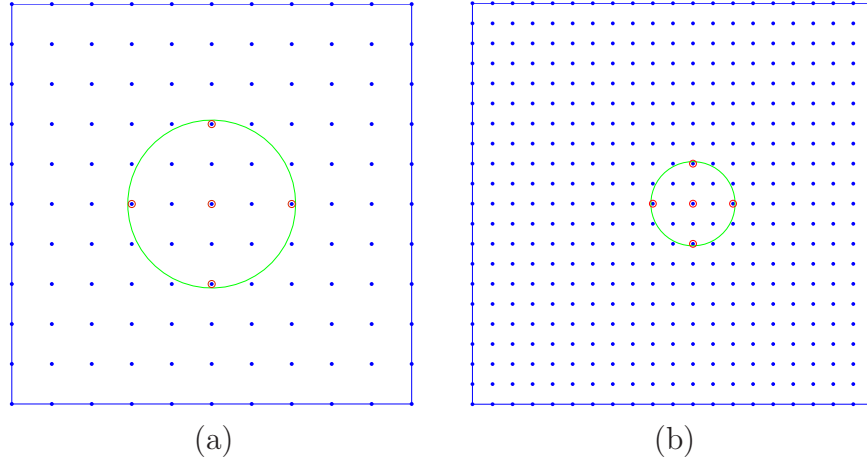


Figure 3.4: Poisson equation in a regular domain: discretisation with uniform distribution of (a) 11×11 nodes, (b) 21×21 nodes. The small circles are RBF centers and the big one is subdomain Ω_I .

Table 3.1: Poisson equation in a regular domain: uniform discretisations with MIRBFN

No. points	L_2^ϕ	$L_2^{\xi\eta}$	$\text{cond}(A)$	β	$\frac{R_s}{h}$	$\frac{\text{CPU time}}{\text{second}}$
3×3	0.4415	1.1413	51.7250	12	2.1	0.15
7×7	0.0252	0.0219	512.8116	12	2.1	0.30
11×11	0.0036	0.0041	813.8110	12	2.1	0.59
21×21	4.4864e-4	5.5402e-4	2.2514e3	12	2.1	2.07
25×25	2.5203e-4	3.1671e-4	2.9034e3	12	2.1	3.07
31×31	1.2419e-4	1.5922e-4	4.1964e3	12	2.1	5.13
41×41	5.0132e-5	6.5620e-5	6.1935e3	12	2.1	10.59
61×61	1.4217e-5	1.9006e-5	1.5362e4	12	2.1	35.84
81×81	5.9951e-6	8.0377e-6	3.5862e4	12	2.1	90.0
91×91	4.2892e-6	5.6966e-6	5.2312e4	12	2.1	136.40
101×101	3.2363e-6	4.2199e-6	7.4923e4	12	2.1	197.11
121×121	2.1324e-6	2.6352e-6	9.037e4	12	2.1	374.7
	$O(h^{3.32})$	$O(h^{3.38})$				

Table 3.2: Poisson equation in a regular domain: uniform discretisations with global IRBFN

No. points	L_2^ϕ	$L_2^{\xi\eta}$	$\text{cond}(A)$	β	$\frac{\text{CPU time}}{\text{second}}$
7×7	0.0245	0.0273	1.6043e4	1	0.161
11×11	0.0038	0.0048	2.5617e4	1	0.179
21×21	7.4562e-5	1.5070e-4	5.8907e4	1	2.462
31×31	1.2924e-5	2.3775e-5	1.2225e5	1	30.064
41×41	4.3906e-6	7.9095e-6	2.0292e5	1	149.319
51×51	2.1210e-6	3.7691e-6	3.0404e5	1	535.049
61×61	1.3851e-6	2.1592e-6	7.0649e4	1	1674.980
	$O(h^{4.71})$	$O(h^{4.52})$			

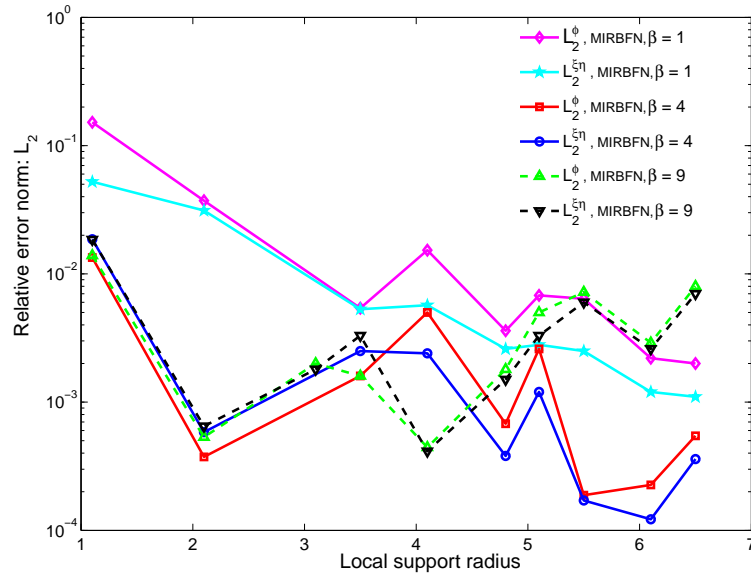


Figure 3.5: Poisson equation in a regular domain with uniform distribution of 21×21 nodes: influence of the local support radius on the accuracy of the solution.

Table 3.3: Poisson equation in a regular domain: unstructured nodes with MIRBFN

No. points	L_2^ϕ	$L_2^{\xi\eta}$	$\text{cond}(A)$	β	$\frac{R_s}{h}$	h	$\frac{\text{CPU time}}{\text{second}}$
88	0.2833	0.1438	1.6887e5	10	2.1	0.1250	0.73
108	0.0402	0.0613	4.5345e5	10	2.1	0.1200	0.80
327	0.0077	0.0057	6.2091e7	10	2.1	0.0685	2.23
691	0.0018	0.0019	4.5704e8	10	2.1	0.0507	5.65
1723	7.2107e-4	5.7631e-4	1.3461e8	10	2.1	0.0308	22.12
2248	3.3681e-4	2.5718e-4	1.2765e8	12	2.1	0.0272	35.58
	$O(h^{3.78})$	$O(h^{3.82})$					

each subdomain is 5 as shown in Figure 3.4. The numbers of centers to represent the integration constants p_{1I} and p_{2I} are 3 and 6, respectively. The values of β in equation (1.8) for both cases are listed in Tables 3.1 and 3.3.

The influences of local support radius $\frac{R_s}{h}$ and β on the accuracy of the solution are numerically studied in this example. Figure 3.5 shows the relative error norms (L_2^ϕ and $L_2^{\xi\eta}$) obtained by the present MIRBFN method with different values of $\frac{R_s}{h}$ while β is fixed. On the other hand, the results with different values of β and fixed local support radius are displayed in Figure 3.6. It can be seen that the values around 2 for $\frac{R_s}{h}$ are not only able to capture well the solution

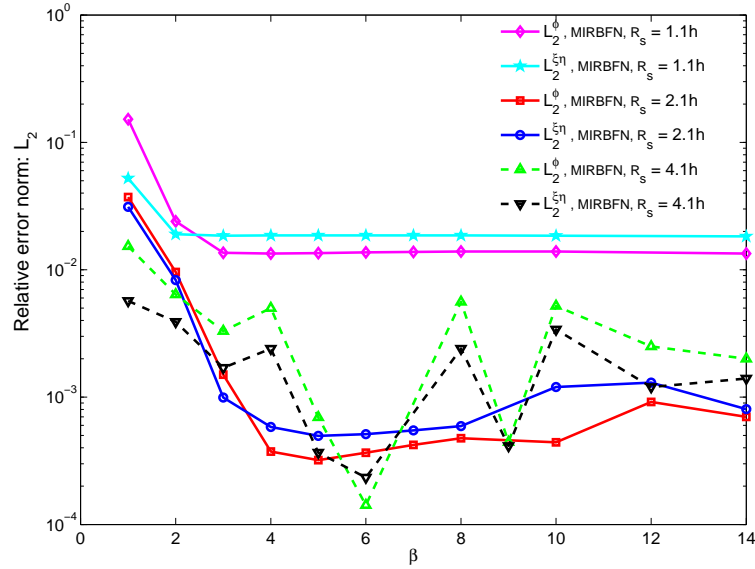


Figure 3.6: Poisson equation in a regular domain with uniform distribution of 21×21 nodes: influence of the RBF width β on the accuracy of the solution.

but also keep the matrix small, as long as β is large enough.

To study the convergence of the method, a number of discretization refinements and the relative L_2 error norms for function values L_2^ϕ and its derivatives $L_2^{\xi\eta}$ are reported in Tables 3.1 and 3.3 for uniform and unstructured cases, respectively. As shown in these tables and Figures 3.7 and 3.9, very good accuracy and stability are obtained. The convergence rates for $\phi(x, y)$ and $(\xi(x, y), \eta(x, y))$ are $O(h^{3.32})$ and $O(h^{3.38})$, respectively, for uniform distribution, and, $O(h^{3.78})$ and $O(h^{3.82})$, respectively, for unstructured nodes. It can be seen that the condition numbers in the case of uniform distribution are relatively smaller than those in the case of random distribution (Table 3.3) since there is a relatively larger number of nodes in each subdomain in the case of random distribution.

The results in Tables 3.1-3.2 and Figure 3.7 indicate that the global IRBFN gives higher orders of convergence. Nonetheless, the condition numbers by the MIRBFN method are slightly better in comparison with those by the global IRBFN method, as listed in Tables 3.1 and 3.2, although β is set quite large for the MIRBFN method. Furthermore, the MIRBFN method is much more efficient than the global IRBFN method as can be seen in Figure 3.10.

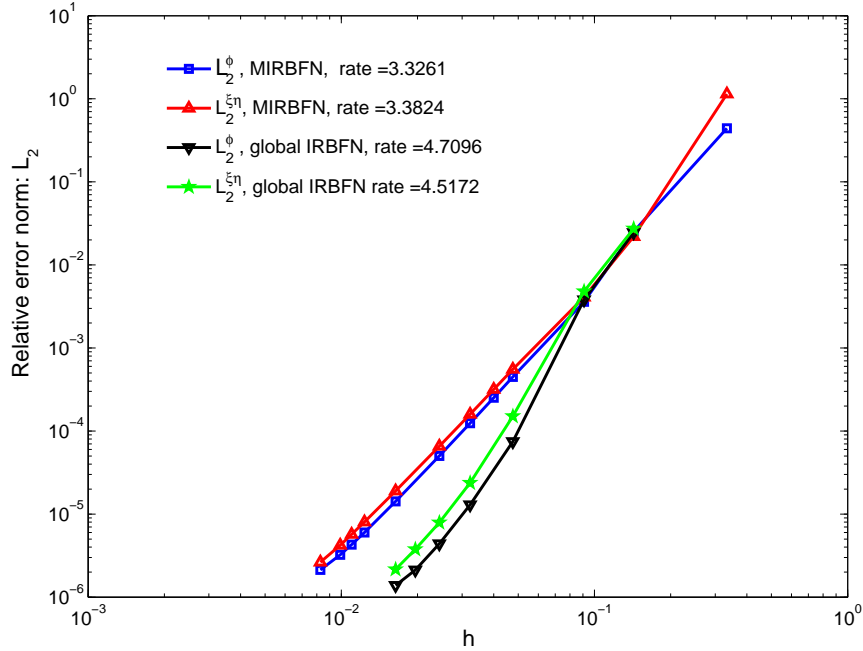


Figure 3.7: Poisson equation in a regular domain with uniform distribution of nodes: relative error norms L_2^ϕ and $L_2^{\xi\eta}$, and associated convergence rates.

Poisson equation in an irregular domain

The Poisson equation in example 3.3.1 is examined in a complicated irregular domain as shown in Figure 3.11. The Dirichlet boundary conditions on the upper edge and the left edge are given as below

$$\phi(0, y) = \cos(\pi y), \quad \text{on } x = 0, \quad (3.37a)$$

$$\phi(x, 0) = \cos(\pi x), \quad \text{on } y = 0. \quad (3.37b)$$

The Neumann boundary conditions on the inner arc and the outer arc are, respectively

$$n_x \frac{\partial \phi(x, y)}{\partial x} + n_y \frac{\partial \phi(x, y)}{\partial y} = q(x, y), \quad \text{on } x^2 + y^2 = 1, \quad (3.38a)$$

$$n_x \frac{\partial \phi(x, y)}{\partial x} + n_y \frac{\partial \phi(x, y)}{\partial y} = q(x, y), \quad \text{on } x^2 + y^2 = 4, \quad (3.38b)$$

where $q(x, y) = -n_x \pi \sin(\pi x) \cos(\pi y) - n_y \pi \cos(\pi x) \sin(\pi y)$.

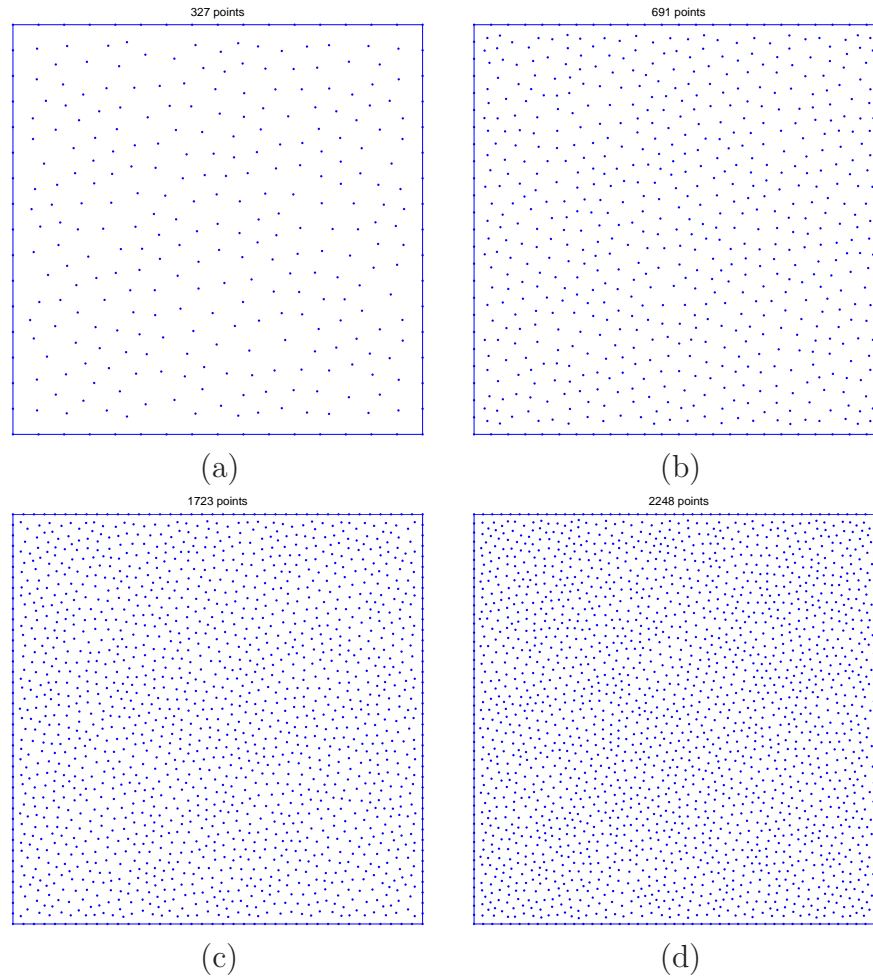


Figure 3.8: Poisson equation in a regular domain: discretisation with unstructured distribution of (a) 327 nodes, (b) 691 nodes, (c) 1723 nodes and (d) 2248 nodes.

The complexity is increased with the Neumann boundary conditions on two curved boundaries. The structured domain discretisation is described as follows. A uniformed grid covering the domain is generated, then the points outside the domain and on the curves are removed. Finally, the points on the inner and outer arcs are generated uniformly.

In the case of structured discretisation (Figure 3.11), the local support radius $\frac{R_s}{h}$ is set at 4.1, β is 9, the maximum number of centers in each subdomain is 13. The relative L_2 error norms L_2^ϕ and $L_2^{\xi\eta}$ associated with the structured node discretizations are presented in Table 3.4 and in Figure 3.13. It can be observed that high orders of convergence are obtained with a large support radius, namely

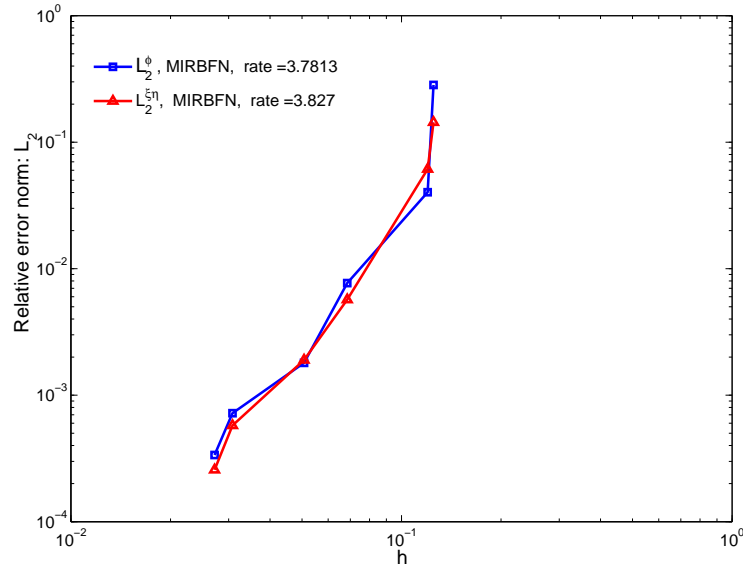


Figure 3.9: Poisson equation in a regular domain: relative error norms L_2^ϕ and $L_2^{\xi\eta}$, and associated convergence rates obtained by MIRBFN method with unstructured nodes.

$O(h^{4.06})$ and $O(h^{3.96})$ for the function and its derivatives, respectively. However, the condition numbers are much larger than those in the previous example. For unstructured node distributions (Figure 3.12), the corresponding parameters and obtained results are presented in Table 3.6 and Figure 3.14. The results indicate that the solution by the proposed method apparently converges at the rates of $(O^{3.80})$ and $(O^{3.50})$ for L_2^ϕ and $L_2^{\xi\eta}$, respectively.

Figures 3.13 and 3.15 show a comparison between the MIRBFN method and

Table 3.4: Poisson equation in an irregular domain: structured dicerizations with MIRBFN

No. points	L_2^ϕ	$L_2^{\xi\eta}$	cond(A)	β	$\frac{R_s}{h}$	h	$\frac{CPU\ time}{second}$
51	3.4762e-1	5.4441e-1	3.1001e5	9	4.1	0.25	0.83
87	2.8487e-2	5.2716e-002	1.9944e6	9	4.1	0.181	1.31
266	1.4620e-3	3.8399e-3	2.0634e7	9	4.1	0.0095	3.86
595	5.0421e-4	8.7207e-4	6.4519e8	9	4.1	0.0065	11.55
1029	1.7279e-4	4.0659e-4	6.2724e8	9	4.1	0.0048	23.05
1574	8.5957e-5	2.4792e-4	4.1291e8	9	4.1	0.039	43.17
2266	3.6035e-5	8.0371e-5	6.5102e9	9	4.1	0.039	84.48
3413	3.0210e-5	5.0281e-5	1.9016e8	9	4.1	0.033	172.53
	$O(h^{4.06})$	$O(h^{3.96})$					

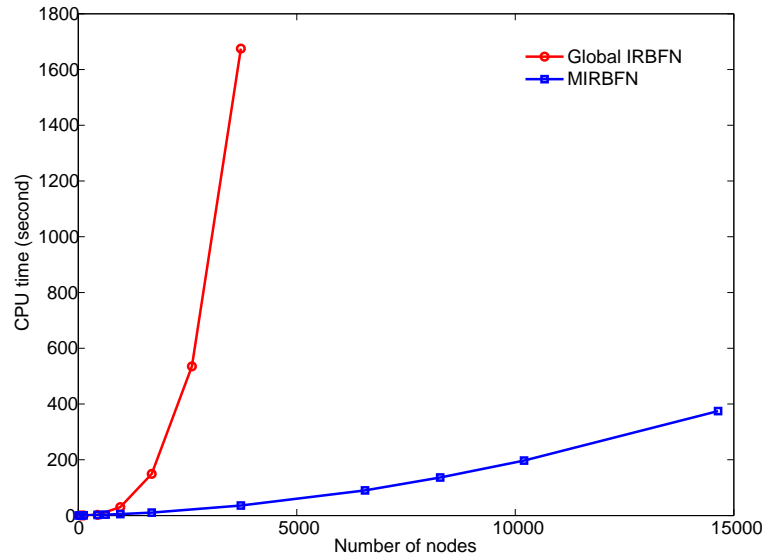


Figure 3.10: Poisson equation in a regular domain with uniform distribution of nodes: CPU times of MIRBFN method versus that of global IRBFN method.

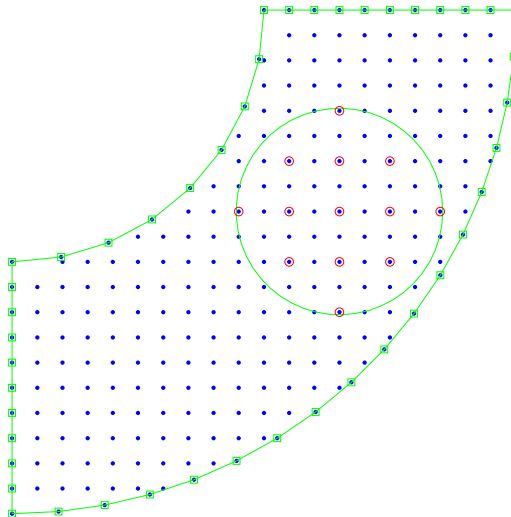


Figure 3.11: Poisson equation in an irregular domain: structured discretisation with 266 nodes.

Table 3.5: Poisson equation in an irregular domain: structured discretizations with global IRBFN

No. points	L_2^ϕ	$L_2^{\xi\eta}$	$\text{cond}(A)$	β	h	$\frac{\text{CPU time}}{\text{second}}$
84	1.8247e-1	2.8821e-1	7.2784e4	1	0.1818	1.457
270	4.7780e-2	7.9363e-2	4.1412e5	1	0.0952	2.20
592	3.2654e-3	1.0017e-2	7.4161e6	1	0.0645	5.809
1017	2.0561e-3	9.0760e-3	2.0139e7	1	0.0488	37.059
1577	9.0259e-4	2.7085e-3	2.8683e8	1	0.0392	125.515
3068	5.5965e-4	2.5365e-3	2.3056e7	1	0.0282	1442.613
	$O(h^{3.38})$	$O(h^{2.77})$				

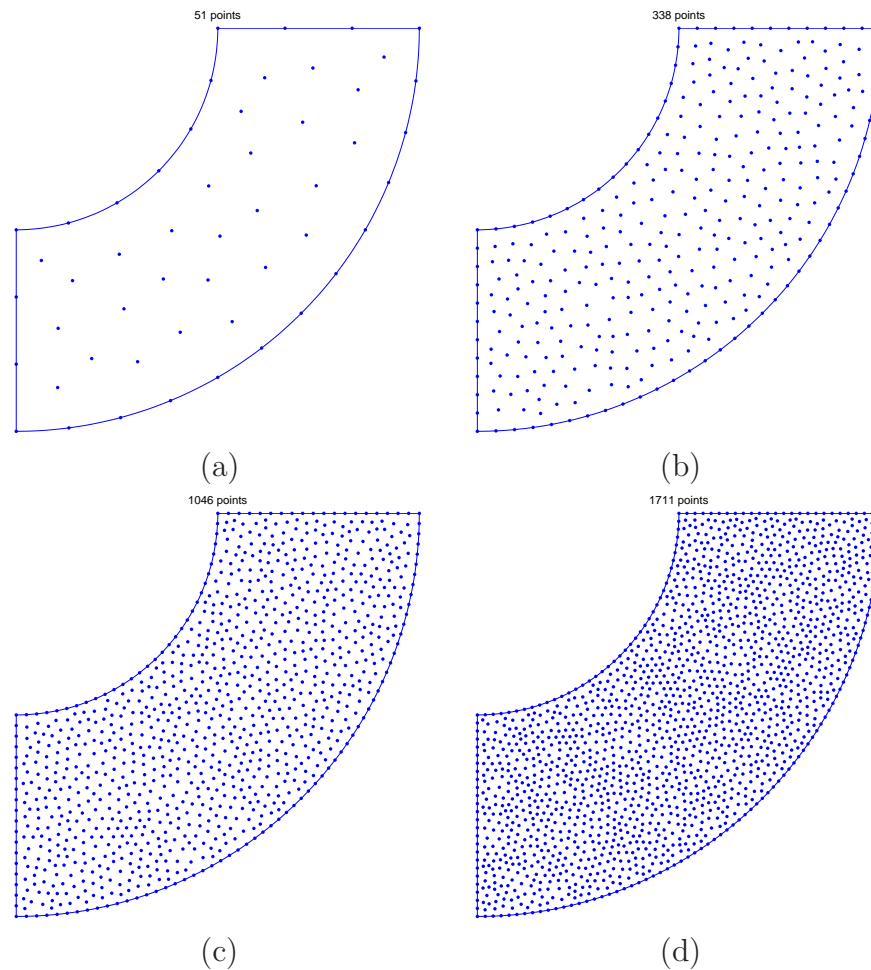


Figure 3.12: Poisson equation in an irregular domain: discretisation with unstructured distribution of (a) 51 nodes, (b) 338 nodes, (c) 1046 nodes and (d) 1711 nodes.

the global IRBFN method (structured discretisation). It is interesting that not only the efficiency but also the accuracy and the convergence rates of the former are superior to those of the latter.

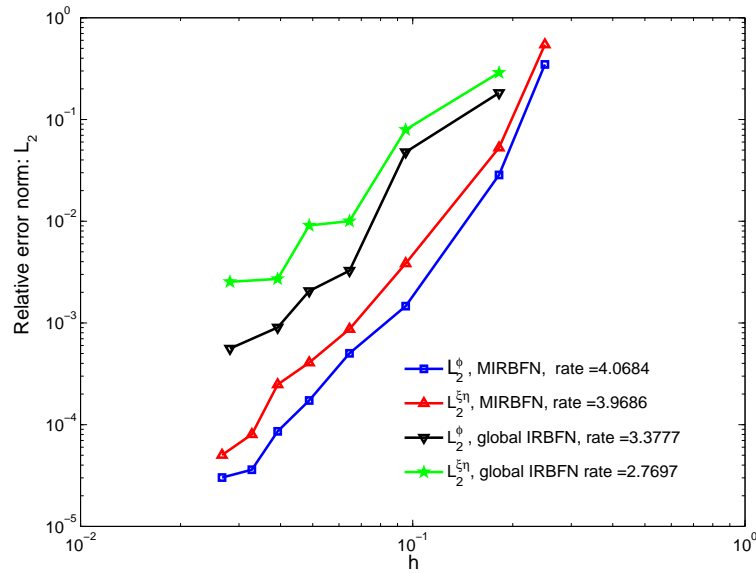
3.3.2 Linear elasticity problems

Cantilever Beam

A cantilever beam subjected to parabolic shear load at the end $x = 0$ as shown in Figure 3.16 is considered in this example.

Table 3.6: Poisson equation in an irregular domain: unstructured discretisation with MIRBFN

No. points	L_2^ϕ	$L_2^{\xi\eta}$	cond(A)	β	$\frac{R_s}{h}$	h	$\frac{CPU\ time}{second}$
51	1.9465e-1	1.9142e-1	7.5387e4	14	3.1	2.7337e-1	4.775
338	2.4059e-3	6.7564e-3	4.4212e6	14	3.1	1.1182e-1	22.017
1046	7.1240e-4	1.7302e-3	9.0038e6	12	3.1	5.9731e-2	89.633
1486	4.2708e-4	8.4299e-4	7.5913e7	12	3.1	5.3098e-2	203.883
1711	1.4251e-4	2.1264e-4	1.4224e8	8	3.1	4.8722e-2	
	$O(h^{3.80})$	$O(h^{3.50})$					

Figure 3.13: Poisson equation in an irregular domain with regular distribution of nodes: relative error norms L_2^ϕ and $L_2^{\xi\eta}$, and associated convergence rates.

The following parameters are used for the problem: $L = 4.8$ and $D = 1.2$. The beam has a unit thickness. Young's modulus is $E = 3 \times 10^6$, Poisson's ratio $\mu = 0.3$ (also $\mu = 0.5$) and the integrated parabolic shear force $P = 100$. Plane stress condition is assumed and there is no body force.

The exact solution to this problem was given by Timoshenko and Goodier Timoshenko and Goodier (1970) as

$$\sigma_{xx}(x, y) = \frac{-Pxy}{I}, \quad (3.39a)$$

$$\sigma_{yy}(x, y) = 0, \quad (3.39b)$$

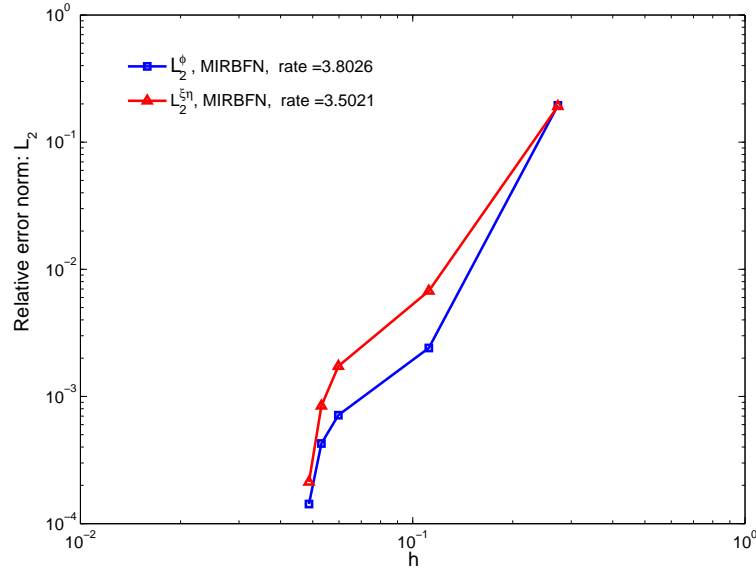


Figure 3.14: Poisson equation in an irregular domain with unstructured distribution of nodes: relative error norms L_2^ϕ and $L_2^{\xi\eta}$, and associated convergence rates.

Table 3.7: Cantilever beam: uniform discretizations with MIRBFN ($\mu = 0.3$).

No. points	L_2^u	L_2^σ	cond(A)	β	$\frac{R_s}{h}$	h	$\frac{CPU\ time}{second}$
20×5	1.9598e-1	3.3652e-1	4.1516e6	8	2.1	0.240	0.60
36×9	1.4986e-2	2.5489e-2	1.4193e8	10	2.1	0.133	1.84
68×17	1.2182e-3	2.1326e-3	3.0383e6	14	2.1	0.070	6.98
124×31	5.8434e-4	5.7764e-4	4.0336e6	14	2.1	0.039	43.78
164×41	2.2892e-4	2.3983e-4	8.3453e6	14	2.1	0.029	109.42
204×51	1.1069e-4	1.2366e-4		14	2.1	0.024	230.01
244×61	5.9462e-5	7.2455e-5		14	2.1	0.020	438.98
	$O(h^{3.04})$	$O(h^{3.26})$					

$$\tau_{xy}(x, y) = \frac{-P}{2I} \left(\frac{D^2}{4} - y^2 \right). \quad (3.39c)$$

The displacements are given by

$$u_x = -\frac{Px^2y}{2EI} - \frac{\mu Py^3}{6EI} + \frac{Py^3}{6IG} + y \left(\frac{PL^2}{2EI} - \frac{PD^2}{8IG} \right), \quad (3.40)$$

$$u_y = \frac{\mu Pxy^2}{2EI} + \frac{Px^3}{6EI} - \frac{PL^2x}{2EI} + \frac{PL^3}{3EI}, \quad (3.41)$$

where $I = D^3/12$ is the moment of inertia of the cross section of the beam, $G = E/(2(1 + \mu))$ the modulus of elasticity in shear. The exact displacement

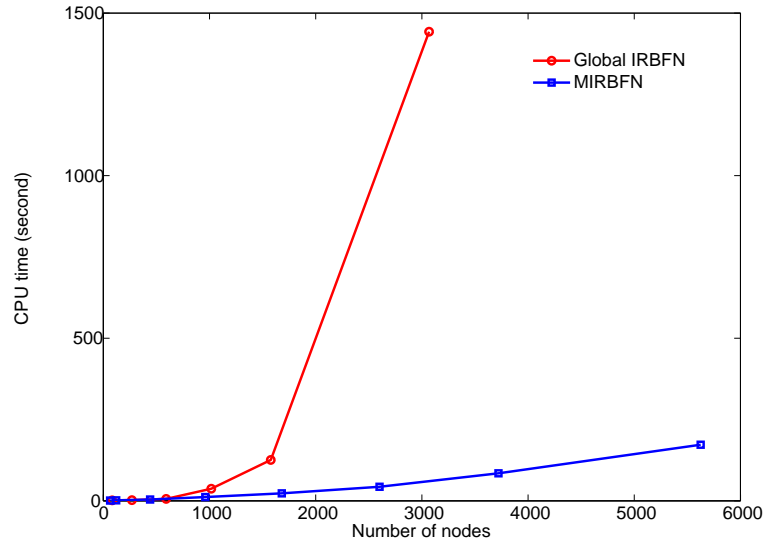


Figure 3.15: Poisson equation in an irregular domain with structured points: CPU times of MIRBFN method versus that of global IRBFN method.

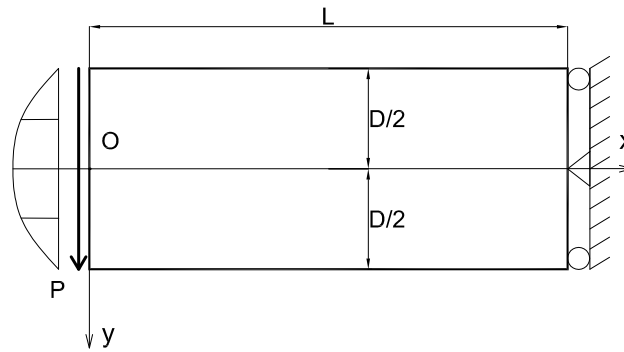


Figure 3.16: Cantilever beam: a mathematical model.

(3.40) and (3.41) are imposed on $x = L$ while the shear load is applied on $x = 0$ and the upper and lower edges are traction free.

Both regular and irregular distributions of nodes used for this problem are displayed in Figures 3.17 and 3.19, respectively. The local support radius is $\frac{R_s}{h} = 2.1$. The values of β are listed in Tables 3.7, 3.8 and 3.10. The scheme for selection of RBF centers for both regular and irregular node distributions is similar to that in example 3.3.1. In addition, the effect of incompressibility, i.e. $\mu = 0.5$, is also studied here.

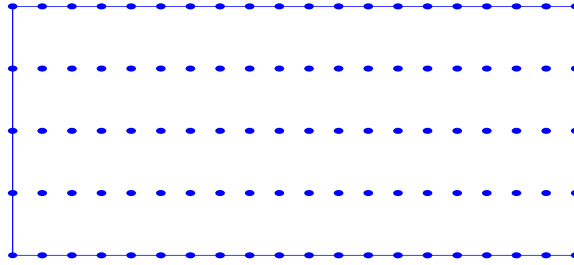
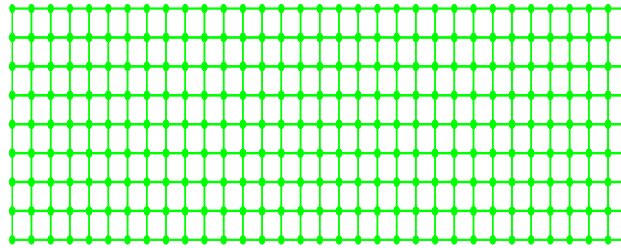
Figure 3.17: Cantilever beam: discretisation with 20×5 nodes.Figure 3.18: Cantilever beam: a FEM mesh with 8×32 Q4 elements.

Figure 3.20 shows the shear stress s_{xy} for $\mu = 0.3$ at $x = 2.4686$ obtained by the present method with 36×9 nodes. A very good agreement between the obtained result and the exact solution can be observed in this figure.

To study the convergence of the method, a number of different uniform node distributions is used for computation as presented in the Tables 3.7 and 3.8. For $\mu = 0.3$, the relative L_2 error norms for displacement and stress are shown in Table 3.7 and Figure 3.21, the convergence rates of displacement and stress are $O(h^{3.04})$ and $O(h^{3.26})$, respectively. In the case of incompressible materials ($\mu =$

Table 3.8: Cantilever beam: uniform discretizations with MIRBFN ($\mu = 0.5$).

No. points	L_2^u	L_2^σ	$\text{cond}(A)$	β	$\frac{R_s}{h}$	h	$\frac{\text{CPU time}}{\text{second}}$
20×5	1.0069e-1	1.9291e-1	2.3672e7	8	2.1	0.240	0.60
36×9	2.0936e-2	5.3772e-2	4.2607e7	10	2.1	0.133	1.81
68×17	7.8576e-4	1.6020e-3	2.1090e6	14	2.1	0.070	6.77
124×31	4.3029e-4	4.1872e-4	2.8678e6	14	2.1	0.039	41.12
164×41	1.6292e-4	1.6988e-4	5.7418e6	14	2.1	0.029	106.48
204×51	7.7595e-5	8.7489e-5		14	2.1	0.024	235.5
244×61	4.1951e-5	5.2041e-5		14	2.1	0.020	475.7
	$O(h^{3.07})$	$O(h^{3.39})$					

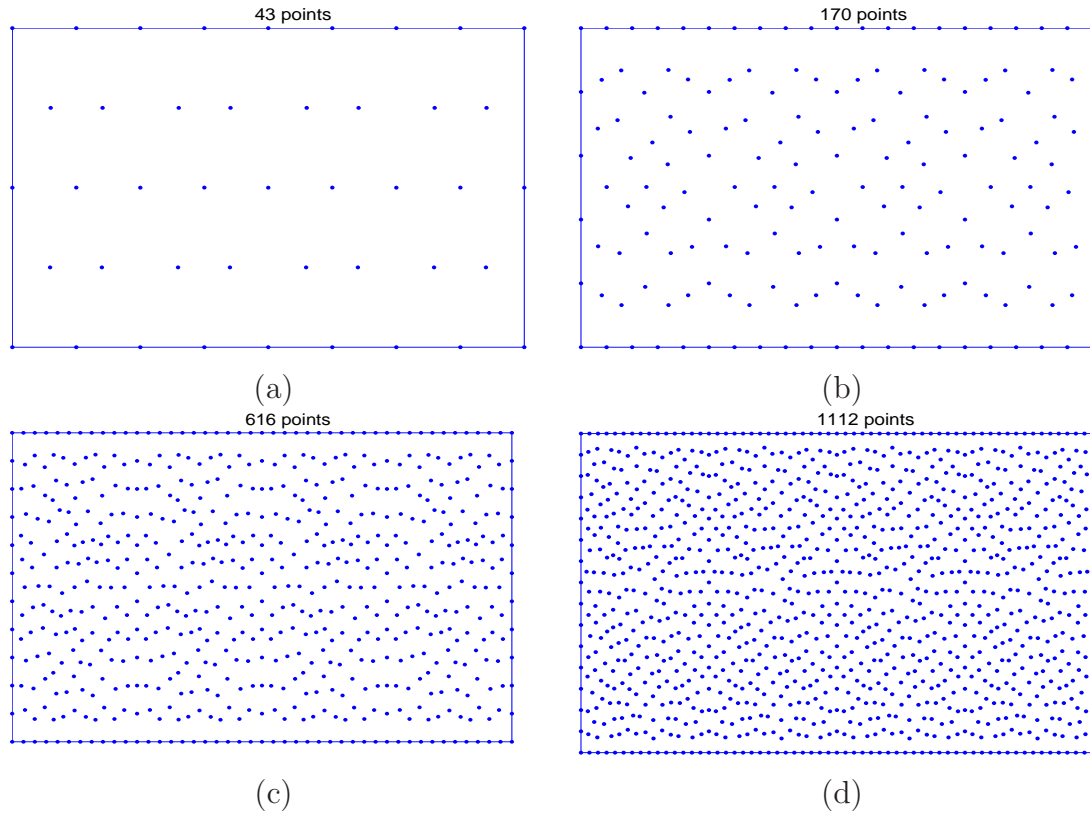


Figure 3.19: Cantilever beam: discretisation with unstructured distribution of (a) 43 nodes, (b) 170 nodes, (c) 616 nodes, and (d) 1112 nodes.

0.5), the relative L_2 error norms for displacement and stress are presented in Table 3.8 and Figure 3.21. Very good orders of convergence are achieved, namely $O(h^{3.07})$ and $O(h^{3.39})$ for displacement and stress, respectively. Furthermore, the results shown in Figure 3.21 indicate that the present method does not suffer from any volumetric locking.

The behaviour of the MIRBFN method in the case of irregular discretisation

Table 3.9: Cantilever beam: uniform discretizations with global IRBFN ($\mu = 0.3$).

No. points	L_2^u	L_2^σ	$\text{cond}(A)$	β	h	$\frac{\text{CPU time}}{\text{second}}$
20×5	4.5356e-2	2.5571e-1	1.7953e6	1	0.2400	0.408
36×9	5.2822e-3	4.0279e-2	5.2505e6	1	0.1333	2.068
68×17	1.5706e-3	2.6022e-3	6.5476e7	1	0.0706	68.088
124×31	3.8901e-4	4.3698e-4	3.1351e8	1	0.0387	2351.78
164×41	2.1295e-4	2.2075e-4		1	0.0293	51201.338
	$O(h^{3.06})$	$O(h^{3.39})$				

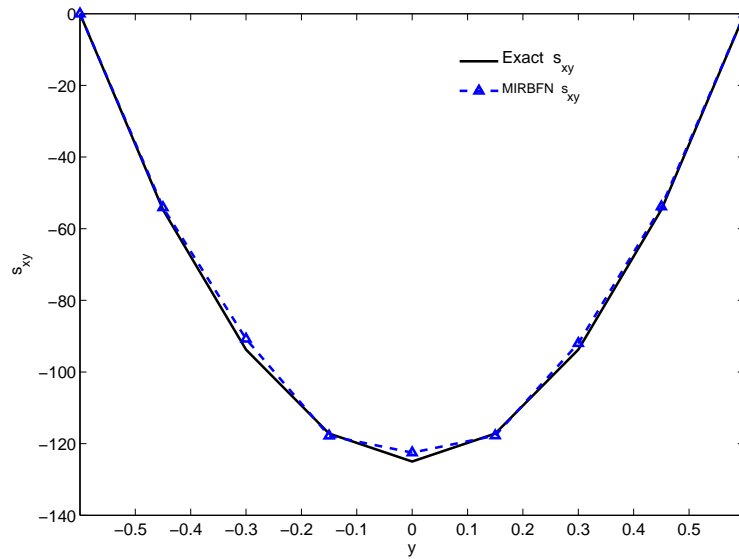


Figure 3.20: Cantilever beam: s_{xy} at $x = 2.4686$ with 36×9 nodes ($\mu = 0.3$).

Table 3.10: Cantilever beam: unstructured nodes with MIRBFN ($\mu = 0.3$).

No. points	L_2^u	L_2^σ	$\text{cond}(A)$	β	$\frac{R_s}{h}$	h	$\frac{\text{CPU time}}{\text{second}}$
43	6.5385e-1	6.9895e-1	2.6549e6	10	2.1	4.6860e-1	0.715
170	2.7461e-2	5.5154e-2	3.9549e7	10	2.1	2.4000e-1	2.079
616	7.2999e-3	3.1141e-2	7.4558e7	10	2.1	1.2507e-1	7.888
1112	4.9025e-4	3.0318e-3	1.0345e9	10	2.1	1.0454e-1	20.190
	$O(h^{4.21})$	$O(h^{3.07})$					

is also examined with four nodal configurations as shown in Figure 3.19. The obtained results with the MIRBFN method and $\mu = 0.3$ are shown in Table 3.10 and Figure 3.22. The orders of convergence of the present method are $O(h^{4.21})$ and $O(h^{3.07})$ for displacement and stress, respectively.

In comparison with the global IRBFN method, the MIRBFN method achieves similar accuracy and convergence rates as can be observed in Tables 3.7 and 3.9, and in Figure 3.21 as well. The present method is apparently much more efficient than the global IRBFN method (Figure 3.23).

The obtained results are also compared with those by FEM using four-node quadrilateral element (Table 3.11). Figure 3.21 shows that both accuracy and order of convergence of the MIRBFN method are superior to those of FEM, e.g.

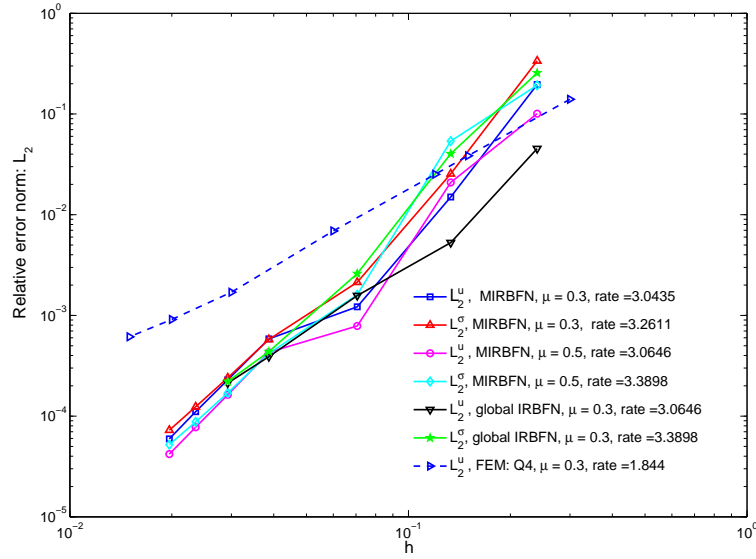


Figure 3.21: Cantilever beam: L_2 relative error norms for displacement and stress for $\mu = 0.3$ and $\mu = 0.5$, with associated convergence rates.

Table 3.11: Cantilever beam: structured FEM mesh with four-node quadrilateral element (Q4) ($\mu = 0.3$).

No. elements	L_2^u	h	$\frac{CPU\ time}{second}$
16×4	1.3991e-1	0.40	0.1806
32×8	3.8516e-2	0.1714	0.4395
40×10	2.5191e-2	0.1333	1.7111
80×20	6.9048e-3	0.0631	8.4087
160×40	1.6994e-3	0.0307	21.5620
240×60	9.1261e-4	0.0203	47.9957
320×80	6.1308e-4	0.0152	307.579
$O(h^{1.84})$			

the L_2^u convergence rates are $O(h^{3.04})$ and $O(h^{1.84})$ for the MIRBFN method and the FEM, respectively. The computing cost of the MIRBFN method is higher than that of the FEM for the same number of nodes. However, the MIRBFN method is more efficient than the FEM for the same accuracy, for example, it takes the MIRBFN method 6.98 seconds for $L_2^u = 1.2182 \times 10^{-3}$ while the FEM needs 21.56 seconds with $L_2^u = 1.6994 \times 10^{-3}$ as exhibited in Figure 3.23, Table 3.7 and Table 3.11.

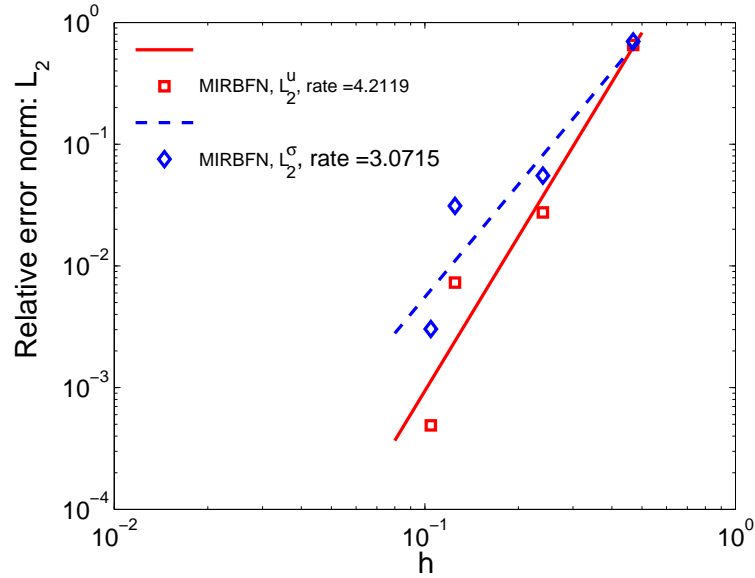


Figure 3.22: Cantilever beam: L_2 relative error norms for displacement and stress, and associated convergence rates for $\mu = 0.3$ with different unstructured nodal configurations.

Infinite plate with a circular hole

In this example, an infinite plate with a circular hole subjected to unidirectional tensile load of 1.0 in the x direction is analyzed as shown in Figure 3.24. The radius of hole is taken as 1 unit. Owing to symmetry, only the upper right quadrant $[0, 3] \times [0, 3]$ of the plate is modeled as shown in Figure 3.25.

In this problem, plane stress conditions are assumed with elastic isotropic properties $E = 10^3$, $\mu = 0.3$ (also $\mu = 0.5$). The exact solution to this problem was given by Timoshenko and Goodier Timoshenko and Goodier (1970) as follows

$$\sigma_x(x, y) = \sigma \left[1 - \frac{a^2}{r^2} \left[\frac{3}{2} \cos(2\theta) + \cos(4\theta) \right] + \frac{3a^4}{2r^4} \cos(4\theta) \right], \quad (3.42a)$$

$$\sigma_y(x, y) = -\sigma \left[\frac{a^2}{r^2} \left[\frac{1}{2} \cos(2\theta) - \cos(4\theta) \right] + \frac{3a^4}{2r^4} \cos(4\theta) \right], \quad (3.42b)$$

$$\tau_{xy}(x, y) = -\sigma \left[\frac{a^2}{r^2} \left[\frac{1}{2} \sin(2\theta) + \sin(4\theta) \right] - \frac{3a^4}{2r^4} \sin(4\theta) \right], \quad (3.42c)$$

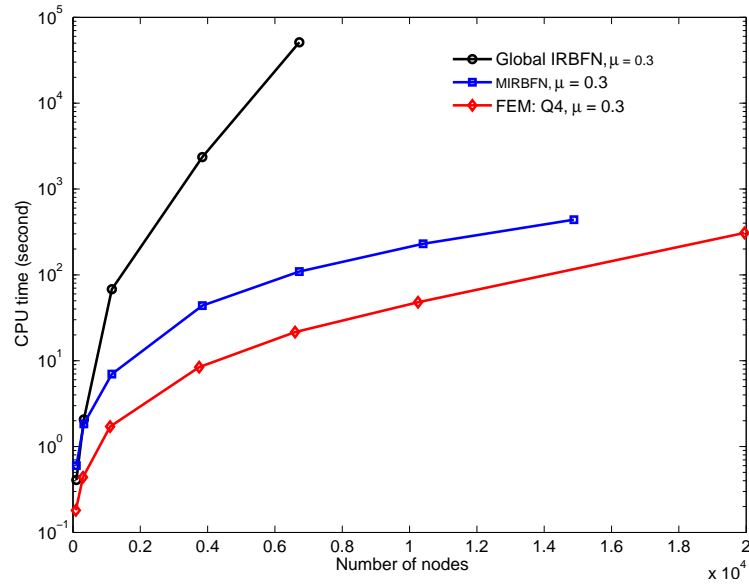


Figure 3.23: Cantilever beam: CPU times of MIRBFN method versus that of FEM and global IRBFN method.

where (r, θ) are the polar coordinates, a the radius of the hole.

The corresponding displacements are given by

$$u_x(x, y) = \sigma \frac{(1 + \mu)}{E} \left[\frac{1}{1 + \mu} r \cos(\theta) + \frac{2}{1 + \mu} \frac{a^2}{r} \cos(\theta) + \frac{1}{2} \frac{a^2}{r} \cos(3\theta) - \frac{1}{2} \frac{a^4}{r^3} \cos(3\theta) \right] \quad (3.43a)$$

$$u_y(x, y) = \sigma \frac{(1 + \mu)}{E} \left[\frac{-\mu}{1 + \mu} r \sin(\theta) + \frac{1 - \mu}{1 + \mu} \frac{a^2}{r} \sin(\theta) + \frac{1}{2} \frac{a^2}{r} \sin(3\theta) - \frac{1}{2} \frac{a^4}{r^3} \sin(3\theta) \right] \quad (3.43b)$$

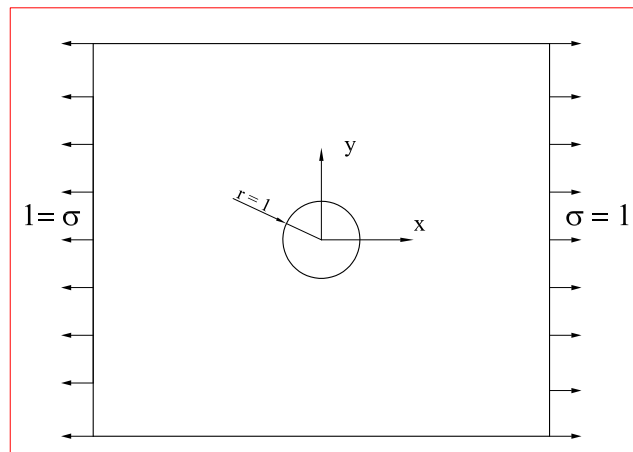


Figure 3.24: Infinite plate with a circular hole.

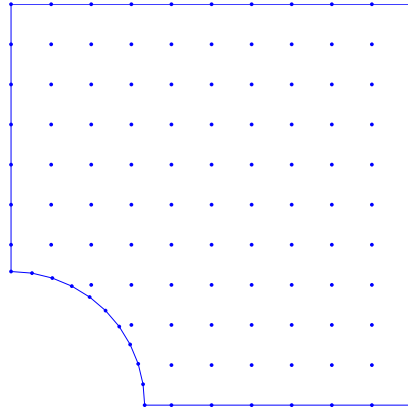


Figure 3.25: Infinite plate with a circular hole: computational domain with 119 nodes.

Table 3.12: Infinite plate with a circular hole: structured discretisation with MIRBFN ($\mu = 0.3$).

No. points	L_2^u	L_2^σ	$\text{cond}(A)$	β	$\frac{R_s}{h}$	h	$\frac{\text{CPU time}}{\text{second}}$
50	3.0520e-1	2.6147e-1	6.7532e4	4	2.1	0.50	0.54
119	9.2110e-2	8.1240e-2	8.3533e6	4	2.1	0.30	1.03
409	1.0837e-2	1.2229e-2	6.1059e4	4	2.1	0.15	3.25
1129	8.7872e-4	2.6677e-3	2.0085e5	4	2.1	0.088	10.56
3085	1.8647e-4	4.2703e-4	4.4334e5	4	2.1	0.052	44.36
	$O(h^{3.61})$	$O(h^{3.02})$					

The boundary conditions of the problem are as follows. The traction boundary conditions corresponding to the exact solution for the infinite plate are applied on the top and right edges, the symmetric conditions are applied on the left and bottom edges, and the curved edge is traction free.

To solve the problem, the computational domain is discretized in the same manner as in example 3.3.1. The support radius is $\frac{R_s}{h} = 2.1$, the value of β

Table 3.13: Infinite plate with a circular hole: structured discretisation with MIRBFN ($\mu = 0.5$).

No. points	L_2^u	L_2^σ	$\text{cond}(A)$	β	$\frac{R_s}{h}$	h	$\frac{\text{CPU time}}{\text{second}}$
50	7.8208e-1	5.7769e-1	1.1433e5	4	2.1	0.50	0.54
119	1.0186e-1	8.2598e-2	5.0328e6	4	2.1	0.30	1.01
409	1.3343e-2	1.4314e-2	5.5146e4	4	2.1	0.15	3.20
1129	9.5928e-4	2.7873e-3	2.0372e5	4	2.1	0.088	10.48
3085	4.0203e-4	4.6366e-4	6.0161e5	4	2.1	0.052	43.06
	$O(h^{3.68})$	$O(h^{3.27})$					

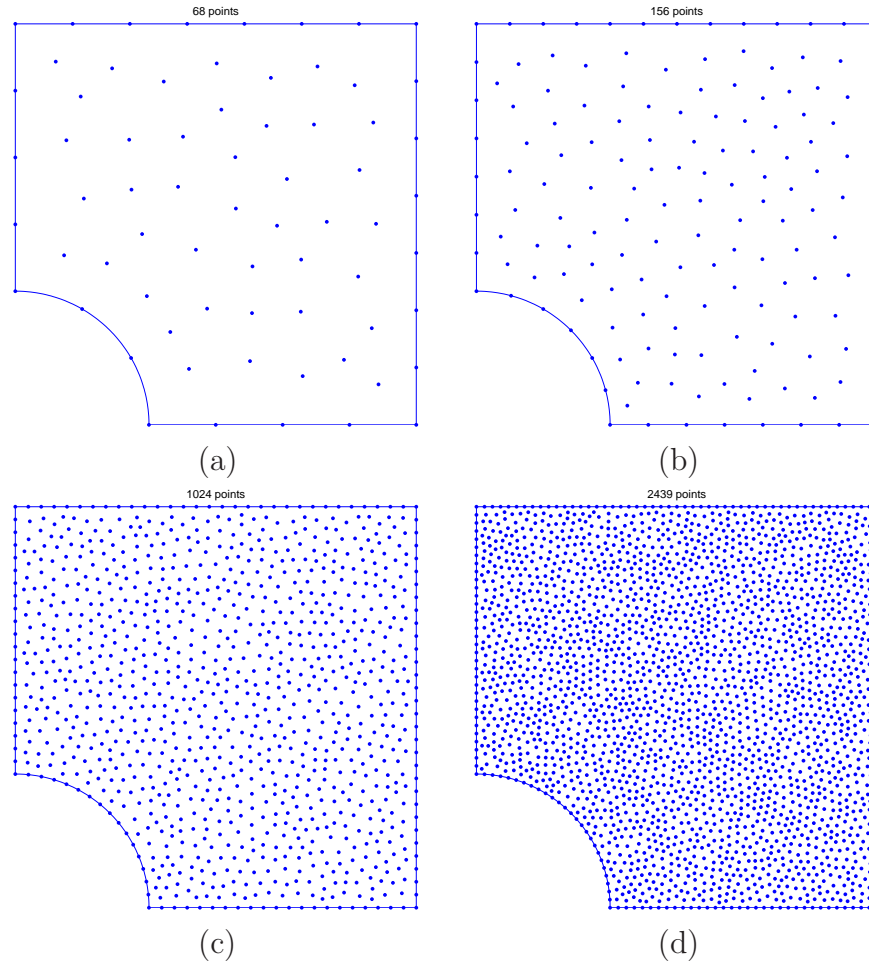


Figure 3.26: Infinite plate with a circular hole: discretisation with unstructured distribution of (a) 68 nodes, (b) 156 nodes, (c) 1024 nodes, and (d) 2439 nodes.

varies between 3 and 4 as in Tables 3.12, 3.13 and 3.15, and the RBF centers are identical to the nodes in each subdomain.

A comparison between the stress s_x along $x = 0$ obtained by the MIRBFN with a structured discretisation of 409 nodes and the exact solution are presented in Figure 3.27. The result indicates that the solution obtained by the proposed method agrees well with the exact one.

The convergence of the present method in the case of structured node distribution (Figure 3.25) is reported in Table 3.12 and Figure 3.28 for $\mu = 0.3$, and in Table 3.13 and Figure 3.28 for the case of incompressible materials. The present method appears to converge at the rates of $O(h^{3.61})$ for displacement

Table 3.14: Infinite plate with a circular hole: structured discretisation with global IRBFN ($\mu = 0.3$).

No. points	L_2^u	L_2^σ	$\text{cond}(A)$	β	h	$\frac{\text{CPU time}}{\text{second}}$
119	1.3243e-1	1.1085e-1	7.0056e5	1	0.2727	0.413
409	2.3900e-2	1.5925e-2	1.4568e6	1	0.1429	2.222
886	4.8966e-3	3.3027e-3	3.3118e6	1	0.0968	21.323
3085	2.5075e-4	7.2314e-4	4.3415e6	1	0.0517	977.988
	$O(h^{3.78})$	$O(h^{3.08})$				

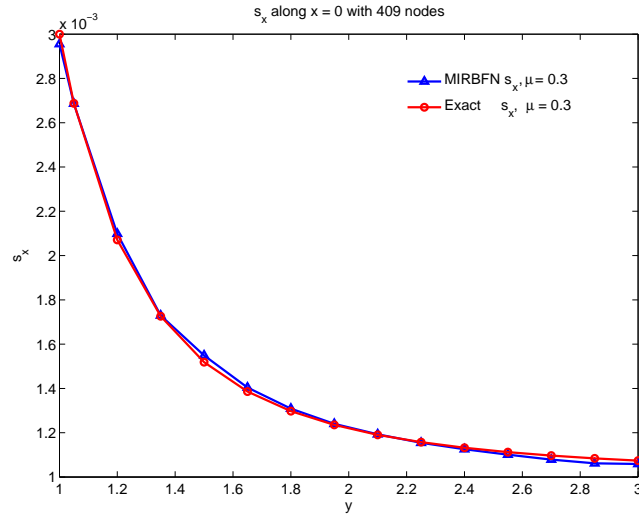


Figure 3.27: Infinite plate with a circular hole: s_x along $x = 0$ with 409 nodes ($\mu = 0.3$).

and $O(h^{3.02})$ for stress in the case of $\mu = 0.3$. In the case of incompressible materials, the orders of convergence are $O(h^{3.68})$ and $O(h^{3.27})$ for displacement and stress, respectively.

The performance of the MIRBFN method is also tested with irregular node distributions as shown in Figure 3.26. The obtained results are presented in Table 3.15 and Figure 3.29, which show that the convergence rates are $O(h^{3.60})$ and $O(h^{2.50})$ for displacement and stress, respectively.

Again, the MIRBFN method achieves similar accuracy and convergence rates in comparison with those of the global IRBFN method as shown in Table 3.12 and 3.14, and in Figure 3.28. Clearly, the efficiency of the present method is superior to that of the global IRBFN (Figure 3.30).

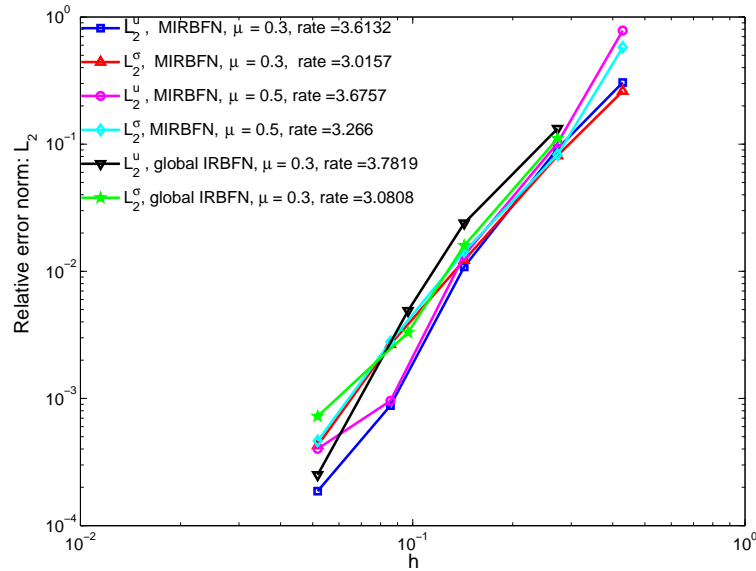


Figure 3.28: Infinite plate with a circular hole: L_2 relative error norms for displacement and stress for $\mu = 0.3$ and $\mu = 0.5$. Convergence rates are also shown.

Table 3.15: Infinite plate with a circular hole: unstructured node distribution with MIRBFN ($\mu = 0.3$).

No. points	L_2^u	L_2^σ	$\text{cond}(A)$	β	$\frac{R_s}{h}$	h	$\frac{\text{CPU time}}{\text{second}}$
68	7.5923e-1	8.0880e-1	4.9714e4	4	2.1	5.0000e-1	1.383
156	2.3616e-1	3.4100e-1	2.9975e5	4	2.1	3.0888e-1	2.911
479	1.0531e-2	4.0582e-2	2.7228e6	4	2.1	1.6343e-1	8.729
1024	5.0684e-3	2.2821e-2	6.2775e6	3	2.1	1.1346e-1	23.620
2439	9.9303e-4	8.2974e-3	1.2450e8	3	2.1	7.5139e-2	81.186
	$O(h^{3.60})$	$O(h^{2.50})$					

Mode I crack problem

Consider an infinite plate containing a straight crack of length $2a$ and loaded by a remote uniform stress field σ as shown in Figure 3.31. Along ABCD the closed form solution in terms of polar coordinates in a reference frame (r, θ) centered at the crack tip is given by

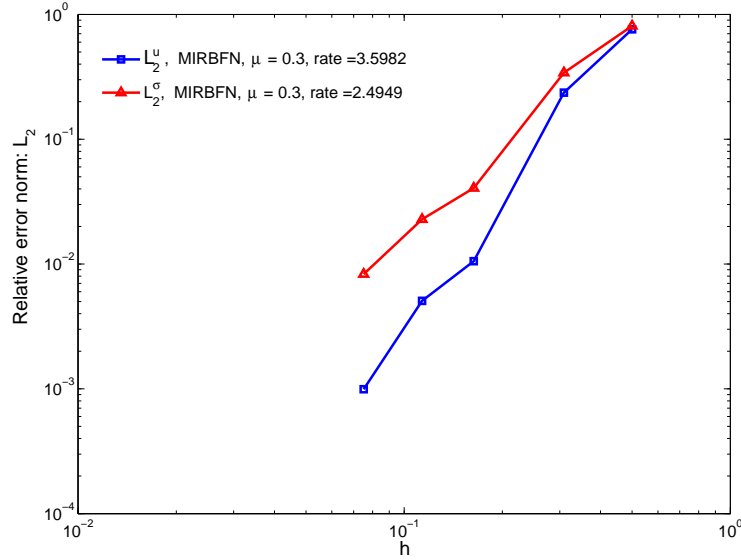


Figure 3.29: Infinite plate with a circular hole: L_2 relative error norms for displacement and stress for $\mu = 0.3$ with unstructured nodes. Convergence rates are also shown.

$$\sigma_x = \frac{K_I}{\sqrt{r}} \cos \frac{\theta}{2} \left(1 - \sin \frac{\theta}{2} \sin 3\frac{\theta}{2} \right), \quad (3.44a)$$

$$\sigma_y = \frac{K_I}{\sqrt{r}} \cos \frac{\theta}{2} \left(1 + \sin \frac{\theta}{2} \sin 3\frac{\theta}{2} \right), \quad (3.44b)$$

$$\tau_y = \frac{K_I}{\sqrt{r}} \sin \frac{\theta}{2} \cos \frac{\theta}{2} \cos 3\frac{\theta}{2}, \quad (3.44c)$$

for stress and

$$u_x = \frac{2(1+\mu)}{\sqrt{2\pi}} \frac{K_I}{E} \sqrt{r} \cos \frac{\theta}{2} \left(2 - 2\mu - \cos^2 \frac{\theta}{2} \right), \quad (3.45a)$$

$$u_y = \frac{2(1+\mu)}{\sqrt{2\pi}} \frac{K_I}{E} \sqrt{r} \sin \frac{\theta}{2} \left(2 - 2\mu - \cos^2 \frac{\theta}{2} \right), \quad (3.45b)$$

for displacement, where $K_I = \sigma\sqrt{\pi a}$ is the stress intensity factor, μ Poisson's ratio and E Young modulus, ABCD a square of $10 \times 10 \text{ mm}^2$, $a = 100 \text{ mm}$, $E = 10^7 \text{ N/mm}^2$, $\mu = 0.3$ (also $\mu = 0.5$), $\sigma = 10^4 \text{ N/mm}^2$. Plane strain condition is assumed and the body force is zero. The computational domain ABCD is shown in Figure 3.31. Owing to symmetry, only upper half of ABCD, namely

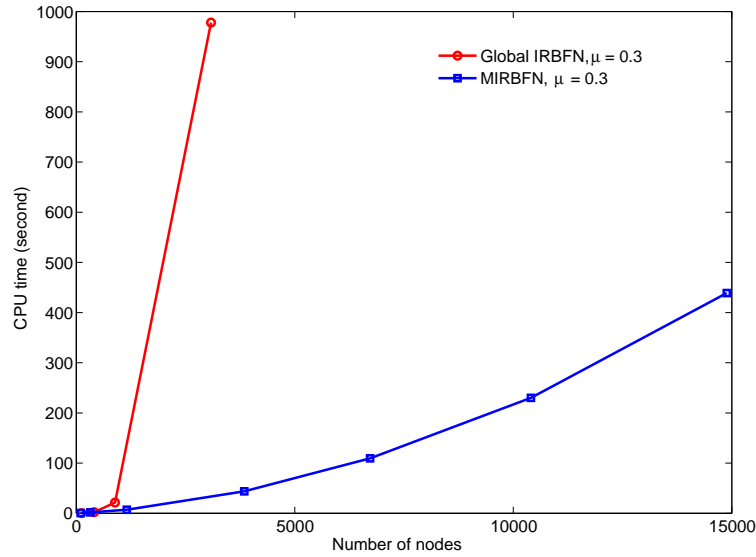


Figure 3.30: Infinite plate with a circular hole: CPU times of MIRBFN method versus that of global IRBFN method.

Table 3.16: Center crack problem: uniform discretisations with MIRBFN ($\mu = 0.3$).

No. points	L_2^u	L_2^σ	$\text{cond}(A)$	β	$\frac{R_s}{h}$	h	$\frac{\text{CPU time}}{\text{second}}$
10×10	0.2017	1.3794	2.7726e5	0.01	1.1	1.0	0.53
14×14	0.13882	0.6583	6.7641e5	0.01	1.1	0.714	0.94
16×16	0.0909	0.5043	4.7002e5	0.01	1.1	0.625	1.22
20×20	0.0374	0.2327	5.1297e5	0.01	1.1	0.50	1.85
24×24	0.0269	0.1887	1.6910e6	0.01	1.1	0.416	2.68
	$O(h^{2.47})$	$O(h^{2.38})$					

CDEFG as shown in Figure 3.32, is analyzed. The segment of crack denoted by EF has a length of $b = 5 \text{ mm}$. The boundary condition of the problem is as follows. The traction free boundary condition is applied on the crack while the displacement field given in equations (3.45) is imposed on the remaining boundaries.

It is known that stress tends to infinity when r tends to 0. Thus, to alleviate the oscillation due to the effect of singularity, the support radius R_s and β are selected as small as possible. For this example, $\frac{R_s}{h}$ and β are set 1.1 and 0.01, respectively, and the RBF centers are chosen to be identical to the nodes in each subdomain.

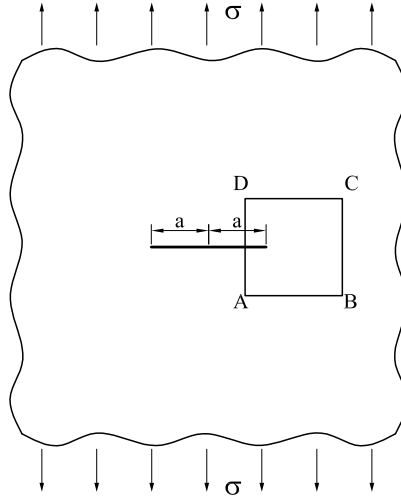


Figure 3.31: Infinite cracked plate under remote tension.

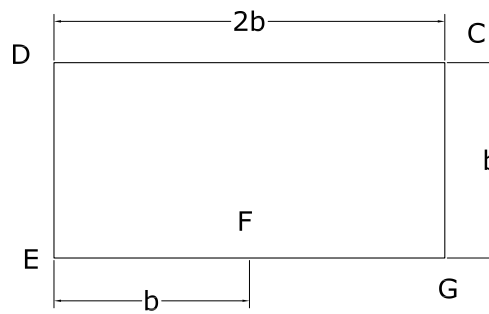


Figure 3.32: Infinite cracked plate: analyzed portion.

The performance of the present method in this singular problem is examined by employing a number of uniform data point distributions as displayed in the Tables 3.16 and 3.17. The results with 24×24 nodes ($\mu = 0.3$) are plotted in Figures 3.33-3.35 as follows. Figures 3.33 and 3.34 exhibit displacement u_x and u_y , respectively, in comparison with those of analytical solution. Figures 3.35 (a) and (b) depict stress s_x and s_y by MIRBFN method, respectively, and the corresponding exact solutions. Some oscillation can be observed in these figures due to singularity of stress with C_0 continuity of displacement and C_∞ property of IRBFNs. This oscillation is known as the Gibbs phenomenon in RBF-based methods (Jung, 2007) where numerical oscillations occur around a jump discontinuity because of high order approximation by RBF. Nevertheless,

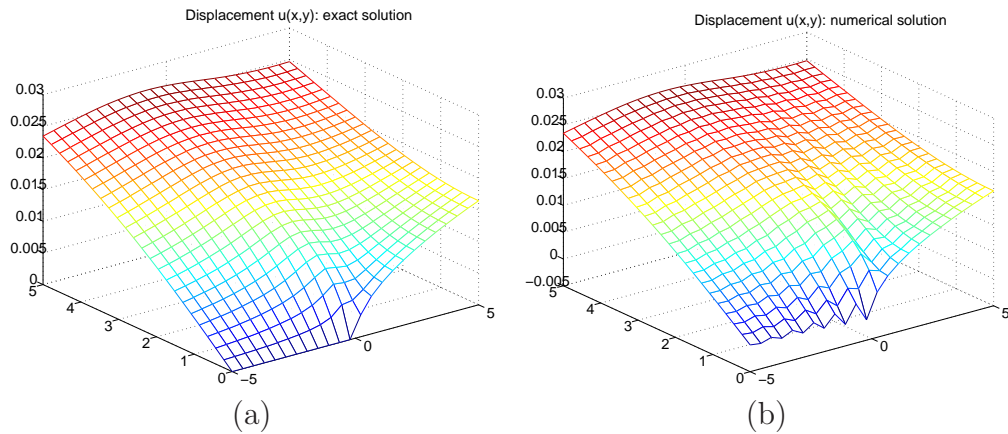


Figure 3.33: Infinite cracked plate: u_x obtained by (a) exact solution and (b) MIRBFN method with 24×24 nodes ($\mu = 0.3$).

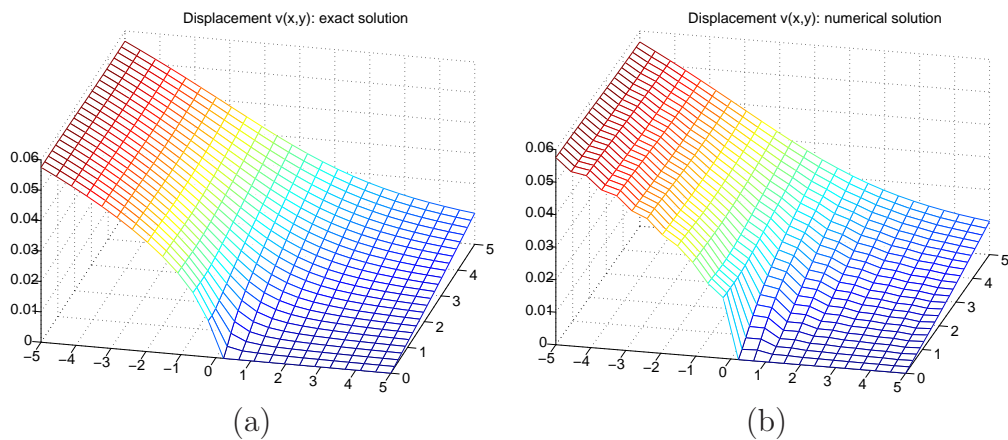


Figure 3.34: Infinite cracked plate: u_y obtained by (a) exact solution and (b) MIRBFN method with 24×24 nodes ($\mu = 0.3$).

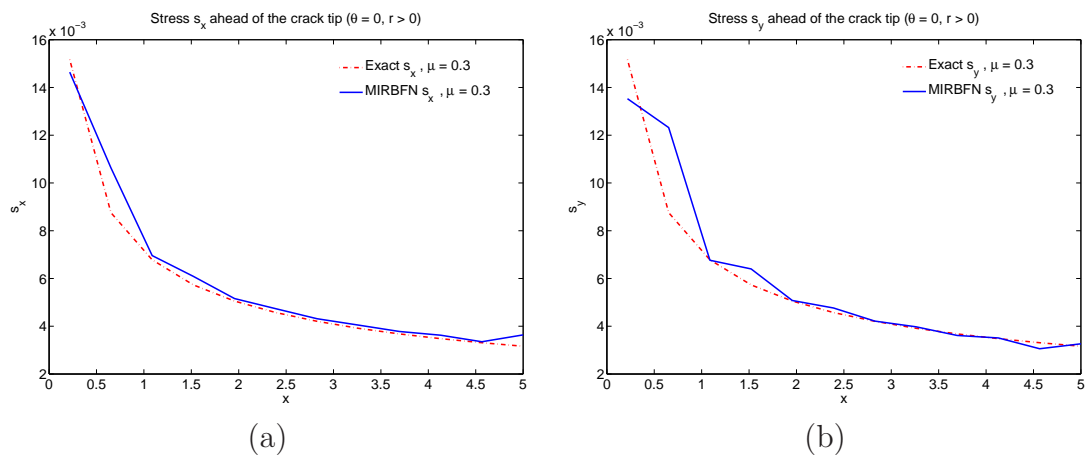
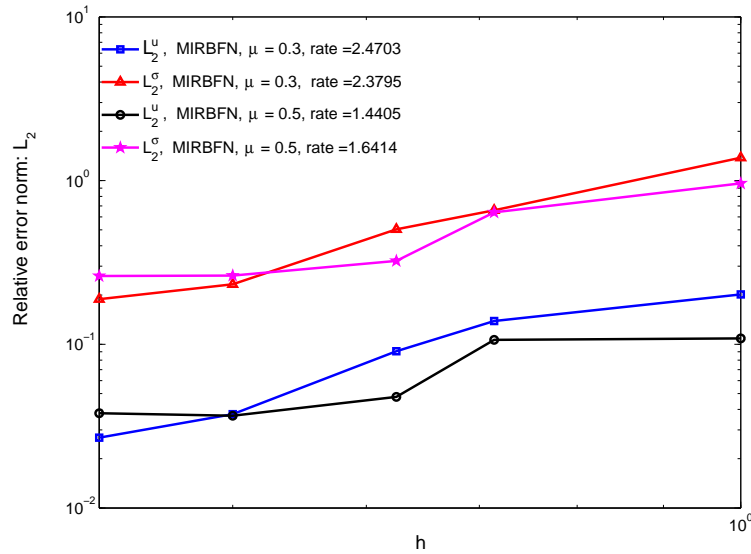


Figure 3.35: Infinite cracked plate - stress ahead of the crack-tip ($\theta = 0, r > 0$): (a) s_x and (b) s_y obtained by MIRBFN method and exact solutions with 24×24 nodes ($\mu = 0.3$).

Table 3.17: Center crack problem: uniform discretizations with MIRBFN ($\mu = 0.5$).

No. points	L_2^u	L_2^σ	$\text{cond}(A)$	β	$\frac{R_s}{h}$	h	$\frac{\text{CPU time}}{\text{second}}$
10×10	0.1087	0.9622	1.4859e5	0.01	1.1	1.0	0.53
14×14	0.1064	0.6401	2.9922e5	0.01	1.1	0.714	0.94
16×16	0.0477	0.3233	2.8071e5	0.01	1.1	0.625	1.22
20×20	0.0366	0.2627	5.3818e5	0.01	1.1	0.50	1.85
24×24	0.0379	0.2613	4.9657e5	0.01	1.1	0.416	2.73
	$O(h^{1.44})$	$O(h^{1.64})$					

Figure 3.36: Infinite cracked plate: L_2 relative error norms for displacement and stress, and associated convergence rates for $\mu = 0.3$ and $\mu = 0.5$.

the obtained results are in good agreement with the analytical ones and the present MIRBFN method is able to capture highly steep gradients.

The convergence of the method can be seen in Tables 3.16 and 3.17, and in Figure 3.36. In the case of $\mu = 0.3$, high convergence rates of $O(h^{2.47})$ and $O(h^{2.38})$ for displacement and stress, respectively, are obtained. It is apparent that the accuracy of stress field is considerably reduced in comparison with that of displacement due to the presence of singularity (Figure 3.36.). For incompressible materials, the convergence rates reduce to $O(h^{1.44})$ and $O(h^{1.64})$ for displacement and stress, respectively.

3.4 Concluding remarks

In this chapter, we propose a locally supported RBF interpolation method, namely MIRBFN, with the main features as follows.

- The proposed method is a locally supported approximation method. As a consequence, the resultant interpolation matrices are sparse and banded, resulting in improved efficiency in comparison with those of standard RBF methods.
- The shape functions of the MIRBFN method possesses the Kronecker- δ property that facilitates the imposition of the essential boundary conditions.
- The present method offers high orders of convergence and is applicable to scattered node distribution, arbitrary domain and highly steep gradient problems.

Moreover, the proposed interpolation method is implemented in the collocation of the first-order system formulation resulting in an integration-free meshless method which enjoys high convergence rate and very good accuracy. The moving IRBFN method is also developed with weak form approach (chapter 4), and further developed for discontinuous problems such as strain localization as well as elasto-plastic problems (chapter 7) and cracks (chapter 8).

Chapter 4

A Moving IRBFN-based Galerkin meshless method

A novel meshless method based on Radial Basis Functions (RBF) and variational principle (global weak form) is presented in this chapter. In this method, the global integrated RBFN is localized and coupled with the moving least square method via the partition of unity concept. As a result, the system matrix is symmetric, sparse and banded. The trial and test functions satisfy the Kronecker-delta property, i.e. $\phi_i(\mathbf{x}_j) = \delta_{ij}$. Therefore, the essential boundary conditions are imposed in strong form as in the FEMs. Moreover, the proposed method is applicable to scattered distributions of nodes and arbitrary domains. The method is examined with several numerical examples and the results indicate that the accuracy and the rate of convergence of the proposed method are superior to those of the EFG method using linear basis functions. In addition, the method does not exhibit any volumetric locking near the limit of incompressible material.

4.1 Introduction

In recent years meshless methods have achieved remarkable progress. Among meshless methods, the Element Free Galerkin (EFG) method introduced by Belytschko et al. (1994) has attracted much attention and been successfully applied to various engineering computations owing to its flexibility in solving problems with moving boundaries and moving discontinuities such as evolving crack (Rabczuk and Belytschko, 2004a; Rabczuk et al., 2007b; Rabczuk and Areias, 2006; Rabczuk and Belytschko, 2007b) and shear band formation (Rabczuk et al., 2004, 2007a; Rabczuk and Samaniego, 2008).

In comparison with FEM, the EFG meshless method enjoys a number of advantages. For example, the latter does not require a mesh for the interpolation process; offers a higher order of continuity; and may not suffer so much degradation in accuracy as nodal arrangements are irregular. Moreover, it is easier for adaptivity (Rabczuk and Belytschko, 2005a) and able to alleviate the effects of volumetric locking at the limit of incompressible materials provided that the local support radius is large enough. However, the major disadvantage of EFG as well as Moving Least Square (MLS) based meshless methods is that the shape functions lack the Kronecker-delta property, i.e. $\phi_i(\mathbf{x}_j) \neq \delta_{ij}$. The essential boundary conditions are not easy to be imposed accurately as in the FEMs due to this inequality. Attempts to overcome this shortcoming include Lagrange multiplier and penalty method (Zhu and Atluri, 1998), Nitsche's method (Fernández-Mández and Huerta, 2004), point collocation (Wanger and Liu, 1999), singular weight functions (Kaljevic and Saigal, 1997), coupling with FEM (Belytschko et al., 1995b; Rabczuk et al., 2006). Another alternative approach to address this limitation is employing the interpolation techniques that possess the Kronecker-delta property in constructing the shape functions of meshless Galerkin method. Examples include point interpolation meshless method (Wang and Liu, 2002), radial point interpolation method (Liu et al., 2005a), and moving kriging method (Gu, 2003).

Motivated by the former works, this chapter proposes a novel meshless method based on Moving Integrated Radial Basis Function Network (MIRBFN) of Le et al. (2010c) and (global weak form) Galerkin formulation, namely Moving IRBFN Galerkin (MIRBFNG) meshless method. In the present method, the shape functions are constructed within subdomains instead of the global domain. The system matrix is thus sparse and banded. The shape functions satisfy the Kronecker-delta property, therefore, essential boundary conditions are imposed easily and straightforwardly as in the FEMs. Moreover, the proposed method is applicable to irregular distributions of nodes and arbitrary domains. The remaining of this chapter is organized as follows. The Galerkin formulation for elasticity problems is presented in section 4.2. Section 4.3 reports the numerical experiments and section 4.4 draws some conclusions.

4.2 Variational form of two dimensional elasticity problems

Consider the following two-dimensional problem on a domain Ω bounded by $\Gamma = \Gamma_u \cup \Gamma_t$

$$\nabla \cdot \boldsymbol{\sigma} + \mathbf{b} = 0 \quad \text{in } \Omega, \quad (4.1a)$$

$$\mathbf{u} = \bar{\mathbf{u}} \quad \text{on } \Gamma_u, \quad (4.1b)$$

$$\boldsymbol{\sigma} \cdot \mathbf{n} = \bar{\mathbf{t}} \quad \text{on } \Gamma_t, \quad (4.1c)$$

in which $\boldsymbol{\sigma}$ is the stress tensor, which corresponds to the displacement field \mathbf{u} and \mathbf{b} the body force, \mathbf{n} the outward unit normal to Γ_t . The superimposed bar denotes prescribed value on the boundary.

The weak form for the above equations is expressed as

$$\int_{\Omega} \delta(\nabla_s \mathbf{u})^T \boldsymbol{\sigma} d\Omega = \int_{\Omega} \delta \mathbf{u}^T \mathbf{b} d\Omega + \int_{\Gamma_t} \delta \mathbf{u}^T \bar{\mathbf{t}} d\Gamma, \quad (4.2)$$

where the subscript s denotes the symmetric part of the gradient operator. Discretization of Equation (4.2) with Moving IRBFN as described in section 3.2.2 yields

$$\mathbf{K} \mathbf{u} = \mathbf{f}, \quad (4.3)$$

where

$$\mathbf{K}_{ij} = \int_{\Omega} \mathbf{B}_i^T \mathbf{C} \mathbf{B}_j d\Omega, \quad (4.4)$$

$$\mathbf{f}_i = \int_{\Gamma_t} \Phi_i \bar{\mathbf{t}} d\Gamma + \int_{\Omega} \Phi_i \mathbf{b} d\Omega, \quad (4.5)$$

$$\mathbf{B}_i = \begin{bmatrix} D_x^i & 0 \\ 0 & D_y^i \\ D_y^i & D_x^i \end{bmatrix}. \quad (4.6)$$

It is noted that the moving shape functions and their derivatives (constructed in section 3.2) are used for Φ_i in (4.5), and D_x^i and D_y^i in (4.6).

For the linear Hookean constitutive relation, the matrix \mathbf{C} in the case of plane stress is

$$\mathbf{C} = \frac{E}{1 - \nu^2} \begin{pmatrix} 1 & \nu & 0 \\ \nu & 1 & 0 \\ 0 & 0 & \frac{1-\nu}{2} \end{pmatrix}, \quad (4.7)$$

where E is elastic modulus and ν Poisson ratio.

As a global weak form discretisation, a background mesh independent of data nodes is necessary for numerical integration of Equations (4.4)-(4.5), and Gaussian quadrature is employed for the numerical integration in this chapter. The remarkable feature of the present method is that the essential boundary condition is imposed easily and straightforwardly as in the FEM.

4.3 Numerical examples

For an error estimation and convergence study, the displacement norm and energy norm are defined as follows

$$\text{displacement norm} = \sqrt{\int_{\Omega} (\mathbf{u}^{num} - \mathbf{u}^{exact})^T (\mathbf{u}^{num} - \mathbf{u}^{exact}) d\Omega}, \quad (4.8)$$

$$\text{energy norm} = \sqrt{\frac{1}{2} \int_{\Omega} (\boldsymbol{\varepsilon}^{num} - \boldsymbol{\varepsilon}^{exact})^T (\boldsymbol{\sigma}^{num} - \boldsymbol{\sigma}^{exact}) d\Omega}, \quad (4.9)$$

where the superscripts *num* and *exact* denote numerical and exact solutions, respectively; the stress and strain components are presented in vector form $\boldsymbol{\sigma}$ and $\boldsymbol{\varepsilon}$, respectively.

The convergence order of the solution with respect to the refinement of spatial discretization is assumed to be in the form of

$$\text{error}(h) \approx \zeta h^{\lambda} = O(h^{\lambda}), \quad (4.10)$$

where h is the maximum nodal spacing, ζ and λ are the parameters of the exponential model, which are found by general linear least square formula.

It is noted that the scheme for selection of RBF centers presented in section 3.2 is also applied in this chapter and the present results are compared with

those obtained by the EFG method which only uses linear basis function. In the following numerical examples, α and β are referred to as the scale factor of the radius of the domains of influence and the shape parameter of the RBF given in (1.8), respectively. α is defined by $\alpha = R_s/h$, where R_s is the radius of the domains of influence (see equation (3.15)).

4.3.1 One dimensional example

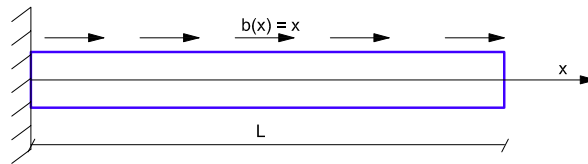


Figure 4.1: One dimensional example: a mathematical model.

Consider a one-dimensional bar of unit length ($L = 1$) subjected to a linear body force of magnitude x as shown in Figure 4.1. The bar is fixed at the left end and traction free at the right end. The cross sectional area of the bar is of unit value and the modulus of elasticity is $E = 1$.

The equilibrium equation and boundary conditions for this problems are as follows.

$$E \frac{\partial^2 u}{\partial x^2} + x = 0, \quad 0 \leq x \leq 1 \quad (4.11)$$

$$u(0) = 0, \quad (4.12)$$

$$\frac{\partial u}{\partial x}(1) = 0. \quad (4.13)$$

The exact solution to the problem is given by

$$u(x) = \frac{1}{E} \left[\frac{1}{2}x - \frac{x^3}{6L^2} \right]. \quad (4.14)$$

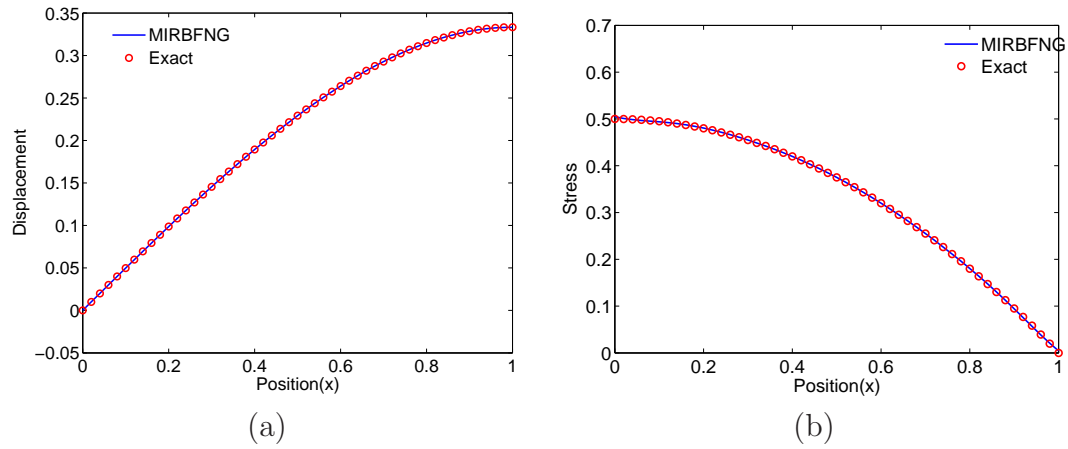


Figure 4.2: One dimensional example: the results obtained by present method with 9 nodes are interpolated with 50 nodes, (a) displacement and (b) stress.

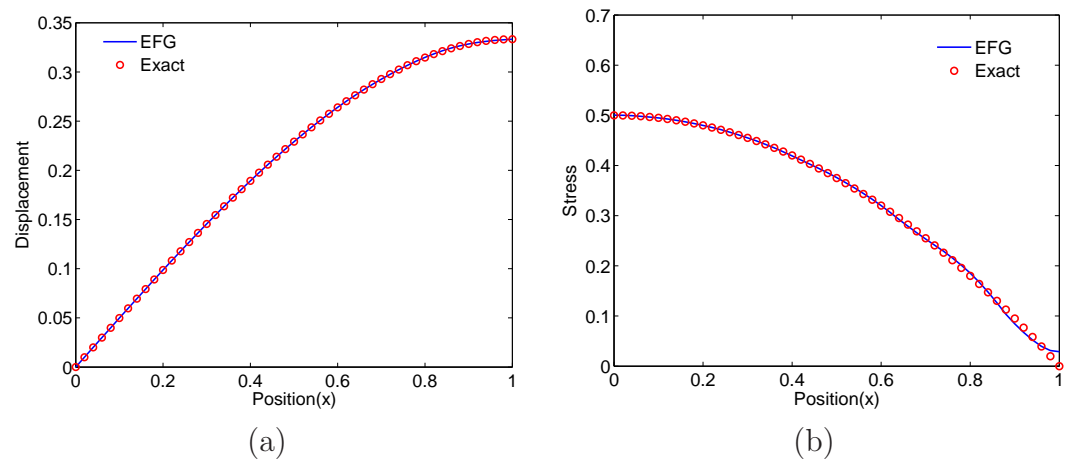


Figure 4.3: One dimensional example: the results obtained by the EFG method with 9 nodes are interpolated with 50 nodes, (a) displacement and (b) stress.

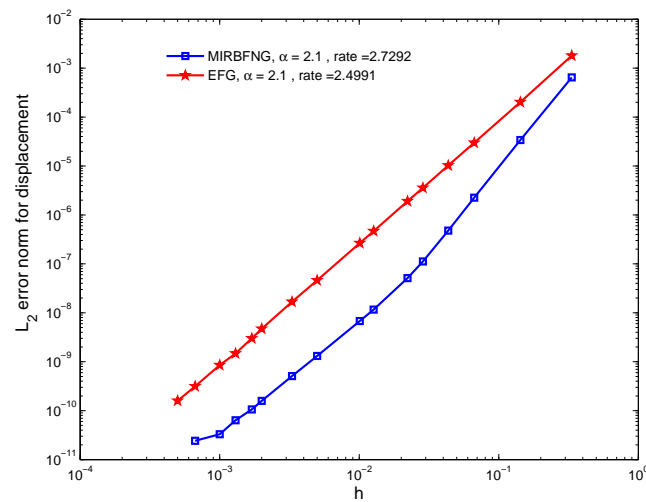


Figure 4.4: One dimensional example: L_2 error norm for displacement.

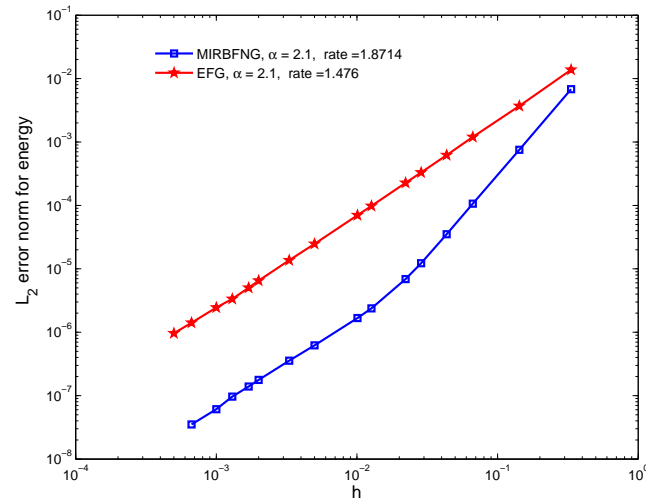


Figure 4.5: One dimensional example: L_2 error norm for energy.

In this example, the domain is uniformly discretised, α and β are set at 2.1 and 4, respectively. Seven Gauss points are employed in each cell (defined by two nearest nodes) for the numerical integration.

Figure 4.2 shows the numerical solution obtained by the present method with uniform distribution of 9 nodes and the results are interpolated at 50 points. It can be seen that the numerical solution excellently agrees with the exact solution. Moreover, the accuracy of the present method is favourably compared with that of the EFG method as shown in Figures 4.2-4.3.

The rates of convergence of the present method, using displacement and energy norms are 2.73 and 1.87, respectively, while those of the EFG method are 2.50 and 1.48, respectively, as displayed in Figures 4.4-4.5.

4.3.2 Cantilever Beam

The present method is now verified, using the problem of a cantilever beam subject to parabolic shear load at the end $x = 0$ as shown in Figure 4.6. The following parameters are used for the problem: $L = 4.8$ and $D = 1.2$. The

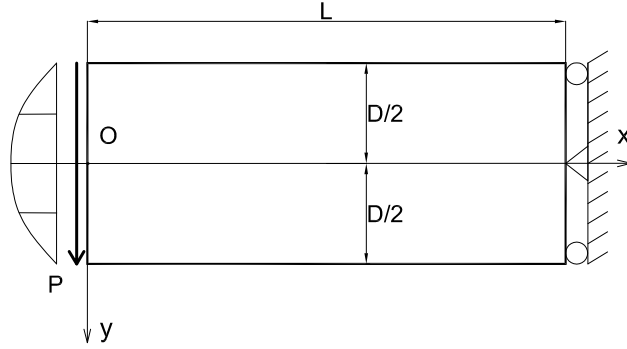
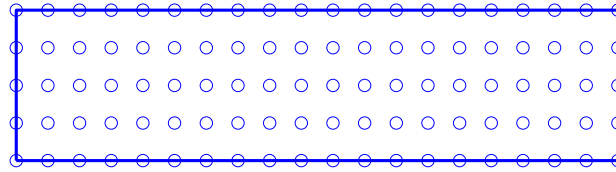


Figure 4.6: Cantilever beam: a mathematical model.

Figure 4.7: Cantilever beam: discretisation model with 20×5 nodes.

beam has a unit thickness. Young's modulus is $E = 3 \times 10^6$, Poisson's ratio is $\mu = 0.3$ (also $\mu = 0.4999$) and the integrated parabolic shear force is $P = 100$. Plane stress condition is assumed and there is no body force.

The exact solution to this problem was given by Timoshenko and Goodier (1970) as

$$\sigma_{xx}(x, y) = \frac{-Pxy}{I}, \quad (4.15a)$$

$$\sigma_{yy}(x, y) = 0, \quad (4.15b)$$

$$\tau_{xy}(x, y) = \frac{-P}{2I} \left(\frac{D^2}{4} - y^2 \right). \quad (4.15c)$$

The displacements are given by

$$u_x = -\frac{Px^2y}{2EI} - \frac{\mu Py^3}{6EI} + \frac{Py^3}{6IG} + y \left(\frac{PL^2}{2EI} - \frac{PD^2}{8IG} \right), \quad (4.16)$$

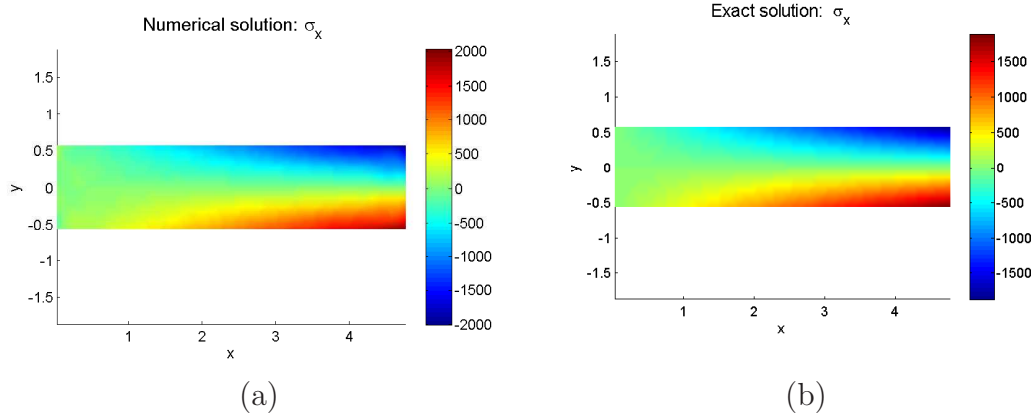


Figure 4.8: Cantilever beam: σ_x given by (a) MIRBFNG with 20×5 nodes and (b) Exact solution.

$$u_y = \frac{\mu P x y^2}{2EI} + \frac{P x^3}{6EI} - \frac{P L^2 x}{2EI} + \frac{P L^3}{3EI}, \quad (4.17)$$

where $I = D^3/12$ is the moment of inertia of the cross section of the beam (of unit thickness), $G = E/(2(1 + \mu))$ the modulus of elasticity in shear.

The exact displacements (4.16) and (4.17) are applied on the Dirichlet boundary $x = L$.

To solve this problem, uniform distributions of nodes (Figure 4.7) are considered. The scale factor of local support α is set at 2.1. β is 9. Background meshes of four-node cell with 4×4 Gauss quadrature points per cell are used for the numerical integration.

Figure 4.8 illustrates the comparison between the stress (σ_x) obtained by the proposed method with 20×5 nodes and the exact one. Figures 4.9 and 4.10 show the convergence behaviour of the method in displacement norm and energy norm, respectively. High orders of convergence achieved by the present method can be observed in the figures, i.e. $O(h^{5.21})$ and $O(h^{2.95})$ ($\mu = 0.3$) for L_2 error norms using displacement and energy, respectively. The plots (Figure 4.8) together with the error norm (Figures 4.9-4.10) show an excellent agreement between the numerical results and the analytical solution. Furthermore, the numerical results in the case of $\mu = 0.4999$ indicate that the MIRBFNG method

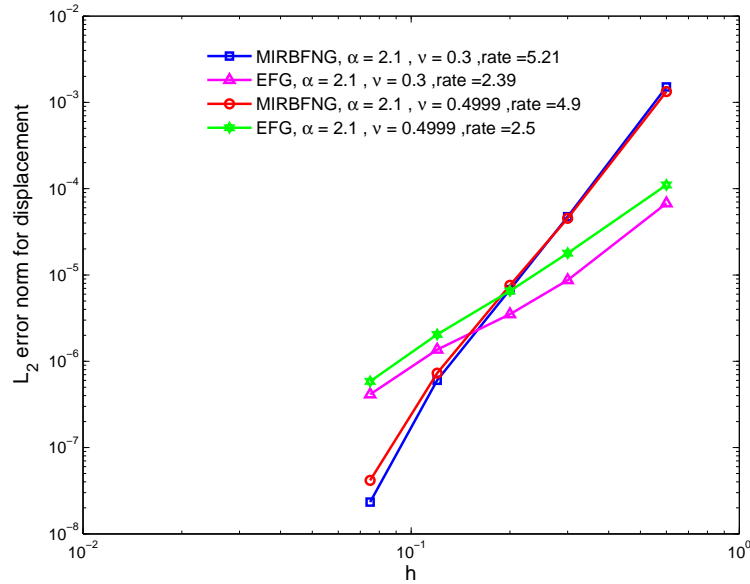


Figure 4.9: Cantilever beam: L_2 error norm for displacement.

does not suffer from any volumetric locking near the limit of incompressible material.

For the purpose of comparison, the same configurations of nodes, local supports and background meshes are used for the EFG method with 4×4 Gaussian quadrature points in each integration cell. The comparison shows that the rates of convergence and the accuracy achieved by the present method are superior to those obtained by the EFG as shown in the above figures.

To study the performance of the method with sets of scattered nodes ($\mu = 0.3$), the domain of interest is discretised with 125, 225, 633, 803, 1020, 1725 and 2502 unstructured nodes as depicted in Figure 4.11. The convergence of τ_{xy} at $x = 2.40$ is revealed in Figure 4.12. It can be observed that the method performs very well with scattered distribution of nodes. The convergence rates using displacement and energy norms obtained by the present method are 3.95 and 1.72, respectively.

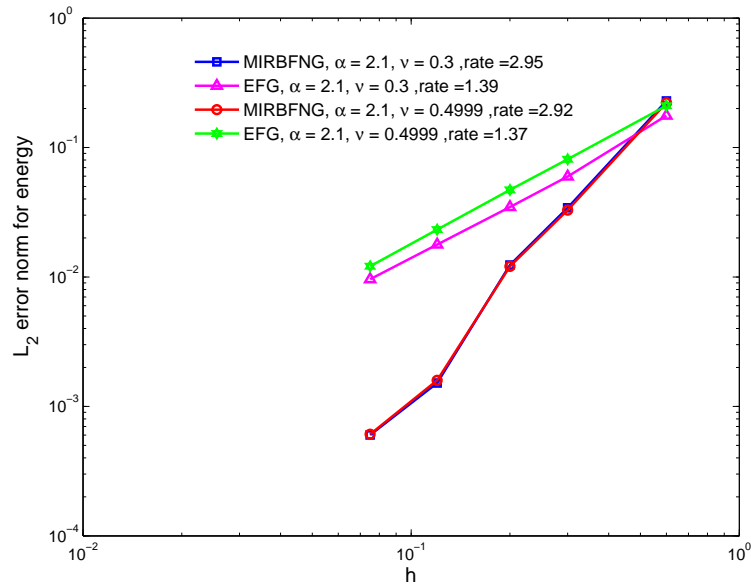
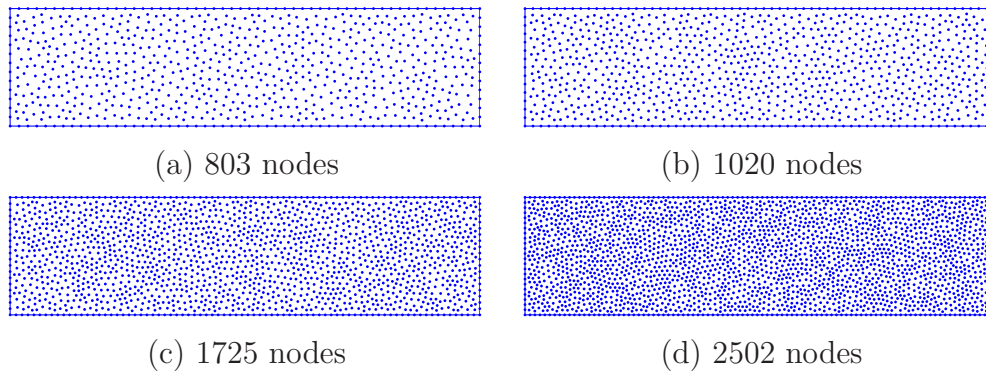
Figure 4.10: Cantilever beam: L_2 error norm for energy.

Figure 4.11: Cantilever beam: unstructured discretisations.

4.3.3 Infinite plate with a circular hole

In this example, an infinite plate with a circular hole subjected to unidirectional tensile load of 1.0 in the x direction as shown in Figure 4.15 is analyzed. The radius of the hole is taken as 1 unit. Owing to symmetry, only the upper right quadrant $[0, 4] \times [0, 4]$ of the plate is modeled as shown in Figure 4.16.

In this problem, plane stress conditions are assumed with elastic isotropic properties $E = 10^3$, $\mu = 0.3$. The exact solution to this problem was given by Timoshenko and Goodier Timoshenko and Goodier (1970) as follows.

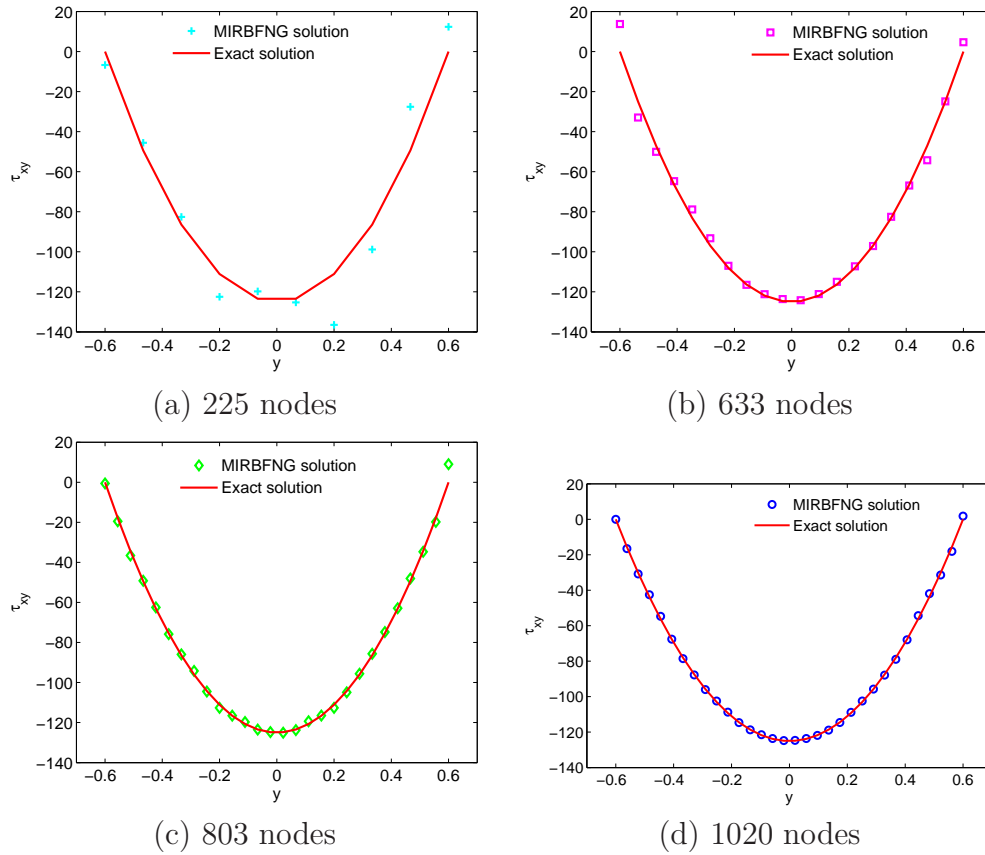


Figure 4.12: Cantilever beam: convergence of τ_{xy} at $x = 2.40$ with unstructured nodal refinement.

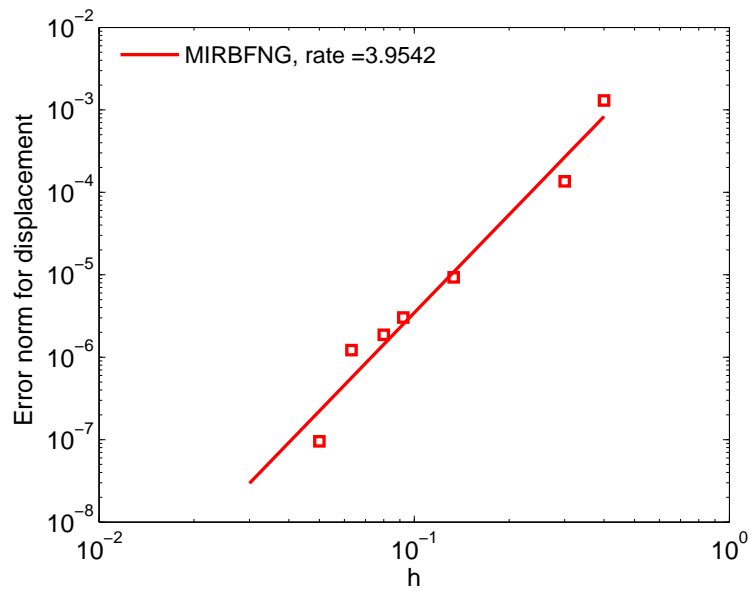


Figure 4.13: Cantilever beam: L_2 error norm for displacement with unstructured nodes.

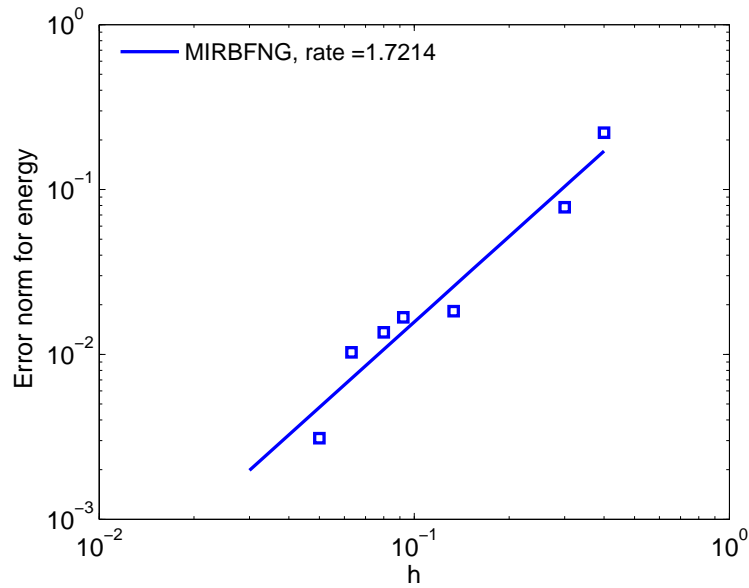


Figure 4.14: Cantilever beam: L_2 error norm for energy with unstructured nodes.

$$\sigma_x(x, y) = \sigma \left[1 - \frac{a^2}{r^2} \left[\frac{3}{2} \cos(2\theta) + \cos(4\theta) \right] + \frac{3a^4}{2r^4} \cos(4\theta) \right], \quad (4.18a)$$

$$\sigma_y(x, y) = -\sigma \left[\frac{a^2}{r^2} \left[\frac{1}{2} \cos(2\theta) - \cos(4\theta) \right] + \frac{3a^4}{2r^4} \cos(4\theta) \right], \quad (4.18b)$$

$$\tau_{xy}(x, y) = -\sigma \left[\frac{a^2}{r^2} \left[\frac{1}{2} \sin(2\theta) + \sin(4\theta) \right] - \frac{3a^4}{2r^4} \sin(4\theta) \right], \quad (4.18c)$$

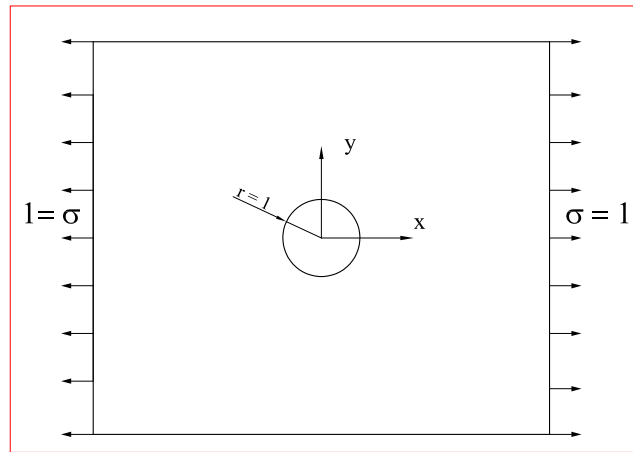


Figure 4.15: Infinite plate with a circular hole.

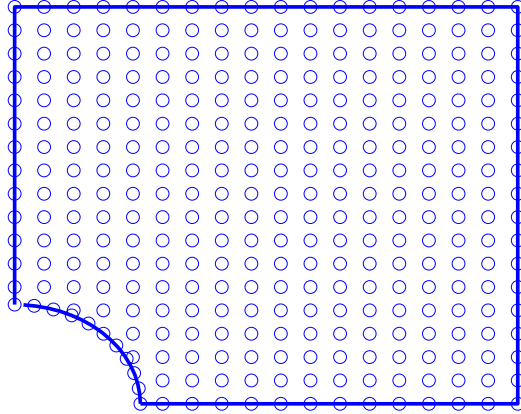


Figure 4.16: Infinite plate with a circular hole: computational domain discretization with 315 nodes.

where (r, θ) are the polar coordinates, a the radius of the hole.

The corresponding displacements are given by

$$u_x(x, y) = \sigma \frac{(1 + \mu)}{E} \left[\frac{1}{1 + \mu} r \cos(\theta) + \frac{2}{1 + \mu} \frac{a^2}{r} \cos(\theta) + \frac{1}{2} \frac{a^2}{r} \cos(3\theta) - \frac{1}{2} \frac{a^4}{r^3} \cos(3\theta) \right] \quad (4.19a)$$

$$u_y(x, y) = \sigma \frac{(1 + \mu)}{E} \left[\frac{-\mu}{1 + \mu} r \sin(\theta) + \frac{1 - \mu}{1 + \mu} \frac{a^2}{r} \sin(\theta) + \frac{1}{2} \frac{a^2}{r} \sin(3\theta) - \frac{1}{2} \frac{a^4}{r^3} \sin(3\theta) \right] \quad (4.19b)$$

The boundary conditions of the problem are as follows. The tractions which correspond to the exact solution for the infinite plate are applied on the top and right edges, the symmetric conditions are applied on the left and bottom edges, and the edge of the hole is traction free.

The problem is discretised as shown in Figure 4.16. The value of α and β are 1.5 and 1, respectively. The number of Gaussian quadrature points per integration cell is 4×4 .

To study the convergence of the method, a number of configurations of 50, 120, 315, 511 nodes is considered. Figures 4.17-4.18 show that the present method achieves excellent accuracy and high rates of convergence, i.e. 2.91 and 1.45 using displacement and energy norms, respectively. Again, it can be seen that the accuracy and the convergent rates of the proposed method are favourably

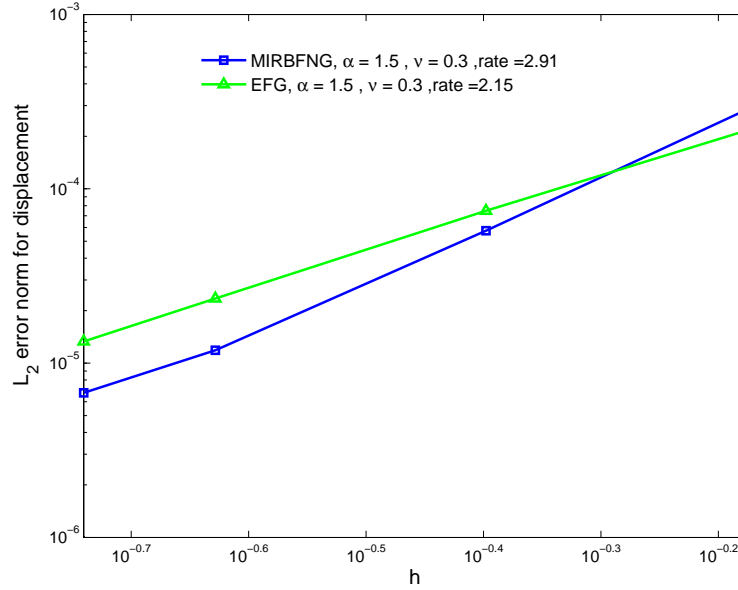


Figure 4.17: Infinite plate with a circular hole: L_2 error norm for displacement.

compared with those of the EFG method as shown in the figures.

4.3.4 Mode I crack problem

Consider an infinite plate containing a straight crack of length $2a$ and loaded by a remote uniform stress field σ as shown in Figure 4.19. Under plane strain condition, the closed form solution in terms of polar coordinates in a reference frame (r, θ) centered at the crack tip is given by (body force is zero)

$$\sigma_x = \frac{K_I}{\sqrt{r}} \cos \frac{\theta}{2} \left(1 - \sin \frac{\theta}{2} \sin 3\frac{\theta}{2} \right), \quad (4.20a)$$

$$\sigma_y = \frac{K_I}{\sqrt{r}} \cos \frac{\theta}{2} \left(1 + \sin \frac{\theta}{2} \sin 3\frac{\theta}{2} \right), \quad (4.20b)$$

$$\tau_{xy} = \frac{K_I}{\sqrt{r}} \sin \frac{\theta}{2} \cos \frac{\theta}{2} \cos 3\frac{\theta}{2}, \quad (4.20c)$$

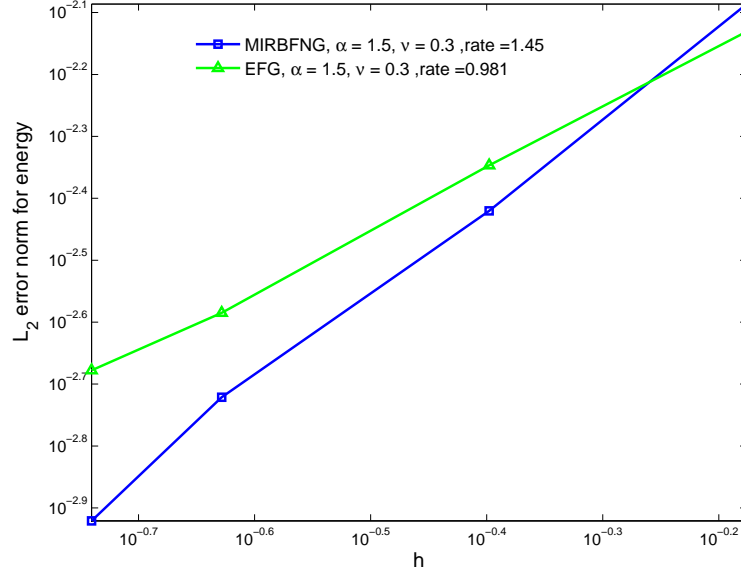


Figure 4.18: Infinite plate with a circular hole: L_2 error norm for energy.

and the closed form of near tip displacement field is given by

$$u_x = \frac{2(1+\mu)}{\sqrt{2\pi}} \frac{K_I}{E} \sqrt{r} \cos \frac{\theta}{2} \left(2 - 2\mu - \cos^2 \frac{\theta}{2} \right), \quad (4.21a)$$

$$u_y = \frac{2(1+\mu)}{\sqrt{2\pi}} \frac{K_I}{E} \sqrt{r} \sin \frac{\theta}{2} \left(2 - 2\mu - \cos^2 \frac{\theta}{2} \right), \quad (4.21b)$$

where $K_I = \sigma\sqrt{\pi a}$ is the stress intensity factor, μ is Poisson's ratio and E is Young modulus. ABCD is a square of $10 \times 10 \text{ mm}^2$, $a = 100 \text{ mm}$; $E = 10^7 \text{ N/mm}^2$, $\mu = 0.3$ (also $\mu = 0.4999$), $\sigma = 10^4 \text{ N/mm}^2$.

The computational domain ABCD is shown in Figure 4.19. Owing to symmetry, only the upper half of ABCD, namely CDEFG as shown in Figure 4.20, is analyzed. The segment of the crack denoted by EF has a length of $b = 5 \text{ mm}$. The boundary condition of the problem is as follows. The traction free boundary condition is applied on the crack while the displacement field given in equation (4.21) is imposed on the remaining boundaries.

In this example, the domain of interest is uniformly discretised. α and β are 1.1 and 1, respectively. 2×2 Gauss quadrature points per integration cell are

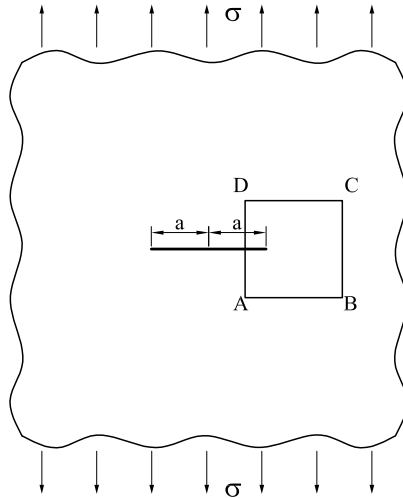


Figure 4.19: Infinite cracked plate under remote tension.

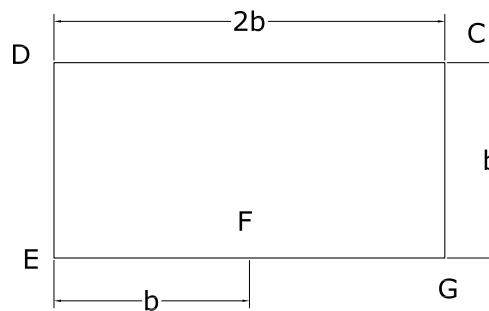


Figure 4.20: Infinite cracked plate: analyzed portion.

used for the numerical integration.

The numerical solutions to displacement and stress obtained with 20×10 nodes ($\mu = 0.3$) and the analytical solutions are plotted in Figures 4.21-4.23. The comparison indicates an excellent agreement between the solutions obtained by the proposed method and the exact solutions.

For convergence study, a number of regular distribution of 4×8 , 8×16 , 12×24 , 16×32 , 20×40 , and 24×48 nodes is employed with $\mu = 0.3$ and $\mu = 0.4999$. The convergence curves for displacement and energy are shown in Figures 4.24 and 4.25, respectively. The orders of convergence using displacement and energy norms are 1.35 and 0.48, respectively, for $\mu = 0.3$. It can be seen that the rate

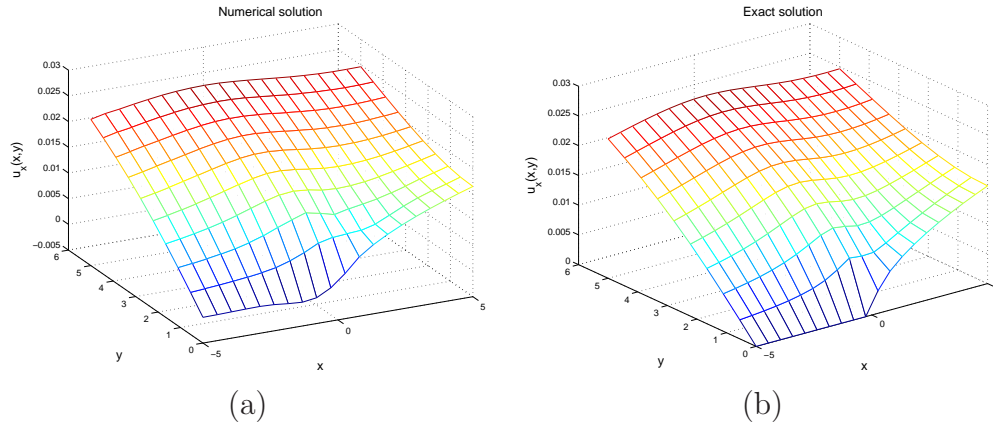


Figure 4.21: Infinite cracked plate: (a) MIRBFNG solution and (b) exact solution of u_x with 20×10 nodes ($\mu = 0.3$).

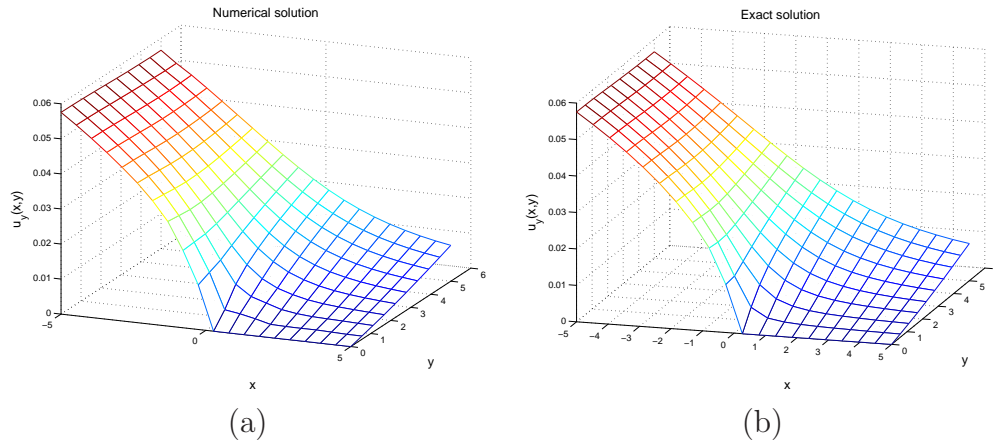


Figure 4.22: Infinite cracked plate: (a) MIRBFNG solution and (b) exact solution of u_y with 20×10 nodes ($\mu = 0.3$).

of convergence for energy is reduced significantly due to singularity in the stress field. Again, the numerical results demonstrate that the method does not show any volumetric locking in the case of $\mu = 0.4999$ (Figures 4.24-4.25).

4.4 Concluding remarks

This chapter proposed a novel meshless method based on the MIRBFN interpolation and Galerkin method for solving PDEs. The key feature of the method is that the shape functions are locally supported and satisfy the Kronecher-delta property. As a result, the essential boundary conditions are imposed exactly

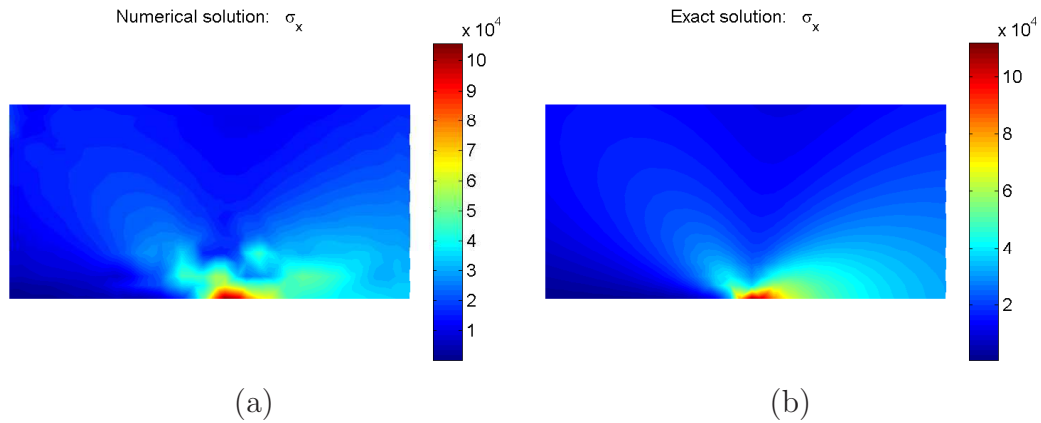


Figure 4.23: Infinite cracked plate: (a) MIRBFNG solution and (b) exact solution of σ_x with 20×10 nodes ($\mu = 0.3$).

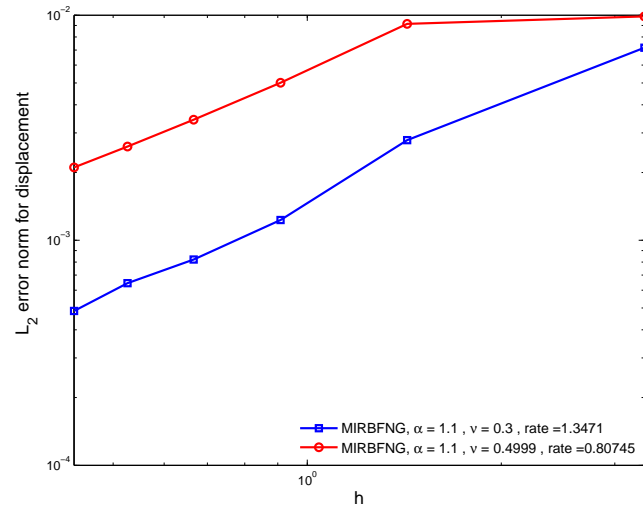


Figure 4.24: Infinite cracked plate: L_2 error norm for displacement.

and straightforwardly in this method. The method is applicable to sets of scattered nodes and irregular domains. Furthermore, the proposed method achieves high orders of convergence and high accuracy with smooth problems. The obtained results also indicate that there is no evidence of volumetric locking with the present method. Furthermore, it is encouraging that the accuracy and the rate of convergence of the method is favourably compared with those of the EFG method.

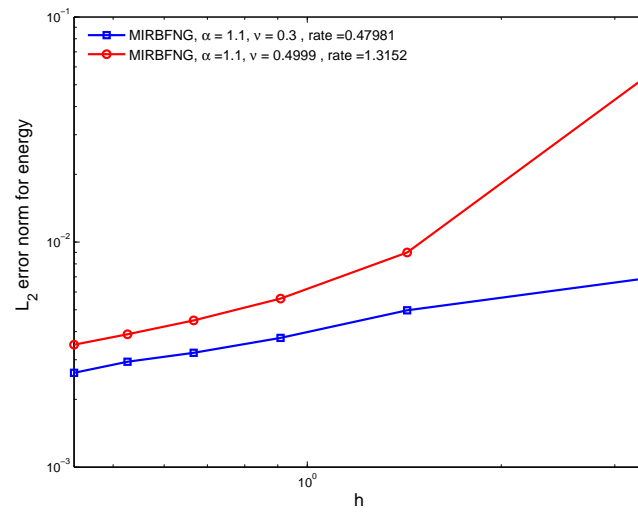


Figure 4.25: Infinite cracked plate: L_2 error norm for energy.

Chapter 5

Modeling dynamic strain localization in quasi-brittle materials with IRBFN collocation technique

This chapter describes the indirect (integrated) radial basis function network (IRBFN) method for the numerical modeling of the dynamics of strain localization due to strain softening in quasi-brittle materials. The IRBFN method is a truly meshless method that is based on a point collocation procedure. A new and effective regularization method is introduced to enhance the performance of the IRBFN method and alleviate the numerical oscillations associated with weak discontinuity at the elastic wave front. The dynamic response of a one dimensional bar is investigated using both local and non-local continuum models. Numerical results, which compare favourably with those obtained by the FEM and the analytical solutions for a local continuum model, demonstrate the efficiency of the present IRBFN approach in capturing large strain gradients encountered in the present problem.

5.1 Introduction

In many engineering structures subjected to extreme loading conditions, the initially smooth distribution of strain may change into a highly localised one. Typically, extremely high strains may occur within a very narrow zone while the remaining part of the structure experiences unloading. Such strain localization usually can be caused by geometrical nonlinearities (e.g., necking of metallic bars) or by material instabilities (e.g., micro-cracking). Mathematically, the onset of strain localization, in the context of a rate-independent local continuum model, leads to loss of hyperbolicity of the governing partial differential equations, i.e. when the matrix of tangent modulus ceases to be positive-definite. From a computational point of view, the loss of hyperbolicity causes numerical difficulties since the mathematical model becomes ill-posed (localised zone of zero volume). To regularize the ill-posed problems, a number of localization limiters have been developed to ensure that localised zones have a finite volume and the problem becomes well-posed. Examples of localisation limiters include non-local models, rate-dependent models, gradient-dependent models, visco-plastic models, damage-based models, cohesive crack models, smear crack models and Cosserat continuum model.

For one dimensional problems (softening bars), some closed-form exact and approximate solutions have been developed by many authors, including, for example, Bazant and Belytschko (1985); Sluys (1992); Xin and Chen (2000); Armero and Park (2003) for the evolution of dynamic strain localization via rate-independent local constitutive models. The above closed-form solutions demonstrated that one of the following two cases is possible. First, if the behaviour of the tensile bars is fully elastic, the displacement field is C^0 continuous, the strain field is discontinuous and the discontinuities propagate as incident as well as reflected waves. Second, if localization occurs, the mathematical model becomes ill-posed in the context of a rate-independent local continuum model as stated above. Hence, numerical methods are not able to capture the solutions

using rate-independent local constitutive models (Bazant and Belytschko, 1985; Sluys, 1992; Askes et al., 1998). Moreover, even if a localization limiter is applied, for an accurate description of the localized zone, a very fine computational mesh is needed, since the strain gradients are very high within localized zones. Hence, robust numerical methods are required to analyze such strain localization phenomena. In general, the position of the localization zone is unknown, therefore, an automatic mesh adaptive procedure is required to increase the efficiency of the numerical method. However, the polynomial approximations in FEM can poorly capture the non-smooth transition between the unloading region with almost constant strain and the localization zone with rapid strain increase (Patzák and Jirásek, 2003) and the FEM results are very sensitive to the computational grids. The extended finite element method (Patzák and Jirásek, 2003), which incorporates special enrichment functions into the shape functions, produces better results, however, the asymptotic solutions are required to be known in advance. Owing the non-local nature of approximations used (Li and Liu, 2000; Batra and Zhang, 2004; Le et al., 2007a), meshless methods possess some advantages in modeling such strain localization problems and provide more continuous solutions than the piece-wise continuous ones obtained from FEM. Thus meshless methods offer effective solutions to the mesh alignment sensitivity in strain localization modelings.

In this study, we report a new numerical method based on radial basis function networks, a truly meshless method, for the analysis of the dynamics of strain localization in 1D problems. The present indirect/integral radial basis function network (IRBFN) method is based on (i) the universal approximation property of RBF networks, (ii) exponential convergence characteristics of the chosen multiquadric (MQ) RBF, (iii) a simple point collocation method of discretisation of the governing equations, and (iv) an indirect/integral (IRBFN) rather than a direct/differential (DRBFN) approach (Kansa, 1990) for the approximation of functions and derivatives. For the DRBFN, Madych and Nelson (1990) showed that the convergence rate is a decreasing function of derivative order. Since the

introduction of the IRBFN approach by Mai-Duy and Tran-Cong (2001, 2005); Kansa et al. (2004); Ling and Trummer (2004), based on the theoretical result of Madych and Nelson (1990), concluded that the decreasing rate of convergence can be avoided in the IRBFN approach. Furthermore, the integration constants arisen in the IRBFN approach are helpful in dealing with problems with multiple boundary conditions (Mai-Duy and Tran-Cong, 2006). However, being a global and high order approximation method, IRBFN based methods also suffer from the Gibbs phenomenon where numerical oscillations occur around a jump discontinuity or near a boundary (Jung, 2007), with consequential deterioration of convergence rate, accuracy and stability. In the case of approximation methods based on multiquadric radial basis function (MQ-RBF), several approaches have been developed to attenuate the Gibbs oscillations. For example, Jung (2007) proposed an adaptive piecewise linear basis functions in the vicinity of the discontinuity; Driscoll and Heryudono (2007) suggested an adaptive residual subsampling methods and Le et al. (2007a) offered a new coordinate mapping (for boundary layer problems). In addition, we introduce a new and effective regularization method based on the IRBFN to alleviate numerical oscillations, which enhances the performance of the present method in dealing with weak discontinuities associated with the strain localization process. The chapter is organized as follows. The physical problem and its mathematical model are defined in section 5.2. The numerical formulation for the mathematical model is presented in section 5.3 which is followed by numerical examples in section 5.4. Section 5.5 concludes the chapter.

5.2 Problem definition

Consider a solid bar of length $2L$, with a unit cross sectional area and mass ρ per unit length as shown in Figure 5.1. Let the bar be loaded by forcing both ends to move simultaneously outward, with a constant opposite velocity of magnitude c . The governing equations are described as follows.

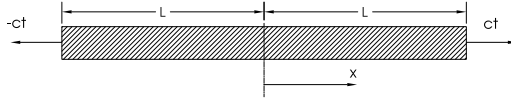


Figure 5.1: A model of uniform bars.

The momentum equation is given by

$$\rho \frac{\partial^2 u(x, t)}{\partial t^2} = \frac{\partial \sigma(x, t)}{\partial x}, \quad (5.1)$$

where x is the coordinate measured from the mid-point of the bar, $-L \leq x \leq L$; t is time $0 \leq t \leq t_{max}$; $u(x, t)$ is the displacement in x the direction and $\sigma(x, t)$ is the stress.

The material behaviour is described by a bilinear constitutive law as presented in Figure 5.2, which exhibits elastic behaviour with Young's modulus E up to strain ε_p at the peak stress f_y (strength), followed by strain-softening (line PF), which has a negative slope E_t up to ε_f , where the stress has a value of zero, finally, followed by a nearly horizontal tail of a very small positive slope E_f .

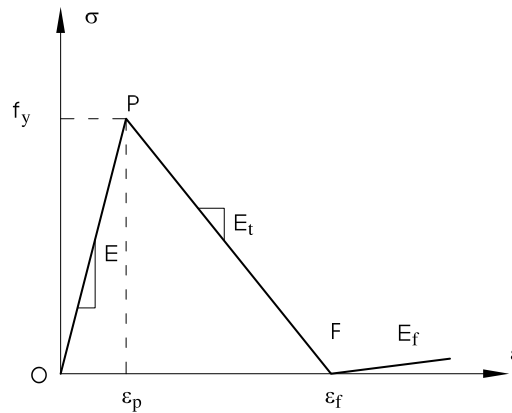


Figure 5.2: A constitutive relation for quasi-brittle materials.

The constitutive relation is thus given by

$$\Delta \sigma(x, t) = \bar{E} \Delta \varepsilon, \quad (5.2)$$

in which $\epsilon = \epsilon(x, t) = \frac{\partial u(x, t)}{\partial x}$ is the strain and \bar{E} is the slope of the stress-strain relation, defined by

$$\bar{E} = \begin{cases} E, & \text{if } \epsilon \leq \epsilon_p, \\ E_t, & \text{if } \epsilon_p \leq \epsilon \leq \epsilon_f, \\ E_f, & \text{if } \epsilon \geq \epsilon_f. \end{cases} \quad (5.3)$$

The boundary conditions are

$$u(x = -L, t) = -ct; \quad u(x = L, t) = ct, \quad \text{for } t \geq 0. \quad (5.4)$$

The initial solutions are taken as follows

$$u(x, t = 0) = 0 \quad \text{and} \quad \frac{\partial u(x, t = 0)}{\partial t} = 0, \quad \text{for } -L \leq x \leq L. \quad (5.5)$$

Due to symmetry, the problem is equivalent to a bar fixed at $x = 0$. Thus the boundary conditions for a half model now become

$$u(x = -L, t) = -ct; \quad u(x = 0, t) = 0, \quad \text{for } t \geq 0. \quad (5.6)$$

The governing equations are non-dimensionalised using the following scheme: characteristic length a ; characteristic time $T = \frac{a}{v_e}$, where $v_e = \sqrt{E/\rho}$ is the elastic wave speed; characteristic stress $\sigma_c = E$; velocities are normalised by v_e , e.g. c/v_e is the dimensionless loading velocity at the ends of the bar. The dimensionless momentum equation is given by

$$\frac{\partial^2 u(x, t)}{\partial t^2} = \left(\frac{ET^2}{\rho a^2} \right) \frac{\partial \sigma(x, t)}{\partial x} = \left(\frac{\bar{E}}{E} \right) \gamma^2 \frac{\partial \epsilon(x, t)}{\partial x}, \quad (5.7)$$

where \bar{E} is given in (5.3), $\gamma = \sqrt{\frac{ET^2}{\rho a^2}} = \frac{v_e T}{a}$.

In the remaining of the chapter, for brevity, in addition to (u, x, t, σ) , c and L are now dimensionless quantities.

5.3 Numerical formulation

Consider an initial-boundary-value problem governed by the second order PDE

$$\frac{\partial u}{\partial t} = q_1 \frac{\partial^2 u}{\partial x^2} + q_2 \frac{\partial u}{\partial x} + q_3 u + q_4, \quad (5.8)$$

where q_1 , q_2 , q_3 and q_4 are the coefficients, $0 \leq t \leq T$ and $x_{min} \leq x \leq x_{max}$, with the boundary and initial conditions

$$u(t, x = x_{min}) = u_1, \quad (5.9)$$

$$\frac{\partial u}{\partial x} \Big|_{(t, x=x_{max})} = u'_N, \quad (5.10)$$

$$u(0, x) = g(x), \quad (5.11)$$

in which u_1 and u'_N are given values, and $g(x)$ is a known function.

5.3.1 Spatial discretisation

In the indirect RBF method (see Mai-Duy and Tran-Cong (2001, 2005); Mai-Duy (2005); Mai-Duy and Tanner (2005)), the formulation of the problem starts with the decomposition of the highest order derivative under consideration into RBFs. The derivative expression obtained is then integrated to yield expressions for lower order derivatives and finally for the original function itself. The present work is concerned with the approximation of a function and its derivatives of order up to 2, the formulation can be thus described as follows (Mai-Cao and

Tran-Cong, 2005; Le et al., 2007a)

$$\frac{d^2u(x, t)}{dx^2} = \sum_{i=1}^m w_i(t)g_i(x) = \sum_{i=1}^m w_i(t)H_i^{[2]}(x), \quad (5.12)$$

$$\begin{aligned} \frac{du(x, t)}{dx} &= \int \sum_{i=1}^m w_i(t)g_i(x)dx + c_1(t) \\ &= \sum_{i=1}^m w_i(t) \int g_i(x)dx + c_1(t) \\ &= \sum_{i=1}^m w_i(t)H_i^{[1]}(x) + c_1(t), \end{aligned} \quad (5.13)$$

$$\begin{aligned} u(x, t) &= \sum_{i=1}^m w_i(t) \int H_i^{[1]}(x)dx + c_1(t)x + c_2(t) \\ &= \sum_{i=1}^m w_i(t)H_i^{[0]}(x) + c_1(t)x + c_2(t), \end{aligned} \quad (5.14)$$

where m is the number of RBFs, $\{g_i(x)\}_{i=1}^m$ is the set of RBFs, $\{w_i(t)\}_{i=1}^m$ is the set of corresponding network weights to be found and $\{H_i^{[j]}(x)\}_{i=1}^m$ ($j = 0, 1$) are new basis functions obtained from integrating the radial basis function $g_i(x)$ once or more times. The multiquadrics function is chosen in the present study

$$g_i(x) = \sqrt{(x - c_i)^2 + a_i^2}, \quad (5.15)$$

where c_i is the RBF center and a_i is the RBF width. The width of the i^{th} RBF can be determined according to the following simple relation

$$a_i = \beta d_i, \quad (5.16)$$

where β is a factor, $\beta > 0$, and d_i is the distance from the i^{th} center to its nearest center. To have the same coefficient vector as (5.14), (5.12) and (5.13) can be rewritten as follows.

$$\frac{d^2u(x, t)}{dx^2} = \sum_{i=1}^m w_i(t)H_i^{[2]}(x) + c_1(t).0 + c_2(t).0, \quad (5.17)$$

$$\frac{du(x, t)}{dx} = \sum_{i=1}^m w_i(t)H_i^{[1]}(x) + c_1(t).1 + c_2(t).0. \quad (5.18)$$

Here we choose the RBF centers c_i to be identical to the collocation points x_i , i.e. $\{c_i\}_{i=1}^m = \{x_i\}_{i=1}^N$. The evaluation of (5.17), (5.18) and (5.14) at a set of N collocation points leads to

$$\mathbf{u}''(t) = \mathbf{H}^{[2]}\mathbf{w}(t), \quad (5.19)$$

$$\mathbf{u}'(t) = \mathbf{H}^{[1]}\mathbf{w}(t), \quad (5.20)$$

$$\mathbf{u}(t) = \mathbf{H}^{[0]}\mathbf{w}(t), \quad (5.21)$$

where

$$\mathbf{u}''(t) = \left[\frac{\partial^2 u_1(t)}{\partial x^2}, \frac{\partial^2 u_2(t)}{\partial x^2}, \dots, \frac{\partial^2 u_N(t)}{\partial x^2} \right]^T, \quad (5.22)$$

$$\mathbf{u}'(t) = \left[\frac{\partial u_1(t)}{\partial x}, \frac{\partial u_2(t)}{\partial x}, \dots, \frac{\partial u_N(t)}{\partial x} \right]^T, \quad (5.23)$$

$$\mathbf{u}(t) = [u_1(t), u_2(t), \dots, u_N(t)]^T, \quad (5.24)$$

$$\mathbf{H}^{[2]} = \begin{pmatrix} H_1^{[2]}(x_1) & H_2^{[2]}(x_1) & \cdots & H_N^{[2]}(x_1) & 0 & 0 \\ H_1^{[2]}(x_2) & H_2^{[2]}(x_2) & \cdots & H_N^{[2]}(x_2) & 0 & 0 \\ \vdots & \vdots & \ddots & \vdots & \vdots & \vdots \\ H_1^{[2]}(x_N) & H_2^{[2]}(x_N) & \cdots & H_N^{[2]}(x_N) & 0 & 0 \end{pmatrix}, \quad (5.25)$$

$$\mathbf{H}^{[1]} = \begin{pmatrix} H_1^{[1]}(x_1) & H_2^{[1]}(x_1) & \cdots & H_N^{[1]}(x_1) & 1 & 0 \\ H_1^{[1]}(x_2) & H_2^{[1]}(x_2) & \cdots & H_N^{[1]}(x_2) & 1 & 0 \\ \vdots & \vdots & \ddots & \vdots & \vdots & \vdots \\ H_1^{[1]}(x_N) & H_2^{[1]}(x_N) & \cdots & H_N^{[1]}(x_N) & 1 & 0 \end{pmatrix}, \quad (5.26)$$

$$\mathbf{H}^{[0]} = \begin{pmatrix} H_1^{[0]}(x_1) & H_2^{[0]}(x_1) & \cdots & H_N^{[0]}(x_1) & x_1 & 1 \\ H_1^{[0]}(x_2) & H_2^{[0]}(x_2) & \cdots & H_N^{[0]}(x_2) & x_2 & 1 \\ \vdots & \vdots & \ddots & \vdots & \vdots & \vdots \\ H_1^{[0]}(x_N) & H_2^{[0]}(x_N) & \cdots & H_N^{[0]}(x_N) & x_N & 1 \end{pmatrix}, \quad (5.27)$$

and

$$\mathbf{w}(t) = [w_1(t), \dots, w_N(t), c_1(t), c_2(t)]^T. \quad (5.28)$$

From an engineering point of view, it would be more convenient to work in the physical space. Owing to the presence of integration constants, the process of converting the networks-weight space into the physical space can also be used to implement Neumann boundary conditions. With the boundary conditions (5.9) and (5.10), the conversion system can be written as

$$\begin{pmatrix} \mathbf{u}(t) \\ u'_N(t) \end{pmatrix} = \mathbf{C}\mathbf{w}(t), \quad (5.29)$$

where \mathbf{C} is the conversion matrix of dimension $(N+1) \times (N+2)$ that comprises the matrix $\mathbf{H}^{[0]}$ and the last row of $\mathbf{H}^{[1]}$. Solving (5.29) yields

$$\mathbf{w}(t) = \mathbf{C}^{-1} \begin{pmatrix} \mathbf{u}(t) \\ u'_N(t) \end{pmatrix}. \quad (5.30)$$

By substituting (5.30) into (5.19) and (5.20), the values of the second and first derivatives of u with respect to x are thus expressed in terms of nodal variable values and Neumann boundary values

$$\mathbf{u}''(t) = \mathbf{H}^{[2]}\mathbf{C}^{-1} \begin{pmatrix} \mathbf{u}(t) \\ u'_N(t) \end{pmatrix} = \mathbf{D}^{[2]} \begin{pmatrix} \mathbf{u}(t) \\ u'_N(t) \end{pmatrix}, \quad (5.31)$$

$$\mathbf{u}'(t) = \mathbf{H}^{[1]}\mathbf{C}^{-1} \begin{pmatrix} \mathbf{u}(t) \\ u'_N(t) \end{pmatrix} = \mathbf{D}^{[1]} \begin{pmatrix} \mathbf{u}(t) \\ u'_N(t) \end{pmatrix}. \quad (5.32)$$

Making use of (5.31) and (5.32), (5.8) can be transformed into the following discrete form

$$\frac{d\mathbf{u}(t)}{dt} = q_1\mathbf{u}''(t) + q_2\mathbf{u}'(t) + q_3\mathbf{u}(t) + \mathbf{q}_4, \quad (5.33)$$

or

$$\frac{d\mathbf{u}}{dt} = q_1\mathbf{D}^{[2]} \begin{pmatrix} \mathbf{u}(t) \\ u'_N(t) \end{pmatrix} + q_2\mathbf{D}^{[1]} \begin{pmatrix} \mathbf{u}(t) \\ u'_N(t) \end{pmatrix} + q_3\mathbf{u}(t) + \mathbf{q}_4, \quad (5.34)$$

where $\mathbf{q}_4 = [q_4, q_4, \dots, q_4]^T$ is an $N \times 1$ vector, and

$$\frac{d\mathbf{u}}{dt} = \left[\frac{du_1(t)}{dt}, \frac{du_2(t)}{dt}, \dots, \frac{du_N(t)}{dt} \right]^T. \quad (5.35)$$

Since the values of u_1 and u'_N are given, the unknown vector becomes

$$[u_2(t), u_3(t), \dots, u_N(t)]^T, \quad (5.36)$$

and hence, the first row in (5.34) will be removed from the solution procedure. The remainder of (5.34) can be integrated in time by using standard solvers such as the Runge-Kutta technique.

5.3.2 Regularization of IRBFNs and capturing of discontinuous strains

When the displacement field is C^0 continuous (e.g., across a bi-material interface or strain localization); it was found to be difficult to capture accurately the resultant discontinuous strains with conventional FEM. The latter can be improved with the introduction of enriched FEM (Patzák and Jirásek, 2003), however, mesh alignment sensitivity remains a drawback at least for quadrilaterals and embedded discontinuity methods (Li and Liu, 2000). On the other hand, several meshfree methods used special shape functions to account for the jump across a discontinuity (Krongauz and Belytschko, 1998; Kim et al., 2007a), which seem to work well if the location of discontinuities are known. It will be seen that the present IRBFN method can capture strain discontinuities without suffering any mesh-alignment sensitivities (IRBFN is a truly meshless method) and without having to know the location of discontinuities in advance. However, being a global and high order approximation, the RBFN still produce some oscillations around the discontinuity (Figure 5.3). In this study, we introduce a new approach where RBFNs can be further regularised to alleviate

oscillatory behaviours near such discontinuities.

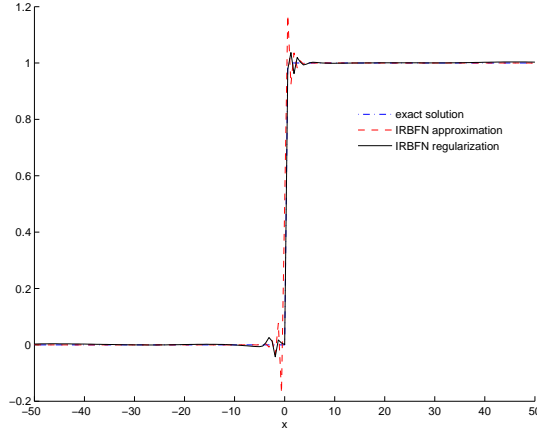


Figure 5.3: Regularization of IRBFNs.

With noisy data, the generalization performance of RBFNs can be improved using regularization techniques presented in Orr (1995b), which are adapted here for IRBFNs. Let $\{(\mathbf{x} = \{x_i\}_{i=1}^N, \hat{\mathbf{y}} = \{\hat{y}_i\}_{i=1}^N)\}$ denote the set of input and $f(\mathbf{x})$ the output in the present IRBFN method, the sum-squared-error is

$$S = \sum_{i=1}^N (\hat{y}_i - f(x_i))^2, \quad (5.37)$$

where N is the number of input data points, $f(x_i)$ is the approximate solution given by (5.14) (or (5.21) in matrix form). The output sensitivity to noisy inputs is minimised by augmenting the sum-squared-error with a smoothing term (Orr, 1995b) as follows.

$$C = \sum_{i=1}^N (\hat{y}_i - f(x_i))^2 + \lambda \sum_{j=1}^m w_j^2, \quad (5.38)$$

where C is a cost function, m is the number of RBF centers, w_j are the network weights, λ is a non-negative regularization parameter. An optimal weight vector \mathbf{w} can be found by minimizing C in (5.38) with respect to network weights $\{w_j\}_{j=1}^m$ as follows. Differentiating the cost function C with respect to the

network weights $\{w_j\}_{j=1}^N$ yields

$$\frac{\partial C}{\partial w_j} = -2 \sum_{i=1}^N (\hat{y}_i - f(x_i)) \frac{\partial f(x_i)}{\partial w_j} + 2\lambda \sum_{j=1}^m w_j. \quad (5.39)$$

From (5.14) or (5.21), $\frac{\partial f(x_i)}{\partial w_j}$ in (5.39) can be found simply as

$$\frac{\partial f(x_i)}{\partial w_j} = H_j^{[0]}(x_i), \quad (5.40)$$

or in compact form

$$\frac{\partial \mathbf{f}}{\partial w_j} = \mathbf{h}_j^{[0]}, \quad (5.41)$$

where

$$\mathbf{f} = [f(x_1), f(x_2), \dots, f(x_N)]^T, \quad (5.42)$$

and

$$\mathbf{h}_j^{[0]} = [H_j^{[0]}(x_1), H_j^{[0]}(x_2), \dots, H_j^{[0]}(x_N)]^T. \quad (5.43)$$

Note that vector $\mathbf{h}_j^{[0]}$ is the j -th column of the matrix $\mathbf{H}^{[0]}$ in (5.27). Substituting (5.41) into (5.39) and equating the results to zero lead to

$$\sum_{i=1}^N f(x_i) H_j^{[0]}(x_i) + \lambda w_j = \sum_{i=1}^N y_i H_j^{[0]}(x_i). \quad (5.44)$$

There are m such equations corresponding to m radial basis functions, $1 \leq j \leq m$, each represents one constraint on the solution. The resultant system of linear equations like (5.44) can be rewritten in matrix form,

$$(\mathbf{H}^{[0]})^T \mathbf{f} + \lambda \mathbf{I}_{m+2} \mathbf{w} = (\mathbf{H}^{[0]})^T \hat{\mathbf{y}}, \quad (5.45)$$

in which \mathbf{I}_{m+2} is an identity matrix of size $(m+2) \times (m+2)$. Solving (5.45) leads to the vector of optimal weights

$$\mathbf{w} = \mathbf{A}^{-1} (\mathbf{H}^{[0]})^T \hat{\mathbf{y}}, \quad (5.46)$$

where

$$\mathbf{A} = (\mathbf{H}^{[0]})^T \mathbf{H}^{[0]} + \lambda \mathbf{I}_{m+2}. \quad (5.47)$$

Since the performance of the IRBFN regularization completely depends on the regularization parameter λ , an optimal λ must be identified to minimise the error. A number of methods predicting an optimal value of λ automatically have been developed (Orr, 1995a,b, 1996) including the re-estimation method using different error prediction criteria, (e.g. cross-validation, generalized cross-validation, Bayesian information criterion, final prediction error, unbiased estimate of variance). In the present work, the generalized cross-validation (GCV) error prediction criterion is employed as follows.

$$\hat{\sigma}^2 = \frac{N \hat{\mathbf{y}}^T \mathbf{P}^2 \hat{\mathbf{y}}}{[\text{trace}(\mathbf{P})]^2}, \quad (5.48)$$

where $\hat{\sigma}^2$ is the variance estimate, N is the number of input data points, \mathbf{P} is the projection matrix, which is defined by

$$\hat{\mathbf{y}} - \mathbf{f} = \hat{\mathbf{y}} - \mathbf{H}^{[0]} \mathbf{A}^{-1} (\mathbf{H}^{[0]})^T \hat{\mathbf{y}} = \mathbf{P} \hat{\mathbf{y}}, \quad (5.49)$$

in which $\mathbf{P} = \mathbf{I}_N - \mathbf{H}^{[0]} \mathbf{A}^{-1} (\mathbf{H}^{[0]})^T$, \mathbf{I}_N is an identity matrix of size $N \times N$. Thus \mathbf{P} relates to the sum-square-error S by

$$S = \hat{\mathbf{y}}^T \mathbf{P}^2 \hat{\mathbf{y}}, \quad (5.50)$$

and the cost function C by

$$C = \hat{\mathbf{y}}^T \mathbf{P} \hat{\mathbf{y}}. \quad (5.51)$$

Since all the above error prediction criteria relate nonlinearly to λ , a method of nonlinear optimization is required for the estimation of λ . Any standard technique of nonlinear optimization such as the Newton method can be used in this circumstance. Alternately, the optimal value of λ can automatically be

determined by a simple iterative procedure (Orr, 1996) as follows.

By differentiating the GCV error prediction and setting the results to zero, a nonlinear equation of λ can be obtained. After some mathematical manipulations, λ can be found iteratively as

$$\lambda = \frac{\hat{\mathbf{y}}^T \mathbf{P}^2 \hat{\mathbf{y}}}{\mathbf{w}^T \mathbf{A}^{-1} \mathbf{w}} \frac{\text{trace}(\mathbf{A}^{-1} - \lambda \mathbf{A}^{-2})}{\text{trace}(\mathbf{P})}, \quad (5.52)$$

where the right hand side contains λ (explicitly as well as implicitly through \mathbf{A}^{-1} and \mathbf{P}). The iterative procedure is started with an initial value of λ for the computation of the right hand side, which is a new estimate of λ , and the process is repeated until convergence.

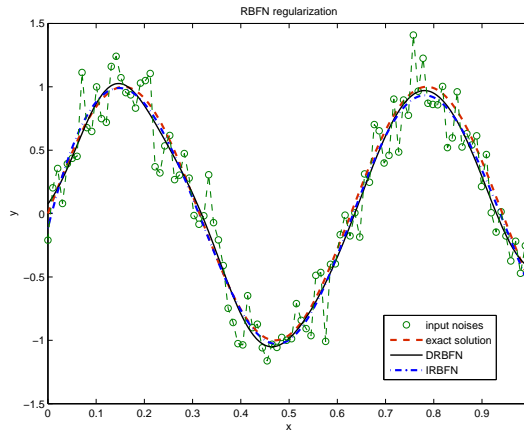


Figure 5.4: Noisy input, exact solution, DRBFN regularization and IRBFN regularization.

The above regularization method is illustrated with a much improved result as shown in Figure 5.3, and further demonstration of the method is given in the following example. Figure 5.4 shows the results using 100 noisy input data points and 300 output (test) values obtained by IRBFN and DRBFN regularization methods. The input data are based on $y = \sin(10x)$, for $0 \leq x \leq 1$, with additional Gaussian noise of standard deviation $\sigma = 0.20$ (the curve with circular marker in Figure 5.4). The target (exact) function $y = \sin(10x)$ is depicted by the dash curve. As shown in Figure 5.4, the IRBFN regularization method

provides a better result (the dot-dash curve) with the mean square error (e_M) of 0.0022 compared with 0.0033 of the DRBFN method (the continuous curve), where e_M is defined as

$$e_M = \frac{\sum_{i=1}^N (f(x_i) - y_i)^2}{N}, \quad (5.53)$$

in which N is the number of test nodes ($N = 300$), $f(x_i)$ the output value and y_i the exact value of the target function. This results is also in good agreement with those of Mai-Duy (2005), which showed that the IRBFN method obtained by integration process leads to a better approximation than the DRBFN method by differential process.

5.4 Numerical examples

For all computations presented in this section, the common dimensionless parameters are chosen as

$$\begin{aligned} L = 50, \quad \gamma^2 = \left(\frac{ET^2}{\rho a^2} \right) = 1, \quad \varepsilon_p = 1, \\ f_y = 1, \quad \left(\frac{\bar{E}_t}{E} \right) = -0.70, \quad \varepsilon_f = 2.4286, \quad \left(\frac{\bar{E}_f}{E} \right) = 10^{-6}. \end{aligned}$$

Those parameters that are specific to each example are described later where appropriate.

5.4.1 Wave propagation in fully elastic bars

A uniform bar is loaded by an extensional velocity c of the two ends as shown in Figure 5.1. Longitudinal elastic wave propagation precedes strain localisation and is considered in this example. Moreover, if c satisfies the condition $c \leq \varepsilon_p/2$, the behaviour of the bar is purely elastic over the whole computational

domain (Bazant and Belytschko, 1985). The differential equation of motion (5.7) reduces to (in dimensionless form)

$$\frac{\partial^2 u(x, t)}{\partial t^2} = \gamma^2 \frac{\partial^2 u(x, t)}{\partial x^2}, \quad (5.54)$$

which is hyperbolic. The exact solution of (5.54) for the given boundary conditions (5.4) and the initial solutions (5.5) can be found in Bazant and Belytschko (1985) and presented for the displacement u and strain ε as follows.

$$u = -c \langle \gamma t - (x + L) \rangle + c \langle \gamma t + (x - L) \rangle, \quad 0 \leq t \leq \left(\frac{1}{\gamma}\right) 2L, \quad (5.55)$$

where the symbol $\langle \rangle$ is defined by

$$\langle A \rangle = \begin{cases} A, & \text{if } A \geq 0, \\ 0, & \text{if } A < 0, \end{cases} \quad (5.56)$$

and

$$\varepsilon = \frac{\partial u}{\partial x} = c [H(\gamma t - (x + L))] + c [H(\gamma t + (x - L))], \quad (5.57)$$

in which H denotes the Heaviside step function, defined by

$$H(x) = \begin{cases} 1, & \text{if } x \geq 0, \\ 0, & \text{if } x < 0. \end{cases} \quad (5.58)$$

The governing equation (5.54) involves second-order derivatives of both space and time, and it is convenient to decouple it into a system of first-order equations in both space and time by introducing new variables r and s as follows. Let

$$r = \gamma \frac{\partial u}{\partial x}, \quad s = \frac{\partial u}{\partial t}, \quad (5.59)$$

and (5.54) is thus equivalent to the system of equations

$$\frac{\partial r}{\partial t} = \gamma \frac{\partial s}{\partial x}, \quad (5.60)$$

$$\frac{\partial s}{\partial t} = \gamma \frac{\partial r}{\partial x}, \quad (5.61)$$

subject to the corresponding boundary conditions

$$s(-L, t) = -c, \quad s(L, t) = c, \quad \forall t \in \left[0, \left(\frac{1}{\gamma}\right) 2L\right], \quad (5.62)$$

and the initial solutions

$$r(x, 0) = 0, \quad s(x, 0) = 0, \quad \forall x \in [-L, L]. \quad (5.63)$$

To reduce the computational cost, a half model is analyzed in this section. The equivalent boundary conditions of the half model are

$$s(-L, t) = -c, \quad s(0, t) = 0, \quad \forall t \in \left[0, \left(\frac{1}{\gamma}\right) 2L\right], \quad (5.64)$$

The numerical formulation presented in section 5.3 is used for solving the system of equations (5.60) and (5.61) with the boundary conditions (5.64) and the initial solutions (5.63), with $c = 0.45\varepsilon_p$. The forward Euler formula is used to perform time integration. To satisfy the CFL condition ($\Delta t \leq \frac{1}{\gamma}\Delta x$), the time step is chosen as $\Delta t = 10^{-2}\frac{1}{\gamma}\Delta x$ in this example. The results presented in this example are achieved with 80 uniform collocation points and $\beta = 1$ in (5.16). Computations are also carried out with 20, 40, 60 and 100 uniformly distributed collocation points. The obtained solution essentially converges when 40 or more collocation points are used. Figure 5.5, Figure 5.6 and Figure 5.7 show the evolution of the displacement and strain, the numerical results and the exact solutions are plotted on the same graphs. First, the displacement and strain waves propagate from the ends to the center of the bar until these

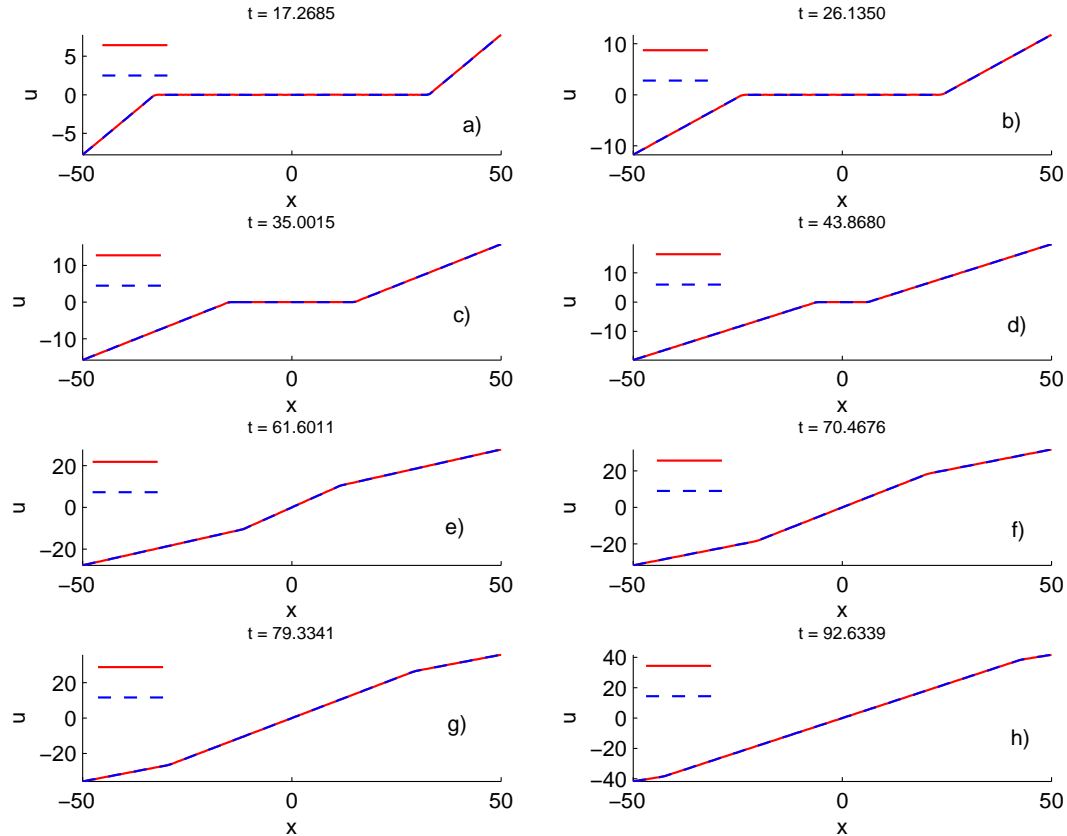


Figure 5.5: Fully elastic bars: the evolution of displacement, the continuous curves denote the IRBFN solutions and the dash ones the exact solution.

incident waves meet each other at the center at time $t = \left(\frac{1}{\gamma}\right) L$. The zero-th order continuous displacement leads to the strain discontinuity whose position evolves with time as shown in the above figures. As a result of the collision of the two incident waves (at $x = 0$), an abrupt jump of value of strain appears at $x = 0$ (Figure 5.8), the strain magnitude is doubled, and the reflection waves propagate outwards to the ends as displayed in Figures 5.5(e)-(f)-(g)-(h), Figure 5.7 and Figure 5.8. The obtained results by the present IRBFN method are in good agreement with the analytical solutions as shown in Figure 5.5-Figure 5.8.

It is shown that the IRBFN can capture the discontinuous strain in this example, however, there are some oscillations due to the violation of the smoothness assumption inherent in the RBFN approximation. This situation can be improved with regularisation as discussed in section 5.3.2. When the regularisation

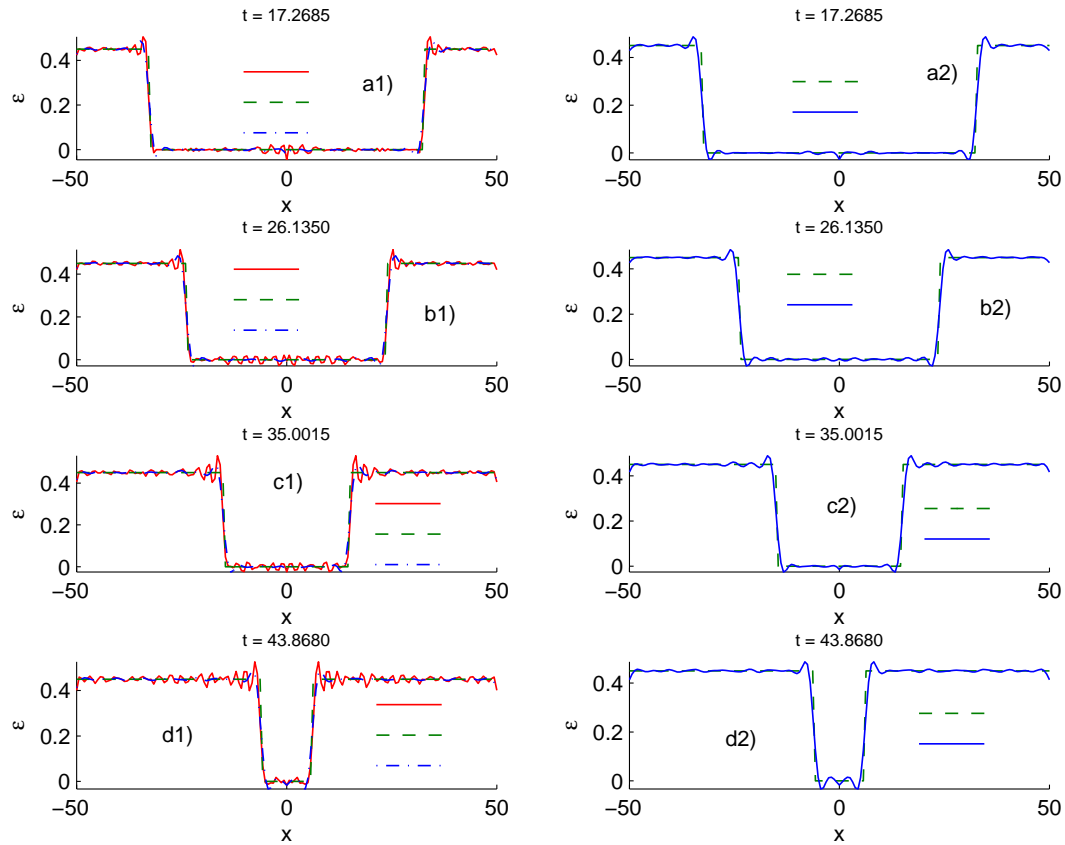


Figure 5.6: Fully elastic bars: the propagation of step function waves of strain: the continuous curves denote the IRBFN solutions, the dashed ones exact solutions and the dot-dashed curves indicate the IRBFN regularized results on the left column. On the right column, the non-regularized results are removed for clarity.

parameter λ is set to be equal to 0.07135, it can be seen that the obtained strains shown on the right columns in Figure 5.6 and Figure 5.7 are much smoother and closer to the exact solutions than those by the standard IRBFN method shown on the left columns of the same figures. Thus, good results are achieved with a general global regularisation of the IRBFNs in contrast with other numerical approaches (discussed in section 5.3.2) where special treatments must be applied at the elemental level (extended FEM) or special shape functions must be used. Moreover, these special treatments require a priori knowledge of the location of discontinuities while the present IRBFN method does not.

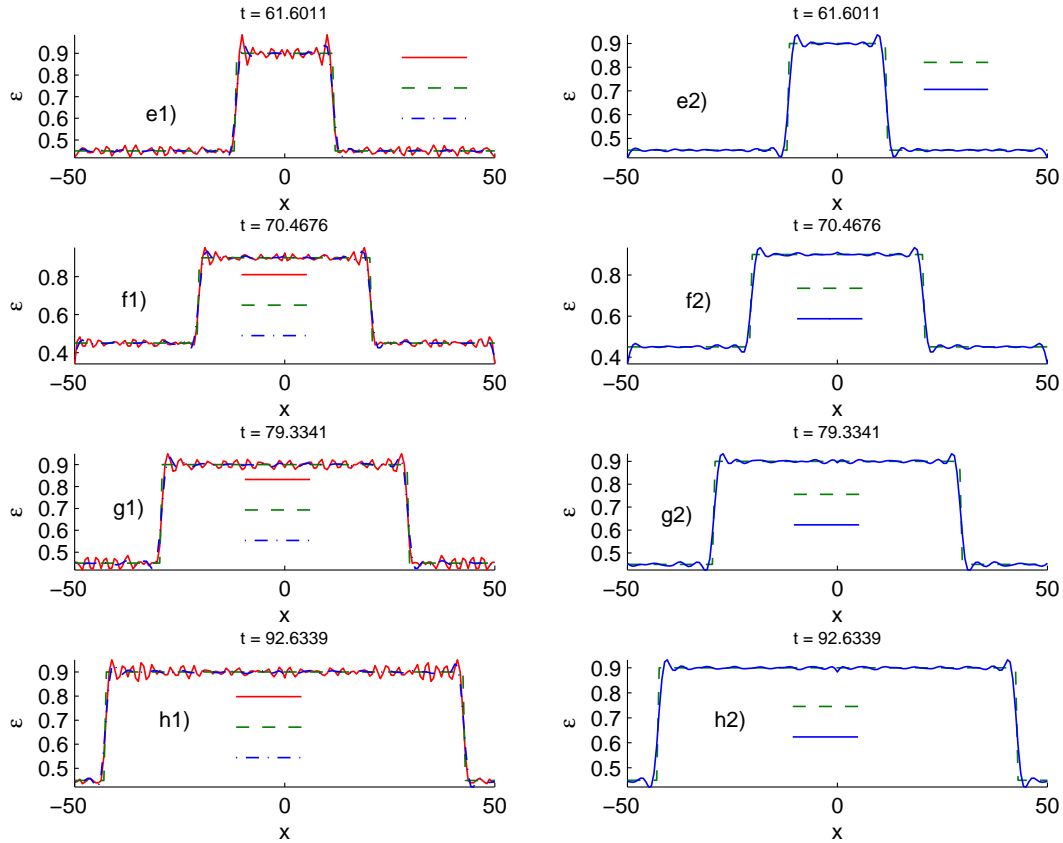


Figure 5.7: Fully elastic bars: the propagation of step function waves of strain: the continuous curves denote the IRBFN solutions, the dashed ones exact solutions and the dot-dashed curves indicate the IRBFN regularized results on the left column. On the right column, the non-regularized results are removed for clarity.

5.4.2 Wave propagation and strain localization in strain-softening bars: local continuum model

In this example, the problem defined in section 6.2 is considered with the prescribed velocities at the ends have $c = 0.85\epsilon_p$, which is above the critical value of $0.5\epsilon_p$. The behaviour of the bar is elastic until the incident waves meet at the center of the bar (i.e. for $0 \leq t \leq L$) as discussed in section 5.4.1. Right after the collision of the incident waves, the strain is doubled to $2c = 1.7\epsilon_p$, causing strain softening and strain localization. From the onset of localization, the computational domain can be divided into two regions with different be-

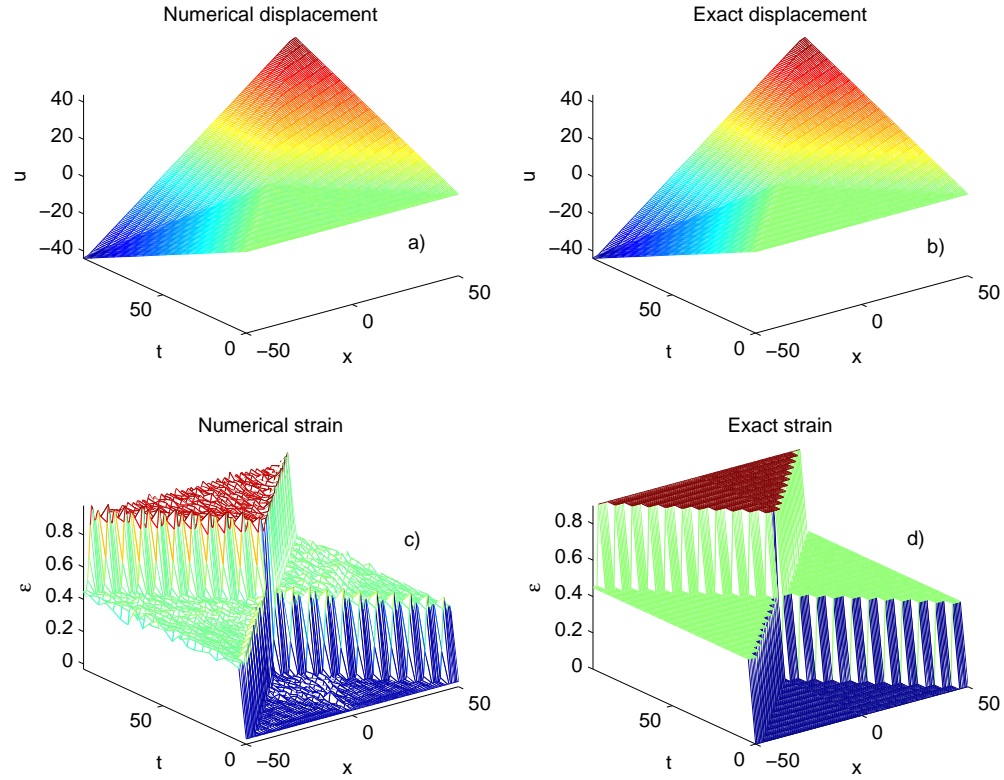


Figure 5.8: Fully elastic bars: the displacement and strain waves propagations.

haviours: the strain softening and localization zone, and the elastic zone. For the elastic domain, the momentum equation (5.7) takes the hyperbolic form of (5.54) which is solved in the same manner as presented in section 5.4.1. For the localized zone, the momentum equation becomes elliptic and is solved by a scheme described as follows.

The elliptic momentum equation of the localized zone is

$$\frac{\partial^2 u(x, t)}{\partial t^2} = -\mu^2 \frac{\partial^2 u(x, t)}{\partial x^2}, \quad (5.65)$$

in which $\mu^2 = \frac{|E_t| ET^2}{E \rho a^2}$, and $|E_t|$ is the absolute value of E_t . (5.65) can be decoupled into a system of first-order equations in both time and space by letting

$$r = -\mu \frac{\partial u}{\partial x}, \quad s = \frac{\partial u}{\partial t}, \quad (5.66)$$

resulting in a system of equations in r and s for the strain-softening zone given by

$$\frac{\partial r}{\partial t} = -\mu \frac{\partial s}{\partial x}, \quad (5.67)$$

$$\frac{\partial s}{\partial t} = \mu \frac{\partial r}{\partial x}. \quad (5.68)$$

At the end of the softening process, fracture and rupture will probably occur, however, a fracture criterion is not included in present study, so the material is assumed to be elastic again with a very small elastic modulus $E_f/E = 10^{-6}$. The governing equations in this stage are the same as those in section 5.4.1, except that the modulus E is replaced by E_f . As before, only a half model needs be discretised (in this case with 80 uniformly distributed nodes). The resultant system of equations is integrated in time by using the forward Euler formula as in section 5.4.1, where the time step is taken as $\Delta t = 0.25 \times 10^{-4} \frac{\Delta x}{\gamma}$ in this example. The solution of (5.67) and (5.68) clearly shows the onset of strain localization, characterized by the sudden jump in velocity, displacement, strain and the rapid descent of stress in the localized zone as exhibited in Figure 5.9 which depicts the evolution of velocity, displacement, strain and stress at the collocation point $x = -0.6329$, which is the nearest point to the $x = 0$ node. In Figure 5.9(d), the stress profile is slightly oscillatory until the loading waves are about to meet. Upon the collision of the incident waves, the stress increases rapidly to the elastic limit f_y then decreases as rapidly down to zero again due to strain-softening. The speedy drop of the stress level is accompanied by the abrupt jump in velocity and rapid increase in displacement and strain as exhibited in Figure 5.9(c)-(a)-(b), respectively. Unstable development follows as the localized zone is unable to carry load while the velocity is increasing, the displacement and strain are growing rapidly, two halves of the bar are moving increasingly in two opposite directions like in mode I crack as shown in Figure 5.10. In the next stage of evolution, the velocity and stress increase very slightly while the displacement and strain are growing continuously and quickly because of elastic loading as can be seen in Figure 5.9. The steep profiles of stress, velocity and strain are well captured by the present explicit method,

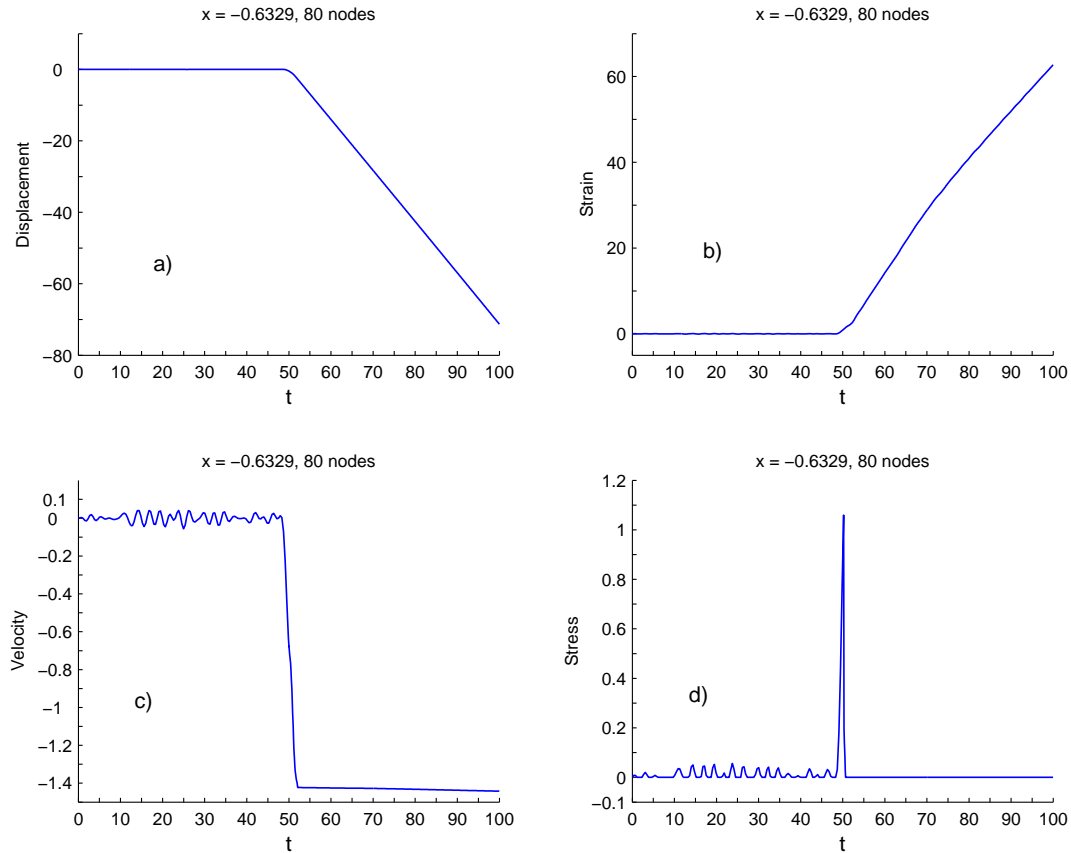


Figure 5.9: Local continuum model: the evolution of: (a) displacement, (b) strain, (c) velocity and (d) stress at $x = -0.6329$ with 80 uniform collocation points.

although with smaller time steps in comparison with other implicit methods. Figure 5.10-Figure 5.12 depict the spatio-temporal evolution of the displacement, velocity and strain, respectively, while Figure 5.13-Figure 5.15 show the spatial distribution of velocity, stress, displacement and strain, respectively, at several time instants. The solutions of the elliptic equations yield a standing wave, which is not able to extend outside the localised zone, as illustrated by the strain wave displayed in Figure 5.12 and Figure 5.15, and the displacement wave in Figure 5.10 and Figure 5.14 as well. When softening occurs, which is the case here, the localised strain softening zone causes reflection waves travelling backwards from the localised front ($x = 0$), due to sudden unloading.

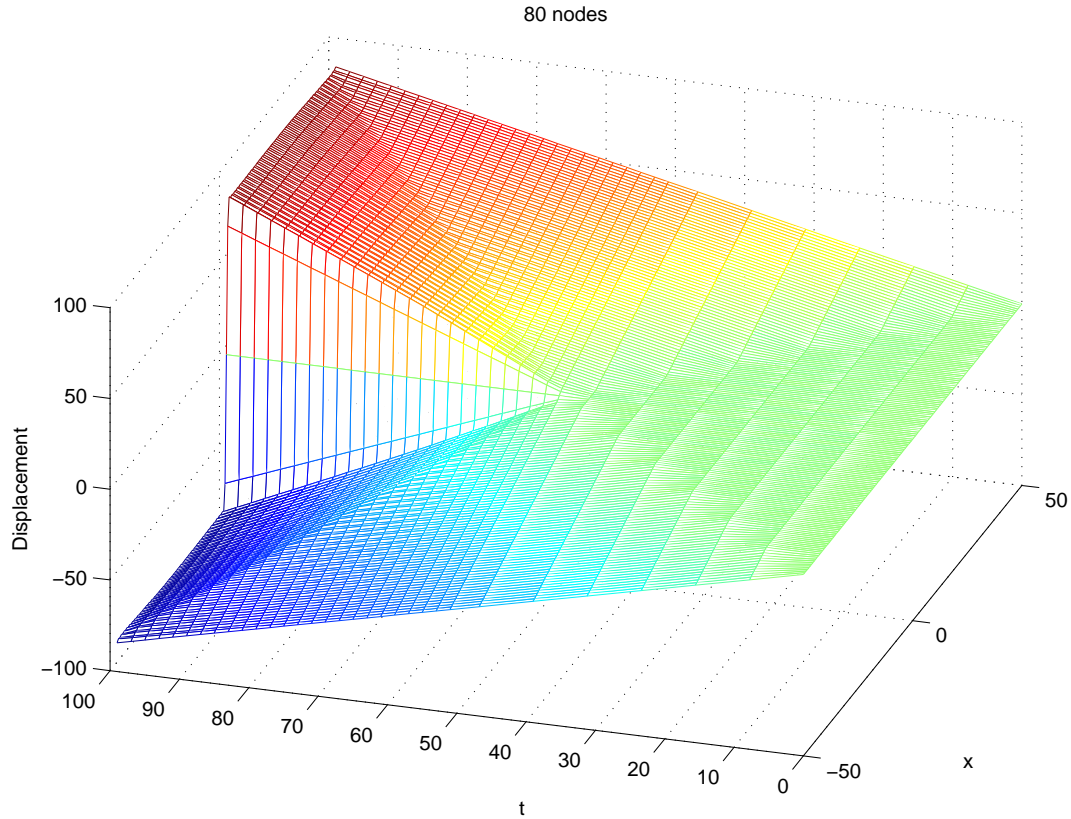


Figure 5.10: Local continuum model: the evolution of displacement with a uniform discretisation of 80 points.

Figure 5.10 and Figure 5.14 expose the development of displacement which grows rapidly as a standing wave confined in a very narrow zone. Correspondingly, the increasingly intensive strain within the localized zone is depicted in Figure 5.12 and Figure 5.15. The velocity is doubled at the onset of localisation and reflected back from the localised zone as shown in Figure 5.11 and Figure 5.13(a). Similarly, displacement, strain and stress waves also reflected from the localised zone. However, unlike the response in purely elastic bars, the reflected strain wave is out of phase with, and therefore cancelling out the incident strain wave of the same magnitude. Due to the nature of the displacement waves the displacement field in the elastic region is C^0 continuous (Figure 5.10 and Figure 5.14). The point of C^0 continuous displacement propagates along the elastic region in both directions depending on the stage of loading. Consequently, a discontinuity occurs in the profile of stress, velocity (Figure 5.13), and strain

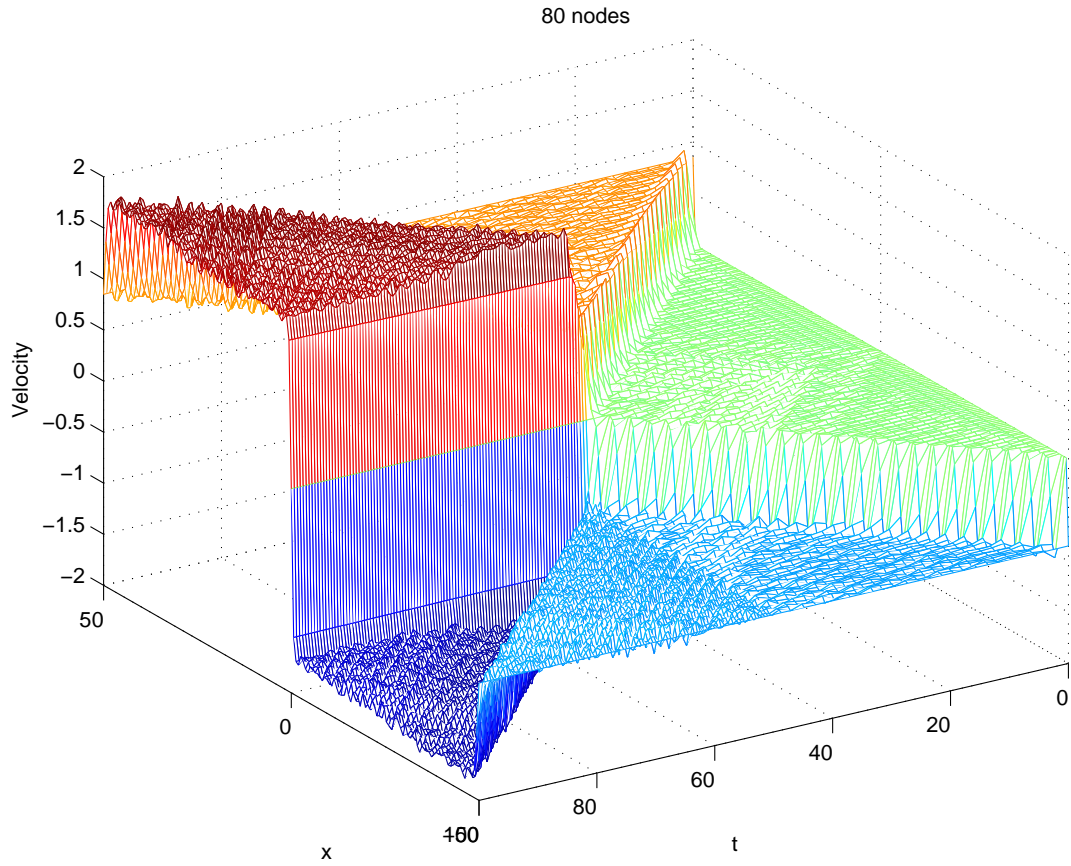


Figure 5.11: Local continuum model: the evolution of velocity with a uniform discretisation of 80 points.

(Figure 5.15). The oscillatory behaviour of the stress is observed in Figure 5.13(b) which was also found in Sluys (1992) and Bazant et al. (1984).

Although the results presented above correspond to an 80 point discretisation, computation is also carried out for 20, 40, 60, 100, 120 point discretisations. As the number of collocation points increases, the bandwidth of the localised zone decreases and the maximum strain increases as shown in Figure 5.14 and Figure 5.15, which is a trend predicted by the exact solution (Bazant and Belytschko, 1985). However, the zero bandwidth and singular strain associated with the exact model solution cannot be expected to be captured by a numerical method. The obtained results in this section compare favourably with those of the FEM (Sluys, 1992; Bazant et al., 1984). It is worth noting that, unlike the

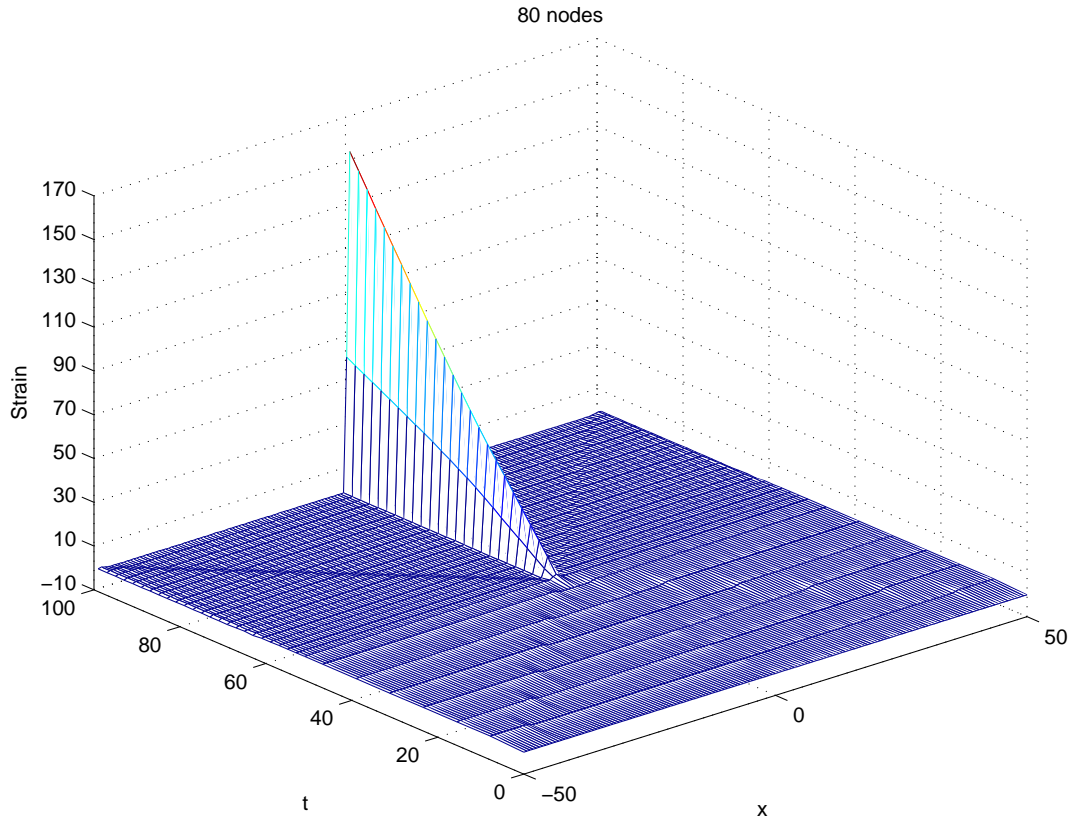


Figure 5.12: Local continuum model: the evolution of strain with a uniform discretisation of 80 points.

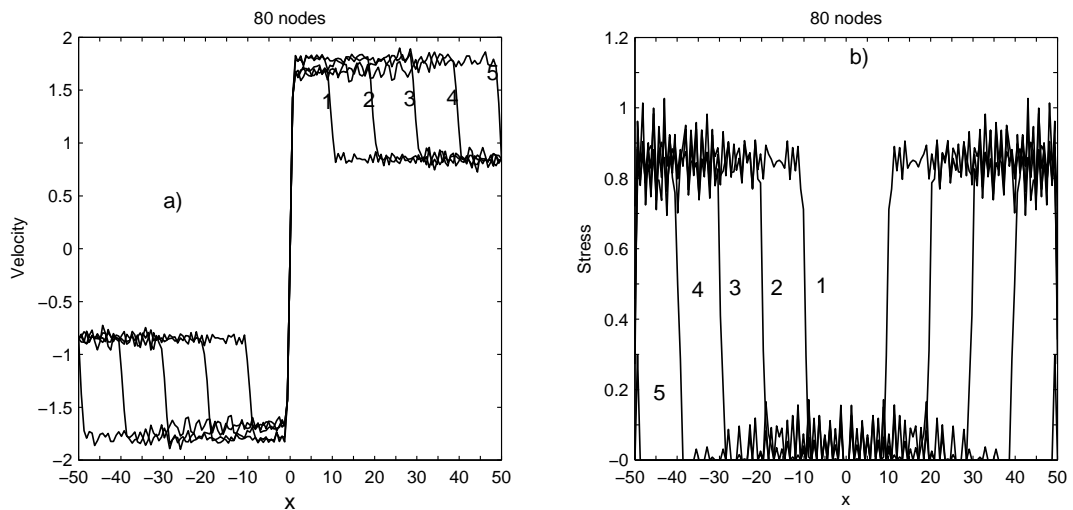


Figure 5.13: Local continuum model: the curve labels represent time levels: 1($t = 60.0$) ; 2($t = 70.0$) ; 3($t = 80.0$) ; 4($t = 90.0$) ; 5($t = 100.0$) (a) the evolution of velocity, (b) stress obtained with a uniform discretisation of 80 points.

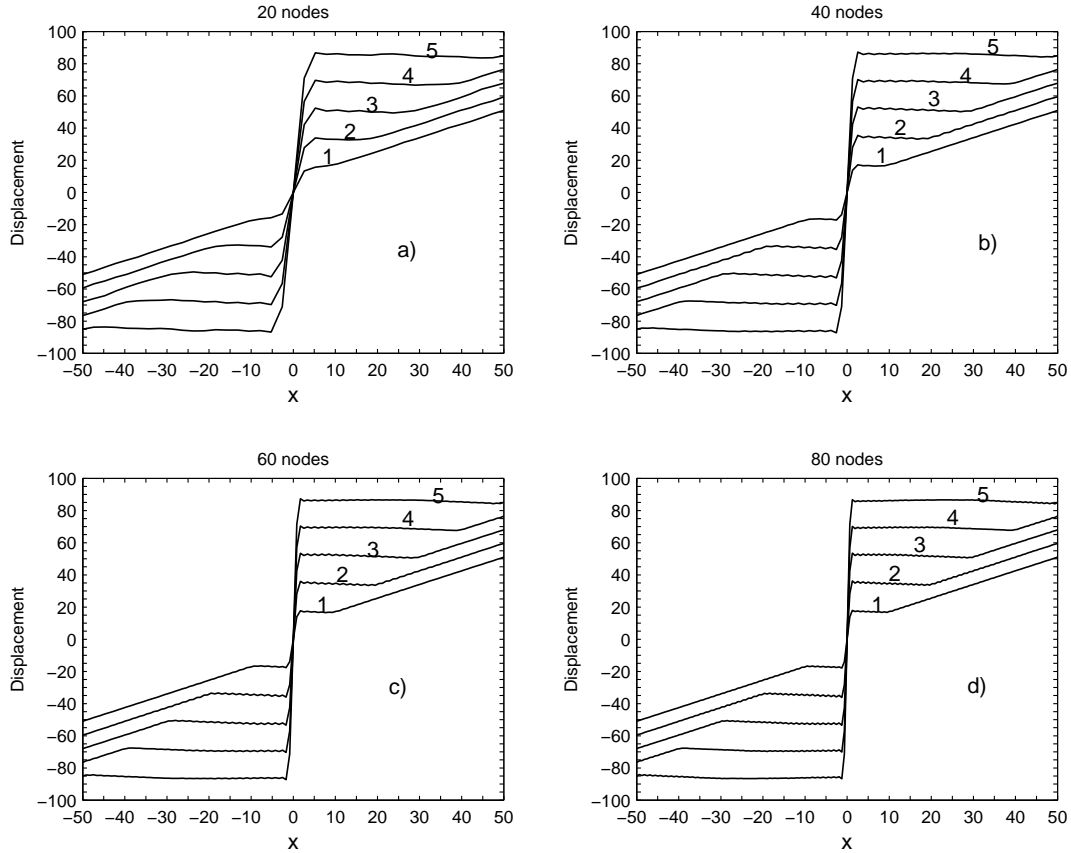


Figure 5.14: Local continuum model: the evolution of displacement at time levels: 1($t = 60.0$) ; 2($t = 70.0$) ; 3($t = 80.0$) ; 4($t = 90.0$) ; 5($t = 100.0$) (the curve labels indicate time levels) (a) 20 points, (b) 40 points, (c) 60 points and (d) 80 points (uniformly discretised).

FEM, the present method does not require a priori knowledge of the location of discontinuities which are well captured by a uniform discretisation.

5.4.3 Wave propagation and strain localization in strain-softening bars: non-local continuum model

In this example, the material is described by a non-local continuum model based on strain averaging or non-local strain. In this model, the local equivalent strain ε is replaced by its non-local counterpart obtained by a weighted average process over a spatial neighbourhood of each point of interest. The non-local strain $\bar{\varepsilon}$

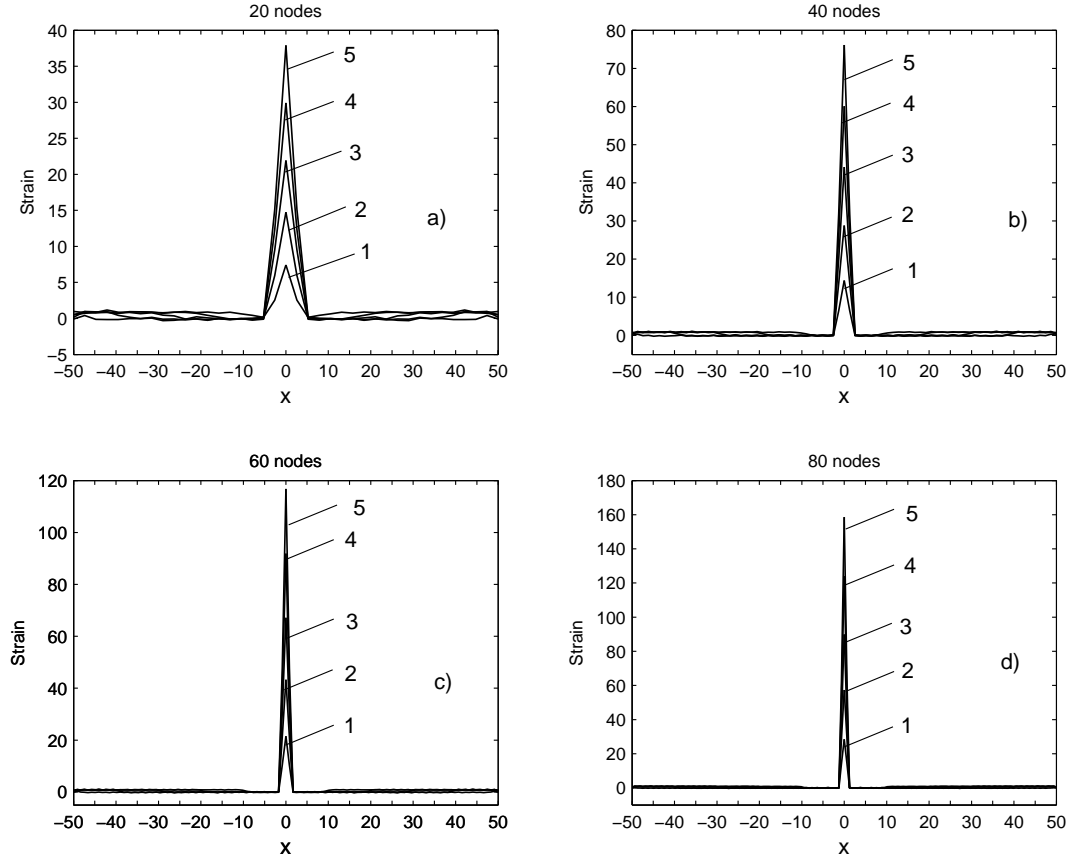


Figure 5.15: Local continuum model: the evolution of strain at time levels: 1($t = 60.0$) ; 2($t = 70.0$) ; 3($t = 80.0$) ; 4($t = 90.0$) ; 5($t = 100.0$) (a) 20 points, (b) 40 points, (c) 60 points and (d) 80 points (uniformly discretised).

is defined by

$$\bar{\varepsilon}(x, t) = \int_V \alpha(x, \xi) \varepsilon(\xi, t) d\xi, \quad (5.69)$$

where $\alpha(x, \xi)$ is a given non-local function. In an infinite body, the weight function is assumed to depend only on the distance $r = \|x - \xi\|$ between the “source” point ξ and the “receive” point x . In the vicinity of a boundary, the weight function is usually rescaled such that the non-local operator does not change the uniform field, this means that the weight function satisfies the normalizing condition

$$\int_V \alpha(x, \xi) d\xi = 1, \quad \forall x \in V. \quad (5.70)$$

This can be achieved by setting

$$\alpha(x, \xi) = \frac{\alpha_0(\|x - \xi\|)}{\int_V \alpha_0(\|x - \zeta\|) d\zeta}, \quad (5.71)$$

where $\alpha_0(r)$ is an even and non-negative function of the distance $r = \|x - \xi\|$, monotonically decreasing for $r \geq 0$. It is often taken as the piecewise polynomial bell-shaped function

$$\alpha_0(r) = \begin{cases} \left[1 - \frac{r^2}{R^2}\right]^2, & \text{if } 0 \leq r \leq R, \\ 0, & \text{if } r > R, \end{cases} \quad (5.72)$$

where R is a parameter related to the internal length of the material. Since R corresponds to the maximum distance of point ξ that affects the non-local average at point x , it is called the *interaction radius* (Patzák and Jirásek, 2003).

The stress-strain relation in (5.2) becomes (in dimensionless form)

$$\bar{\sigma}(x, t) = \frac{\bar{E}}{E} \bar{\varepsilon}(x, t), \quad (5.73)$$

where $\bar{\varepsilon}$ is the non-local strain. Thus the stress in (5.73) is also non-local. In order to evaluate $\bar{\varepsilon}$, it is necessary to compute $\varepsilon(\xi, t)$ in (5.69), which is accomplished as follows. After an IRBFN discretisation, the vectors of unknown nodal displacements and their corresponding first and second derivatives with respect to x are given by (5.21), (5.32) and (5.31), respectively. Thus, the first order derivative of the displacement with respect to x at an arbitrary point ξ can be written as follows.

$$\frac{\partial u(\xi, t)}{\partial x} = \varepsilon(\xi, t) = H^{[1]}(\xi) \mathbf{C}^{-1} \mathbf{u}(t) = D^{[1]}(\xi) \mathbf{u}(t), \quad (5.74)$$

where \mathbf{C}^{-1} and $\mathbf{u}(t)$ are given by (5.30) and (5.21), respectively. $H^{[1]}(\xi)$ and $D^{[1]}(\xi)$ are obtained in the same manner that leads to $\mathbf{H}^{[1]}$ and $\mathbf{D}^{[1]}$ in (5.32),

but with $x = \xi$. Substitution of (5.74) into (5.69) leads to

$$\bar{\varepsilon}(x, t) = \int_{-R}^R \alpha(x, \xi) D^{[1]}(\xi) \mathbf{u}(t) d\xi. \quad (5.75)$$

Since the nodal variable vector $\mathbf{u}(t)$ is independent of the spatial variable, (5.75) can be rewritten as

$$\bar{\varepsilon}(x, t) = \int_{-R}^R \alpha(x, \xi) D^{[1]}(\xi) d\xi \mathbf{u}(t) = B(x) \mathbf{u}(t), \quad (5.76)$$

where

$$B(x) = \int_{-R}^R \alpha(x, \xi) D^{[1]}(\xi) d\xi. \quad (5.77)$$

The momentum equation (5.7) becomes

$$\frac{\partial^2 u(x, t)}{\partial t^2} = \left(\frac{\bar{E}}{E} \right) \left(\frac{ET^2}{\rho a^2} \right) \frac{\partial \bar{\sigma}(x, t)}{\partial x}, \quad (5.78)$$

which, in the elastic case, reduces to

$$\frac{\partial^2 u(x, t)}{\partial t^2} = \gamma^2 \frac{\partial \bar{\varepsilon}(x, t)}{\partial x}. \quad (5.79)$$

Since the stress and strain are non-local, a new system of governing equations is derived by decoupling the momentum equation (5.79) as follows. Let

$$r = \gamma \bar{\varepsilon}(x) = \gamma B(x) \mathbf{u}(t), \quad s = \frac{\partial u}{\partial t}. \quad (5.80)$$

After discretisation, the unknown nodal vectors for r and s are, respectively,

$$\mathbf{r}(t) = [r_1(t), r_2(t), \dots, r_N(t)]^T, \quad (5.81)$$

and

$$\mathbf{s}(t) = [s_1(t), s_2(t), \dots, s_N(t)]^T, \quad (5.82)$$

where N is the number of collocation points.

From (5.80) and (5.82), we have

$$\frac{\partial \mathbf{u}(t)}{\partial t} = \mathbf{s}(t). \quad (5.83)$$

From (5.79), (5.80) and (5.83), the following system of governing equations, which is equivalent to (5.79) (i.e. the elastic case), is obtained

$$\frac{\partial \mathbf{r}(t)}{\partial t} = \gamma \mathbf{B} \mathbf{s}(t), \quad (5.84)$$

$$\frac{\partial \mathbf{s}(t)}{\partial t} = \gamma \frac{\partial \mathbf{r}}{\partial x}, \quad (5.85)$$

where

$$\mathbf{B} = [B(x_1), B(x_2), \dots, B(x_N)]^T, \quad (5.86)$$

with $B(x_i) = \int_{-R}^R \alpha(x_i, \xi) D^{[1]}(\xi) d\xi$, for $i = 1, \bar{N}$

and $\frac{\partial \mathbf{r}}{\partial x}$ is obtained by an IRBFN approximation as

$$\frac{\partial \mathbf{r}(t)}{\partial x} = \mathbf{D}^{[1]} \mathbf{r}(t). \quad (5.87)$$

For the softening response, the corresponding system of governing equations is

$$\frac{\partial \mathbf{r}(t)}{\partial t} = -\mu \mathbf{B} \mathbf{s}(t), \quad (5.88)$$

$$\frac{\partial \mathbf{s}(t)}{\partial t} = \mu \frac{\partial \mathbf{r}}{\partial x}. \quad (5.89)$$

The boundary and initial conditions for r and s are the same as those given in section 5.4.2. As can be seen in the previous two examples, the ramp-like spatial displacement profile results in a discontinuous strain field which can be well captured by the present IRBFN method. However, when a non-local continuum model is used here, the smoothness of the equivalent non-local strain is adversely affected by noises that might exist in the neighbouring strain field. Thus it is found to be advantageous to incorporate IRBFN regularisation into

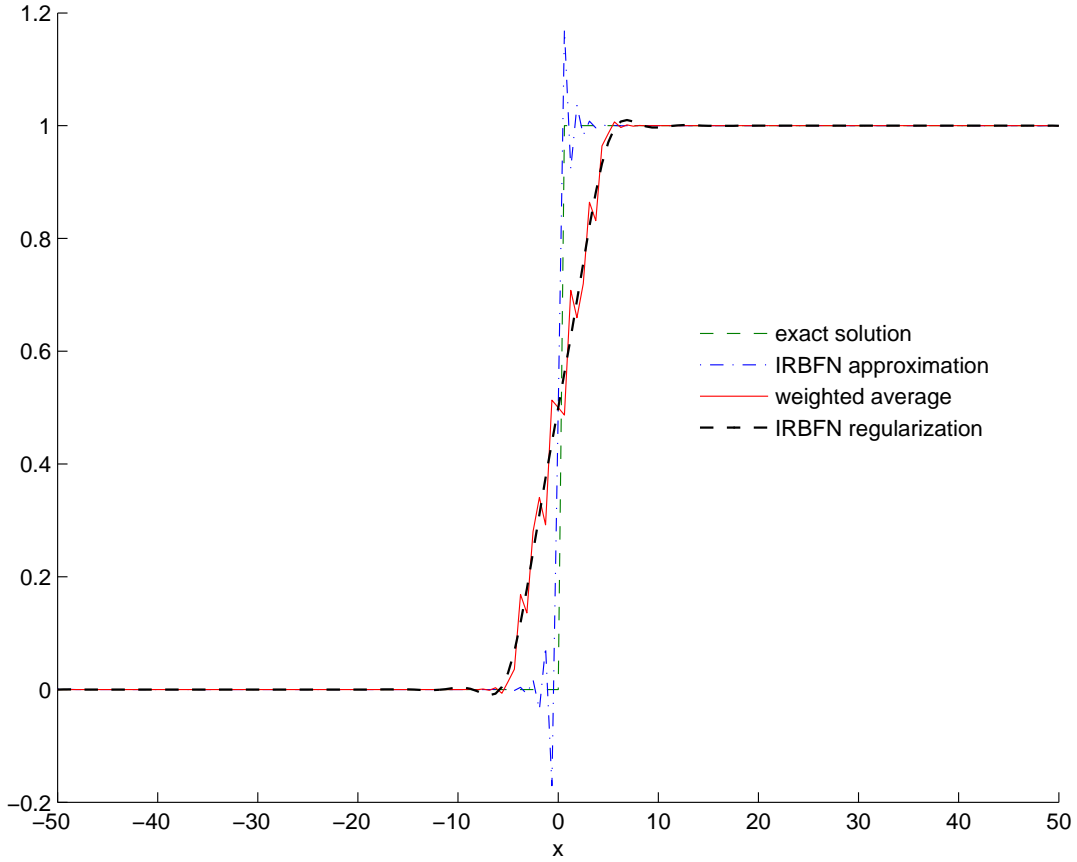


Figure 5.16: Example of IRBFN regularization.

the general IRBFN formulation. The effect of such regularisation is illustrated by considering a ramp function given by

$$\hat{u}(x) = xH(x), \quad \text{for } -50 \leq x \leq 50, \quad (5.90)$$

where H is the Heaviside function defined in (5.58). The exact solution of the first order derivative of $\hat{u}(x)$ with respect to x is

$$\hat{\varepsilon}(x) = \frac{\partial \hat{u}(x)}{\partial x} = H(x). \quad (5.91)$$

Let $\tilde{\varepsilon}(x)$ denote the IRBFN approximation of $\frac{\partial \hat{u}(x)}{\partial x}$, which is determined by

$$\tilde{\varepsilon}(x) \approx \frac{\partial \hat{u}(x)}{\partial x} = D^{[1]}(x)\hat{u}(x), \quad (5.92)$$

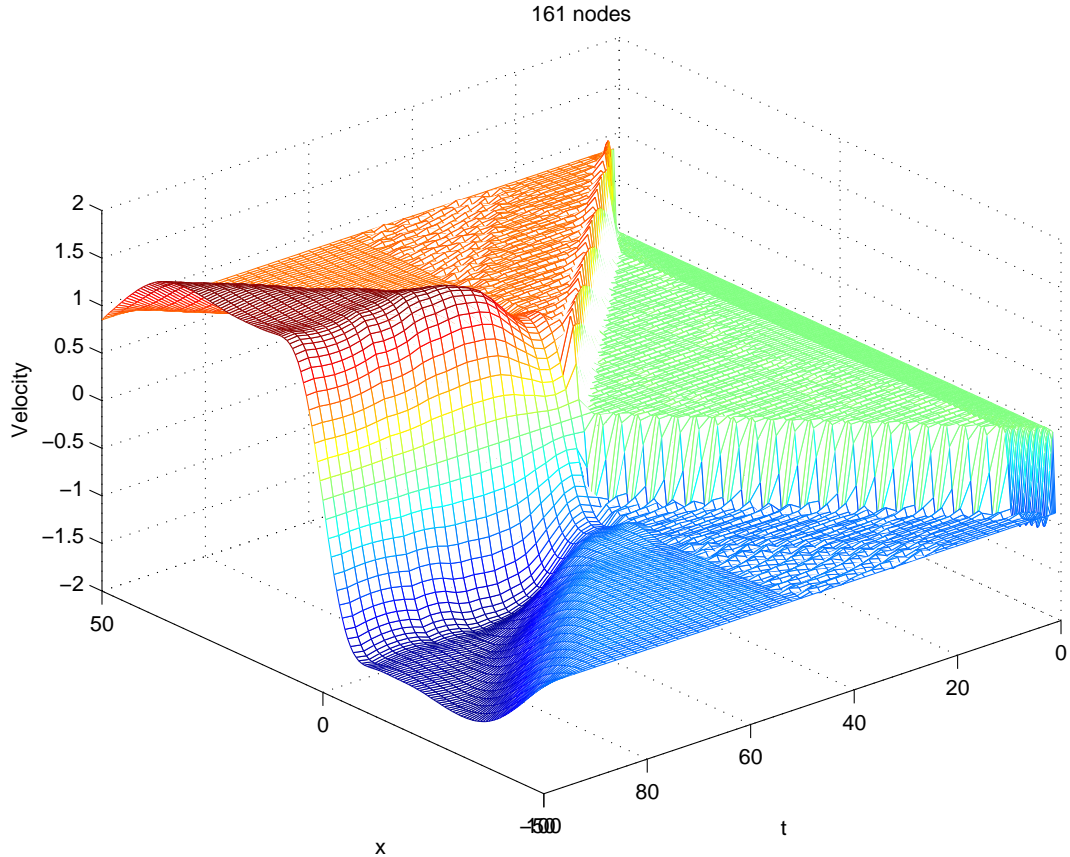


Figure 5.17: Non-local continuum model: the evolution of velocity with a uniform distribution of 161 collocation points.

The weighted average of $\tilde{\varepsilon}(x)$, denoted by $\bar{\tilde{\varepsilon}}(x)$, is achieved by replacing $\varepsilon(\xi, t)$ in (5.69) by $\tilde{\varepsilon}(x)$

$$\bar{\tilde{\varepsilon}}(x) = \int_V \alpha(x, \xi) \tilde{\varepsilon}(x) d\xi, \quad (5.93)$$

The domain is discretised with a uniform distribution of 161 collocation points. The IRBFN parameter $\beta = 1$ in (5.16), the interaction radius $R = 5$ in (5.93) which is integrated with 11-point Gaussian quadrature, and the IRBFN regularisation parameter is $\lambda = 3.391895$. The results shown in Figure 5.16 demonstrate the effectiveness of the present method. In this figure, the exact solution $\hat{\varepsilon}(x)$ is represented by the Heaviside curve; the dot-dashed curve indicates the IRBFN solution $\tilde{\varepsilon}(x)$; the solid curve represents the weighted average of the IRBFN approximation $\bar{\tilde{\varepsilon}}(x)$; the heavy dashed curve represents the regularised weighted average $\bar{\bar{\tilde{\varepsilon}}}(x)$. The above specific parameters, except λ which is depen-

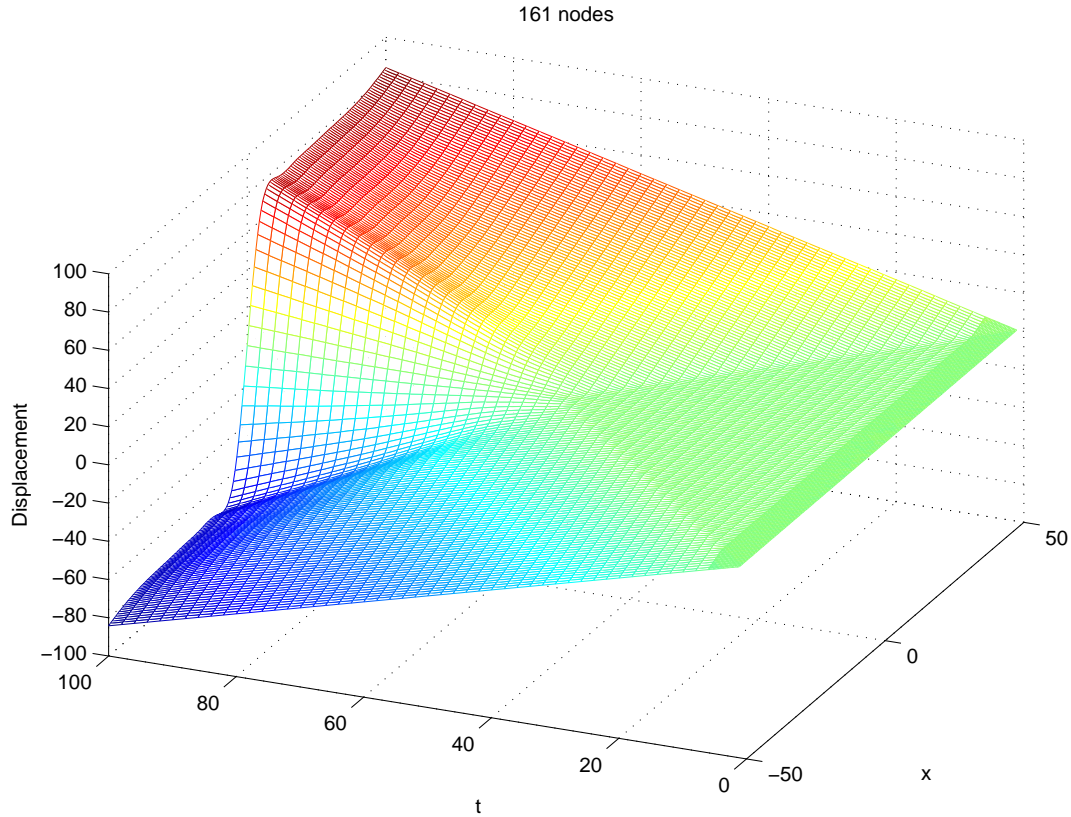


Figure 5.18: Non-local continuum model: the evolution of displacement with a uniform distribution of 161 collocation points.

dent on the number of collocation points, are also used in obtaining the results described below.

Returning to the bar problem, the prescribed end velocities are the same as those given in section 5.4.2, i.e. $c = 0.85\varepsilon_p$. The time step is $10^{-3}\frac{\Delta x}{\gamma}$. Due to the presence of the non-local operator, the full model is analyzed. In fact, in the present computation s is regularised, instead of ε , with similar end results. Figure 5.17-Figure 5.19 exhibit the evolution of velocity, displacement and non-local strain, respectively. Owing to the properties of non-local weighted average operator, the non-local continuum model yields much smoother response than the corresponding results obtained with a local continuum model, although the evolutionary profiles are similar as expected. The effect of standing wave can be seen in Figure 5.18-Figure 5.19 (continuous spatio-temporal representation),

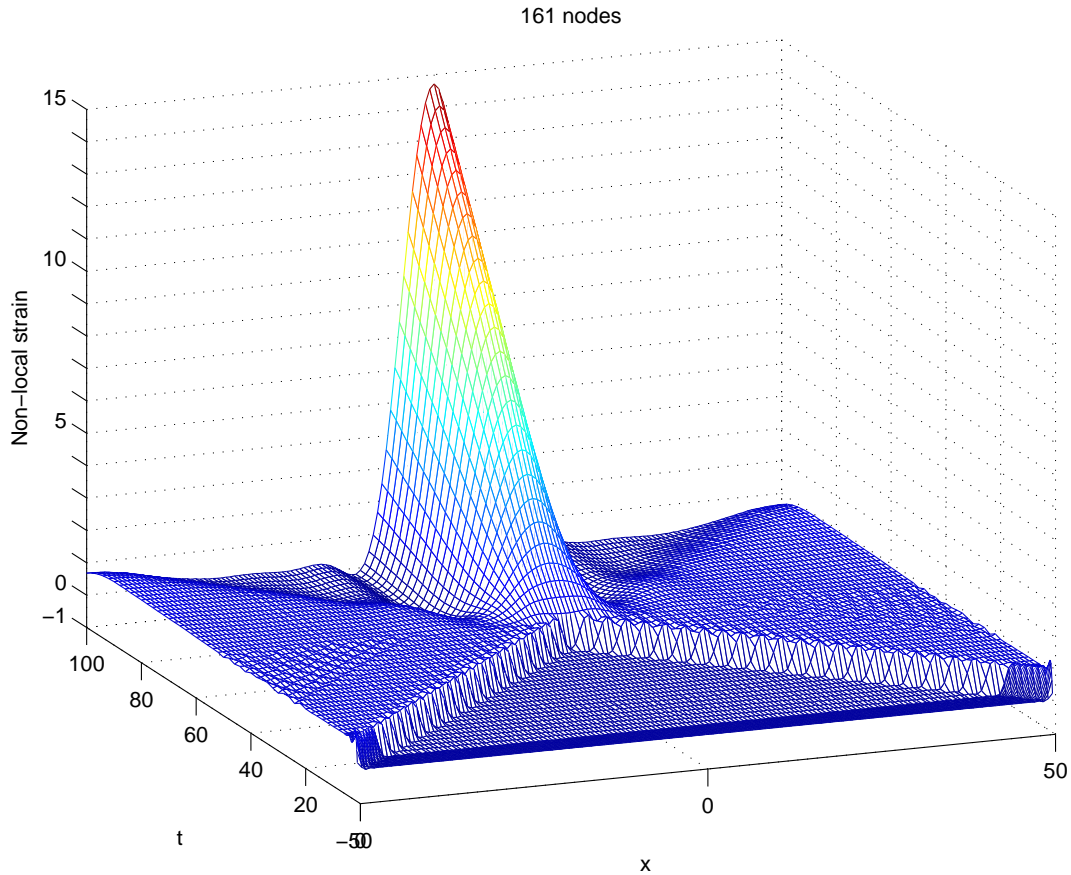


Figure 5.19: Non-local continuum model: the evolution of non-local strain with a uniform distribution of 161 collocation points.

Figure 5.21 and Figure 5.22 (at selected times), which show that the growing displacement and strain are confined to the localised zone. The bandwidth of the localized zone and the magnitude of the localized strain are finite, which is in contrast with the the results obtained with a local continuum model, where the exact solution is singular (zero bandwidth localised zone and hence infinite strain). After the onset of strain localization, the velocity, displacement, strain and stress waves reflected from the localised zone as shown in Figure 5.20-Figure 5.22. However, unlike the case of local continuum model, the wave profiles are smooth. In Figure 5.20(b), the profiles of stress indicate a complicated loading and unloading process after the initiation of strain localization. There are two narrow zones of high stress at the interfaces between the localized zone and the elastic regions. The standing wave causes the stress to rise in the narrow zones

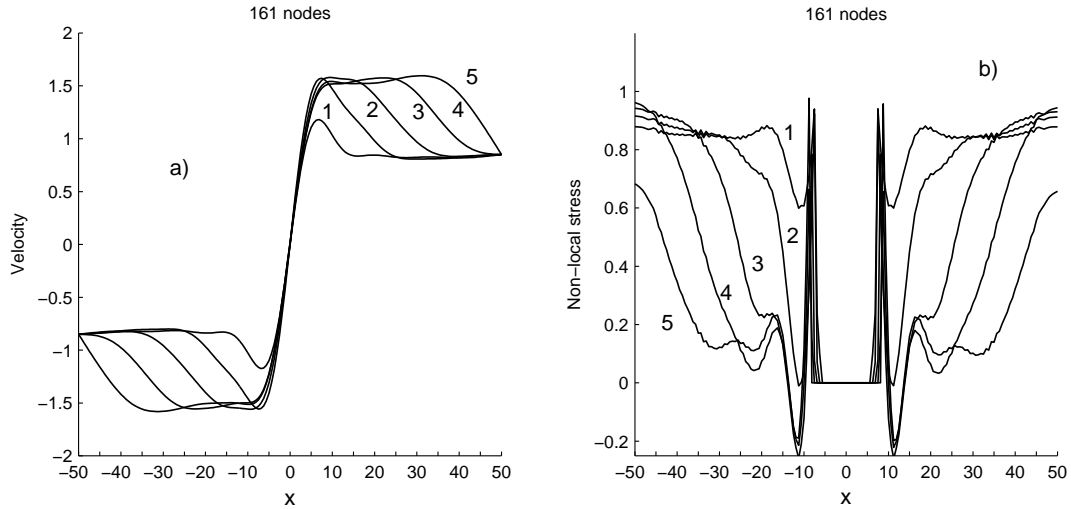


Figure 5.20: Non-local continuum model: the curve labels represent time levels: 1($t = 60.0$) ; 2($t = 70.0$) ; 3($t = 80.0$) ; 4($t = 90.0$) ; 5($t = 100.0$) (a) the evolution of velocity obtained ,(b) stress obtained with a uniform distribution of 161 collocation points

until the elastic limit is reached when sudden unloading occurs due to strain softening effect.

Finally, convergence of the present numerical procedure is demonstrated in Figure 5.23 where the non-local strain profiles (at $t = 70.0$) are displayed for a series of collocation points. As discretisation is refined, it can be seen that the bandwidth converges when the number of collocation points is about 160 while the peak non-local strain varies by only 2.3% when the number of collocation points increases from 161 to 241. The slight variation of the peak non-local strain can be expected since the local strain at the center of the band is singular.

5.5 Conclusion

An IRBFN meshless method is developed and used to simulate the dynamic strain localization of a bar of quasi-brittle material under dynamic tensile loading. Both local and non-local continuum models are used to describe the ma-

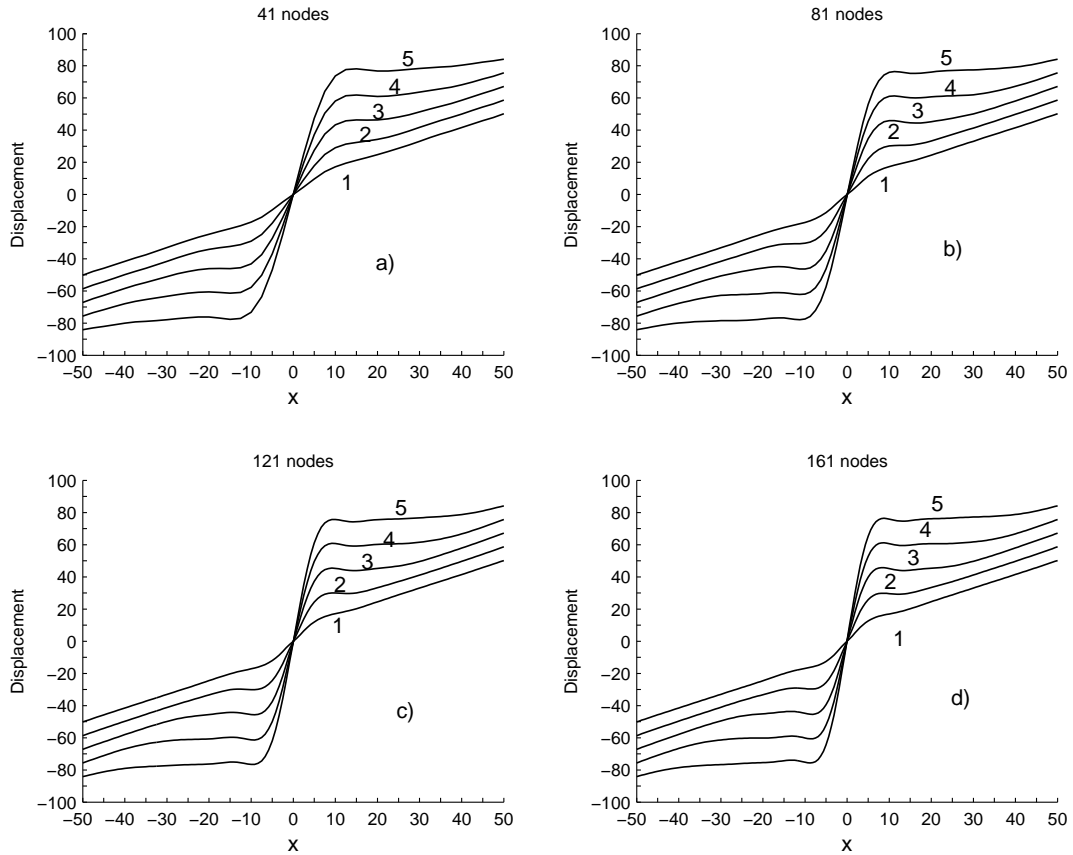


Figure 5.21: Non-local continuum model: the evolution of displacement at time levels: 1($t = 60.0$) ; 2($t = 70.0$) ; 3($t = 80.0$) ; 4($t = 90.0$) ; 5($t = 100.0$) (the curve labels indicate time levels) (a) 41 points, (b) 81 points, (c) 121 points and (d) 161 points uniformly discretised.

terial behaviour. The method incorporates a new general and effective regularization method. The enhanced IRBFN approach is able to alleviate the effect of noisy data and capture very well weak discontinuities typical of wave propagation and strain localisation. The present method is able to achieve these results using only uniformly distributed collocation points and requiring no prior knowledge of the location of discontinuities.

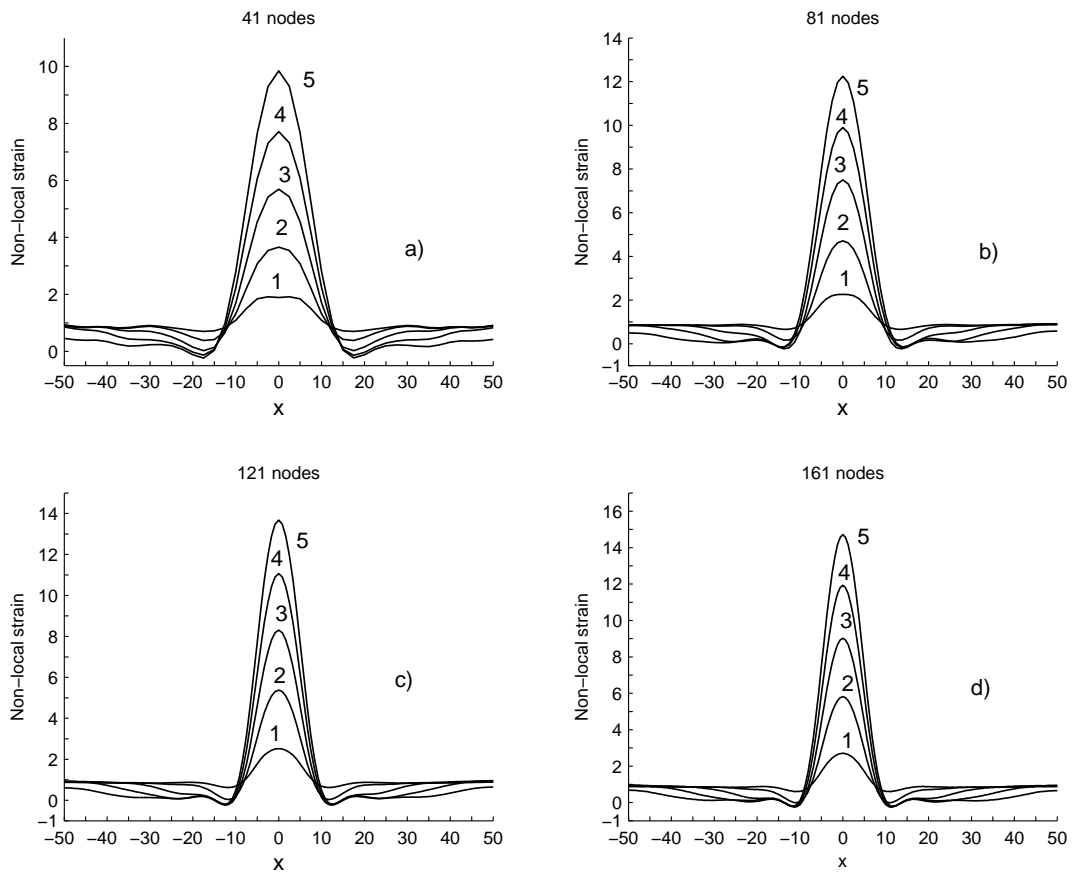


Figure 5.22: Non-local continuum model: the evolution of non-local strain at time levels: 1($t = 60.0$) ; 2($t = 70.0$) ; 3($t = 80.0$) ; 4($t = 90.0$) ; 5($t = 100.0$) (the curve labels indicate time levels) (a) 41 points, (b) 81 points, (c) 121 points and (d) 161 points uniformly discretised.

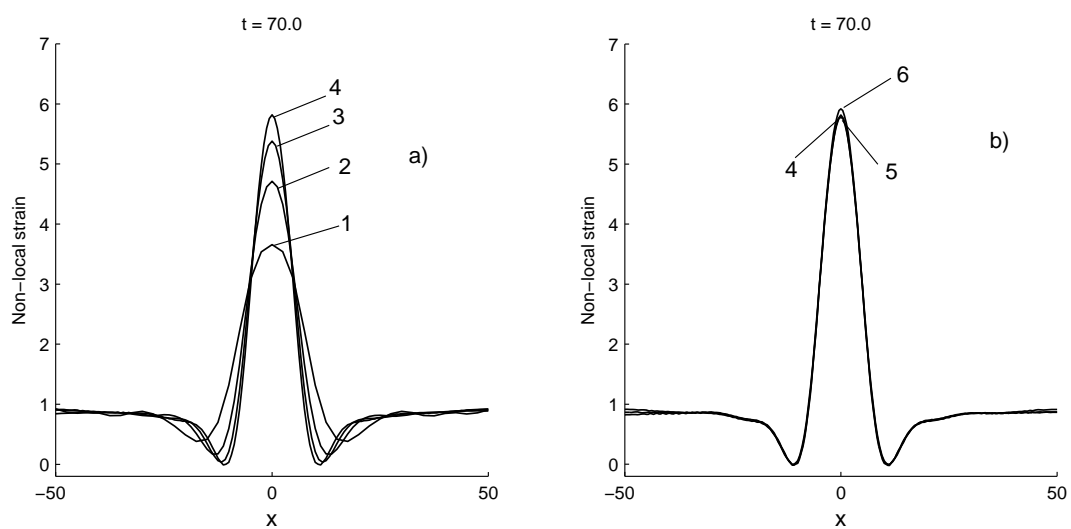


Figure 5.23: Non-local continuum model: convergence of the solution, the curve labels indicate number of collocation points (CP) as follows. 1(41 CPs, $\lambda = 3.39150$); 2(81 CPs, $\lambda = 3.39150$); 3(121 CPs, $\lambda = 3.39150$); 4(161 CPs, $\lambda = 3.391895$); 5(201 CPs, $\lambda = 6.2267131$); 6(241 CPs, $\lambda = 7.8271318$) at the time $t = 70.0$.

Chapter 6

Modeling strain localization in elasto- thermo-viscoplastic materials with IRBFN collocation technique

This chapter presents a numerical simulation of the formation and evolution of strain localization in elasto-thermo-viscoplastic materials (adiabatic shear band) by the indirect (integrated) radial basis function network (IRBFN) method. The effects of strain and strain rate hardening, plastic heating, and thermal softening are considered. The IRBFN method is enhanced by a new coordinate mapping which helps capture the steep spatial structure of the resultant band. The discrete IRBFN system is integrated in time by the implicit fifth-order Runge-Kutta method. The obtained results are compared with those of the Modified Smooth Particle Hydrodynamics (MSPH) method and Chebychev Pseudo-spectral (CPS) method

6.1 Introduction

Strain localization in elasto-thermo-visco-plastic materials is a phenomenon that occurs during high strain-rate plastic deformation, such as machining, forging, shock impact loading, ballistic impact and penetration, and has been proposed as an explanation for deep earthquakes (Walter, 1992). In particular, a shear band is a narrow, nearly planar or two dimensional region of very large shear strain and strain rate. The formation of shear bands often precedes the rupture in materials. Even when the rupture does not occur, the development of shear bands generally reduces the performance of the material. Hence, an understanding of shear-band morphology and evolution is an important prerequisite to improve material processes and manufacturing techniques. Shear bands are commonly of isothermal or adiabatic types (Molinari and Clifton, 1987). Isothermal shear bands form as a result of strain softening, and thermal softening plays a negligible role in the process. On the other hand, adiabatic shear bands, in which thermal softening plays a primary role, form as a result of an autocatalytic process: an increase in strain rate in a weaker zone causes a local increase in temperature which in turn creates a further increase in strain rate. Once a band is fully formed, the two sides of the region are displaced relative to each other, much like a mode II or mode III crack, but the material still retains full physical continuity from one side to the other.

This chapter focuses on adiabatic shear bands. The equations governing the evolution of adiabatic shear bands are coupled, highly nonlinear and stiff, and it is not simple, even for one-dimensional problems, to obtain close form solutions that could describe a range of constitutive, boundary, and initial conditions. For a number of special cases, close form exact and approximate solutions have been developed by many authors, for example, Rice and Rudnicki (1980); Molinari and Clifton (1987); Wright (1990); Sherif and Shawki (1992), just to name a few, to capture some of the fundamental characteristics of strain localization. Generally, numerical solutions are helpful in a parametric study to cover a range

of possible behaviours. However, it could be costly to resolve shear bands fully in a large scale computation since the morphology of a shear band exhibits very fine transverse scales, with aspect ratios of the high shear region usually in the hundreds or even thousands (Wright, 2002). Thus it is highly desirable to have effective and efficient numerical methods for the analysis of strain localisation problems. The spectral method (Bayliss et al., 1994) is particularly effective and efficient, but generally restricted to simple geometries. The finite element method (FEM) (Wright and Walter, 1987; Batra and Kim, 1991; Walter, 1992) has been used to analyze shear strain localization problems with good results for 1D cases, since the Lagrangian finite element mesh is not badly distorted and small element size of $O(10^{-7})$ enables one to capture the high strain. However, the FEM has many drawbacks in 2D or 3D strain localization problems. In contrast to the FEM, meshless methods (Li and Liu, 2000; Batra and Zhang, 2004) offer some advantages, including (i) shape functions are constructed by using a highly smooth window function, (ii) purely displacement-based formulation is possible without incurring volumetric locking within a range of support size of the window functions (Li and Liu, 2000), and (iii) approximations are non-local. Thus, meshless methods provide more continuous solutions than the piece-wise continuous ones obtained by the FEM. These properties provide an effective remedy for the mesh alignment sensitivity in the computation of strain localization.

In this study, we report a new numerical method based on radial basis function networks, a truly meshless method, for analysis of the dynamics of strain localization in 1D problems. The present indirect/integral radial basis function network (IRBFN) method is based on (i) the universal approximation property of RBF networks, (ii) exponential convergence characteristics of the chosen multiquadric (MQ) RBF, (iii) a simple point collocation method of discretisation of the governing equations, and (iv) an indirect/integral (IRBFN) rather than a direct/differential (DRBFN) approach (Kansa, 1990) for the approximation of functions and derivatives. For the DRBFN, (Madych and Nelson, 1990) showed

that the convergence rate is a decreasing function of derivative order. Since the introduction of the IRBFN approach by Mai-Duy and Tran-Cong (2001, 2005); Kansa et al. (2004), and Ling and Trummer (2004), based on the theoretical result of Madych and Nelson (1990), concluded that the decreasing rate of convergence can be avoided in the IRBFN approach. Furthermore, the integration constants arisen in the IRBFN approach are helpful in dealing with problems with multiple boundary conditions (Mai-Duy and Tran-Cong, 2006). In addition, a new coordinate mapping is here introduced to help capture the characteristics of extremely thin boundary layers (i.e. the localised shear bands). The chapter is structured as follows. The physical problem and its mathematical model are defined in section 6.2. The numerical formulation of the mathematical model is presented in section 6.3 which is followed by numerical examples in section 6.4. Some conclusions are drawn in section 6.5.

6.2 Problem definition

We consider the unidirectional shearing of an infinite slab of half thickness \bar{H} , and of an elasto-thermo-viscoplastic material. In this section we use the overbar to represent dimensional quantities, the subscript comma to denote the partial differentiation with respect to the variable indicated by the subscript. The unknowns are the shear stress \bar{s} , the particle velocity \bar{v} , the plastic strain γ and the temperature measured from the reference value $\bar{\Theta}$. In addition, the strain hardening parameter Ψ is also introduced as in Walter (1992) and Bayliss et al. (1994).

Let \bar{y} be the coordinate across the slab with origin on the middle plane, i.e. $-\bar{H} \leq \bar{y} \leq \bar{H}$, and \bar{t} denote time. The mathematical model for this problem can be found in Walter (1992); Wright (2002) and Bayliss et al. (1994), and is reproduced here as follows.

$$\bar{v}_{,\bar{t}} = \frac{\bar{s}_{,\bar{y}}}{\bar{\rho}}, \quad (6.1a)$$

$$\bar{s}_{,\bar{t}} = \bar{\mu}(\bar{v}_{,\bar{y}} - \bar{\gamma}_{,\bar{t}}), \quad (6.1b)$$

$$\bar{\rho}\bar{c}\bar{\Theta}_{,\bar{t}} = \bar{k}\bar{\Theta}_{,\bar{y}\bar{y}} + \bar{s}\bar{\gamma}_{,\bar{t}}, \quad (6.1c)$$

$$\bar{\Psi}_{,\bar{t}} = \frac{\bar{s}\bar{\gamma}_{,\bar{t}}}{\bar{\kappa}(\bar{\Psi})}, \quad (6.1d)$$

where $\bar{\rho}$ is the density, \bar{c} the specific heat, \bar{k} the thermal conductivity, $\bar{\mu}$ the shear modulus, and $\bar{\kappa}$ a strain hardening factor. The constitutive relation between \bar{s} , $\bar{\Psi}$, $\bar{\Theta}$ and $\bar{\gamma}_{,\bar{t}}$ is given by

$$\bar{s} = \bar{\kappa}(\bar{\Psi})g(\bar{\Theta})f(\bar{\gamma}_{,\bar{t}}), \quad (6.2)$$

where g a thermal softening factor, and f a strain rate hardening factor. Different material models can be obtained with appropriate choices of these factors, which will be illustrated when we consider examples in section 6.4. The problem is assumed to be symmetric about the middle plane $\bar{y} = 0$. The slab is subjected to a constant shearing velocity $\pm\bar{v}^0$ prescribed at the top and bottom surfaces of the slab, respectively. The surfaces are thermally insulated and all plastic work is converted into heat. The above assumptions lead to the following boundary conditions

$$\bar{v}(0, \bar{t}) = 0, \quad \bar{v}(\bar{H}, \bar{t}) = \bar{v}_0, \quad \bar{\Theta}_{,\bar{y}}(0, \bar{t}) = 0, \quad \bar{\Theta}_{,\bar{y}}(\bar{H}, \bar{t}) = 0. \quad (6.3)$$

The nominal strain rate is

$$\dot{\bar{\gamma}}^0 = \bar{\gamma}_{,\bar{t}}^0 = \frac{\bar{v}^0}{\bar{H}}, \quad (6.4)$$

where the time derivatives are from now on indicated by a dot over the variable. The variables are non-dimensionalised as follows.

$$\begin{aligned} y &= \frac{\bar{y}}{\bar{H}}, & t &= \bar{t}\dot{\bar{\gamma}}^0, & \dot{\bar{\Psi}} &= \frac{\dot{\bar{\Psi}}}{\dot{\bar{\gamma}}^0}, & v &= \frac{\bar{v}}{\bar{H}\dot{\bar{\gamma}}^0}, & s &= \frac{\bar{s}}{\bar{\kappa}^0}, \\ \Theta &= \frac{\bar{\rho}\bar{c}\bar{\Theta}}{\bar{\kappa}^0}, & \kappa &= \frac{\bar{\kappa}}{\bar{\kappa}^0}, & \dot{\bar{\gamma}} &= \frac{\dot{\bar{\gamma}}}{\dot{\bar{\gamma}}^0}, & k &= \frac{\bar{k}}{\bar{\rho}\bar{c}\bar{H}^2\dot{\bar{\gamma}}^0}, \\ \rho &= \frac{\bar{\rho}\bar{H}^2(\dot{\bar{\gamma}}^0)^2}{\bar{\kappa}^0}, & \mu &= \frac{\bar{\mu}}{\bar{\kappa}^0}, & b &= \bar{b}\dot{\bar{\gamma}}^0, & a &= \frac{\bar{a}\bar{\kappa}^0}{\bar{\rho}\bar{c}}, \end{aligned}$$

where \bar{a} is the thermal softening parameter, \bar{b} is the strain-rate hardening parameter, $\bar{\kappa}_0$ is the yield stress in the quasi-static isothermal simple shear test. The dimensionless governing equations are given by

$$\dot{v} = \frac{s_{,y}}{\rho}, \quad (6.5a)$$

$$\dot{s} = \mu(v_{,y} - \dot{\gamma}), \quad (6.5b)$$

$$\dot{\Theta} = k\Theta_{,yy} + s\dot{\gamma}, \quad (6.5c)$$

$$\dot{\Psi} = \frac{s\dot{\gamma}}{\kappa(\Psi)}. \quad (6.5d)$$

The constitutive relation is

$$s = \kappa(\Psi)g(\Theta)f(\dot{\gamma}). \quad (6.6)$$

The boundary conditions are

$$v(0, t) = 0, \quad v(1, t) = 1, \quad \Theta_{,y}(0, t) = 0, \quad \Theta_{,y}(1, t) = 0. \quad (6.7)$$

From (6.5a) and (6.7), the boundary conditions for shear stress can be found easily as

$$s_{,y}(0, t) = 0, \quad s_{,y}(1, t) = 0. \quad (6.8)$$

We will present a meshless numerical method for solving (6.5a)-(6.8) in the next section, and in section 6.4 we will present results for two particular models, namely the thermal imperfection and the strength imperfection cases.

6.3 Resolution of very large spatial gradients

The IRBFN procedure in section 5.3 is here employed to approximate spatial variables. In addition, a new coordinate mapping is introduced to capture the spatial structure of the shear bands as follows.

It has been shown that the IRBFN method can capture sharp gradients in some PDE solutions (Mai-Duy and Tran-Cong, 2003) with relatively coarse uniform spatial discretisation. However, with extremely sharp gradients in a solution, the option of uniformly refining the discretisation is not efficient or even effective. The computing of such extremely sharp gradients can be achieved effectively and efficiently with appropriate coordinate mappings of a relatively coarse, originally uniform discretisation. A very good mapping can be introduced as follows.

Consider the singularly perturbed boundary value problem (BVP)

$$\epsilon u''(x) + p(x)u'(x) + q(x)u(x) = f(x), \quad \forall x \in [a, b], \quad (6.9)$$

subject to the boundary conditions

$$u(a) = u_a, \quad u(b) = u_b, \quad (6.10)$$

where $\epsilon > 0$ denotes a fixed small constant. In many cases, (6.9) possesses boundary layers, i.e. regions of rapid change in the solution as $\epsilon \rightarrow 0$. Hence, in solving (6.9) with a point collocation method, the number of collocation points needs to be very large as $\epsilon \rightarrow 0$ to obtain an accurate solution. For a good resolution of the solution structure, at least one of collocation points must lie in the boundary layer (Tang and Trummer, 1996; Ling and Trummer, 2006). For example, if $\epsilon \ll 1$ and the problem possesses a boundary layer of width $O(\epsilon)$, then on a uniform grid with $O(N^{-1})$ spacing between the points we would need $N = O(\epsilon^{-1})$, which is not practical in most cases.

We transform the BVP (6.9) via the variable transformation $x \mapsto y(x)$ into a new BVP

$$\epsilon v''(y) [y'(x)]^2 + P(y)v'(y) + Q(y)v(y) = F(y), \quad \forall y \in [a, b], \quad (6.11)$$

subject to boundary conditions

$$v(a) = u_a, \quad v(b) = u_b, \quad (6.12)$$

where $v(y) = u(x(y))$, and the transformed coefficients are given by

$$P(y) = \epsilon y''(x) + p(x)y'(x), \quad Q(y) = q(x), \quad F(y) = f(x). \quad (6.13)$$

In this mapping, x represents the physical space and y the computational space. Without loss of generality, we assume that $[a, b] = [-1, 1]$. Consider the one-to-

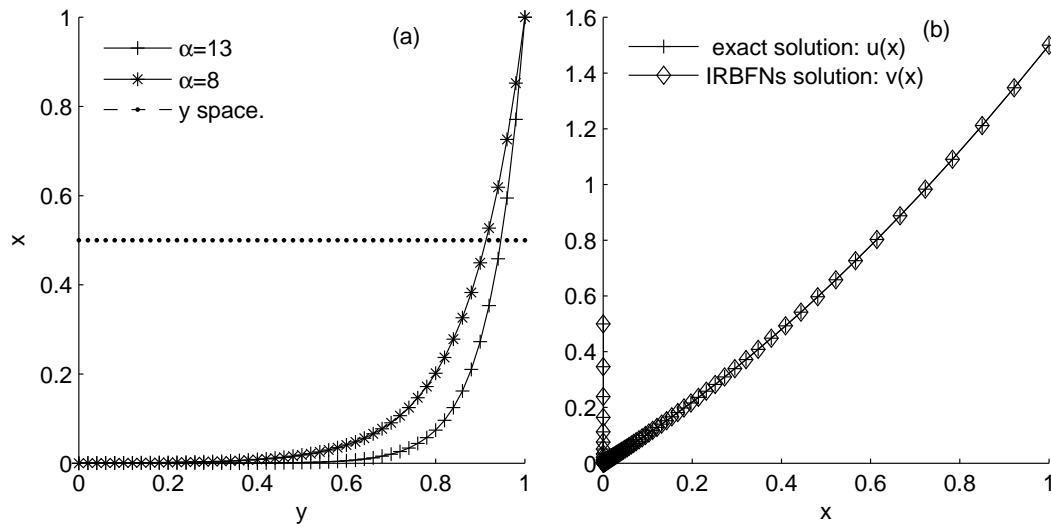


Figure 6.1: (a) Coordinate mapping with 61 collocation points, uniformly spaced in the computational space y , (b) IRBFN solution $v(x)$ and exact solution $u(x)$ of (6.18) with $\epsilon = 10^{-6}$, $\alpha = 13$, on the physical space x .

one mapping given by

$$x(y) = \frac{\sinh(\alpha y)}{\sinh(\alpha)}, \quad (6.14)$$

where $\alpha > 0$ is a parameter that allows control of the discretisation, the smaller the value of ϵ is, the larger the value of α is required. From (6.14) the inverse mapping and the derivatives of y with respect to x can be determined simply

$$y(x) = \frac{\operatorname{arcsinh}(\lambda x)}{\alpha}, \quad (6.15)$$

$$y'(x) = \frac{\lambda}{(1 + \lambda^2 x^2)^{\frac{1}{2}} \alpha}, \quad (6.16)$$

$$y''(x) = \frac{-\lambda^3 x}{(1 + \lambda^2 x^2)^{\frac{3}{2}} \alpha}, \quad (6.17)$$

where $\lambda = \sinh(\alpha)$. As shown in the Figure 6.1(a), the physical space x is very dense around the layer's location $x = 0$ while the computational space y is uniform.

Note that the transform (6.14) also maps the interval $[-1, 0]$ and $[0, 1]$ onto themselves. Hence, if (6.9) has only one boundary layer on the left (or central or right), we can translate the physical space to $[-1, 0]$ (or $[-1, 1]$ or $[0, 1]$) to avoid unnecessary collocation points in the non-steep region.

To illustrate the above mapping, we let $p(x) = 1$, $q(x) = 0$, $f(x) = x + 1 + \epsilon$, $[a, b] = [0, 1]$, $u_a = 0.5$ and $u_b = 1.5$ in (6.9), obtaining

$$\epsilon u''(x) + u'(x) = x + 1 + \epsilon, \quad \forall x \in [0, 1], \quad u(0) = 0.5, \quad u(1) = 1.5, \quad (6.18)$$

which has an exact solution given by

$$u(x) = \frac{1}{2} \left(e^{-\frac{\epsilon}{x}} + x^2 + 2x \right). \quad (6.19)$$

For $\epsilon = 10^{-6}$, the IRBFN solution in the physical space with 61 collocation points, $\alpha = 13$, are shown in the Figure 6.1(b), which shows that the numerical solution is quite indistinguishable from the exact solutions. For $\epsilon = 10^{-12}$, we can capture an accurate solution by using 161 collocation points and $\alpha = 29$.

6.4 Numerical examples

6.4.1 Example 1: A model of thermal imperfection

In this example we consider a specific case of the general unidirectional shearing problem defined in section 6.2 where the thermal softening factor in (6.6) is given by

$$g(\Theta) = (1 - a\Theta), \quad (6.20)$$

the strain hardening factor by

$$\kappa(\Psi) = \left(1 + \frac{\Psi}{\Psi_0}\right)^n, \quad (6.21)$$

and the strain rate hardening factor by

$$f(\dot{\gamma}) = (1 + b\dot{\gamma})^m. \quad (6.22)$$

For comparison purpose, the initial conditions and boundary conditions are taken to be the same as in Batra and Zhang (2004). The latter are described earlier by (6.7) and the former are given by

$$\begin{aligned} v(0, y) &= y, \quad \Psi(0, y) = 0.1, \quad \gamma = 0.0692, \\ \Theta(0, y) &= 0.1003 + 0.1(1 - y^2)^9 e^{-5y^2}, \\ s(0, y) &= \left(1 + \frac{0.1}{\Psi_0}\right)^n (1 - a\Theta(0, y))(1 + b)^m, \end{aligned}$$

where the second term on the right-hand side of the expression for the temperature Θ represents a thermal imperfection. With the half thickness of the slab $\bar{H} = 2.58\text{mm}$, the nominal strain rate is $\bar{\gamma}_t^0 = 500\text{s}^{-1}$ and the dimensionless parameters are

$$\begin{aligned} \rho &= 3.982 \times 10^{-5}, \quad \mu = 240.3, \quad a = 0.4973, \quad n = 0.09, \\ \kappa &= 3.978 \times 10^{-3}, \quad \Psi_0 = 0.017, \quad m = 0.025, \quad b = 5 \times 10^{-6}. \end{aligned}$$

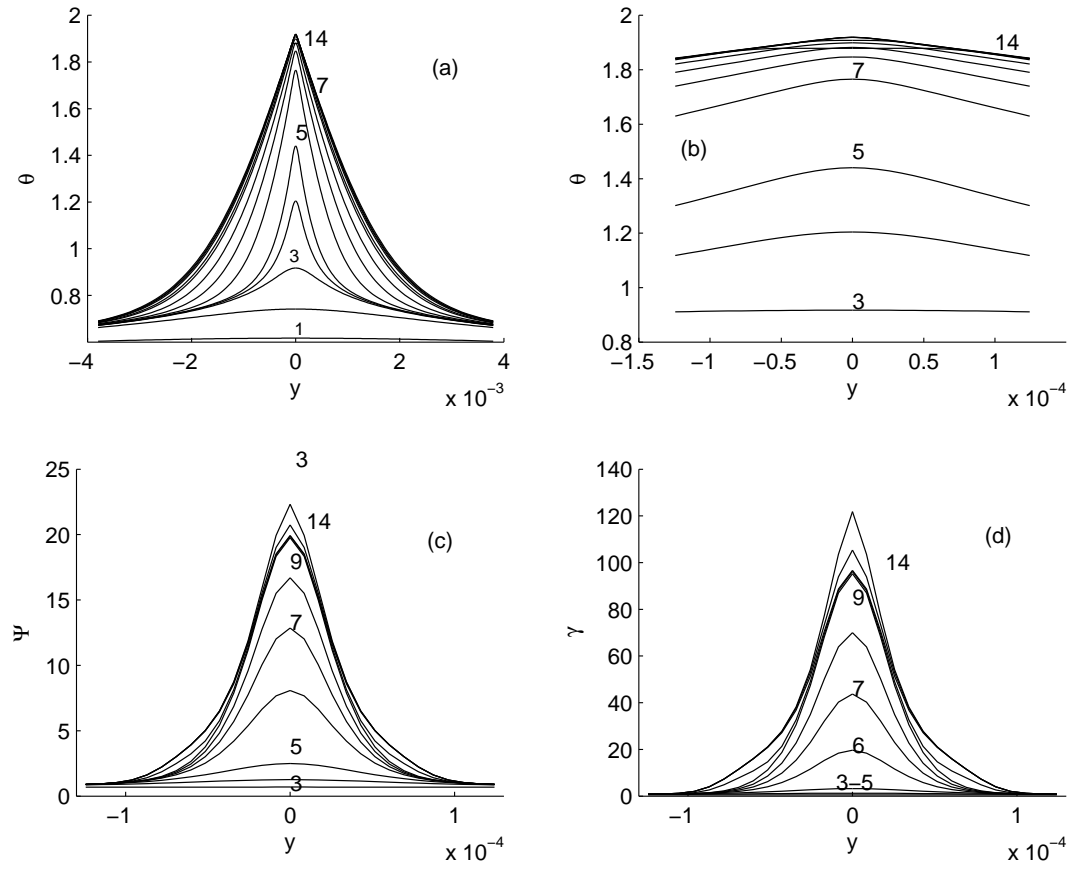


Figure 6.2: The curve labels indicate time levels (μs): 1(59.489); 2(60.257); 3(60.433); 4(60.477); 5(60.507); 6(60.602); 7(60.702); 8(60.804); 9(60.903); 10(60.934); 11(60.975); 12(60.992); 13(61.003); 14(61.019). (a) Evolution of temperature, (b) the temperature in the neighbourhood of $y = 0$ showing that the solution is highly consistent with the boundary conditions at $y = 0$, (c) evolution of Ψ , (d) evolution of plastic train.

The discretisation of the governing equations yields a system of fully coupled, stiff and nonlinear ordinary differential equations (ODEs) which are integrated with respect to time t using an implicit 5th Runge-Kutta method with subroutine RADAU5 developed by Hairer et al. (1987); Hairer and Wanner (1996). The subroutine automatically adjusts the time step size to compute the solutions within the prescribed accuracy. The results presented in this chapter are obtained by setting $RTOL = 10^{-7}$ and $ATOL = 10^{-7}$ in RADAU5.

The results presented in this section are obtained with 261 collocation points and the value of α in the mapping (6.14) is 9, β in (5.16) is 1. The evolutions of

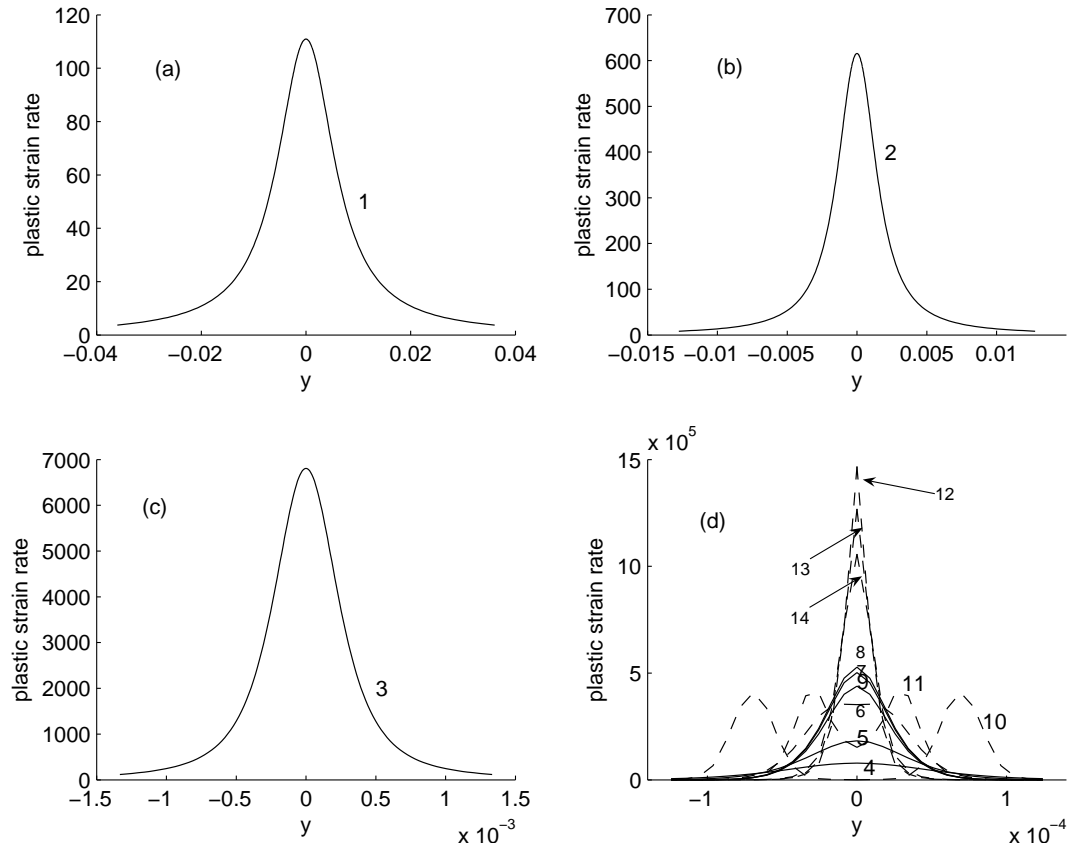


Figure 6.3: The evolution of plastic strain rate $\dot{\gamma}$. The curve labels indicate time levels (μs): 1(59.489); 2(60.257); 3(60.433); 4(60.477); 5(60.507); 6(60.602); 7(60.702); 8(60.804); 9(60.903); 10(60.934); 11(60.975); 12(60.992); 13(61.003); 14(61.019).

the spatial profile of the temperature Θ , plastic strain γ , and strain hardening parameter Ψ , are shown in Figure 6.2; the plastic strain rate in Figure 6.3; stress and velocity in Figure 6.4. These figures show that the solution is highly consistent with the boundary conditions at $y = 0$ (and at $y = \pm 1$, although not shown on the plots). From Figure 6.2 it can be observed that the plastic strain increases rapidly in the neighbourhood of $y = 0$ where the band of high shear strains becomes less and less diffuse, reaching a minimum with a very high corresponding plastic strain level before becoming more and more diffuse again. Similar patterns of development are observed for the temperature, strain hardening parameter, plastic strain rate and velocity as shown in Figures 6.3 and 6.4. In contrast, the spatial profile of stress evolves slightly differently which will be discussed in more detail later. Although banding of high shear

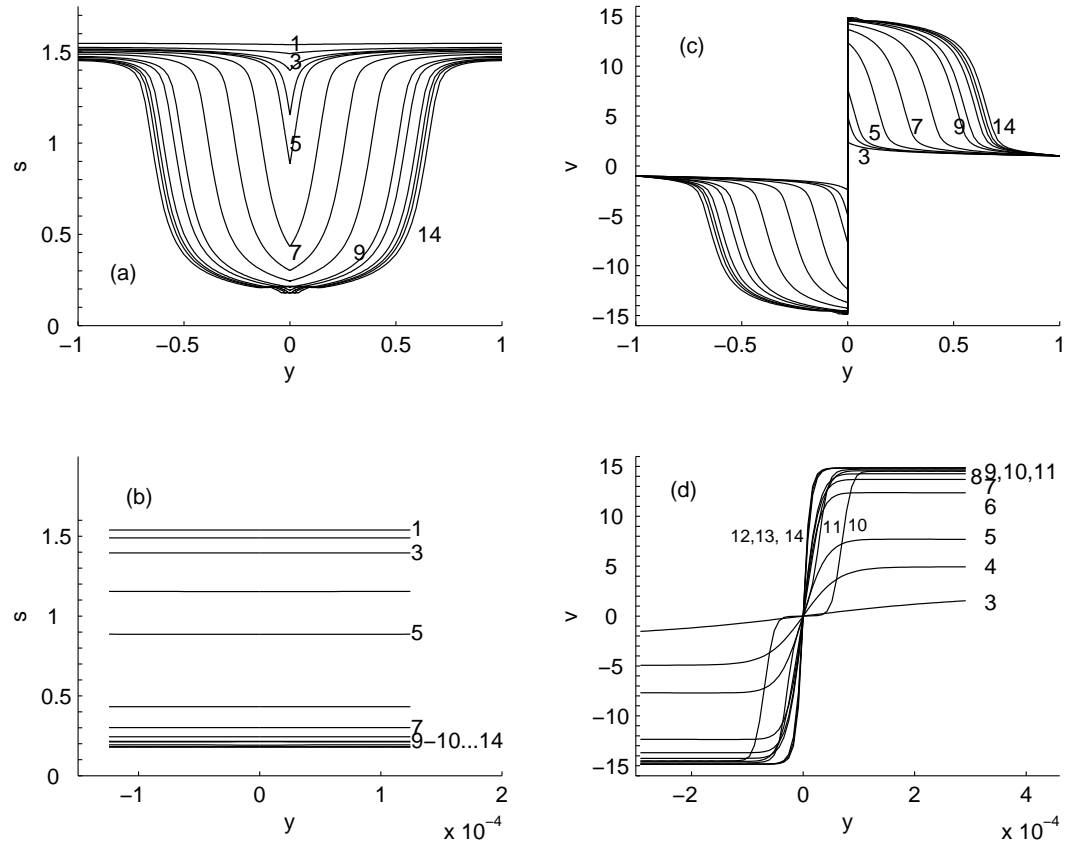


Figure 6.4: The curve labels indicate time levels (μs): 1(59.489); 2(60.257); 3(60.433); 4(60.477); 5(60.507); 6(60.602); 7(60.702); 8(60.804); 9(60.903); 10(60.934); 11(60.975); 12(60.992); 13(61.003); 14(61.019). (a) Spatial structure of shear stress at different times, (b) the shear stress in the neighbourhood of $y = 0$ showing that the solution is highly consistent with the boundary conditions at $y = 0$, (c) spatial structure of particles velocity at different times of localization, (d) the structure of the velocity boundary layer.

strains is apparent, the smooth spatial profiles do not provide a clear and unique bandwidth. Thus we define the limit of the high shear band as the position where the temperature equals 40% of the peak temperature at the center of the band (This criterion is somewhat arbitrary, for example, Batra and Zhang (2004) used a value of 40% while Bayliss et al. (1994) preferred 50%). The bandwidth evolves with time, for example when the plastic strain rate at $y = 0$ reaches its maximum value (at $t = 60.8385\mu\text{s}$), the extent of the corresponding bandwidth is $y = \pm 0.00252$. Hence the width of the shear band is $2 \times 0.00252 \times 2580 = 13.0\mu\text{m}$. The dimensionless half bandwidths correspond to different time levels (in parentheses) are 0.0688 (3), 0.0257 (4), 0.0102 (5), 0.00279 (6), 0.00237

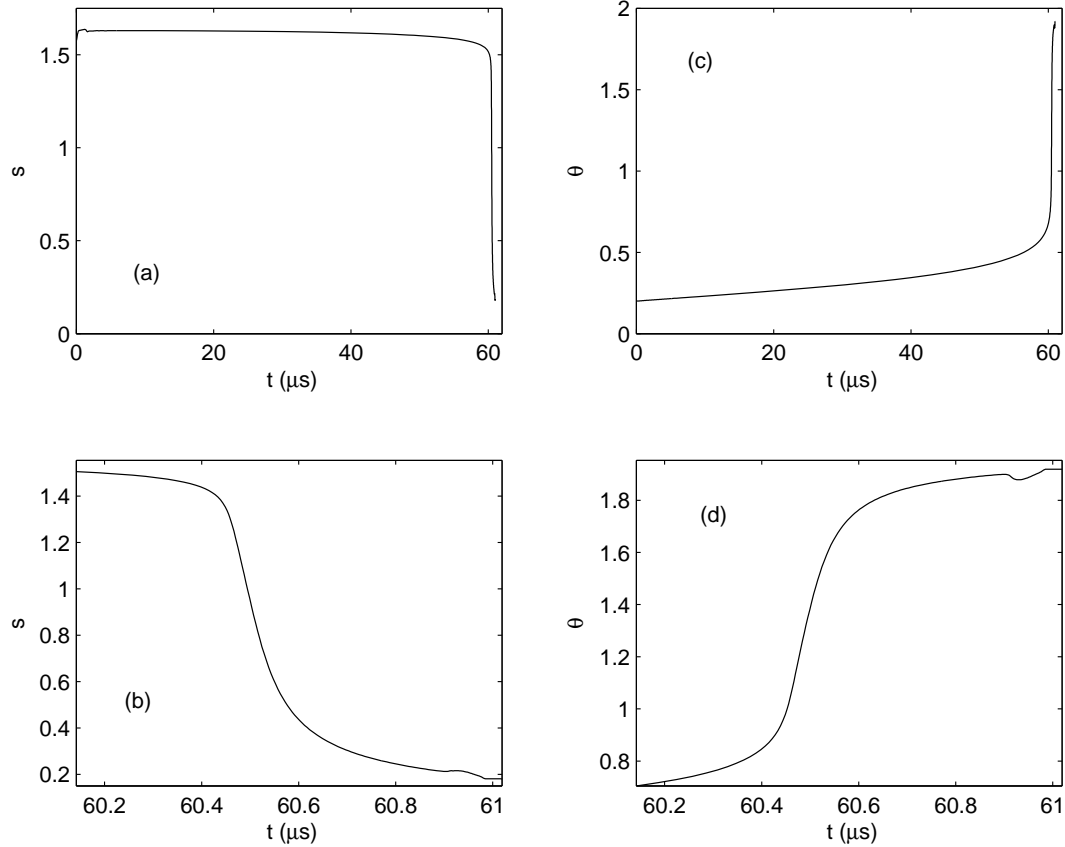


Figure 6.5: (a) and (b) evolution of shear stress at $y = 0$, (c) and (d) evolution of temperature at $y = 0$.

(7),0.002468 (8),0.00264 (9),0.00274 (10),0.00276 (11), which indicate that the shear band becomes narrowest (around time level 7 or $60.702 \mu\text{s}$) before the plastic strain rate peaks between time levels 8 ($60.804 \mu\text{s}$) and 9 ($60.903 \mu\text{s}$).

Figures 6.5(a)-(d) show the evolution of the shear stress and temperature at $y = 0$. As can be seen in Figure 6.5(a), the shear stress initially increases slightly (from the initial value of 1.575) since strain and strain rate hardening effects are stronger than the thermal softening effect. As time progresses, the increase in plastic work causes increase in Θ and the thermal softening effect tends to compensate the strain and strain rate hardening effects. In the next phase of the evolution, Θ increases very slowly (Figure 6.5(c)) and the thermal softening effect becomes gradually stronger than strain and strain rate hardening effects, and the shear stress decreases very slowly as shown in Figure 6.5(a). Further

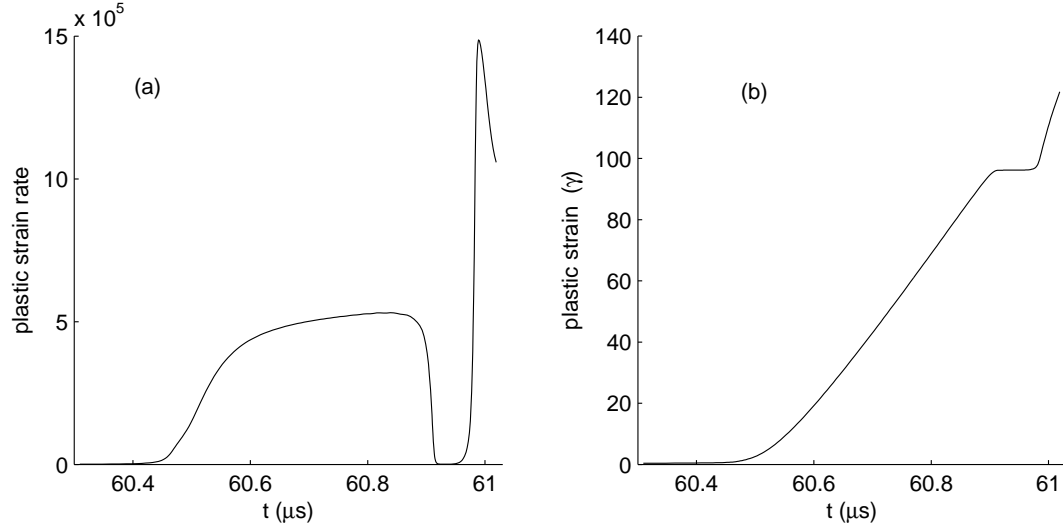


Figure 6.6: (a) Evolution of plastic strain rate $\dot{\gamma}$ at $y=0$, (b) evolution of plastic strain at $y=0$.

evolutions of the stress and velocity profiles indicate unstable development, i.e. the shear stress at $y=0$ is decreasing rapidly and the two halves of the slab (corresponding to $H \geq y > 0$ and $-H \leq y < 0$) are shearing relative to each other increasingly like rigid bodies. The instability can be seen more clearly by observing the evolution of shear stress (Figure 6.5) and plastic strain rate (Figure 6.6) at $y=0$. The latter varies gradually and unremarkably up to $t = 60 \mu\text{s}$, and shortly after which time, suddenly and steeply, i.e. by about five orders of magnitude in less than $0.5 \mu\text{s}$. After reaching the peak value of 5.3145×10^5 at $t = 60.8385 \mu\text{s}$, the plastic strain rate quickly drops to a value very close to zero (i.e. 674 compared with the peak value of 5.3145×10^5) before showing a very small and slow increase, followed quickly by another sharp rise to a second peak (14.865×10^5) nearly three times the first one, as shown in Figure 6.6. Although the stress decreases rapidly and the plastic strain rate increases even more rapidly, the evolution is smooth and therefore it is not possible to define the onset of instability uniquely. Here we define the onset of the strain localization instability as the point when the rate of change of stress with time continues to increase monotonically and rapidly. We detect this point

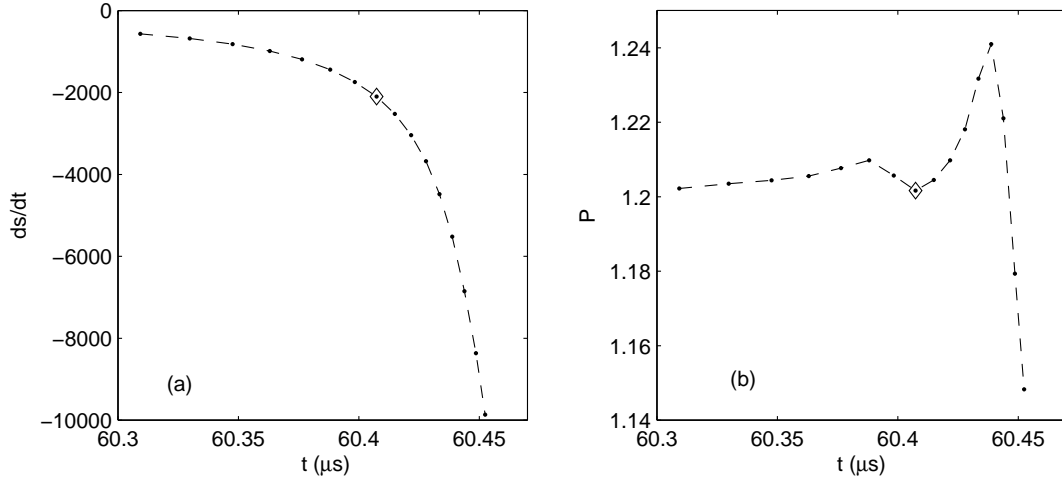
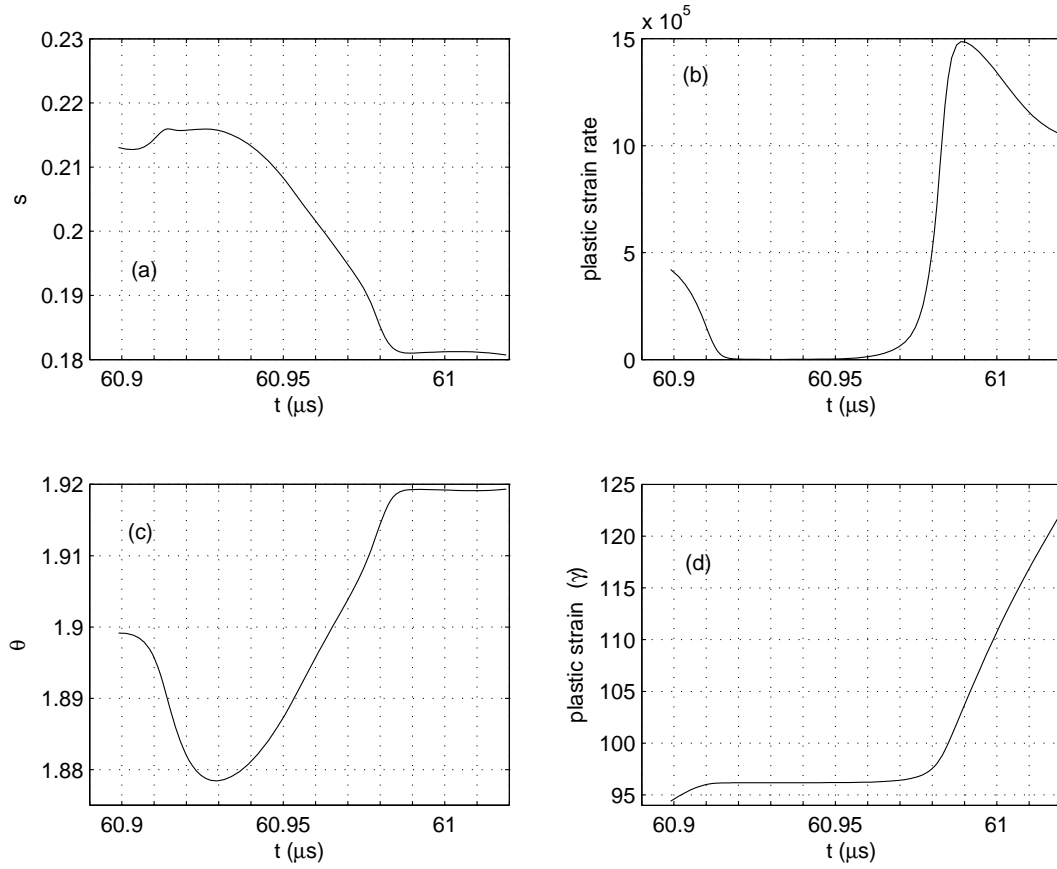


Figure 6.7: The behaviour of the shear stress at $y = 0$ around the onset of localisation. P is defined by (6.23).

by examining the ratio P defined as

$$P = \frac{\left. \frac{ds}{dt} \right|_{t_{n+1}}}{\left. \frac{ds}{dt} \right|_{t_n}}, \quad (6.23)$$

for several time levels n . The instability is thus found to occur at $t = 60.407\mu\text{s}$ as shown in Figure 6.7. Figures 6.2, 6.3, 6.4 show that the interaction between the strain hardening and thermal softening effects, coupled with thermal diffusion and mechanical loading, gives rise to interesting mechanical response of the slab. The initially slow thermal diffusion, relative to the rate of mechanical loading, allows the thermal imperfection to cause local heating, which in turn causes thermal softening in a narrow band. As the thermal softening effect grows stronger than the strain and strain rate hardening effects, the plastic strain rate increases sharply and the shear stress drops suddenly at the band center. Thermal diffusion also becomes more extensive and the extent of the softened material propagates outwards as shown in Figure 6.4. Continued shearing of the slab after the onset of strain localization exhibits more interesting interaction between thermal softening and strain and strain rate hardening effects, giving rise to apparent elastic unloading in the neighbourhood of $y = 0$ as shown in Figures 6.8 and 6.9 while plastic deformation continues on either sides of the band center as shown in Figure 6.3(d). However, high rate of plastic deformation

Figure 6.8: More detailed evolutions at $y = 0$.

quickly resumes as shown by the same figures.

6.4.2 Example 2: A model of strength imperfection

In this section, we consider another specific case of the general unidirectional shearing problem defined in section 6.2, where the strain rate hardening factor f is the same as in the previous example (i.e. given by (6.22)), and the thermal softening factor in (6.2) is given by

$$g(\bar{\Theta}) = e^{-\bar{a}\bar{\Theta}}. \quad (6.24)$$

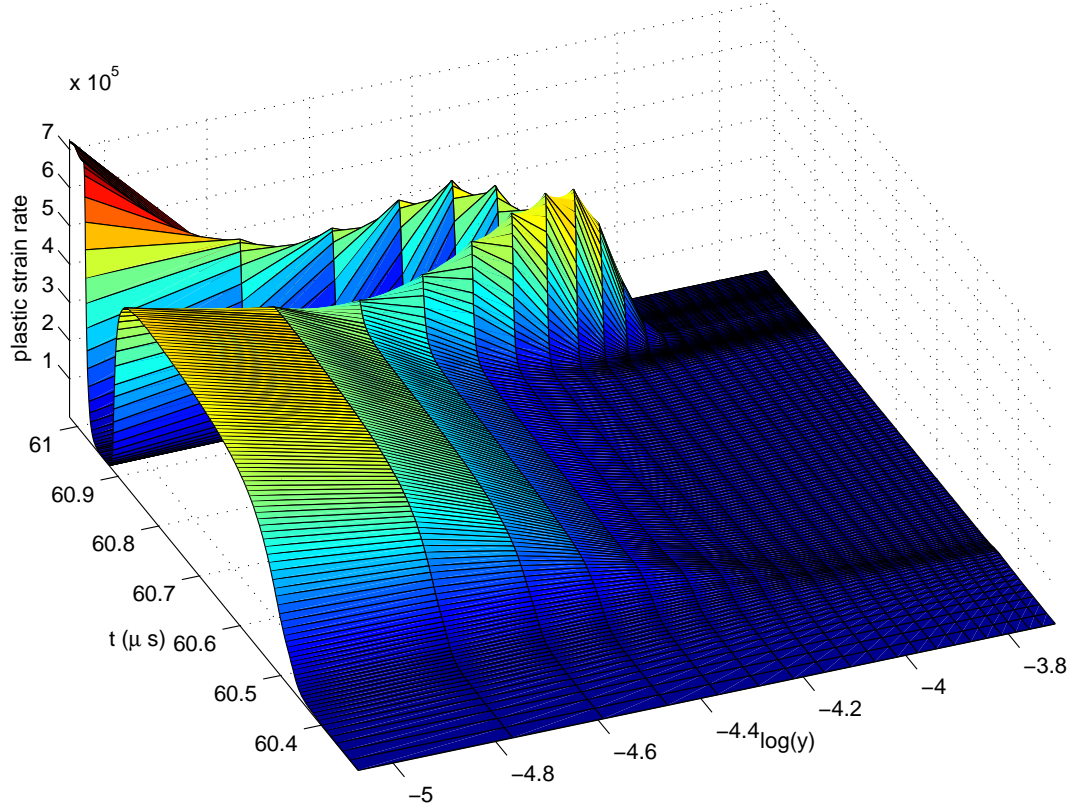


Figure 6.9: Evolution of the spatial profile of the plastic strain rate.

Following Bayliss et al. (1994), the strain hardening factor $\bar{\kappa}(\Psi)$ in (6.1d) is now taken as

$$\bar{\kappa}(\Psi) = \left(1 - 0.005(1 - \bar{y}^2)^{50} e^{-500\bar{y}^2}\right) \bar{\kappa}_0 \left(1 + \frac{\Psi}{\Psi_0}\right)^n, \quad (6.25)$$

where the leading factor represents a strength imperfection. (6.24) and (6.25) are rewritten in dimensionless form as follows.

$$g(\Theta) = e^{-a\Theta}. \quad (6.26)$$

$$\kappa(\Psi) = \left(1 - 0.005(1 - y^2)^{50} e^{-500y^2}\right) \left(1 + \frac{\Psi}{\Psi_0}\right)^n, \quad (6.27)$$

To compare the results of the present method with those obtained by other methods, we use the same parameters, boundary and initial conditions as in Walter (1992) and Bayliss et al. (1994). The boundary conditions are described

earlier by (6.7) and the initial conditions are

$$\begin{aligned} v(0, y) &= y, \quad s(0, y) = 0, \quad \gamma(0, y) = 0, \\ \Theta(0, y) &= 0.1(1 - y^2)^9 e^{-5y^2}, \quad \Psi(0, y) = 0. \end{aligned} \quad (6.28)$$

The half thickness of the slab \bar{H} and the nominal strain rate $\dot{\gamma}^0$ are taken as 3.47mm and 1000s⁻¹, respectively. Other parameters are

$$\begin{aligned} \bar{\rho} &= 7860\text{kgm}^{-3}, \quad \bar{\mu} = 80\text{GPa}, \quad \bar{\kappa}_0 = 602\text{MPa}, \quad \bar{a} = 6.43 \times 10^{-4}\text{s}^{-1}, \\ \bar{b} &= 1 \times 10^4\text{Js}^2(\text{kgm}^2)^{-1}, \quad \Psi_0 = 0.017, \quad \bar{c} = 473\text{J}(\text{kg}^\circ\text{C})^{-1}, \\ \bar{k} &= 49.2\text{J}(\text{ms}^\circ\text{C})^{-1}, \quad m = 0.0251, \quad n = 0.09. \end{aligned}$$

The results presented in this section are obtained with 221 collocation points, the value of α in the mapping (6.14) is 8 and β in (5.16) is 1. The results obtained here are in good qualitative agreement with those of Bayliss et al. (1994), who also studied the sensitivity of the material response to imperfections. Figure 6.10 reveals the spatial structure of the particle velocity v at selected points of time, which shows that the strength imperfection (weakness) at the band center leads to a fast process of softening in a narrow band around $y = 0$, manifested by a sudden and dramatic increase in the particle velocity due to the sudden drop in shear stress. The characteristics of shear banding are further exposed in Figure 6.11 which shows that plastic strain rate, plastic strain, temperature and stress are more or less constant within very narrow bands around $y = 0$. Figure 6.11 also shows that there are two evolutionary stages of the shear band. In the first stage, the band narrows up to time instant around $t = 0.77145$ (instant 6) and the field variable profiles are self-similar. The band then widens in the second stage from around time instant $t = 0.77254$ (instant 7) onwards. The bandwidth evolution can be quantified by defining the extent of the bandwidth as the position where the value of a physical property (Θ , γ , or $\dot{\gamma}$) drops to 50% of its value at the band center (here we use the 50% criterion in order to compare our results with those of Bayliss et al. (1994)).

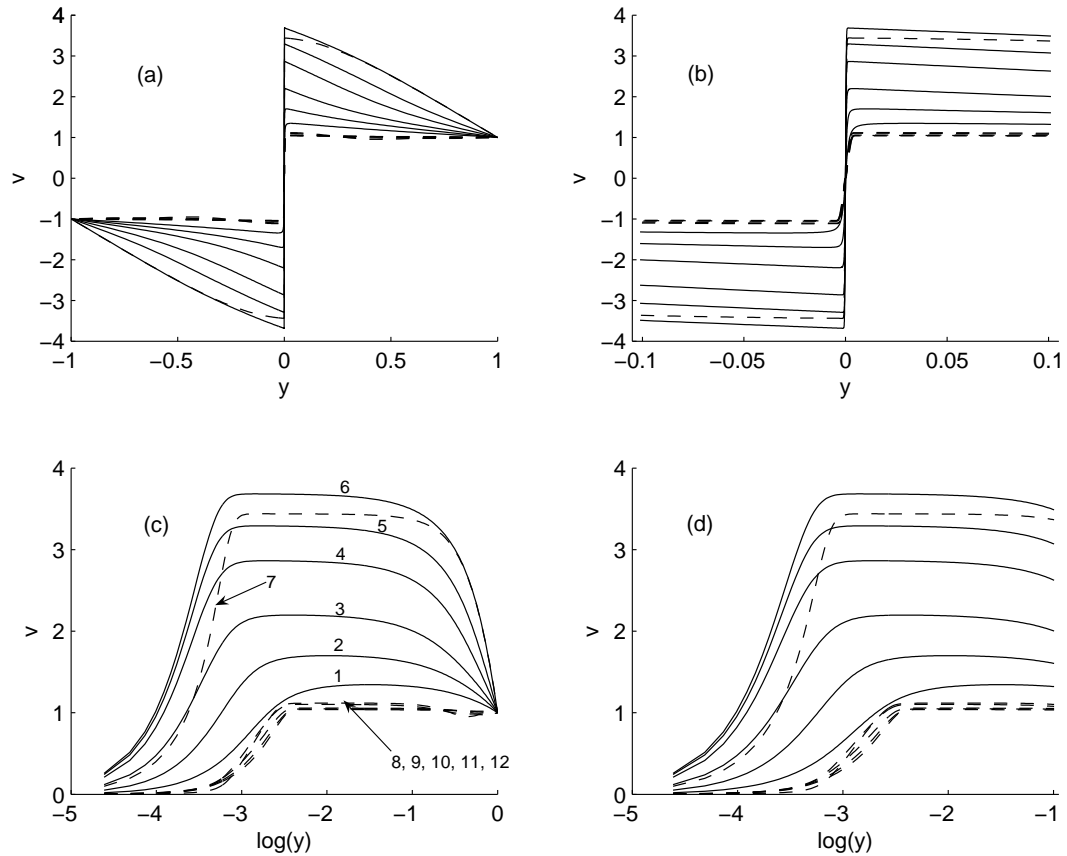


Figure 6.10: The spatial structure of particle velocity at selected points of time: (a) full linear scale, (c) semi-log scale $0 < y \leq 1$, (b) behaviour in the neighbourhood of $y = 0$, linear scale, (d) behaviour in the neighbourhood of $y = 0$, semi-log scale $y > 0$. The band narrowing stage (the solid curves) includes instants of $t = 0.76963(1)$, $0.77020(2)$, $0.77056(3)$, $0.77091(4)$, $0.77116(5)$, $0.77145(6)$ and the band widening or post-localization stage (the dash curves) includes instants $t = 0.77254(7)$, $0.78364(8)$, $0.78815(9)$, $0.79408(10)$, $0.79763(11)$, $0.80000(12)$.

The bandwidths are shown in Figure 6.12, confirming the band narrowing and widening stages as observed above, with the bandwidth for the plastic strain rate being the thinnest and for temperature the thickest. There is a smooth transitional region between the central shear band and the outer material where the plastic strain rate, plastic strain and temperature profiles remain virtually unchanged with time. However, the stress profile continues to evolve everywhere, with stress level generally dropping due to the softening effect, except some temporary hardening at the band center (Figure 6.13).

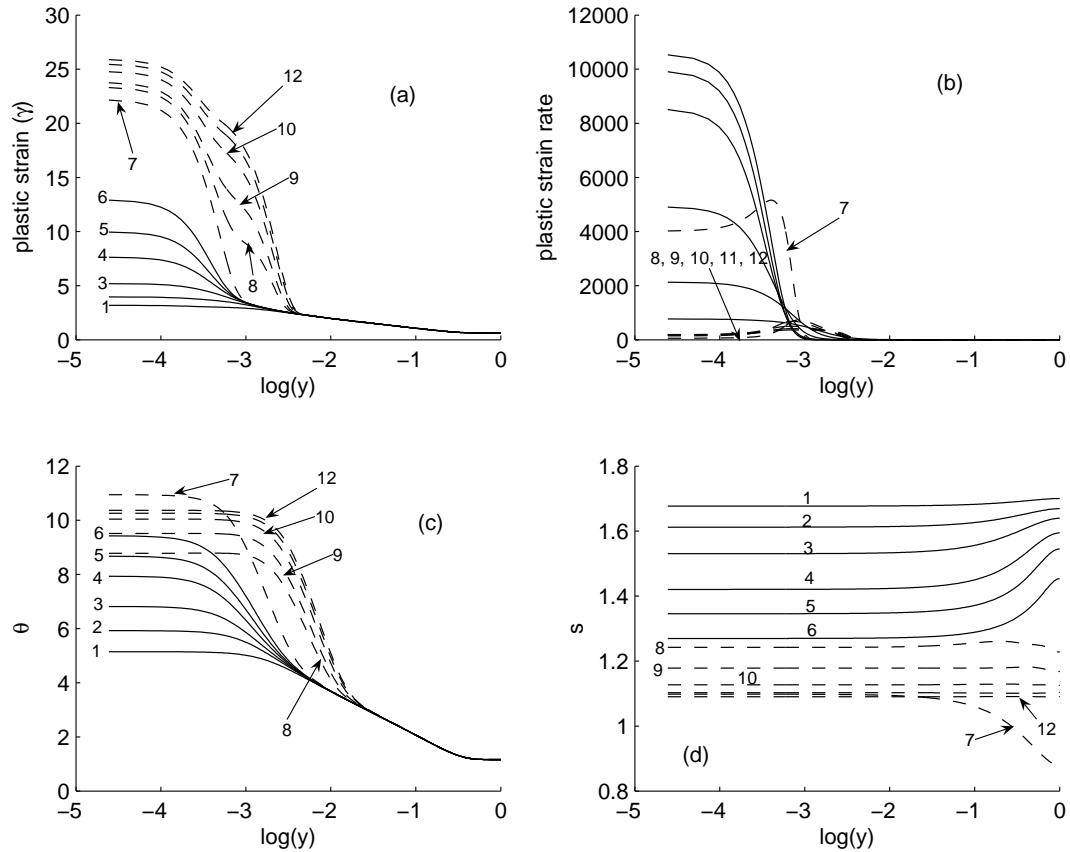


Figure 6.11: The spatial structure of field variables at selected points of time (a) plastic strain, (b) plastic strain rate, (c) temperature, (d) shear stress. The band narrowing stage (the solid curves) includes instants of $t = 0.76963(1)$, $0.77020(2)$, $0.77056(3)$, $0.77091(4)$, $0.77116(5)$, $0.77145(6)$ and the band widening or post-localization stage (the dash curves) includes instants $t = 0.77254(7)$, $0.78364(8)$, $0.78815(9)$, $0.79408(10)$, $0.79763(11)$, $0.80000(12)$.

Figure 6.13 shows the timing of key events during the process of strain localization. The plastic strain rate rises rapidly and attains its peak value at $t_1 = 0.77154$, followed by the temperature peaking at $t_2 = 0.77250$, and the stress at $t_3 = 0.77440$. By using the criterion (6.23) as in example 1, the onset of localization is found to occur at $t = 0.76976$, which is when the rate of temperature increase starts to rise rapidly as shown in Figure 6.14. This figure also shows that the strength imperfection is such that the thermal diffusion process is much slower than the rate of heat generated by plastic work which causes rapid localised increase of Θ . The high temperature triggers a dramatic thermal softening process with a very brief period of elastic unloading. Although

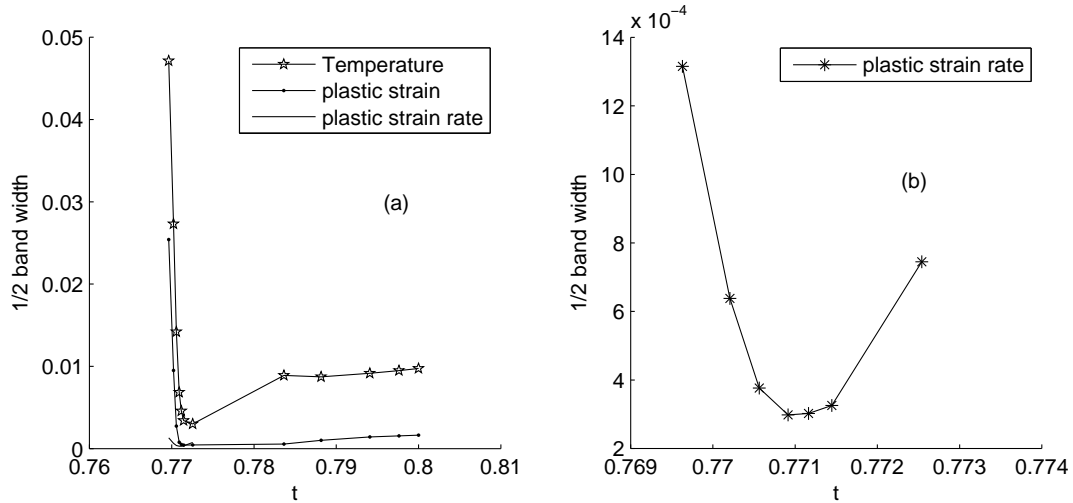


Figure 6.12: Evolution of bandwidths shows the band narrowing stage followed by the band widening stage, and the bandwidth based on the plastic strain rate is the narrowest while the one based on temperature is the widest.

strain hardening becomes stronger briefly, thermal softening dominates and the band widens. Soon after the onset of localisation, $\dot{\gamma}$ at $y = 0$ reaches a peak value $\dot{\gamma}_{peak} = 10606.778$ at time $t = t_1 = 0.77154$ while the strain hardening parameter Ψ is still growing. At this time, Θ is still increasing and shear stress decreasing. After attaining the maximum value, $\dot{\gamma}$ drops rapidly to near zero then rises slowly. There are small oscillations in the behaviour of $\dot{\gamma}$ in this regime, which was also found in Bayliss et al. (1994). As the plastic strain rate drops, the rate of plastic heating becomes slower and thermal diffusion becomes briefly dominant between $t_2 = 0.77250$ and $t_4 = 0.77759$ when the rate of plastic heating is again faster, causing further temperature rise. At $t = t_1 = 0.77154$ the bandwidths are 6.43×10^{-3} , 8.40×10^{-4} , 6.75×10^{-4} based on Θ , γ , $\dot{\gamma}$ respectively, which are compared with the corresponding values of 6.08×10^{-3} , 7.61×10^{-4} , 3.92×10^{-4} obtained by Bayliss et al. (1994).

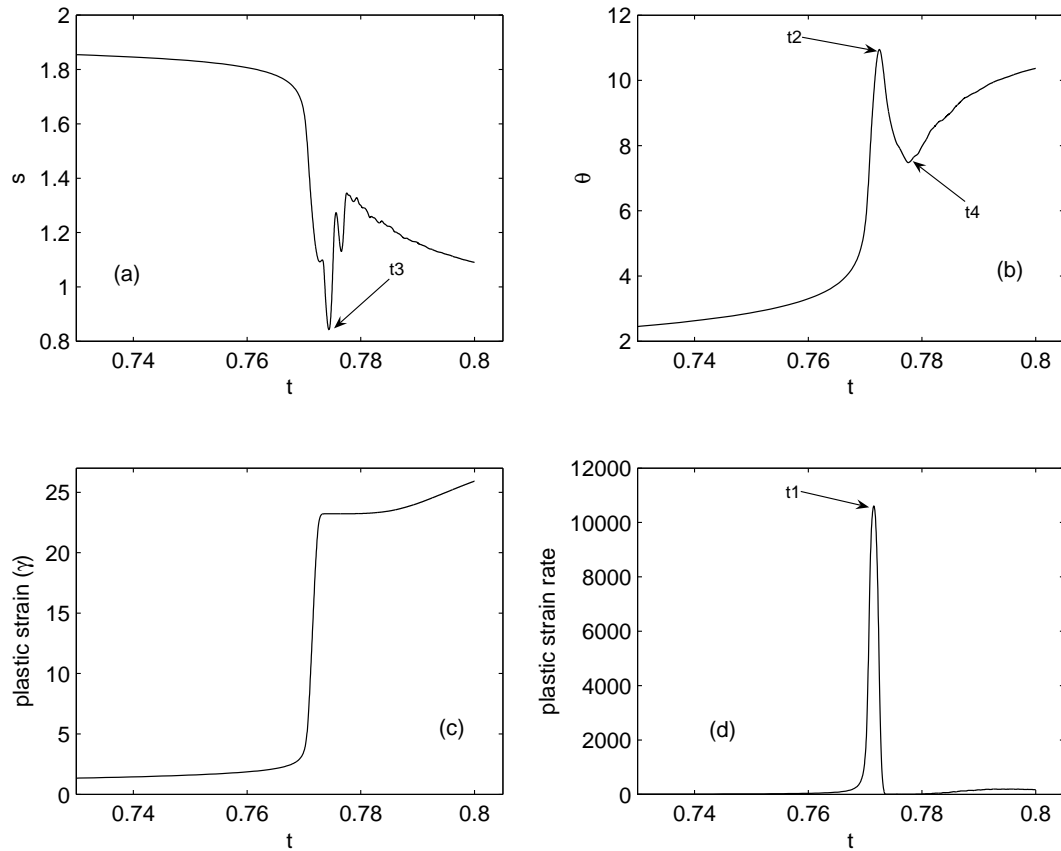


Figure 6.13: The evolution of (a) shear stress, (b) temperature, (c) plastic strain, (d) plastic strain rate at $y = 0$. A peak value of the plastic strain rate of 10606.778 occurs at $t_1 = 0.77154$, the temperature of 10.9490 at $t_2 = 0.77250$, the stress of 0.84238 at $t_3 = 0.77440$, and a second peak (local minimum of 7.4781) of temperature at $t_4 = 0.77759$. Thus $t_1 < t_2 < t_3 < t_4$.

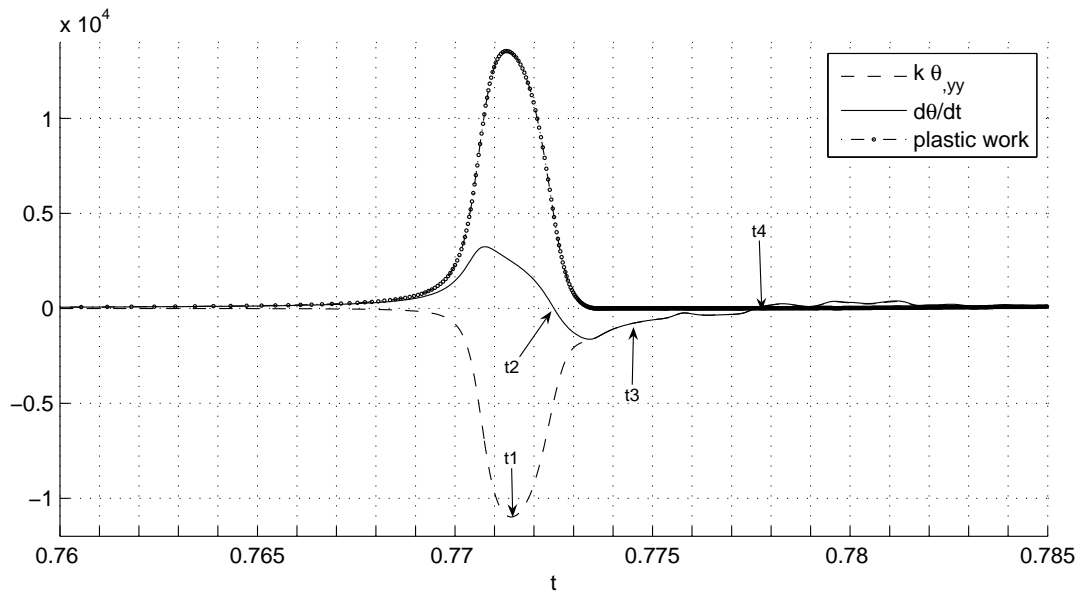


Figure 6.14: The interaction between thermal diffusion and plastic heating at $y = 0$: the dash curve depicts the evolution of the effect of thermal diffusion, $k\Theta_{,yy}$, dash-dot curve the effect of plastic heating $s\dot{\gamma}$, and the solid curve the combined effect $\frac{d\Theta}{dt} = k\Theta_{,yy} + s\dot{\gamma}$ of thermal diffusion and plastic heating. The onset of strain localisation occurs at $t = 0.76976$. Some key events occur at $t_1 = 0.77154 < t_2 = 0.77250 < t_3 = 0.77440 < t_4 = 0.77759$, as identified in the previous figure.

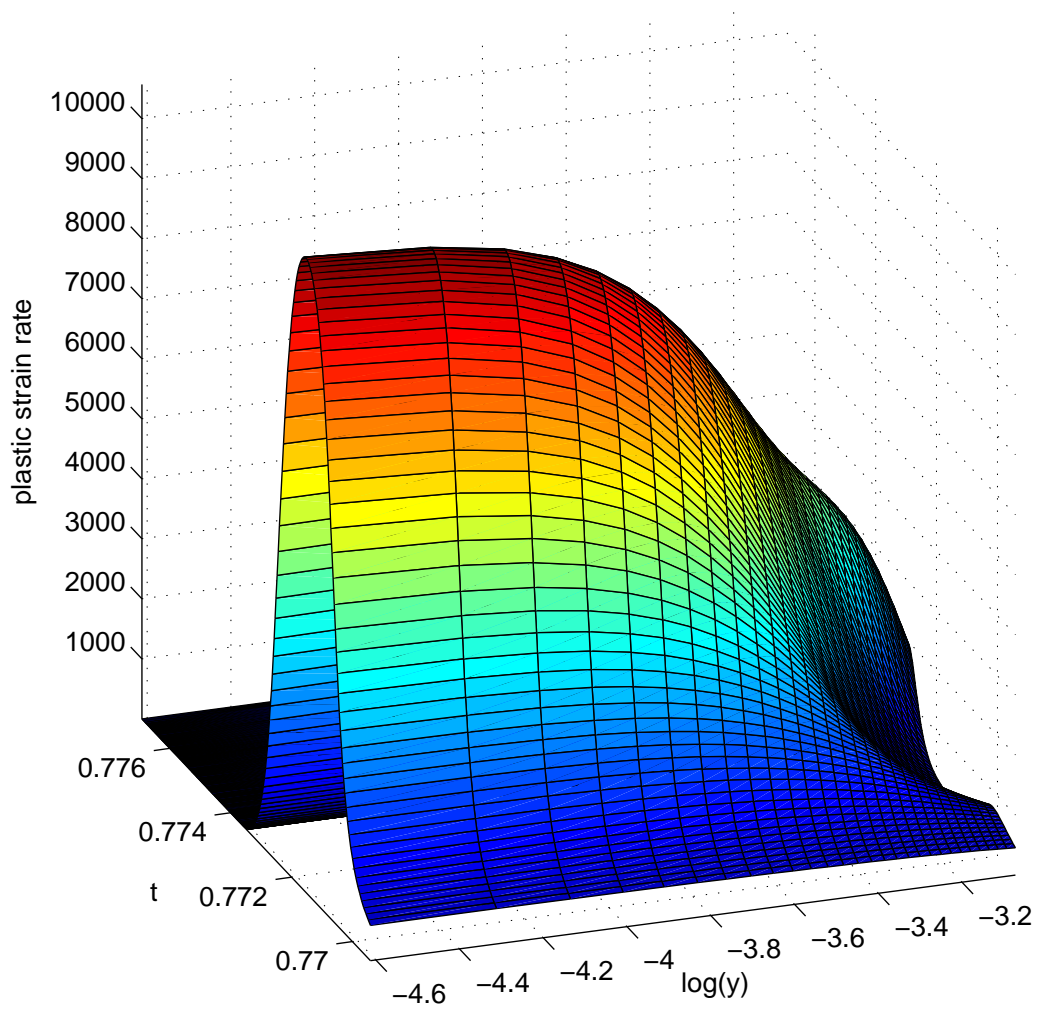


Figure 6.15: The evolution of plastic strain rate $\dot{\gamma}$.

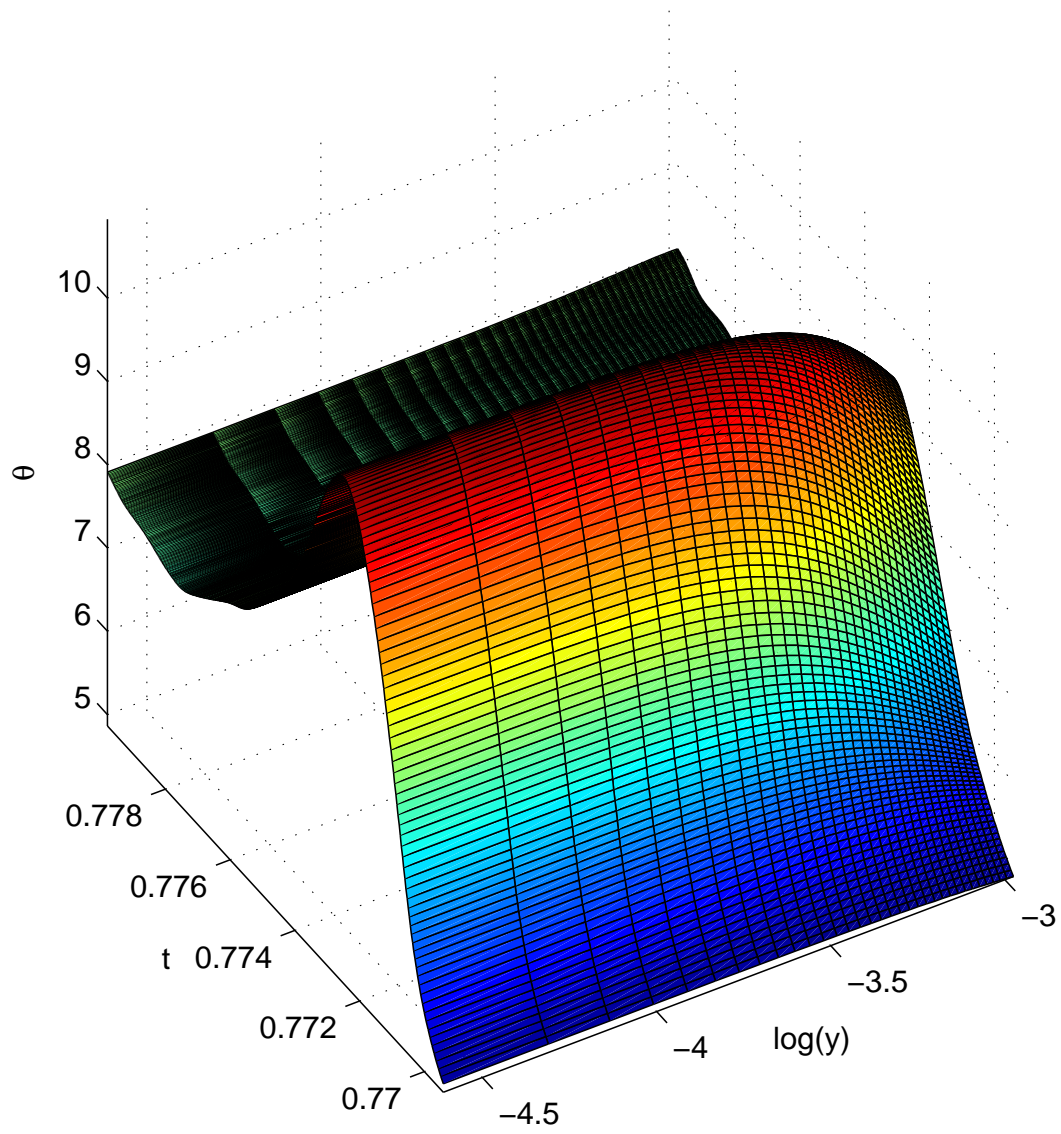


Figure 6.16: The evolution of temperature.

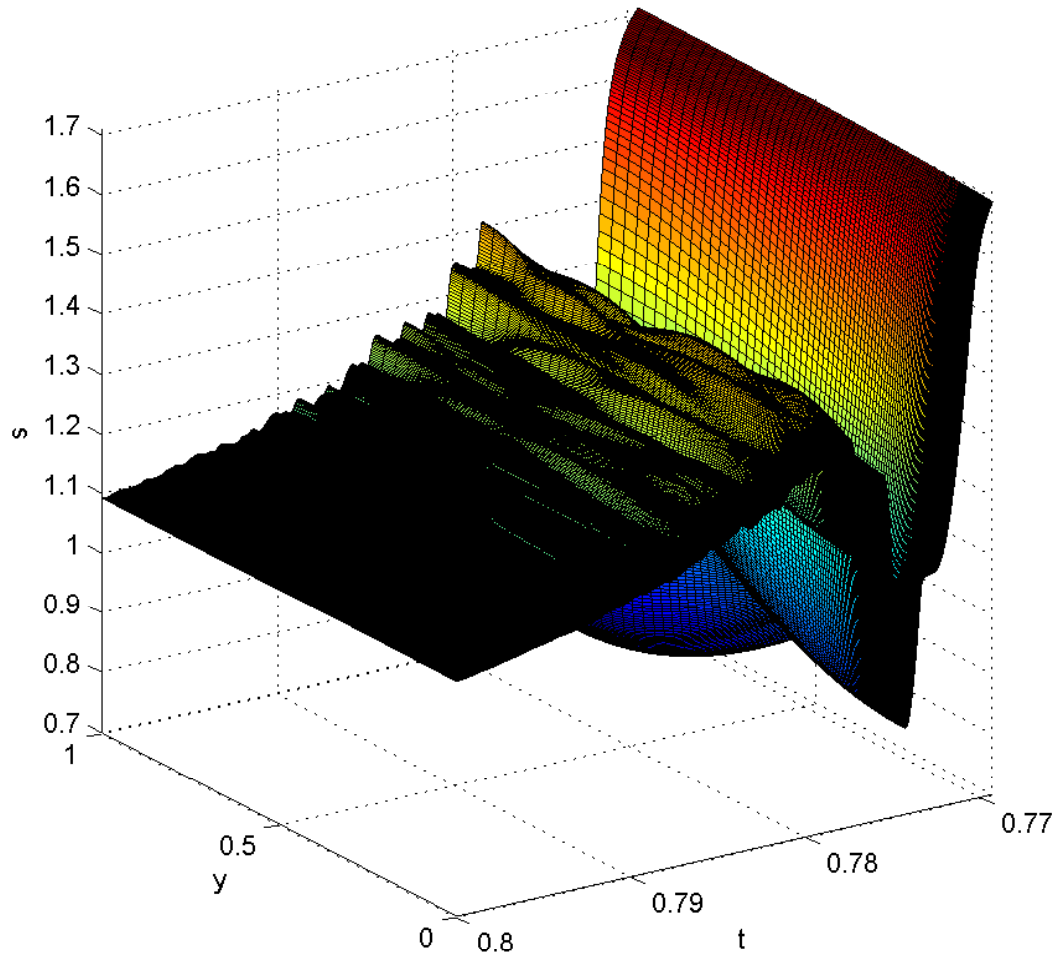


Figure 6.17: The evolution of shear stress.

The evolution of plastic strain rate $\dot{\gamma}$, and temperature Θ in the localized region during the severe localization are visualised in Figure 6.15 and Figure 6.16 respectively. In Figure 6.17, the evolution of shear stress s over the whole domain is depicted. The spatial profile of the shear stress s is very uniform before the shear stress reaches its minimum at t_3 , followed by mildly oscillatory behaviour, a behaviour not observed in the thermal imperfection model considered in example 1 above. The present results are compared with those obtained by the Modified Smooth Particle Hydrodynamics method (MSPH) (Batra and Zhang, 2004) and Chebyshev Pseudo Spectral method (CPS) (Bayliss et al., 1994) in Tables 6.1-6.2. Despite general qualitative agreement between the methods and some excellent quantitative agreements, there are some large differences between

the numerical results. For the timing of key events, t_1, t_2, t_3, t_4 , the present results fall between the MSPH and the CPS results and are much closer to the latter (within 7%), although the time lags $t_2 - t_1, t_3 - t_1, t_4 - t_1$ are virtually identical between the present IRBFN and the MSPH methods. In contrast, the results for $\dot{\gamma}_{peak}, \Theta_{peak}, s_{min}, \Theta_{min}, \gamma_{t_1}$ and γ_{t_2} are much closer to those obtained by the MSPH method.

Table 6.1: Comparison of the results between methods: The results obtained by the present IRBFN method are generally between those by the MSPH and the CPS methods, except for the case of Θ_{min} and γ_{t_1} .

	t_1	t_2	t_3	t_4	$\dot{\gamma}_{peak}$	Θ_{peak}	s_{min}	Θ_{min}	γ_{t_1}	γ_{t_2}
MSPH	0.9445	0.9455	0.9474	0.9505	11500	11	0.78	7.4	11	24
IRBFN	0.7715	0.7725	0.7744	0.7776	10606	10.95	0.84	7.48	14.0	22.1
CPS	0.7239	0.7252	0.7268	0.7284	5300	8.61	1.22	6.95	6.8	11.7

Table 6.2: Comparison of the time lags between methods: agreement is generally excellent, except that the CPS results show an earlier occurrence of the local temperature minimum.

	$t_2 - t_1$	$t_3 - t_1$	$t_4 - t_1$
MSPH	0.001	0.0029	0.0060
IRBFN	0.001	0.0029	0.0061
CPS	0.0013	0.0029	0.0045

6.4.3 Convergence characteristics

For example 1, we use six discretisations ($\{N_i\}_{i=1}^{p=6} = \{61, 101, 141, 181, 221, 261\}$) uniformly spaced collocation points, i.e. spacing $h_i = 1/N_i$) to study the convergence of our method. Due to a lack of exact solution, an estimate of “error” is computed as follows. For each level of discretisation, the governing equations are integrated to a specified time instant just after the onset of localisation ($t = 60.507\mu\text{s}$ and $t = 0.77115$ for example 1 and 2, respectively) to obtain the

spatial profile of the temperature at this time instant. Then the temperatures at $Q = 300$ points are computed by interpolation (i.e. by the close form RBFN just found) and the discrete relative L_2 error is computed as

$$N_e = \sqrt{\frac{\sum_{j=1}^Q (\Theta_j^i - \Theta_j^p)^2}{\sum_{j=1}^Q (\Theta_j^p)^2}}, \quad i = 1, 2, \dots, p-1,$$

where $p = 6$ for example 1 and 5 for example 2. Similarly, for example 2, we use five discretisations ($\{N_i\}_{i=1}^{p=5} = \{61, 101, 141, 181, 221\}$ uniformly spaced collocation points). Figure 6.18 shows that the “error” is proportional to $O(h^{2.48})$ and $O(h^{4.12})$ for example 1 and 2, respectively. If we set the error at 10^{-2} , we would need 143 collocation points for example 1, and 98 for example 2. In the case of example 1, Batra and Zhang (2004) used 442 nodes in their investigation by the FE and MSPH methods, while in the case of example 2, Bayliss et al. (1994) used 61 points in their CPS method.

6.5 Conclusion

We use the meshless IRBFN method to analyze the strain localization of an elasto-thermo-visco-plastic slab under simple shearing. We introduce a new coordinate mapping that allows very high resolution of the spatial structure of the resultant localised shear band with a relatively small number of computational degrees of freedom, distributed uniformly in the computational domain. The effects of elastic unloading, strain and strain rate hardening, thermal softening, heat conduction are considered. Either the thermal imperfection in the initial conditions or the strength imperfection in the constitutive relation can lead to severe strain localization, i.e. in a very narrow adiabatic shear band characterised by very high plastic strain rate, rapid increase of temperature and sudden drop of shear stress. The dynamics of formation and evolution as well as the spatial structures of the resultant adiabatic shear band are investi-

gated. We define a criterion that allows a consistent determination of the onset of localization. The present results are compared favourably with those of the Modified Smooth Particle Hydrodynamics method (Batra and Zhang, 2004), and somewhat less efficient than the Chebyshev Pseudo Spectral method (Bayliss et al., 1994). The governing equations are not integrated further since we are not considering any fracture criterion.

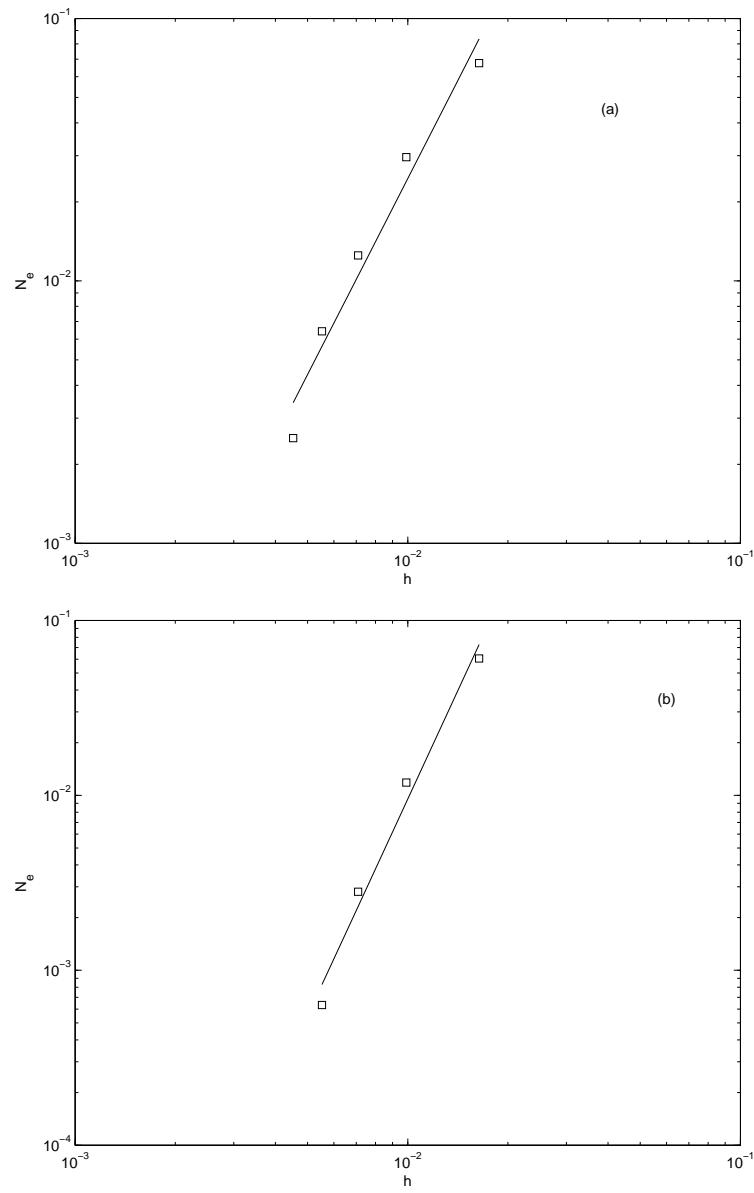


Figure 6.18: Convergence characteristics: (a) thermal imperfection model, (b) strength imperfection model.

Chapter 7

Modeling elasto-plastic and strain localization problems in two dimensions with MIRBFN meshless method

7.1 Introduction

Numerical simulation of shear bands and other material instability phenomena has become of considerable interest because of its importance in prediction of failure of materials. It is known that the classical rate-independent plasticity theory does not possess an intrinsic length scale, which leads to numerical pathologies in simulation of strain localization such as mesh size and mesh alignment sensitivities as mentioned in section 1.1. Several regularization mechanisms have been introduced in constitutive model, including non-local models (Patzák and Jirásek, 2003; Le et al., 2007b, 2008a), rate-dependent models (Le et al., 2006, 2007a), gradient-dependent models, visco-plastic models (Wang et al., 1997), damage-based models (de Borst, 2002), and Cosserat continuum

model (Sluys, 1992; Alsaleh, 2004). See sections 1.1 and 1.2 for a more detailed literature review of numerical modeling of shear bands.

This chapter reports a further development of the MIRBFN Galerkin method developed in Chapters 3 and 4 for elasto-plastic and strain localization problems in two dimensions. Two constitutive models, namely elasto-plastic materials with linear strain hardening and elasto-visco-plastic materials with strain softening, are considered. In addition, preliminary results are also reported. The rest of the chapter is organized as follows. Section 7.2 describes the constitutive models. Section 7.3 presents the numerical algorithms of the present method and section 7.4 reports some preliminary results. Section 7.5 concludes the chapter.

7.2 Constitutive models

7.2.1 Rate-independent elasto-plastic materials

A classical rate-independent isotropic hardening (softening) elasto-plasticity model (Simo and Huges, 1998) is presented as follows. In this plasticity theory, the strain rate tensor is decomposed into an elastic $\dot{\boldsymbol{\epsilon}}_e$ and a plastic $\dot{\boldsymbol{\epsilon}}_p$ part according to

$$\dot{\boldsymbol{\epsilon}} = \dot{\boldsymbol{\epsilon}}_e + \dot{\boldsymbol{\epsilon}}_p. \quad (7.1)$$

Therefore the stress-strain relation can be written in a rate form as

$$\dot{\boldsymbol{\sigma}} = \mathbf{D}_e (\dot{\boldsymbol{\epsilon}} - \dot{\boldsymbol{\epsilon}}_p), \quad (7.2)$$

where \mathbf{D}_e is the isotropic elastic constitutive tensor. The plastic strain rate tensor is written as the product of a non-negative scalar $\dot{\gamma}$ and the gradient of

the yield surface

$$\dot{\boldsymbol{\epsilon}}_p = \dot{\gamma} \frac{\partial f(\boldsymbol{\sigma}, \kappa)}{\partial \boldsymbol{\sigma}}, \quad (7.3)$$

where f is the yield function, which is defined by

$$f(\boldsymbol{\sigma}, \kappa) = 0, \quad (7.4)$$

where κ is a scalar value, namely hardening or softening parameter which is dependent on the strain history. For example, κ can be integrated in time via

$$\kappa = \int_0^t \sqrt{\frac{2}{3}(\dot{\boldsymbol{\epsilon}}_p)^T \dot{\boldsymbol{\epsilon}}_p} dt. \quad (7.5)$$

The Prager's consistency condition is

$$\dot{f}(\boldsymbol{\sigma}, \kappa) = 0, \quad (7.6)$$

which can be rewritten in another form as follows.

$$\mathbf{n}^T \dot{\boldsymbol{\sigma}} + \frac{\partial f}{\partial \kappa} \dot{\kappa} = 0, \quad (7.7)$$

where \mathbf{n} is the gradient of the yield surface

$$\mathbf{n} = \frac{\partial f}{\partial \boldsymbol{\sigma}}. \quad (7.8)$$

The yield criterion and the loading (unloading) conditions can be expressed in Kuhn-Tucker form as

$$\dot{\gamma} \geq 0, \quad f \leq 0, \quad \dot{\gamma} f = 0. \quad (7.9)$$

From (7.2),(7.3) and (7.7), $\dot{\gamma}$ can be determined by

$$\dot{\gamma} = \frac{\mathbf{n}^T \mathbf{D}_e \dot{\boldsymbol{\epsilon}}}{h^* + \mathbf{n}^T \mathbf{D}_e \mathbf{m}}, \quad (7.10)$$

where h^* is the hardening (softening) modulus.

The relation between stress rate and strain rate is obtained by substitution of (7.10) in (7.2) as follows.

$$\dot{\boldsymbol{\sigma}} = \left[\mathbf{D}_e - \frac{\mathbf{D}_e \mathbf{m} \mathbf{n}^T \mathbf{D}_e}{h^* + \mathbf{n}^T \mathbf{D}_e \mathbf{m}} \right] \dot{\boldsymbol{\varepsilon}}. \quad (7.11)$$

The expression in brackets is called the continuum tangent stiffness matrix. The integration of this rate equation can be done via explicit or implicit scheme such as Euler forward or Euler backward formula.

7.2.2 Rate-dependent elasto-visco-plastic materials

In the Perzyna's viscoplastic model (Simo and Huges, 1998), the viscoplastic strain rate is defined as

$$\dot{\boldsymbol{\varepsilon}}_{vp} = \dot{\gamma} \frac{\partial f(\boldsymbol{\sigma}, \kappa)}{\partial \boldsymbol{\sigma}}, \quad (7.12)$$

where

$$\dot{\gamma} = \frac{1}{\eta} \langle f(\boldsymbol{\sigma}, \kappa) \rangle, \quad (7.13)$$

in which η is a fluidity parameter. The notation $\langle \cdot \rangle$ is defined as

$$\langle x \rangle = \begin{cases} x, & \text{if } x > 0, \\ 0, & \text{otherwise.} \end{cases} \quad (7.14)$$

7.3 Numerical algorithms

7.3.1 Weak form of MIRBFN meshless method

The weak form for the governing equations with quasi-static assumption is expressed as

$$\int_{\Omega} \delta(\nabla_s \mathbf{u})^T \boldsymbol{\sigma} d\Omega = \int_{\Omega} \delta \mathbf{u}^T \mathbf{b} d\Omega + \int_{\Gamma_t} \delta \mathbf{u}^T \bar{\mathbf{t}} d\Gamma, \quad (7.15)$$

where the subscript s denotes the symmetric part of the gradient operator.

Linearisation of Equation (7.15) in conjunction with MIRBFN as described in section 3.2.2 and nonlinear constitutive stress-strain relation (plasticity) yields

$$\mathbf{K}^T \Delta \mathbf{u} = \mathbf{f}^{ext} - \mathbf{f}^{int}(\mathbf{u}) \quad (7.16)$$

$$\mathbf{u}_{n+1}^{k+1} = \mathbf{u}_{n+1}^k + \Delta \mathbf{u}, \quad (7.17)$$

where \mathbf{f}^{int} and \mathbf{f}^{ext} are respectively internal and external force vectors, \mathbf{u} the displacement vector, k and n denote the k th iteration and the n th loading step, respectively. \mathbf{K}^T , \mathbf{f}^{ext} and $\mathbf{f}^{int}(\mathbf{u})$ are defined by

$$\mathbf{K}_{ij}^T = \int_{\Omega} \mathbf{B}_i^T \mathbf{D}^{ep} \mathbf{B}_j d\Omega, \quad (7.18)$$

$$\mathbf{f}_i^{ext} = \int_{\Gamma_t} \phi_i \bar{\mathbf{t}} d\Gamma + \int_{\Omega} \phi_i \mathbf{b} d\Omega, \quad (7.19)$$

$$\mathbf{f}_i^{int}(\mathbf{u}) = \int_{\Omega} \mathbf{B}_i^T \boldsymbol{\sigma} d\Omega, \quad (7.20)$$

in which \mathbf{D}^{ep} is the tensor of consistent tangent elastoplastic modulus and \mathbf{B} given by

$$\mathbf{B}_i = \begin{bmatrix} (\Phi_x)_i & 0 \\ 0 & (\Phi_y)_i \\ (\Phi_y)_i & (\Phi_x)_i \end{bmatrix}. \quad (7.21)$$

7.3.2 Radial return mapping scheme

elasto-plasticity

A radial return mapping algorithm to update stress and internal variables for von Mises materials and plane strain case (Simo and Huges, 1998; Krenk, 2009) is as follows.

Given the increment of strain

$$\Delta \boldsymbol{\varepsilon} = \boldsymbol{\varepsilon}_{n+1} - \boldsymbol{\varepsilon}_n, \quad (7.22)$$

corresponding to a typical (pseudo-) time increment $[t_n, t_{n+1}]$, and given the state variables $[\boldsymbol{\sigma}_n, \kappa_n]$ at t_n , the elastic trial state variables are

$$\Delta \boldsymbol{\sigma} = \mathbf{D}_e \Delta \boldsymbol{\varepsilon}, \quad (7.23)$$

$$\boldsymbol{\sigma}_{n+1}^{trial} = \boldsymbol{\sigma}_n + \Delta \boldsymbol{\sigma}, \quad (7.24)$$

$$\mathbf{s}_{n+1}^{trial} = \text{dev}[\boldsymbol{\sigma}_{n+1}^{trial}], \quad (7.25)$$

$$\kappa_{n+1}^{trial} = \kappa_n. \quad (7.26)$$

Having computed the elastic trial state, the next step is to check whether $\boldsymbol{\sigma}_{n+1}^{trial}$ lies inside or outside of the trial yield surface as follows.

- If $\boldsymbol{\sigma}_{n+1}^{trial}$ lies inside of the yield surface, i.e. if

$$f^{trial} = \|\mathbf{s}_{n+1}^{trial}\| - \sqrt{\frac{2}{3}} (\sigma_{Y0} + h^* \kappa_{n+1}^{trial}) \leq 0, \quad (7.27)$$

then the process within the interval $[t_n, t_{n+1}]$ is purely elastic and the trial state is the solution to the integration problem, i.e.

$$\boldsymbol{\varepsilon}_{n+1} = \boldsymbol{\varepsilon}_{n+1}^{trial},$$

$$\boldsymbol{\sigma}_{n+1} = \boldsymbol{\sigma}_{n+1}^{trial},$$

$$\kappa_{n+1} = \kappa_{n+1}^{trial},$$

- Otherwise, the process is elasto-plastic and the following return mapping is employed.

In the case of linear isotropic hardening (softening), increment of plastic

multiplier $\Delta\gamma$ is given by

$$\Delta\gamma = \frac{f^{trial}}{2\tilde{G} + \frac{2h^*}{3}}, \quad (7.28)$$

where \tilde{G} is the shear modulus.

Then the state variables are updated as follows.

$$\begin{aligned} \boldsymbol{\varepsilon}_{n+1} &= \boldsymbol{\varepsilon}_n + \Delta\boldsymbol{\varepsilon}, \\ \kappa_{n+1} &= \kappa_n + \sqrt{\frac{2}{3}}\Delta\gamma, \\ \boldsymbol{\sigma}_{n+1} &= \tilde{K}\text{trace}[\boldsymbol{\varepsilon}_{n+1}]\mathbf{1} + \mathbf{s}_{n+1}^{trial} - 2\tilde{G}\Delta\gamma \frac{\mathbf{s}_{n+1}^{trial}}{\|\mathbf{s}_{n+1}^{trial}\|}, \end{aligned}$$

where \tilde{K} is the bulk modulus, and

$$\mathbf{1} = [1 \quad 1 \quad 1 \quad 0]^T.$$

The consistent elasto-plastic tangent modulus \mathbf{D}^{ep} is computed by

$$\mathbf{D}_{n+1}^{ep} = \tilde{K}\mathbf{1} \otimes \mathbf{1} + 2\tilde{G}\Theta_{n+1} \left[\mathbf{I} - \frac{1}{3}\mathbf{1} \otimes \mathbf{1} \right] - 2\tilde{G}\bar{\Theta}_{n+1} \left[\frac{\mathbf{s}_{n+1}^{trial}}{\|\mathbf{s}_{n+1}^{trial}\|} \otimes \frac{\mathbf{s}_{n+1}^{trial}}{\|\mathbf{s}_{n+1}^{trial}\|} \right], \quad (7.29)$$

where

$$\begin{aligned} \Theta_{n+1} &= 1 - \frac{2\tilde{G}\Delta\gamma}{\|\mathbf{s}_{n+1}^{trial}\|}, \\ \bar{\Theta}_{n+1} &= \frac{1}{1 + \frac{\sigma_{Y0} + h^*\kappa_{n+1}}{3\tilde{G}}} - (1 - \Theta_{n+1}), \end{aligned}$$

$$\mathbf{I} = \begin{bmatrix} 1 & 0 & 0 & 0 \\ 0 & 1 & 0 & 0 \\ 0 & 0 & 1 & 0 \\ 0 & 0 & 0 & \frac{1}{2} \end{bmatrix}.$$

Extension to elasto-visco-plasticity

The extension of the above radial return mapping to the elasto-visco-plastic model presented in section 7.2.2 requires some minor modifications, which are discussed in the sequel. Starting from (7.13), we define the increment of visco-plastic multiplier $\Delta\gamma^{vp}$ as

$$\Delta\gamma^{vp} = \frac{\Delta t}{\eta} \langle f(\boldsymbol{\sigma}_{n+1}, \kappa_{n+1}) \rangle. \quad (7.30)$$

Due to the fact that in rate-dependent plasticity the loading-unloading conditions are missing, the computation of $\Delta\gamma^{vp}$ is carried out (for $f^{trial} > 0$) by inverting (7.30) to obtain

$$f_{n+1} = f(\boldsymbol{\sigma}_{n+1}, \kappa_{n+1}) = \frac{\eta\Delta\gamma^{vp}}{\Delta t}. \quad (7.31)$$

The relation between f_{n+1} and f_{n+1}^{trial} is

$$f_{n+1} = f_{n+1}^{trial} - (2\tilde{G} + \frac{2}{3}h^*)\Delta\gamma^{vp}. \quad (7.32)$$

Accordingly, one obtains

$$\Delta\gamma^{vp} = \frac{f_{n+1}^{trial}}{\frac{\eta}{\Delta t} + 2\tilde{G} + \frac{2h^*}{3}}, \quad (7.33)$$

which differs from (7.28) only for the presence of the term $\frac{\eta}{\Delta t}$ in the denominator, which somehow plays the same role as a hardening modulus.

Finally, the tangent visco-plastic modulus is given by

$$\mathbf{D}_{n+1}^{ep} = \tilde{K}\mathbf{1}\otimes\mathbf{1} + 2\tilde{G}\tilde{\Theta}_{n+1} \left[\mathbf{I} - \frac{1}{3}\mathbf{1}\otimes\mathbf{1} \right] - 2\tilde{G}\tilde{\Theta}_{n+1} \left[\frac{\mathbf{s}_{n+1}^{trial}}{\|\mathbf{s}_{n+1}^{trial}\|} \otimes \frac{\mathbf{s}_{n+1}^{trial}}{\|\mathbf{s}_{n+1}^{trial}\|} \right], \quad (7.34)$$

where

$$\Theta_{n+1} = 1 - \frac{2\tilde{G}\Delta\gamma^{vp}}{\|\mathbf{s}_{n+1}^{trial}\|},$$

$$\bar{\Theta}_{n+1} = \frac{1}{\frac{\eta}{2G\Delta t} + 1 + \frac{h}{3G}} - \frac{2\tilde{G}\Delta\gamma^{vp}}{\|\mathbf{s}_{n+1}^{trial}\|}.$$

7.3.3 Orthogonal residual solver

An elegant procedure, namely orthogonal residual method, originally devised by Krenk (Krenk, 1995; Krenk and Hededal, 1995; Kouhia, 2008), is used in this chapter. In this method the load is adjusted in such a way that the residual force is orthogonal to the current displacement increment. This method is well suited with the use of iterative solvers since it does not need a block elimination scheme. The method is supplemented with displacement increment control (Krenk, 2009), leading to improved robustness of algorithm. The supplemented version of the method is briefly presented as follows.

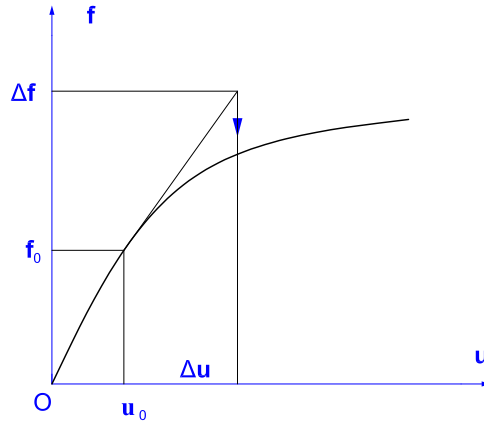


Figure 7.1: Schematic representation of orthogonal residual method.

 Algorithm 8.1. Orthogonal residual procedure

initial state: \mathbf{u}_0 , \mathbf{f}_0^{ext} , $\Delta \mathbf{u} = 0$

Load increment $n = 1, 2, \dots, n_{max}$

$$\Delta \mathbf{u}_1 = (\mathbf{K}^T)^{-1} \Delta \mathbf{f}^{ext}$$

if $(\Delta \mathbf{u}_1)^T \Delta \mathbf{u} < 0$ then

$$\Delta \mathbf{u}_1 = -\Delta \mathbf{u}_1, \Delta \mathbf{f}^{ext} = -\Delta \mathbf{f}^{ext}$$

$$\Delta \mathbf{u} = \min(1, u_{max}/\|\Delta \mathbf{u}_1\|) \Delta \mathbf{u}_1$$

Iteration $i = 1, 2, \dots, i_{max}$

$$\Delta \mathbf{f}^{int} = \mathbf{f}^{int}(\mathbf{u}_{n-1} + \Delta \mathbf{u}) - \mathbf{f}_{n-1}^{ext}$$

$$\xi = \frac{(\Delta \mathbf{f}^{int})^T \Delta \mathbf{u}}{(\Delta \mathbf{f}^{ext})^T \Delta \mathbf{u}}$$

$$\mathbf{R} = \xi \Delta \mathbf{f}^{ext} - \Delta \mathbf{f}^{int}$$

$$\delta \mathbf{u} = (\mathbf{K}^T)^{-1} \mathbf{R}$$

Stop iteration if $\frac{\|\mathbf{R}\|}{\|\Delta \mathbf{f}^{ext}\|} < Tolerance$

Update the state variables:

$$\mathbf{u}_n = \mathbf{u}_{n-1} + \Delta \mathbf{u}$$

$$\mathbf{f}_n = \mathbf{f}_{n-1} + \xi \Delta \mathbf{f}$$

Stop load increment if $n > n_{max}$ or $\|\mathbf{f}^{ext}\| > \|\mathbf{f}_{max}^{ext}\|$

Let the equilibrium equation to be solved for be of the form

$$\mathbf{f}^{int}(\mathbf{u}) = \mathbf{f}^{ext}. \quad (7.35)$$

Consider a single load step, let $(\mathbf{u}_0, \mathbf{f}_0^{ext})$ be the last established equilibrium state. A load increment $\Delta \mathbf{f}^{ext}$ is applied, and the corresponding displacement increment is

$$\mathbf{K}^T \Delta \mathbf{u} = \Delta \mathbf{f}^{ext}. \quad (7.36)$$

This leads to the predicted displacement $\mathbf{u}_0 + \Delta \mathbf{u}$ and internal force $\mathbf{f}^{int}(\mathbf{u}_0 + \Delta \mathbf{u})$. The load increment is now adjusted by a scaled load increment $\xi \Delta \mathbf{f}^{ext}$

instead of $\Delta \mathbf{f}^{ext}$ as illustrated in Figure 7.1. The associated residual force \mathbf{R} is

$$\begin{aligned}\mathbf{R} &= \mathbf{f}_0^{ext} + \xi \Delta \mathbf{f}^{ext} - \mathbf{f}^{int}(\mathbf{u}_0 + \Delta \mathbf{u}) = \xi \Delta \mathbf{f}^{ext} - \mathbf{f}^{int}(\mathbf{u}_0 + \Delta \mathbf{u}) - \mathbf{f}^{int}(\mathbf{u}_0) \\ &= \xi \Delta \mathbf{f}^{ext} - \Delta \mathbf{f}^{int},\end{aligned}\tag{7.37}$$

where ξ is the scaling factor whose optimal value is determined from orthogonality condition of \mathbf{R} and $\Delta \mathbf{u}$

$$\mathbf{R}^T \Delta \mathbf{u} = 0.\tag{7.38}$$

Substitution of (7.37) into (7.38) leads to

$$\xi = \frac{(\Delta \mathbf{f}^{int})^T \Delta \mathbf{u}}{(\Delta \mathbf{f}^{ext})^T \Delta \mathbf{u}}.\tag{7.39}$$

When the optimal residual \mathbf{R} has been reached, a sub-increment of displacement $\delta \mathbf{u}$ is determined from

$$\mathbf{K}^T \delta \mathbf{u} = \mathbf{R}.\tag{7.40}$$

The orthogonal residual procedure is summarized in Algorithm 8.1.

7.4 Preliminary results

7.4.1 Elasto-plastic constitutive model with linear strain hardening

Consider a finite plate with a circular hole in uniaxial tension as shown in Figure 7.2, where $H = 2$, $W = 6$ and $R = 1$. Owing to symmetry, a quarter of the plate is modeled as depicted in Figure 7.3. The material parameters are taken as, the elastic modulus $E = 100$, Poisson ratio $\nu = 0.3$, the initial yield stress $\sigma_{Y0} = 1$, the hardening modulus $h^* = 10$. Here the von Mises yield function is

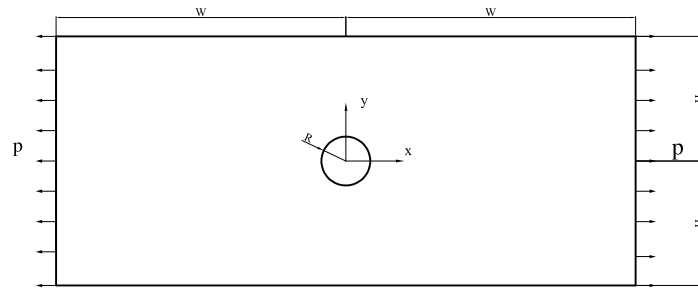


Figure 7.2: A holed plate in uniaxial tension: a mathematical model.

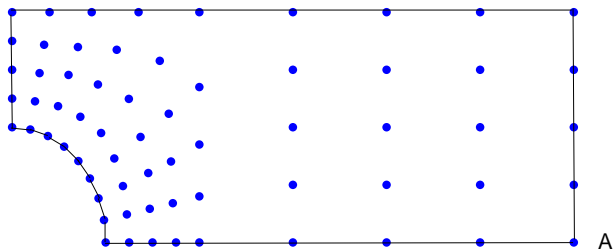


Figure 7.3: A holed plate in uniaxial tension: discretization.

used for the yield criterion.

The obtained results with 65 unstructured nodes (Figure 7.3) are as follows. Figure 7.4 shows equilibrium path of the problem at load-step 45 (using displacement of node A). The evolution of the equivalent plastic strain at Gauss points is presented in Figures 7.5-7.7. The corresponding von Mises stress at Gauss points at load-step 45 is also plotted in Figure 7.8.

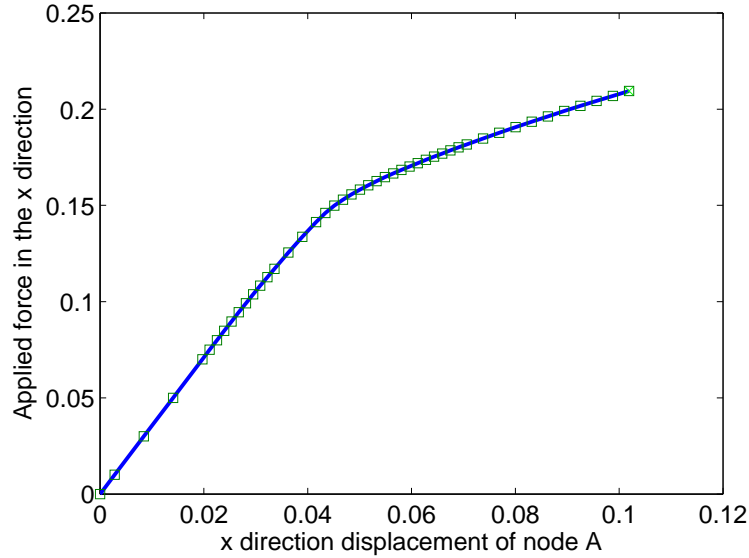


Figure 7.4: A holed plate in uniaxial tension with elasto-plastic constitutive model: load versus displacement.

7.4.2 Elasto-visco-plastic constitutive model with linear strain softening

The previous problem is considered here with a elasto-visco-plastic constitutive relation with linear strain softening. All the parameters are the same as in the previous example except that the softening modulus $h^* = -50$ and a displacement $\delta u = v_0 t$ is applied on the left and right edges instead of the traction, where the velocity $v_0 = 0.1$ and the time increment $\Delta t = 0.01$. The Perzyna elasto-visco-plastic model is used with the fluidity parameter $\eta = 70$.

The discretised model is the same as that in previous example. The obtained results are shown in Figures 7.9-7.12. The effect of strain softening can be observed in Figure 7.9, which shows the equilibrium path of the problem at load-step 15 (using displacement of node A). The evolution of strain localization is depicted in Figures 7.10-7.11, which plot the equivalent plastic strain at Gauss points at load-steps 10 and 15, respectively. The associated von Mises stress at load-step 15 is also displayed in Figure 7.12.

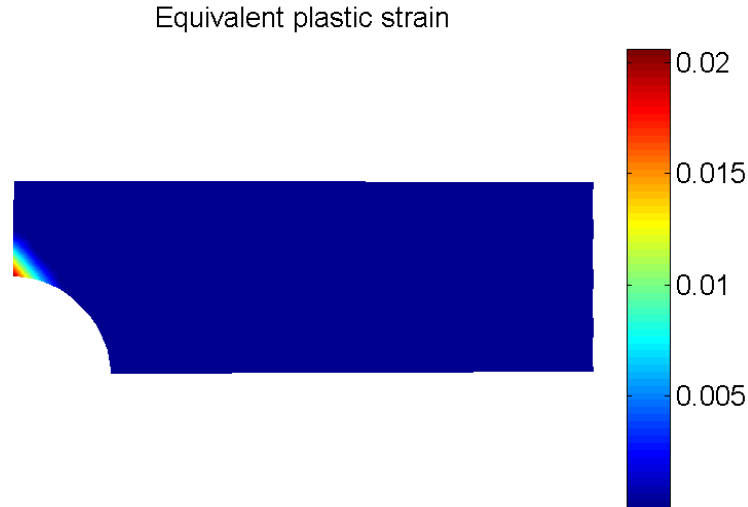


Figure 7.5: A holed plate in uniaxial tension with elasto-plastic constitutive model: equivalent plastic strain at load-step 15.

7.5 Conclusion

In this chapter, the MIRBFNG meshless method has been further developed for plasticity and strain localization problems in two dimensions. Two constitutive relations, namely elasto-plasticity with strain hardening and elasto-visco-plasticity with strain softening, are considered. The method is illustrated with examples in section 7.4. The preliminary results indicate that the present method is successfully applied to non-linear plasticity and strain localization problems.

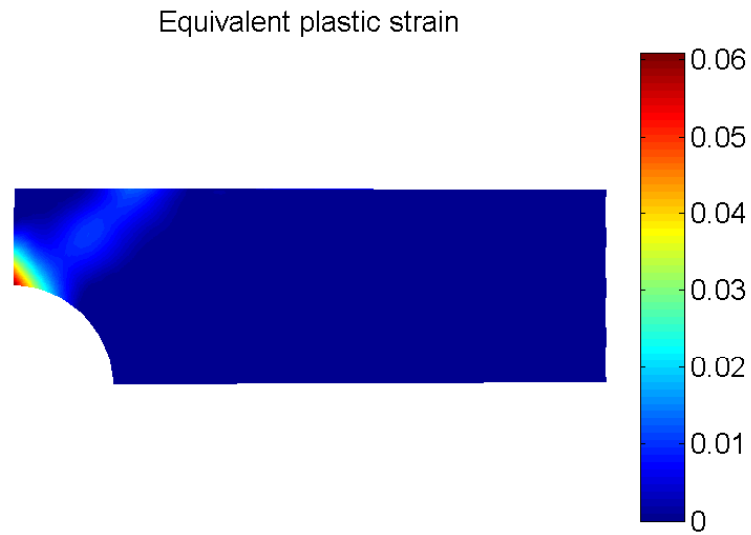


Figure 7.6: A holed plate in uniaxial tension with elasto-plastic constitutive model: equivalent plastic strain at load-step 25.

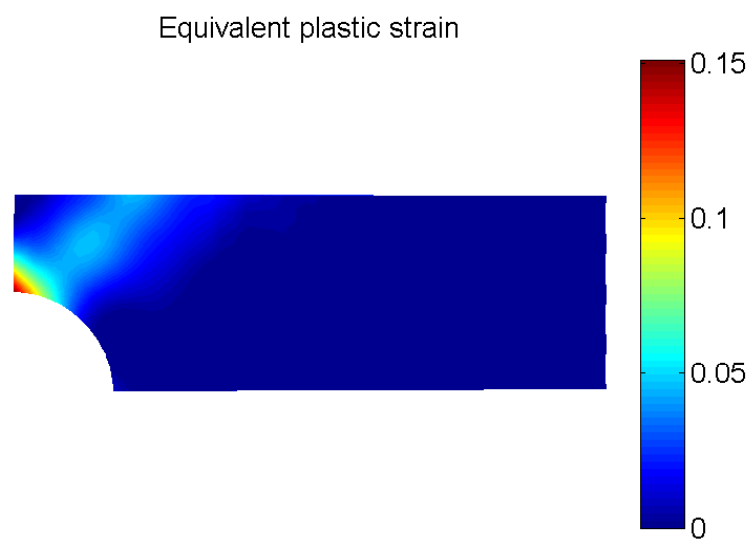


Figure 7.7: A holed plate in uniaxial tension with elasto-plastic constitutive model: equivalent plastic strain at load-step 45 .

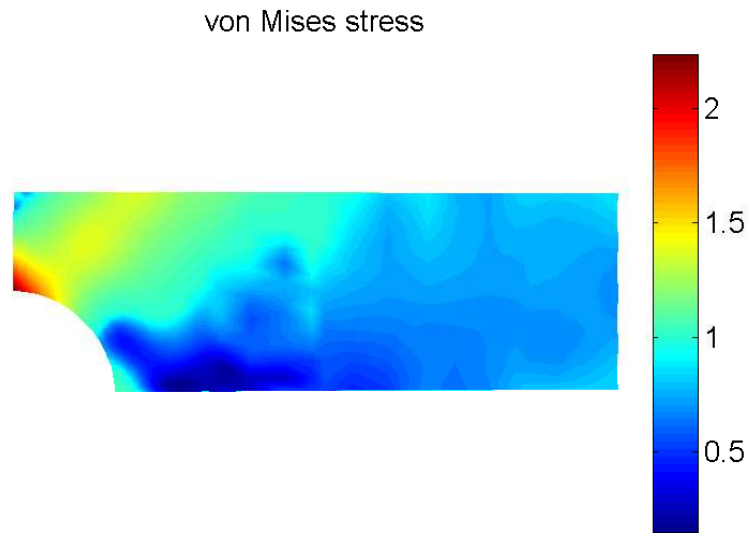


Figure 7.8: A holed plate in uniaxial tension with elasto-plastic constitutive model: von Mises stress at load-step 45.

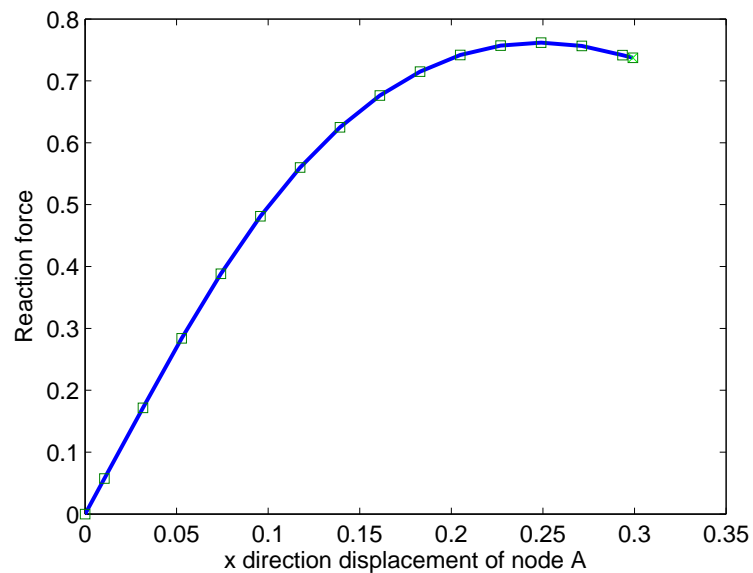


Figure 7.9: A holed plate in uniaxial tension with elasto-visco-plastic constitutive model with linear strain softening: load versus displacement.

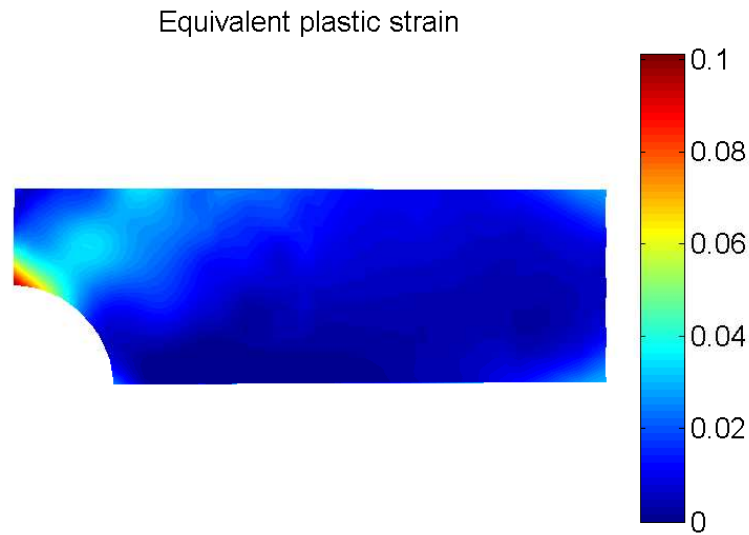


Figure 7.10: A holed plate in uniaxial tension with elasto-visco-plastic constitutive model with linear strain softening: strain localization at load-step 10.

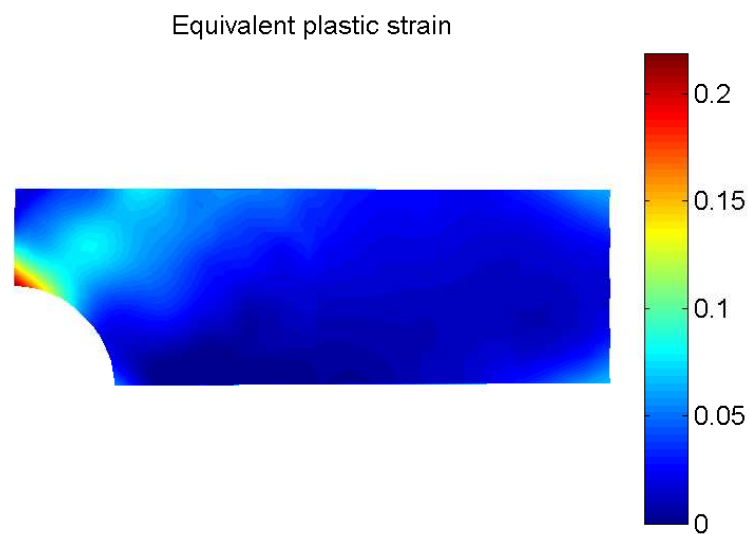


Figure 7.11: A holed plate in uniaxial tension with elasto-visco-plastic constitutive model with linear strain softening: strain localization at load-step 15.

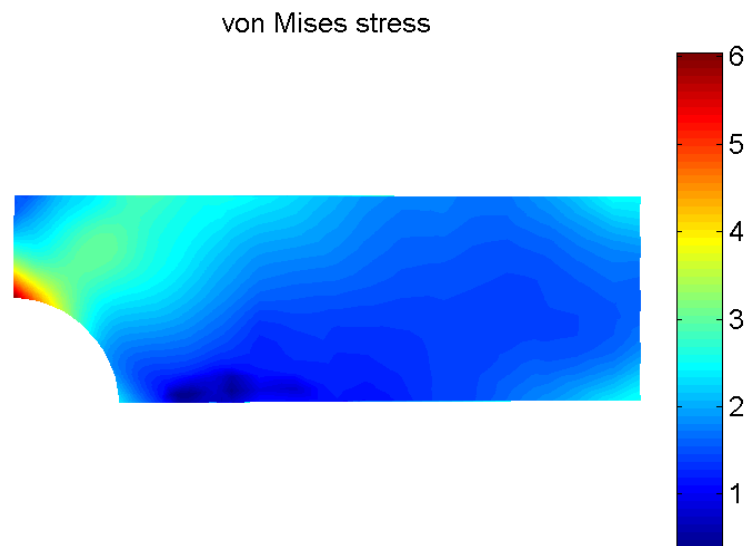


Figure 7.12: A holed plate in uniaxial tension with elasto-visco-plastic constitutive model with linear strain softening; von Mises stress at load-step 15.

Chapter 8

Modeling elasto-static crack problems with an extended MIRBFN (XMIRBFN) meshless method

This chapter presents a new meshless method based on MIRBFN Galerkin meshless method and local partition of unity enrichment for linear crack problems. In the present method, the shape functions are constructed within subdomains instead of the global domain. The system matrix is thus sparse and banded. The feature of the method is that the shape functions satisfy the Kronecker-delta property, which facilitates the imposition of essential boundary conditions. The method is verified by various benchmark examples and compared with the extended finite element method (XFEM) and the element free Galerkin (EFG) method. The results demonstrate that the present method achieves high accuracy and rates of convergence.

8.1 Introduction

Fracture mechanics is of major importance in engineering design and prediction of life of structures. Although this discipline has been the object of intensive research interest in the academic community in the last decades, numerical modeling of fracture mechanics still faces challenges. Several methods developed to model cracks have been reported in finite element and meshless literatures.

In the finite element method, simplified approaches have been introduced for crack problems, including adaptive remeshing (Pastor et al., 1991; Potyondy et al., 1995; Askes, 2000; Schollmann et al., 2003; Patzák and Jirásek, 2004; Li et al., 2005) and element deletion (Fan and Fish, 2008). Although these approaches are useful, more accurate methods are necessary for certain classes of problems. A very accurate method among the FEMs is the extended finite element method (XFEM) (Belytschko and Black, 1999; Moës et al., 1999a; Bordas et al., 2008a), in which the solution space is enriched by a priori knowledge about the behaviour of the solution near a discontinuity with the use of the partition of unity concept. Recently developed XFEM has been proven to be an efficient tool for computational fracture mechanics, including multiple-cracks simulation (Budyn et al., 2004). This method can also deal with arbitrary crack or shear band propagation without adaptive remeshing. Difficulties occur in the so-called blending regions (Chessa et al., 2003), i.e. regions that are partially enriched. Partition of unity does not hold in the blending regions leading to inaccurate solutions. However, such difficulties in the blending region can be overcome by shifting in partition of unity method or using a ramp function to localize the enrichment functions (Fries, 2008).

In contrast to the FEM, meshless methods offer some advantages that include inter alia higher order continuity, non-local approximation, insensitivity to mesh distortion, ease in h-refinement and no need for mesh generation. Thus, meshless methods provide more continuous solutions than the piece-wise continuous

ones obtained by the FEM. Among the meshless methods, the element free Galerkin method (EFG) (Belytschko et al., 1994), which is based on moving least square approximations, is one of the most frequently used meshless methods. This method has been very successfully applied to fracture mechanics and discontinuous problems such as cracks and shear bands (Rabczuk et al., 2007a; Rabczuk and Samaniego, 2008; Bordas et al., 2008c; Rabczuk et al., 2007c). Recently, partition of unity based enrichment functions have been introduced in the EFG method (Rabczuk and Belytschko, 2004a, 2007a) to further improve its performance with discontinuous problems. Reviews of meshless methods can be found in Belytschko et al. (1996b) and Nguyen et al. (2008a), for example. However, the major disadvantage of the EFG as well as moving least square (MLS) based meshless methods is that the shape functions lack the Kronecker-delta property, i.e. $\phi_i(\mathbf{x}_j) \neq \delta_{ij}$. Therefore, essential boundary conditions cannot be imposed in strong form as in the FEM. Attempts to overcome this shortcoming include Lagrange multiplier and penalty method (Zhu and Atluri, 1998), Nitsche's method (Fernández-Mández and Huerta, 2004), point collocation (Wanger and Liu, 1999), singular weight functions (Kaljevic and Saigal, 1997), and coupling with FEM (Belytschko et al., 1995b; Rabczuk et al., 2006).

This chapter presents a novel meshless approach based on MIRBFN Galerkin meshless method (Le et al., 2010c,b) and local partition of unity enrichment, namely eXtended MIRBFN (XMIRBFN) Galerkin meshless method, for elasto-static crack problems. In the present method, the shape functions are constructed within subdomains instead of the global domain. The system matrix is thus sparse and banded. The shape functions satisfy the Kronecker-delta property, therefore, essential boundary conditions are imposed easily and straightforwardly as in the FEMs. The remaining of this chapter is organized as follows. The local PU enrichment of MIRBFN approximation is briefly presented in section 8.2.1 followed by the Galerkin discretization for elasto-static crack problems in section 8.2.2. Section 8.3 reports the benchmark verification

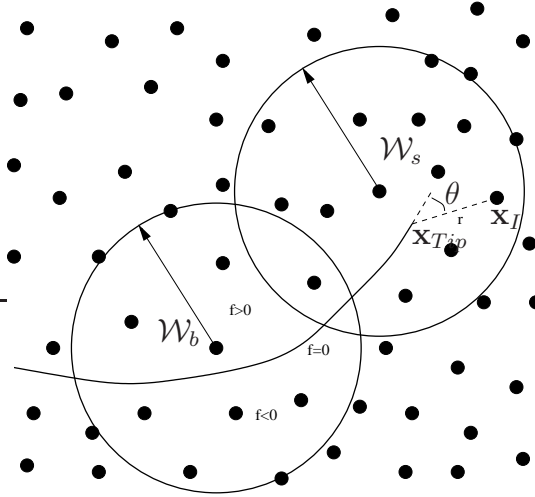


Figure 8.1: Domain of influence of nodes partially and completely cut by a crack

and section 8.4 draws some conclusions.

8.2 Extended Moving IRBFN procedure

8.2.1 Local PU enrichment

The displacement field is decomposed into a standard part \mathbf{u}_{std} and a discontinuous part \mathbf{u}_{enr}

$$\mathbf{u}(\mathbf{x}) = \mathbf{u}_{std}(\mathbf{x}) + \mathbf{u}_{enr}(\mathbf{x}), \quad (8.1)$$

where \mathbf{u}_{std} is approximated by the ‘standard’ MIRBFN procedure constructed in section 3.2.

The discontinuous displacement approximation is only required in a sub-domain influence by the crack as illustrated in Figure 8.1. The approximation of the discontinuous displacement field can be written as (Moës et al., 1999a; Ventura et al., 2002; Rabczuk and Zi, 2007)

$$\mathbf{u}_{enr}(\mathbf{x}) = \sum_{J \in \mathcal{N}^{step}} \Phi_J(\mathbf{x}) [H(\mathbf{x}) - H(\mathbf{x}_J)] \mathbf{a}_J + \sum_{K \in \mathcal{N}^{Tip}} \Phi_K(\mathbf{x}) \sum_{\kappa=1}^4 [B_\kappa(\mathbf{x}) - B_\kappa(\mathbf{x}_K)] \mathbf{b}_{K\kappa}, \quad (8.2)$$

where \mathcal{N}^{step} is the set of enriched nodes whose support is entirely cut by the crack, \mathcal{N}^{Tip} is the set of nodes whose support is partially cut by the crack (Figure 8.1), $H(\mathbf{x})$ is the step enrichment functions

$$H(\mathbf{x}) = \begin{cases} +1 & \text{if } (\mathbf{x} - \mathbf{x}^*) \cdot \mathbf{n} \geq 0, \\ -1 & \text{otherwise,} \end{cases} \quad (8.3)$$

where \mathbf{x} is a sample point, \mathbf{x}^* (on the crack) is the closest point projection of \mathbf{x} , and \mathbf{n} is the unit outward normal to the crack at \mathbf{x}^* , B_κ is the set of tip enrichment functions

$$\mathbf{B}_\kappa = \left[\sqrt{r} \sin \frac{\theta}{2}, \sqrt{r} \cos \frac{\theta}{2}, \sqrt{r} \sin \frac{\theta}{2} \sin \theta, \sqrt{r} \cos \frac{\theta}{2} \sin \theta \right] \quad (8.4)$$

where r and θ are polar coordinates in the local crack tip coordinate system and \mathbf{a}_J and $\mathbf{b}_{K\kappa}$ are additional unknowns that need to be solved for.

Explicitly, the displacement approximation is

$$\begin{aligned} \mathbf{u}^h(\mathbf{x}) = & \sum_I \Phi_I(\mathbf{x}) \mathbf{u}_I + \sum_{J \in \mathcal{N}^{step}} \Phi_J(\mathbf{x}) [H(\mathbf{x}) - H(\mathbf{x}_J)] \mathbf{a}_J \\ & + \sum_{K \in \mathcal{N}^{Tip}} \Phi_K(\mathbf{x}) \sum_{\kappa=1}^4 [B_\kappa(\mathbf{x}) - B_\kappa(\mathbf{x}_K)] \mathbf{b}_{K\kappa}. \end{aligned} \quad (8.5)$$

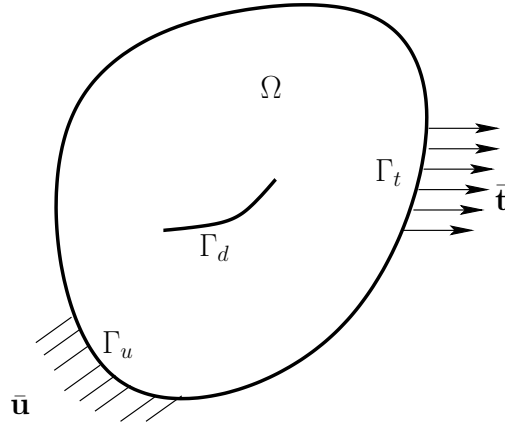


Figure 8.2: A body with internal discontinuous surface subjected to loads.

8.2.2 Variational form of 2D elasticity crack problems

Consider the following two-dimensional problem on a domain Ω bounded by $\Gamma = \Gamma_u \cup \Gamma_t$ as shown in Figure 8.2. The equilibrium equation and boundary conditions are

$$\nabla \cdot \boldsymbol{\sigma} + \mathbf{b} = 0 \quad \text{in } \Omega, \quad (8.6a)$$

$$\mathbf{u} = \bar{\mathbf{u}} \quad \text{on } \Gamma_u, \quad (8.6b)$$

$$\boldsymbol{\sigma} \cdot \mathbf{n} = \bar{\mathbf{t}} \quad \text{on } \Gamma_t, \quad (8.6c)$$

$$\boldsymbol{\sigma} \cdot \mathbf{n} = 0 \quad \text{on } \Gamma_{d^+}, \quad (8.6d)$$

$$\boldsymbol{\sigma} \cdot \mathbf{n} = 0 \quad \text{on } \Gamma_{d^-}, \quad (8.6e)$$

$$\mathbf{n}^- = \mathbf{n}^+ = \mathbf{n}, \quad (8.6f)$$

in which $\boldsymbol{\sigma}$ is the stress tensor, which corresponds to the displacement field \mathbf{u} and \mathbf{b} is the body force, \mathbf{n} the outward unit normal to Γ_t and Γ_d (discontinuous surface). The superimposed bar denotes prescribed values on the boundary.

The weak form for the above equations is expressed as

$$\int_{\Omega} \delta(\nabla_s \mathbf{u})^T \boldsymbol{\sigma} d\Omega = \int_{\Omega} \delta \mathbf{u}^T \mathbf{b} d\Omega + \int_{\Gamma_t} \delta \mathbf{u}^T \bar{\mathbf{t}} d\Gamma, \quad (8.7)$$

where the subscript s denotes the symmetric part of the gradient operator. Discretization of Equation (8.7) with Equation (8.5) yields

$$\mathbf{K}\mathbf{u} = \mathbf{f}, \quad (8.8)$$

where

$$\mathbf{K}_{ij} = \int_{\Omega} \mathbf{B}_i^T \mathbf{C} \mathbf{B}_j d\Omega, \quad (8.9)$$

$$\mathbf{f}_i = \int_{\Gamma_t} \Phi_i \bar{\mathbf{t}} d\Gamma + \int_{\Omega} \Phi_i \mathbf{b} d\Omega \quad (8.10)$$

$$\mathbf{B}_i = [\mathbf{B}_i^{std} \quad | \quad \mathbf{B}_i^{enr}], \quad (8.11)$$

$$\mathbf{B}_i^{std} = \begin{bmatrix} (\Phi_x)_i & 0 \\ 0 & (\Phi_y)_i \\ (\Phi_y)_i & (\Phi_x)_i \end{bmatrix}, \quad (8.12)$$

$$\mathbf{B}_i^{enr} = \begin{bmatrix} (\Phi_x)_i [\Psi(\mathbf{x}) - \Psi(\mathbf{x}_i)] + \Psi(\mathbf{x})_{,x} \Phi_i & 0 \\ 0 & (\Phi_y)_i [\Psi(\mathbf{x}) - \Psi(\mathbf{x}_i)] + \Psi(\mathbf{x})_{,y} \Phi_i \\ (\Phi_y)_i [\Psi(\mathbf{x}) - \Psi(\mathbf{x}_i)] + \Psi(\mathbf{x})_{,y} \Phi_i & (\Phi_x)_i [\Psi(\mathbf{x}) - \Psi(\mathbf{x}_i)] + \Psi(\mathbf{x})_{,x} \Phi_i \end{bmatrix}, \quad (8.13)$$

where $\Psi(\mathbf{x})$ is either $H(\mathbf{x})$ or $B_{\kappa}(\mathbf{x})$. For a linear Hookean constitutive relation, the matrix \mathbf{C} in the case of plane strain is

$$\mathbf{C} = \frac{E}{(1+\nu)(1-2\nu)} \begin{pmatrix} 1-\nu & \nu & 0 \\ \nu & 1-\nu & 0 \\ 0 & 0 & \frac{1-2\nu}{2} \end{pmatrix}, \quad (8.14)$$

where E is elastic modulus and ν Poisson ratio.

8.2.3 Numerical Integration

As a global weak form, a background mesh independent of nodes is necessary for numerical integration. In this chapter a background mesh of uniform rectangular cells is employed. Gauss quadrature rule is used to obtain the discrete equations. Due to the presence of the discontinuity and singularity at the crack tip, the quadrature cells cut by the crack or containing the crack tips are partitioned into sub-triangles as depicted in Figure 8.3 to further improve the accuracy of the method. Another approach is to modify the quadrature weights (Rabczuk and Areias, 2006; Rabczuk et al., 2007b), which does not require sub-triangulation. Furthermore, care should be taken at crack tips due to the presence of the singularity. To perform more accurate numerical integration with the standard Gauss quadrature points, a mapping method introduced by Nagarajan and Mukherjee (Nagarajan and Mukherjee, 1993; Park et al., 2009) is as follows.

$$T_M : (x, y) \mapsto (\rho, \theta), \quad (8.15)$$

where

$$x = \rho \cos^2 \theta, \quad y = \rho \sin^2 \theta. \quad (8.16)$$

This mapping, which transforms a rectangle into a triangle as shown in Figure 8.4, is able to eliminate the singularity in the integrand. Another approach is to transform the domain integral into a line integral as proposed by Ventura et al. (2009) and in the context of the smoothed finite element method by Bordas

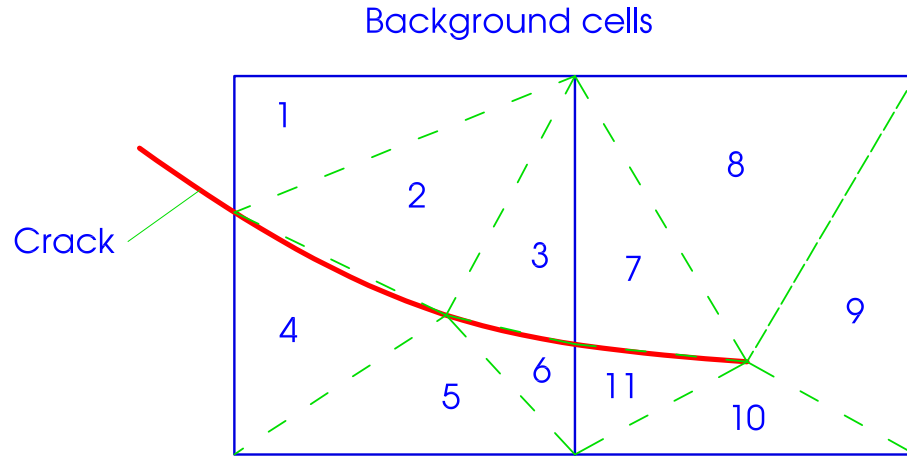


Figure 8.3: Schematic representation of sub-triangulation of integration cells.

et al. (2008b).

8.3 Numerical examples

For an error estimation and convergence study, the displacement error norm and energy error norm are defined as follows

$$\text{displacement norm} = \sqrt{\int_{\Omega} (\mathbf{u}^{num} - \mathbf{u}^{exact})^T (\mathbf{u}^{num} - \mathbf{u}^{exact}) d\Omega}, \quad (8.17)$$

$$\text{energy norm} = \sqrt{\frac{1}{2} \int_{\Omega} (\boldsymbol{\varepsilon}^{num} - \boldsymbol{\varepsilon}^{exact})^T (\boldsymbol{\sigma}^{num} - \boldsymbol{\sigma}^{exact}) d\Omega}, \quad (8.18)$$

where the superscripts *num* and *exact* denote numerical and exact solutions, respectively; the stress and strain components are presented in vector form $\boldsymbol{\sigma}$

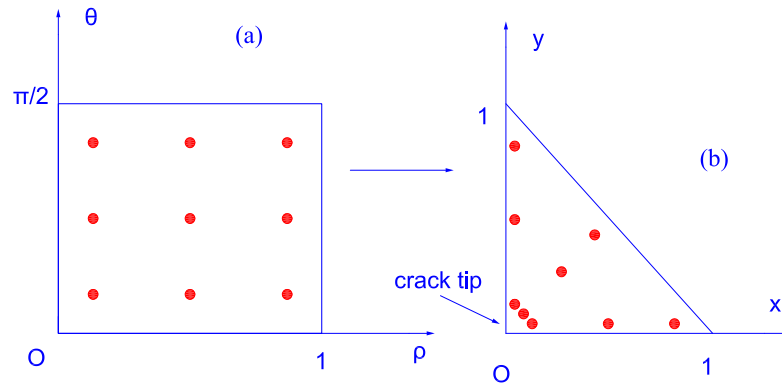


Figure 8.4: Mapping transformation of integration on a rectangle into integration on a unit triangle for near singular enrichment functions.

and ε , respectively.

The convergence order of the solution with respect to the refinement of spatial discretization is assumed to be in the form of

$$\text{error}(h) \approx \zeta h^\lambda = O(h^\lambda), \quad (8.19)$$

where h is the maximum nodal spacing, ζ and λ are the parameters of the exponential model, which are found by general linear least square formula.

In the following numerical examples, α and β are referred to as the scale factor of the radius of the domains of influence and the shape parameter of the RBF given in (1.8), respectively. α is defined by $\alpha = R_s/h$, where R_s is the radius of the domains of influence (see equation (3.15)).

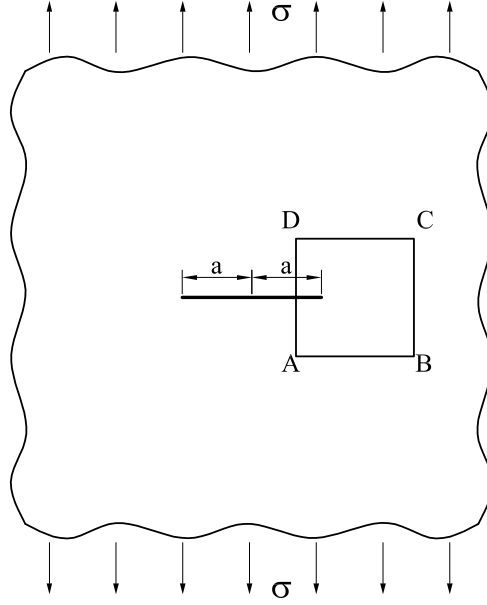


Figure 8.5: Infinite cracked plate under remote tension

8.3.1 Infinite plate with a straight crack

Consider an infinite plate containing a straight crack of length $2a$ and loaded by a remote uniaxial stress field σ as shown in Figure 8.5. Under plane strain condition, the closed form solution in terms of polar coordinates in a reference frame (r, θ) centered at the crack tip is given by (body force is zero)

$$\sigma_x = \frac{K_I}{\sqrt{r}} \cos \frac{\theta}{2} \left(1 - \sin \frac{\theta}{2} \sin 3\frac{\theta}{2} \right), \quad (8.20a)$$

$$\sigma_y = \frac{K_I}{\sqrt{r}} \cos \frac{\theta}{2} \left(1 + \sin \frac{\theta}{2} \sin 3\frac{\theta}{2} \right), \quad (8.20b)$$

$$\tau_y = \frac{K_I}{\sqrt{r}} \sin \frac{\theta}{2} \cos \frac{\theta}{2} \cos 3\frac{\theta}{2}, \quad (8.20c)$$

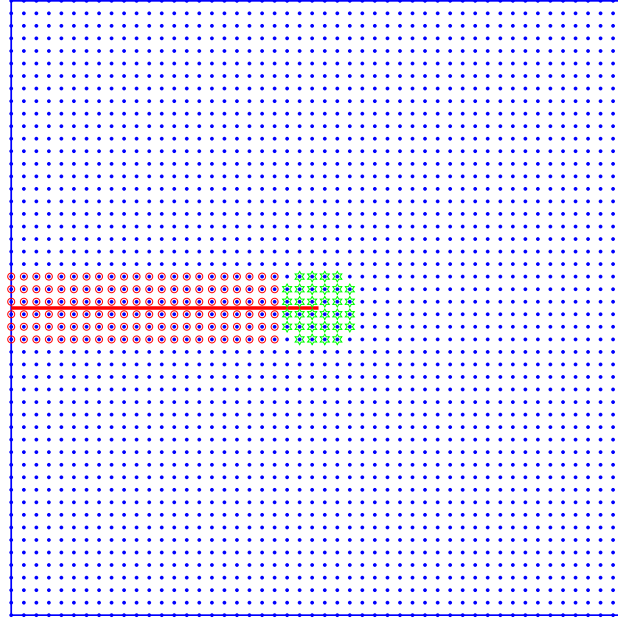


Figure 8.6: Infinite cracked plate: discretised with 50×50 nodes.

and the corresponding displacement field is given by

$$u_x = \frac{2(1 + \mu)}{\sqrt{2\pi}} \frac{K_I}{E} \sqrt{r} \cos \frac{\theta}{2} \left(2 - 2\mu - \cos^2 \frac{\theta}{2} \right), \quad (8.21a)$$

$$u_y = \frac{2(1 + \mu)}{\sqrt{2\pi}} \frac{K_I}{E} \sqrt{r} \sin \frac{\theta}{2} \left(2 - 2\mu - \cos^2 \frac{\theta}{2} \right), \quad (8.21b)$$

where $K_I = \sigma \sqrt{\pi a}$ is the stress intensity factor, μ is Poisson's ratio and E is the Young's modulus. ABCD is a square patch of $2 \times 2 \text{ in}^2$, $a = 100 \text{ in}$; $E = 10^5 \text{ psi}$, $\mu = 0.3$, $\sigma = 1 \text{ psi}$.

The computational domain ABCD shown in Figure 8.5 is discretised as shown in Figure 8.6 where the crack has a length of $b = 1 \text{ in}$. The boundary condition of the problem is as follows. The traction free boundary condition is applied on the crack while the displacement field given in equation (8.21) is imposed on the remaining boundaries.

The influence of β on the accuracy of the method is illustrated in Figure 8.7. It can be seen that the accuracy consistently increases up to $\beta = 5$ and then decreases with higher values of β . This reduction can be explained by the nature

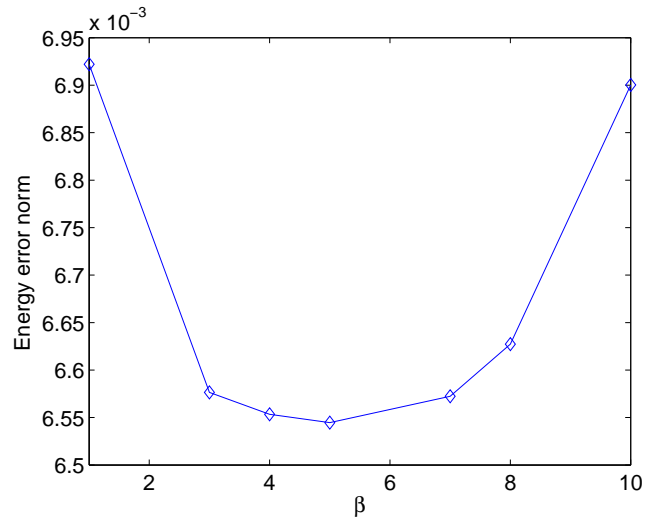


Figure 8.7: Infinite cracked plate: energy error norm versus different values of β with 30×30 nodes ($\alpha = 2.1$).

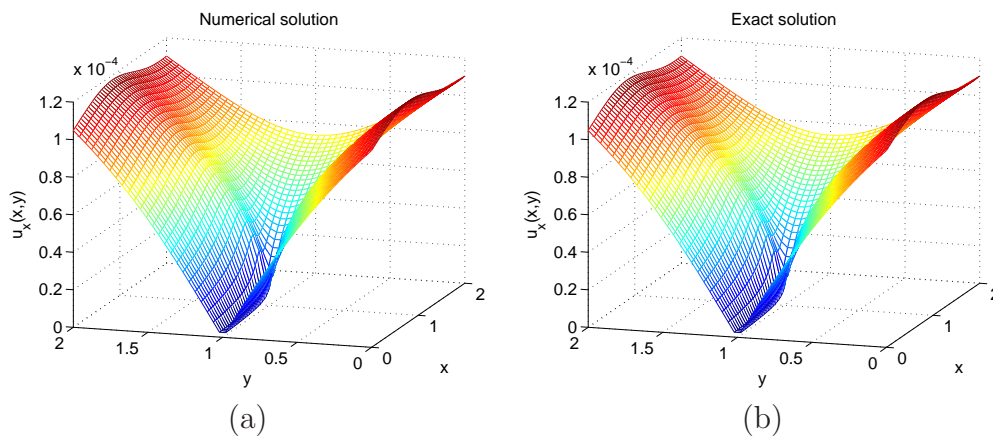


Figure 8.8: Infinite cracked plate: (a) XMIRBFN solution and (b) exact solution to u_x with 50×50 nodes.

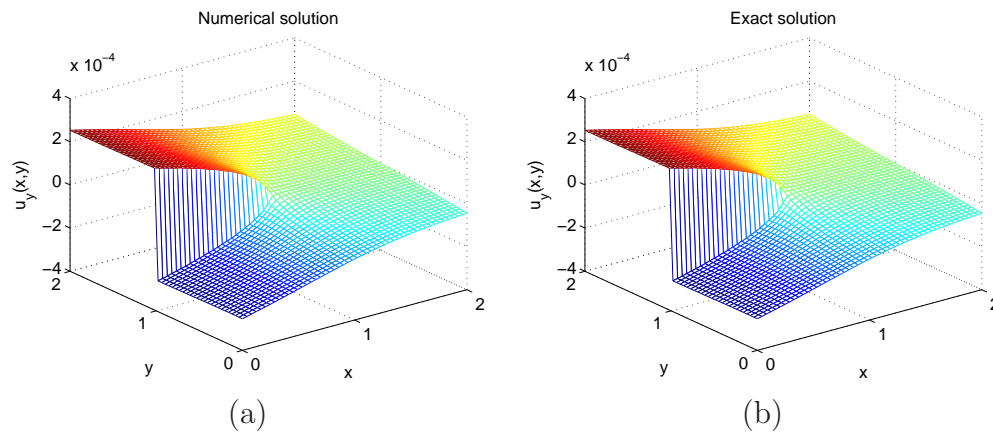


Figure 8.9: Infinite cracked plate: (a) XMIRBFN solution and (b) exact solution to u_y with 50×50 nodes.

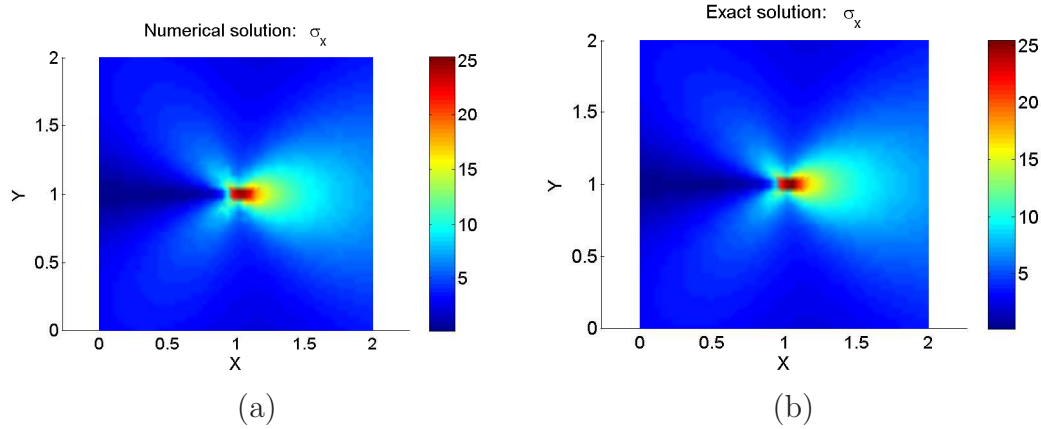


Figure 8.10: Infinite cracked plate: (a) XMIRBFN solution and (b) exact solution to σ_x with 50×50 nodes.

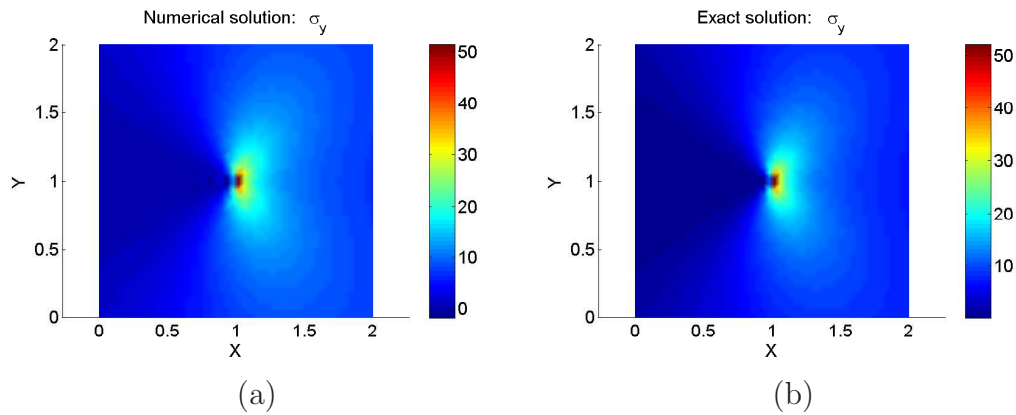


Figure 8.11: Infinite cracked plate: (a) XMIRBFN solution and (b) exact solution to σ_y with 50×50 nodes.

of RBFN approximation since the higher values of β lead to ill-conditioned systems. Therefore, for all numerical examples, β is set to 5, and α is 2.1 since small values of α will keep the method efficient. It is noted that the scheme of selecting RBF centers presented in section 3.2.3 is also applied in this chapter.

The numerical solutions to displacement and stress obtained with 50×50 nodes and the analytical solutions are plotted in Figures 8.8-8.12. The comparison indicates an excellent agreement between the solutions obtained by the proposed method and the exact solutions.

Figure 8.13 and Figure 8.14 show the convergence behaviour of the proposed method with uniform discretisations using displacement error norm and energy

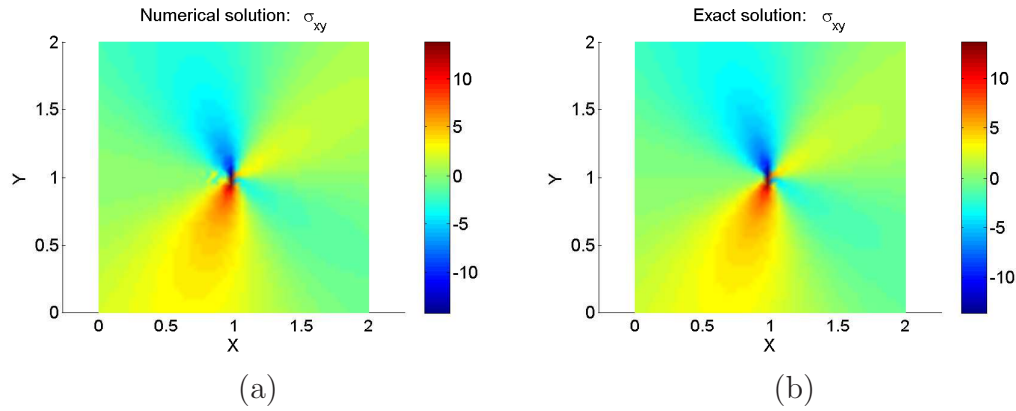


Figure 8.12: Infinite cracked plate: (a) XMIRBFN solution and (b) exact solution to σ_{xy} with 50×50 nodes.

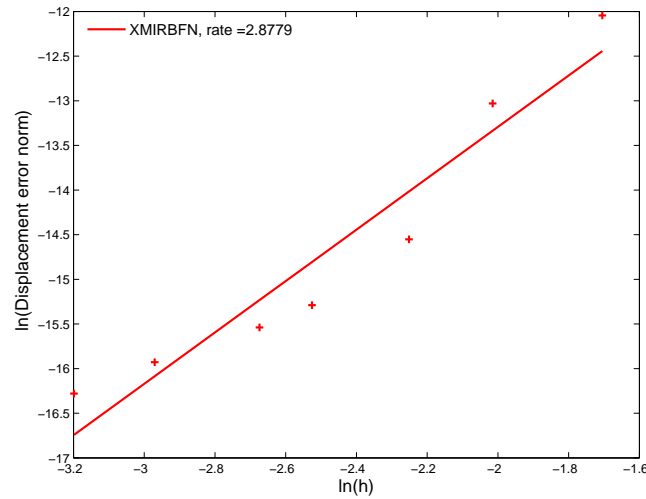


Figure 8.13: Infinite cracked plate: L_2 error norm for displacement.

error norm, respectively. The convergence rates are 2.88 and 1.41 for the former and the latter, respectively. It is noted that the convergence rates of the linear XFEM (Laborde et al., 2005) and the EFG methods (Fleming et al., 1997; Ventura et al., 2002; Rabczuk and Zi, 2007) using energy error norm are 0.50 and 0.86, respectively.

To verify the local convergence near the crack tip with uniform discretisations, the mode I stress intensity factor (SIF) K_I is computed by using the J-integral in its converted form of domain integral (Moës et al., 1999b). Figure 8.15 shows the normalized value of $\frac{K_I}{K_I^{exact}}$ for the various nodal refinements. Figure 8.16

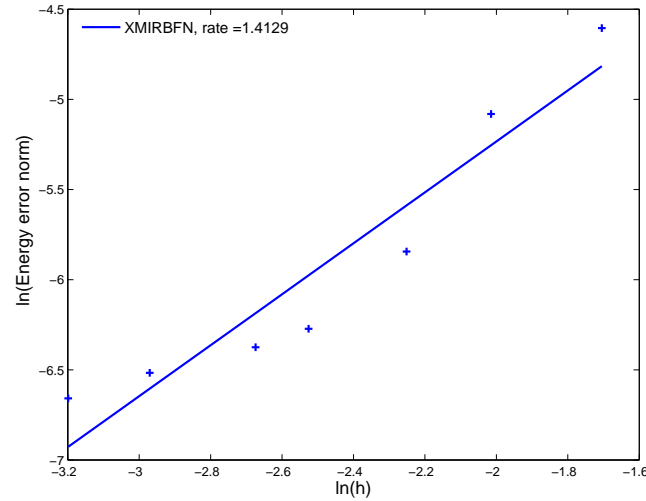


Figure 8.14: Infinite cracked plate: L_2 error norm for energy.

presents the convergence behaviour of K_I , where the relative error in SIF is defined by

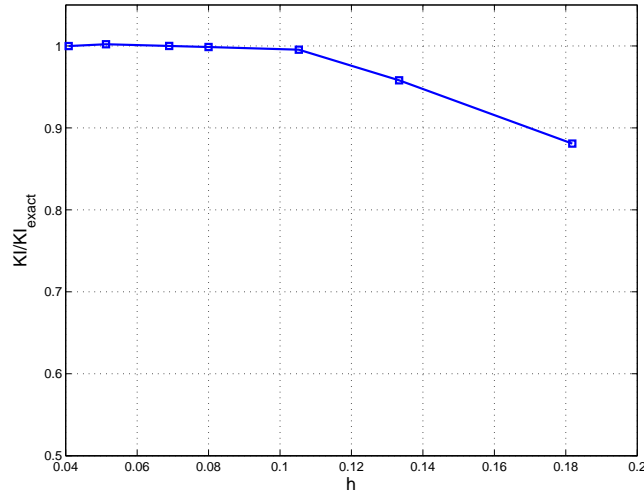
$$\text{error in SIF} = \sqrt{\frac{(K_I - K_I^{exact})^2}{(K_I^{exact})^2}}. \quad (8.22)$$

The figures demonstrate that a very high rate of local convergence is obtained, i.e. 4.395.

8.3.2 Edge-cracked plate under tension

A plate of dimension $1 \times 2 \text{ in}^2$ is loaded in tension with $\sigma = 1.0 \text{ psi}$ over the top edge and bottom edge as shown in Figure 8.17. To get rid of the rigid body mode, the displacement along the y axis is fixed at the bottom right corner, and the plate is clamped at the bottom left corner. The material parameters are 10^3 psi for Young's modulus and 0.3 for Poisson's ratio. The reference mode I SIF as given in Tada et al. (2000) is

$$K_I^{ref} = F\left(\frac{a}{W}\right)\sigma\sqrt{\pi a}, \quad K_{II}^{ref} = 0, \quad (8.23)$$

Figure 8.15: Infinite cracked plate: convergence of K_I .

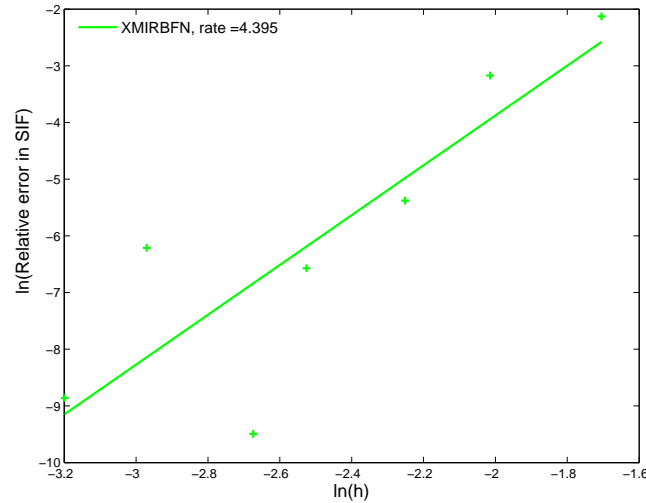
where a is the crack length, W is the plate width, and $F\left(\frac{a}{W}\right)$ is an empirical function. For $a/W \leq 0.6$, the function F is

$$F\left(\frac{a}{W}\right) = 1.12 - 0.231\left(\frac{a}{W}\right) + 10.55\left(\frac{a}{W}\right)^2 - 21.72\left(\frac{a}{W}\right)^3 + 30.39\left(\frac{a}{W}\right)^4. \quad (8.24)$$

Table 8.1: Edge-cracked plate in tension: normalised $\frac{K_I}{K_I^{ref}}$ computed by the present method compared to that of XFEM and EFG

a (in)	XFEM (linear)	XFEM (quadratic)	EFG	XMIRBFN	K_I^{ref}
0.23	0.9202	0.9906	1.0150	0.9935	1.2303
0.50	0.8836	0.9899	1.0025	1.0012	3.5423

The whole domain of interest is discretized with 12×24 nodes as shown in Figure 8.18. The deformed configuration with $a = 0.5$ in is shown in Figure 8.19. The obtained SIF K_I compared with those by the XFEM with 12×12 nodes (Stazi et al., 2003) and the EFG using symmetrical conditions with 11×11 nodes (Belytschko et al., 1995a) are presented in Table 8.1, which indicates that the obtained results are more accurate than those of the XFEM and the EFG methods.

Figure 8.16: Infinite cracked plate: relative error of K_I .

8.3.3 Edge-cracked plate under shear loading

A plate is clamped on the bottom edge and loaded by a shear traction $\tau = 1.0$ *psi* over the top edge as shown in Figure 8.20. The geometric dimensions are $W = 7$ *in*, $H = 16$ *in*, $a = 3.5$ *in*. The material parameters are 3×10^7 *psi* for Young's modulus and 0.25 for Poisson's ratio. The reference mixed mode stress intensity factors as given in Yau and Corten (1980) are

$$\begin{aligned} K_I^{ref} &= 34.0 \text{ psi}\sqrt{\text{in}} \\ K_{II}^{ref} &= 4.55 \text{ psi}\sqrt{\text{in}} \end{aligned} \quad (8.25)$$

Table 8.2: Edge-cracked plate under shearing: K_I and K_{II} computed by the present method

Nodes	XMIRBFN			
	K_I	K_{II}	$\frac{K_I}{K_I^{ref}}$	$\frac{K_{II}}{K_{II}^{ref}}$
6×12	41.1500	4.9355	1.2103	1.0847
10×20	36.4650	4.3881	1.0725	0.9644
12×26	33.5200	4.5415	0.9858	0.9981

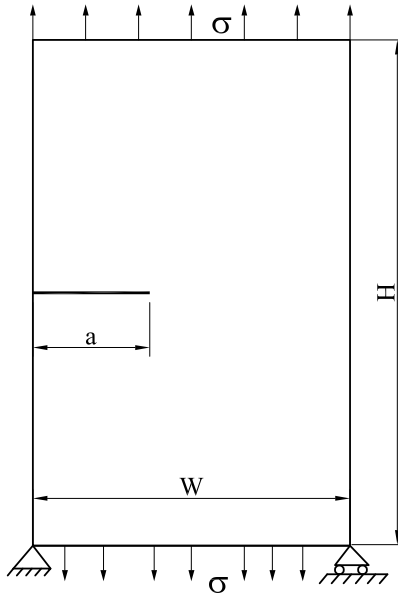


Figure 8.17: Edge-cracked plate under tension

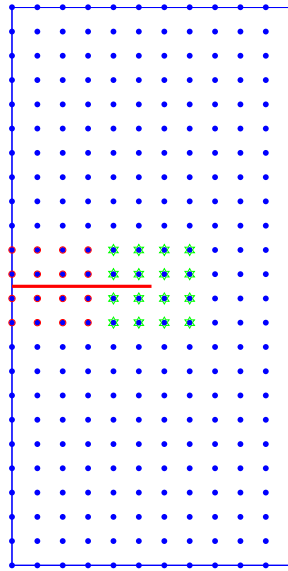
Figure 8.18: Edge-cracked plate under tension: discretization with 12×24 nodes

Table 8.3: Edge-cracked plate under shearing: SIFs by EFG (Fleming et al., 1997)

Nodes	standard EFG		extrinsic EFG		intrinsic EFG	
	$\frac{K_I}{K_I^{ref}}$	$\frac{K_{II}}{K_{II}^{ref}}$	$\frac{K_I}{K_I^{ref}}$	$\frac{K_{II}}{K_{II}^{ref}}$	$\frac{K_I}{K_I^{ref}}$	$\frac{K_{II}}{K_{II}^{ref}}$
5×11	0.7912	0.7538	1.0126	1.0066	0.9482	0.9253
11×29	0.9562	0.9516	1.0062	1.0000	0.9962	0.9978

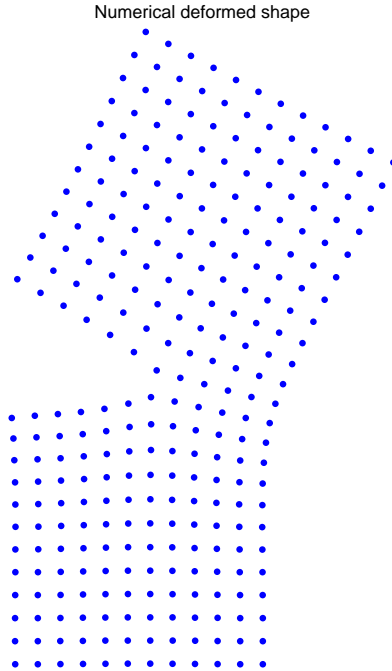


Figure 8.19: Edge-cracked plate under tension: deformed configuration with 12×24 nodes.

The numerical solution to $u_y(x, y)$ with 12×26 nodes is plotted in Figure 8.21. The mixed mode SIFs obtained by the present method with different nodal configurations are given in Table 8.2. It can be seen that the results are in good agreement with those of the EFG method of Fleming et al. (1997), who also used partition of unity enriched EFG formulations (extrinsic and intrinsic), shown in Table 8.3.

8.3.4 Center crack in a finite plate

Consider a finite plate with a center crack under tension. The geometry of the plate is described in Figure 8.22, where a is the half crack length and b is the half width of the plate, $a = 0.25 \text{ in}$, $h = 3 \text{ in}$, $b = 1 \text{ in}$ and $\sigma = 1 \text{ psi}$ is the tensile load applied at the top and the bottom of the plate. The material parameters are $E = 3 \times 10^7 \text{ psi}$, $\mu = 0.25$. To remove the rigid body mode, the displacement along the y axis is fixed at the bottom right corner, and the plate

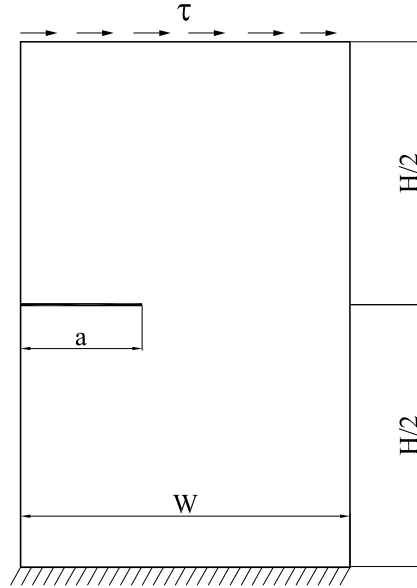


Figure 8.20: Edge-cracked plate under shearing

is clamped at the bottom left corner.

The reference stress intensity factors for this problem (Tada et al., 2000) are

$$K_I^{ref} = \sigma \sqrt{\pi a \sec \frac{\pi a}{2b}}, \quad K_{II}^{ref} = 0 \quad (8.26)$$

The reference SIF for the above parameters is $K_I^{ref} = 0.9220 \text{ psi}\sqrt{\text{in.}}$

The purpose of this example is to illustrate the performance of the method with problems containing multiple crack tips. Thus, the symmetry is not taken into account in order to verify the same behaviour of the two crack tips.

Table 8.4: Center crack in a finite plate: K_I computed by the present method

Nodes	K_I		$\frac{K_I^{tip1}}{K_I^{ref}}$	$\frac{K_I^{tip2}}{K_I^{ref}}$
	tip 1	tip 2		
16×48	0.9023	0.9240	0.9786	1.0022
21×62	0.9212	0.9273	0.9991	1.0057

The numerical solution to $u_y(x, y)$ and the deformation of the plate are displayed in Figures 8.23 and 8.24, respectively. The SIFs K_I with different numbers of

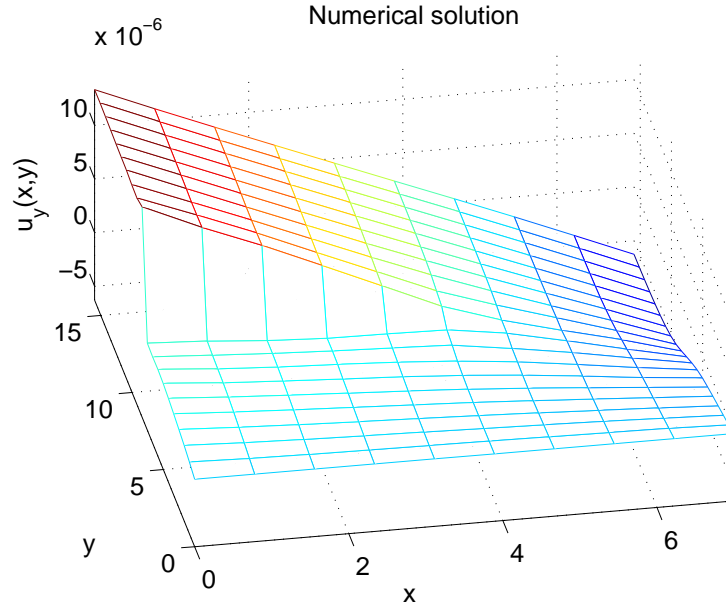


Figure 8.21: Edge-cracked plate under shearing: XMIRBFN solution to $u_y(x, y)$ with 12×26 nodes

nodes compared to the K_I^{ref} are given in Table 8.4. The comparison shows that the obtained results excellently agree with the reference solution and the behaviour at the two crack tips are almost the same.

8.3.5 Double edge crack plate

The last example is another classical problem of fracture mechanics. A double edge crack plate is subjected to tensile stresses, as shown in Figure 8.25. The geometrical parameters are $h = 1.5 \text{ in}$, $b = 0.5 \text{ in}$, $a = 0.25 \text{ in}$. The material parameters are $E = 3 \times 10^7 \text{ psi}$, $\mu = 0.25$. The plate is stretched by a tensile stress $\sigma = 1 \text{ psi}$ at the top and the bottom. To remove the rigid body mode, the displacement along the y axis is fixed at the bottom right corner, and the plate is clamped at the bottom left corner.

The reference SIF given in Tada et al. (2000) is

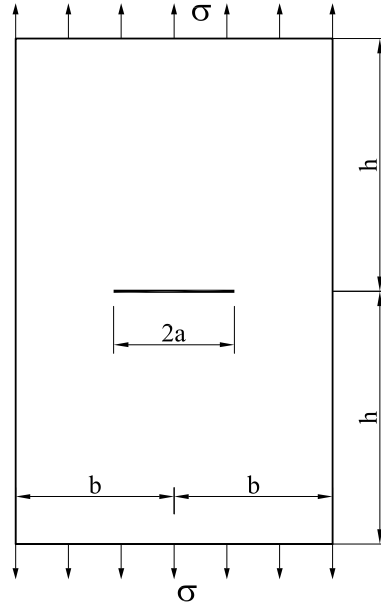


Figure 8.22: Center crack in a finite plate under tension

Table 8.5: Double edge crack plate: K_I computed by the present method

Nodes	K_I		K_I^{ref}
	tip 1	tip 2	
11×32	1.0318	1.0364	1.0305
15×44	1.0307	1.0250	1.0305

$$K_I^{ref} = F\left(\frac{a}{b}\right)\sigma\sqrt{\pi a}, \quad K_{II}^{ref} = 0, \quad (8.27)$$

where

$$F\left(\frac{a}{b}\right) = \left(1 + 0.122 \cos^4 \frac{\pi a}{2b}\right) \sqrt{\frac{2b}{\pi a} \tan \frac{\pi a}{2b}}. \quad (8.28)$$

The domain of interest is discretized with 11×32 and 15×44 nodes. The numerical solutions to displacement $u_x(x, y)$ and $u_y(x, y)$ with 15×44 nodes are plotted in Figures 8.26 and 8.27, respectively. The deformation of the structure is described in Figure 8.28. The SIF by the present method is presented in Table 8.5, which shows a very good agreement between the obtained results and the reference SIF.

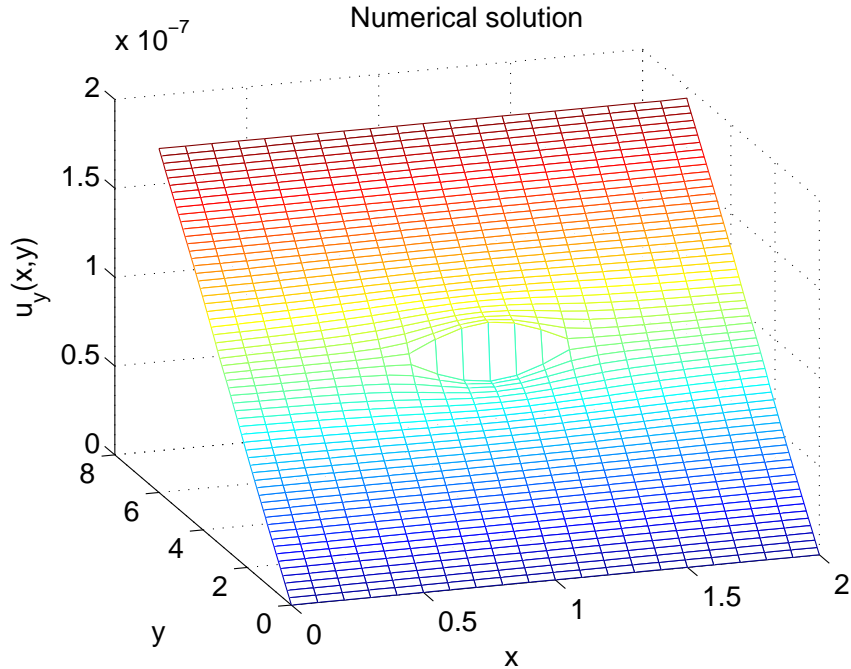


Figure 8.23: Center crack in a finite plate: XMIRBFN solution to $u_y(x, y)$ with 21×62 nodes.

8.4 Conclusion

A new meshless method has been developed for modeling fracture problems by using a local partition of unity enrichment approach. A remarkable feature of the proposed method is that the essential (Dirichlet) boundary conditions are imposed exactly and easily since the shape functions possess the Kronecker-delta property. The numerical experiments demonstrate that the proposed method performs well for linear fracture mechanics problems which encounter the problematic issues of discontinuity and singularity.

In addition, the local support, high convergence rate and high order continuity make MIRBFN very promising for meshless methods. The method is also applicable to other discontinuous problems such as inclusion and bimaterial interface problems, and can be readily extended to nonlinear fracture mechanics problems and three dimensions, which is going to be carried out in our next works.

Numerical deformed shape

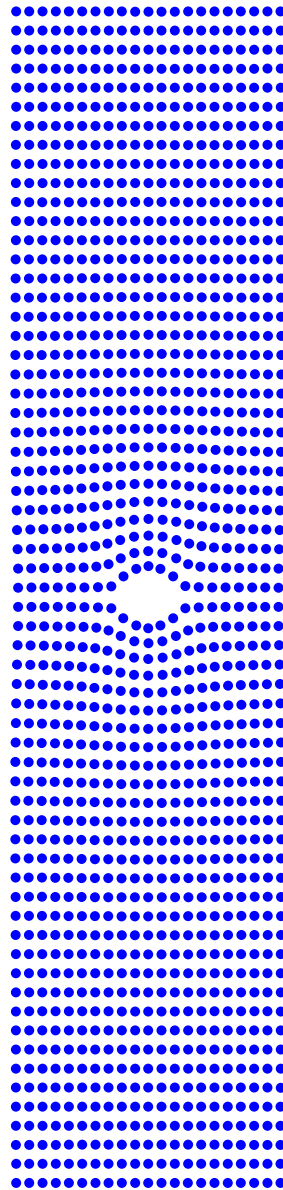


Figure 8.24: Center crack in a finite plate: deformed configuration with 21×62 nodes.

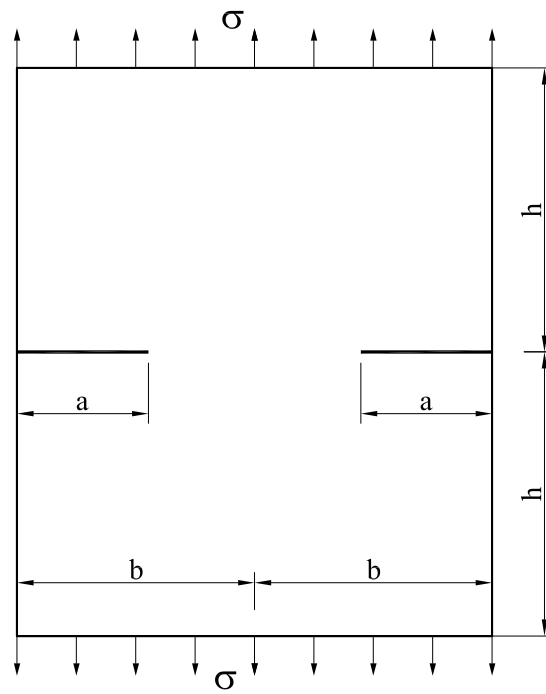
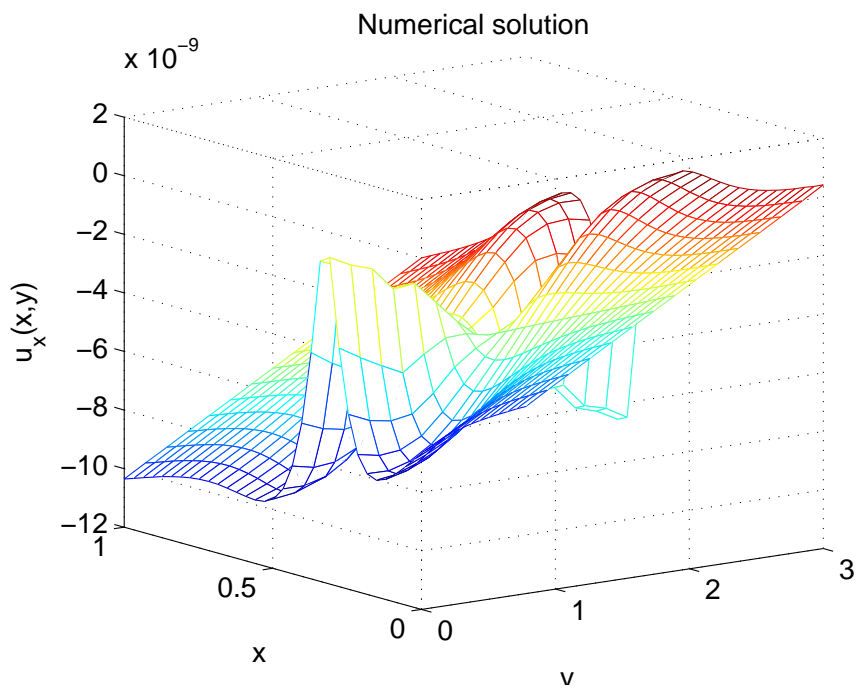


Figure 8.25: Double edge crack plate

Figure 8.26: Double edge crack plate: XMIRBFN solution to $u_x(x,y)$ with 15×44 nodes.

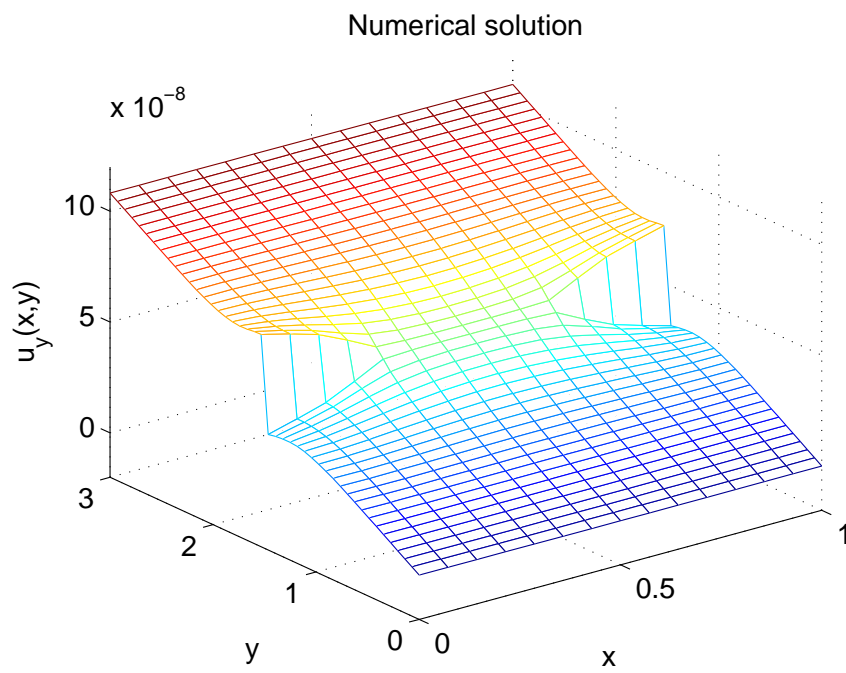


Figure 8.27: Double edge crack plate: XMIRBFN solution to $u_y(x,y)$ with 15×44 nodes.

Numerical deformed shape

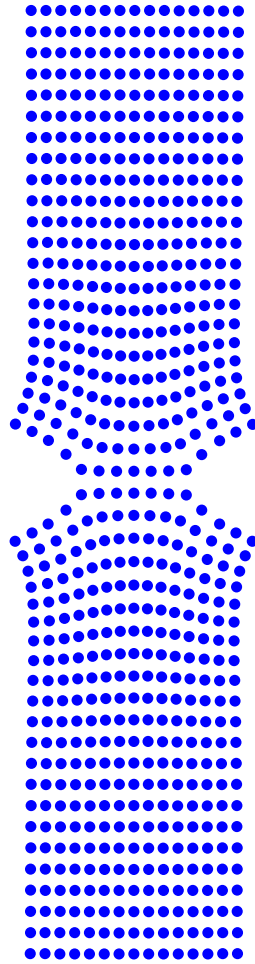


Figure 8.28: Double edge crack plate: deformed configuration with 15×44 nodes.

Chapter 9

Conclusion

The aim of this research is to devise and develop new meshless methods based on RBF networks to model strain localization and fracture phenomena. This has been attained by a number of logical steps in two major parts of the thesis, progressing from developing meshless methods for smooth problems to discontinuous problems. Part I, consisting of chapters 2-4, primarily focuses on devising and developing the new RBF-based meshless methods for PDEs whose solution is smooth, for example, heat transfer, elasticity and crack problems. Part II is concerned with further development and application of the meshless methods in Part I for simulation of discontinuous problems, in particular, strain localization (chapters 5, 6 and 7) and fracture (chapter 8).

The outcome of the current research is the successful formulation and implementation of new meshless methods based on the present MIRBFN procedure. The creation of MIRBFN method is based on the partition of unity concept, where IRBFN and MLS procedures are coupled together. As a result, the proposed MIRBFN method is locally supported and yields sparse and banded interpolation matrices. The computational efficiency are significantly improved in comparison with that of the original global IRBFN method. In addition, the shape functions of MIRBFN satisfy the Kronecker- δ property, which facilitates

the imposition of the essential boundary conditions, and the method is applicable to randomly distributed datasets and arbitrary geometries. Furthermore, MIRBFNs yield high order of convergence and accuracy for function approximation and solution of PDEs owing to the property of PU method (non-local approximation), the universal high order approximation ability offered by RBFs and the avoidance of the reduction in convergence rate caused by differentiation (integral approach). The MIRBFN technique is employed in both strong and weak form approaches to formulate different meshless methods.

Owing to their simplicity and efficiency, strong form meshless methods are implemented by using a collocation procedure with IRBFNs (chapters 2, 5 and 6) and MIRBFNs (chapter 3). To overcome the problem of reduction of accuracy associated with natural (Neumann) boundary conditions in a collocation framework, a first-order system collocation technique is introduced in chapter 2 and successfully applied to various problems including heat transfer, elasticity and crack (reported in chapters 2 and 3). Moreover, the robustness and effectiveness of the IRBFN-based meshless collocation are also successfully demonstrated by simulation of strain localization in quasi-brittle materials (chapter 5) and in elasto-thermo-visco plastic materials (chapter 6), where the occurrence of boundary layer and discontinuity is a significant challenge for numerical methods.

In numerical computation weak form methods are still most frequently used since they yield good stability and reasonable accuracy for many problems. A new weak form meshless method based on MIRBFNs is also proposed and successfully verified with various problems in elasticity, including cracks, in chapter 4. In contrast to collocation approach, in this method both natural and essential boundary conditions are accommodated straightforwardly because of the nature of the weak form approach for the natural BCs and the Kronecker-delta property of MIRBFN shape functions for the essential BCs. The method is further developed for elasto-static crack problems by using a local partition

of unity enrichment technique (chapter 8). A wide range of crack problems including mixed mode, multiple crack tips and multiple cracks is used for testing the performance of the XMIRBFN meshless method. The obtained results in chapter 8 also indicate that the new method is compared favorably with XFEM and very promising for modeling discontinuity problems.

Finally, it is possible to extend the present methods for several 2D and 3D problems, for example,

- modeling of non-linear fracture mechanics including multiple crack initiation, propagation and interaction in 2D and 3D;
- simulation of strain localization (shear bands) in 2D and 3D;
- simulation and prediction crack pattern in composite materials such as reinforced concrete.

Appendix A

Near crack tip asymptotic enrichment functions and computation of stress intensity factor

A.1 Derivatives of near crack tip enrichment functions

To compute the stiffness matrices for nodes enriched by the near tip asymptotic functions Φ_κ , the following expression is to be determined

$$(\Phi_i \Psi_\kappa)_{,x} = (\Phi_i)_{,x} \Psi_\kappa + \Phi_i (\Psi_\kappa)_{,x}, \quad (\text{A.1a})$$

$$(\Phi_i \Psi_\kappa)_{,y} = (\Phi_i)_{,y} \Psi_\kappa + \Phi_i (\Psi_\kappa)_{,y}, \quad (\text{A.1b})$$

where $\Psi_{\kappa,x}$ and $\Psi_{\kappa,y}$ are the derivatives of Ψ_κ with respect to the global Cartesian coordinate system. These derivatives are, at first, found in the local crack

tip coordinate system (x_1, x_2) (Figure A.1), then a vector transformation is used to transform them into the global Cartesian coordinate system (x, y) .

The derivatives of Ψ_κ with respect to the local crack tip coordinate system (x_1, x_2) are given by

$$(\Psi_\kappa)_{,x_1} = (\Psi_\kappa)_{,r}r_{,x_1} + (\Psi_\kappa)_{,\theta}\theta_{,x_1}, \quad (\text{A.2a})$$

$$(\Psi_\kappa)_{,x_2} = (\Psi_\kappa)_{,r}r_{,x_2} + (\Psi_\kappa)_{,\theta}\theta_{,x_2}. \quad (\text{A.2b})$$

The near tip enrichment functions are recalled for ease of reading

$$\Psi_\kappa(r, \theta) = \left\{ \sqrt{r} \sin \frac{\theta}{2}, \sqrt{r} \cos \frac{\theta}{2}, \sqrt{r} \sin \frac{\theta}{2} \sin \theta, \sqrt{r} \cos \frac{\theta}{2} \sin \theta \right\}. \quad (\text{A.3})$$

The derivatives of Ψ_κ with respect to the polar coordinate (r, θ) are

$$(\Psi_1)_{,r} = \frac{1}{2\sqrt{r}} \sin \frac{\theta}{2}, \quad (\Psi_1)_{,\theta} = \frac{\sqrt{r}}{2} \cos \frac{\theta}{2}, \quad (\text{A.4a})$$

$$(\Psi_2)_{,r} = \frac{1}{2\sqrt{r}} \cos \frac{\theta}{2}, \quad (\Psi_2)_{,\theta} = -\frac{\sqrt{r}}{2} \sin \frac{\theta}{2}, \quad (\text{A.4b})$$

$$(\Psi_3)_{,r} = \frac{1}{2\sqrt{r}} \sin \frac{\theta}{2} \sin \theta, \quad (\Psi_3)_{,\theta} = \sqrt{r} \left(\frac{1}{2} \cos \frac{\theta}{2} \sin \theta + \sin \frac{\theta}{2} \cos \theta \right), \quad (\text{A.4c})$$

$$(\Psi_4)_{,r} = \frac{1}{2\sqrt{r}} \cos \frac{\theta}{2} \sin \theta, \quad (\Psi_4)_{,\theta} = \sqrt{r} \left(-\frac{1}{2} \sin \frac{\theta}{2} \sin \theta + \cos \frac{\theta}{2} \cos \theta \right). \quad (\text{A.4d})$$

The derivatives of r and θ with respect to (x_1, x_2) are as follows.

$$r_{,x_1} = \cos(\theta), \quad r_{,x_2} = \sin \theta, \quad (\text{A.5a})$$

$$\theta_{,x_1} = -\sin \theta / r, \quad \theta_{,x_2} = \cos \theta / r. \quad (\text{A.5b})$$

Finally, we have the derivatives of Ψ_κ with respect to the local crack tip system

$$(\Psi_1)_{,x_1} = -\frac{1}{2\sqrt{r}} \sin \frac{\theta}{2}, \quad (\text{A.6a})$$

$$(\Psi_1)_{,x_2} = \frac{1}{2\sqrt{r}} \cos \frac{\theta}{2}, \quad (\text{A.6b})$$

$$(\Psi_2)_{,x_1} = \frac{1}{2\sqrt{r}} \cos \frac{\theta}{2}, \quad (\text{A.7a})$$

$$(\Psi_2)_{,x_2} = \frac{1}{2\sqrt{r}} \sin \frac{\theta}{2}, \quad (\text{A.7b})$$

$$(\Psi_3)_{,x_1} = -\frac{1}{2\sqrt{r}} \sin \frac{3\theta}{2} \sin \theta, \quad (\text{A.8a})$$

$$(\Psi_3)_{,x_2} = \frac{1}{2\sqrt{r}} \left(\sin \frac{\theta}{2} + \sin \frac{3\theta}{2} \cos \theta \right), \quad (\text{A.8b})$$

$$(\Psi_4)_{,x_1} = -\frac{1}{2\sqrt{r}} \cos \frac{3\theta}{2} \sin \theta, \quad (\text{A.9a})$$

$$(\Psi_4)_{,x_2} = \frac{1}{2\sqrt{r}} \left(\cos \frac{\theta}{2} + \cos \frac{3\theta}{2} \cos \theta \right). \quad (\text{A.9b})$$

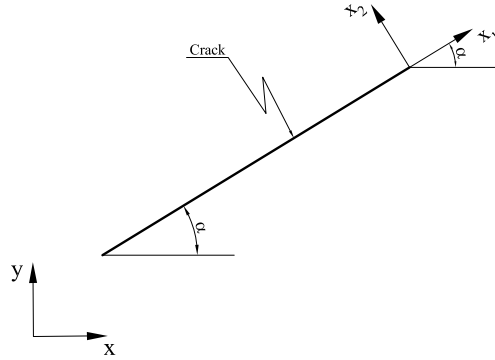


Figure A.1: Global and local coordinate systems

Using a vector transformation, the derivatives of near tip enrichment functions with respect to the global coordinate system are given by

$$(\Psi_\kappa)_{,x} = (\Psi_\kappa)_{,x_1} \cos(\alpha) - (\Psi_\kappa)_{,x_2} \sin(\alpha), \quad (\text{A.10a})$$

$$(\Psi_\kappa)_{,y} = (\Psi_\kappa)_{,x_1} \sin(\alpha) + (\Psi_\kappa)_{,x_2} \cos(\alpha), \quad (\text{A.10b})$$

where α is the inclination angle of the crack with respect to the x axis of the global coordinate system (see Figure A.1).

A.2 Contour integrals and their domain representations in two-dimensions

Among the numerical methods for computing fracture parameters, boundary integral methods (Forth and Keat, 1996; Sladek et al., Jan 2000) and the domain integral method (Shih et al., 1986; Nikishkov and Atluri, 1987; Moran and Shih, 1987) have been proved adequate tools. In this work, the domain integral method, in conjunction with interaction energy integrals, is used to determine mixed-mode stress intensity factors. In the interaction energy integral method, auxiliary fields are introduced and superimposed onto the actual fields satisfying the boundary value problem. By suitably selecting these auxiliary fields, a relationship can be established between the mixed-mode stress intensity factors and the interaction energy integrals. These integrals can be represented in the so-called domain forms and evaluated in a post-processing step, once the solution to the boundary value problem is known.

The energy release rate for general mixed-mode problems in two dimensions can be written as

$$J = \frac{1}{E^*} (K_I^2 + K_{II}^2), \quad (\text{A.11})$$

where E^* is defined as

$$E^* = \begin{cases} \frac{E}{1-\nu^2} & \text{for plane strain,} \\ E & \text{for plane stress} \end{cases} \quad (\text{A.12})$$

Consider a crack in two dimensions. A local Cartesian crack tip coordinate system $(\mathbf{e}_1, \mathbf{e}_2)$ is constructed. Let Γ be a contour encompassing the crack tip and \mathbf{n} be the unit normal to the contour Γ , oriented as shown in Figure A.2.

The contour integral J is defined as (Rice, 1968)

$$J = \int_{\Gamma} \left[W dx_2 - T_i \frac{\partial u_i}{\partial x_1} d\Gamma \right] = \int_{\Gamma} \left[W \delta_{1j} - \sigma_{ij} \frac{\partial u_i}{\partial x_1} \right] n_j d\Gamma, \quad (\text{A.13})$$

where $T_i = \sigma_{ij} n_j$ is the traction on the contour Γ .

Two states of a cracked body are considered. State 1, $(\sigma_{ij}^{(1)}, \epsilon_{ij}^{(1)}, u_i^{(1)})$, corresponds to the present state and state 2, $(\sigma_{ij}^{(2)}, \epsilon_{ij}^{(2)}, u_i^{(2)})$, is an auxiliary state.

The J-integral for the sum of the two states is

$$J^{(1+2)} = \int_{\Gamma} \left[\frac{1}{2} (\sigma_{ij}^{(1)} + \sigma_{ij}^{(2)}) (\epsilon_{ij}^{(1)} + \epsilon_{ij}^{(2)}) \delta_{1j} - (\sigma_{ij}^{(1)} + \sigma_{ij}^{(2)}) \frac{\partial (u_i^{(1)} + u_i^{(2)})}{\partial x_1} \right] n_j d\Gamma. \quad (\text{A.14})$$

Expanding and rearranging terms gives

$$J^{(1+2)} = J^{(1)} + J^{(2)} + I^{(1+2)}, \quad (\text{A.15})$$

where $I^{(1+2)}$ is the interaction integral for states 1 and 2

$$I^{(1+2)} = \int_{\Gamma} \left[W^{(1,2)} \delta_{1j} - \sigma_{ij}^{(1)} \frac{\partial u_i^{(2)}}{\partial x_1} - \sigma_{ij}^{(2)} \frac{\partial u_i^{(1)}}{\partial x_1} \right] n_j d\Gamma, \quad (\text{A.16})$$

where $W^{(1,2)}$ is the interaction strain energy

$$W^{(1,2)} = \sigma_{ij}^{(1)} \epsilon_{ij}^{(2)} = \sigma_{ij}^{(2)} \epsilon_{ij}^{(1)}. \quad (\text{A.17})$$

Writing equation (A.11) for the combined states gives

$$J^{(1,2)} = J^{(1)} + J^{(2)} + \frac{2}{E'} (K_I^{(1)} K_I^{(2)} + K_{II}^{(2)} K_{II}^{(1)}). \quad (\text{A.18})$$

Equating (A.15) and (A.18) leads to the following relationship

$$I^{(1+2)} = \frac{2}{E^*} (K_I^{(1)} K_I^{(2)} + K_{II}^{(2)} K_{II}^{(1)}). \quad (\text{A.19})$$

Making suitable choice of state 2 as the pure mode I asymptotic fields with $K_I^{(2)} = 1, K_{II}^{(2)} = 0$, gives the mode I SIF in terms of the interaction integral

$$K_I^{(1)} = \frac{E^*}{2} I^{(1, \text{Mode I})}. \quad (\text{A.20})$$

Similarly, choosing state 2 as the pure mode II asymptotic fields with $K_{II}^{(2)} = 1, K_I^{(2)} = 0$, gives the mode II SIF in terms of the interaction integral

$$K_{II}^{(1)} = \frac{E^*}{2} I^{(1, \text{Mode II})}. \quad (\text{A.21})$$

The contour integral (A.16) is not well suited for its numerical evaluation. It is useful, therefore, to transform this integral into an equivalent domain form by multiplying the integrand with a sufficiently smooth weighting function $q(\mathbf{x})$ which takes a value of unity on an open set containing the crack tip and vanishes on an outer prescribed contour C_0 .

The interaction integral for states 1 and 2 can be written (see Figure A.2):

$$I^{(1,2)} = \lim_{\Gamma \rightarrow 0} \left\{ \int_{\Gamma \cup C_0 \cup C^+ \cup C^-} \left[W^{(1,2)} \delta_{1j} - \sigma_{ij}^{(1)} \frac{\partial u_i^{(2)}}{\partial x_1} - \sigma_{ij}^{(2)} \frac{\partial u_i^{(1)}}{\partial x_1} \right] q m_j ds \right\}. \quad (\text{A.22})$$

In Figure A.2, let the contour C be the union of the curves Γ, C_0, C^+ and C^- and let m_j be the outward unit normal to the domain A whose boundary is $\partial A = C = \Gamma \cup C_0 \cup C^+ \cup C^-$. The outward unit normal m_j to the domain A is

$$\mathbf{m} = \begin{cases} -\mathbf{n} & \text{on } \Gamma \\ +\mathbf{n} & \text{on } C_0 \cup C^+ \cup C^- \end{cases} \quad (\text{A.23})$$

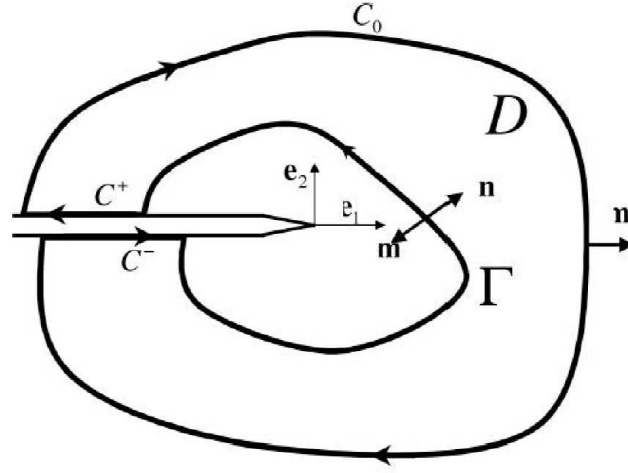


Figure A.2: Domain used for computation of mixed mode stress intensity factors in two dimensional space

From (A.22), and using the result in (A.23), and the divergence theorem the interaction integral can be simplified to

$$I^{(1,2)} = \int_A \left[-W^{(1,2)} \delta_{1j} + \sigma_{ij}^{(1)} \frac{\partial u_i^{(2)}}{\partial x_1} + \sigma_{ij}^{(2)} \frac{\partial u_i^{(1)}}{\partial x_1} \right] \frac{\partial q}{\partial x_j} dA. \quad (\text{A.24})$$

After the solution of the boundary value problem, we obtained the stress and displacement fields of state 1, i.e. $\sigma_{ij}^{(1)}$, $u_i^{(1)}$ and the spatial derivatives of the displacement field in the global Cartesian coordinate system $u_{i,x}^{(1)}$, and $u_{i,y}^{(1)}$. These terms need to be transformed to the local crack tip coordinate system by using an appropriate vector transformation.

The derivatives of the displacement field with respect to x_1, x_2 are given as

$$\begin{pmatrix} u_{1,x_1}^{(1)} & u_{1,x_2}^{(1)} \\ u_{2,x_1}^{(1)} & u_{2,x_2}^{(1)} \end{pmatrix} = \begin{pmatrix} \cos \alpha & \sin \alpha \\ -\sin \alpha & \cos \alpha \end{pmatrix} \begin{pmatrix} u_{1,x}^{(1)} & u_{1,y}^{(1)} \\ u_{2,x}^{(1)} & u_{2,y}^{(1)} \end{pmatrix} \begin{pmatrix} \cos \alpha & -\sin \alpha \\ \sin \alpha & \cos \alpha \end{pmatrix} \quad (\text{A.25})$$

where α is the inclination angle between the local crack tip coordinate system

and the global coordinate system, see Figure A.1.

The stress of state 1 in the local crack tip coordinate system is as follows.

$$\begin{aligned}\sigma_{x_1x_1} &= \frac{\sigma_{xx} + \sigma_{yy}}{2} + \left(\frac{\sigma_{xx} - \sigma_{yy}}{2}\right) \cos(2\alpha) + \tau_{xy} \sin(2\alpha), \\ \sigma_{y_1y_1} &= \frac{\sigma_{xx} + \sigma_{yy}}{2} - \left(\frac{\sigma_{xx} - \sigma_{yy}}{2}\right) \cos(2\alpha) - \tau_{xy} \sin(2\alpha), \\ \sigma_{x_1y_1} &= \tau_{xy} \cos(2\alpha) - \left(\frac{\sigma_{xx} - \sigma_{yy}}{2}\right) \sin(2\alpha).\end{aligned}\tag{A.26}$$

The distribution of weighting function can be determined by the MRBFN interpolation

$$q = \sum_{i=1}^m \Phi_i q_i,\tag{A.27}$$

and,

$$\frac{\partial q}{\partial x} = \sum_{i=1}^m \frac{\partial \Phi_i}{\partial x} q_i.\tag{A.28}$$

A vector transformation is then used to convert $\partial q/\partial x$ to the local crack tip coordinate system $\partial q/\partial x_j$

$$\begin{aligned}q_{,x_1} &= q_{,x} \cos(\alpha) + q_{,y} \sin(\alpha), \\ q_{,x_2} &= -q_{,x} \sin(\alpha) + q_{,y} \cos(\alpha).\end{aligned}\tag{A.29}$$

In the following, the displacement, stress and strain field of the auxiliary field are computed. Since we choose the state 2 as the pure mode I with $K_I = 1$, then we have

$$\begin{aligned}u_i^{(2)} &= \begin{Bmatrix} u_x \\ u_y \end{Bmatrix} = \frac{1}{2\mu} \sqrt{\frac{r}{2\pi}} \begin{Bmatrix} \cos(\theta/2) [\varrho - 1 + 2 \sin^2(\theta/2)] \\ \sin(\theta/2) [\varrho + 1 - 2 \cos^2(\theta/2)] \end{Bmatrix} \\ &= \frac{1}{2\mu} \sqrt{\frac{r}{2\pi}} \begin{Bmatrix} \cos(\theta/2) [\varrho - \cos(\theta)] \\ \sin(\theta/2) [\varrho - \cos(\theta)] \end{Bmatrix},\end{aligned}\tag{A.30}$$

where ϱ and μ are material constants given by

$$\mu = \frac{E}{2(1+\nu)}, \quad \varrho = \begin{cases} 3-4\nu & \text{plane strain,} \\ \frac{3-\nu}{1+\nu} & \text{plane stress,} \end{cases} \quad (\text{A.31})$$

Letting

$$\begin{aligned} A &= \frac{1}{2\mu}; B = \sqrt{\frac{r}{2\pi}}, \\ f_1 &= \cos(\theta/2) [\varrho - \cos(\theta)], \\ f_2 &= \sin(\theta/2) [\varrho - \cos(\theta)]. \end{aligned} \quad (\text{A.32})$$

The strain components of state 2 are

$$\epsilon_{ij}^{(2)} = \frac{1}{2}(u_{i,j}^{(2)} + u_{j,i}^{(2)}). \quad (\text{A.33})$$

The derivatives of the displacement fields are

$$u_{1,1}^{(2)} = A(Bf_{1,1} + \frac{f_1 r_{,1}}{4\pi B}), \quad (\text{A.34a})$$

$$u_{1,2}^{(2)} = A(Bf_{1,2} + \frac{f_1 r_{,2}}{4\pi B}), \quad (\text{A.34b})$$

$$u_{2,1}^{(2)} = A(Bf_{2,1} + \frac{f_2 r_{,1}}{4\pi B}), \quad (\text{A.34c})$$

$$u_{2,2}^{(2)} = A(Bf_{2,2} + \frac{f_2 r_{,2}}{4\pi B}). \quad (\text{A.34d})$$

Since $r_{,1} = \cos(\theta)$, $r_{,2} = \sin(\theta)$, $\theta_{,1} = -\sin(\theta)/r$, and $\theta_{,2} = \cos(\theta)/r$, by using the chain rule, we can write the derivatives of f_1 , f_2 as follows

$$f_{1,1} = f_{1,\theta}\theta_{,1}, \quad f_{1,2} = f_{1,\theta}\theta_{,2}, \quad (\text{A.35a})$$

$$f_{2,1} = f_{2,\theta}\theta_{,1}, \quad f_{2,2} = f_{2,\theta}\theta_{,2}, \quad (\text{A.35b})$$

$$f_{1,\theta} = -\frac{\varrho}{2} \sin \frac{\theta}{2} + \frac{1}{2} \sin \frac{\theta}{2} \cos \theta + \cos \frac{\theta}{2} \sin \theta, \quad (\text{A.36a})$$

$$f_{2,\theta} = \frac{\theta}{2} \cos \frac{\theta}{2} - \frac{1}{2} \cos \frac{\theta}{2} \cos \theta - \sin \frac{\theta}{2} \sin \theta. \quad (\text{A.36b})$$

The stress field of Mode I is given by

$$\begin{aligned} \sigma_{xx}^{(2)} &= \frac{1}{\sqrt{2\pi r}} \cos \frac{\theta}{2} \left(1 - \sin \frac{\theta}{2} \sin \frac{3\theta}{2} \right), \\ \sigma_{yy}^{(2)} &= \frac{1}{\sqrt{2\pi r}} \cos \frac{\theta}{2} \left(1 + \sin \frac{\theta}{2} \sin \frac{3\theta}{2} \right), \\ \sigma_{xy}^{(2)} &= \frac{1}{\sqrt{2\pi r}} \cos \frac{\theta}{2} \sin \frac{\theta}{2} \cos \frac{3\theta}{2}. \end{aligned} \quad (\text{A.37})$$

Since all terms in equation (A.24) are available now, Gaussian quadrature is used for the numerical evaluation of this interaction integral

$$I^{(1,2)} = \sum_{\substack{\text{subcells} \\ \text{in } A}} \sum_{p=1}^{N_{GPS}} \left\{ \left[\sigma_{ij}^{(1)} \frac{\partial u_i^{(2)}}{\partial x_1} - \sigma_{ij}^{(2)} \frac{\partial u_i^{(1)}}{\partial x_1} - W^{(1,2)} \delta_{1j} \right] \frac{\partial q}{\partial x_j} \right\} w_p \det J, \quad (\text{A.38})$$

where the domain A is divided into integration subcells, N_{GPS} is the number of Gauss points per integration cell and w_p the weight. All terms of the state 2 are functions of variables r, θ . Therefore, it is necessary to compute the coordinates of Gauss points in the local crack tip coordinate system.

In the same manner, in order to compute K_{II} , we choose state 2 as the pure Mode II ($K_I^{(2)} = 0$) with $K_{II}^{(2)} = 1$.

References

- M. I. Alsaleh. *Numerical modeling of strain localization in granular materials using Cosserat theory enhanced with microfabric properties*. PhD thesis, Louisiana State University, 2004.
- F. Armero and J. Park. An analysis of strain localization in a shear layer under thermally coupled dynamic conditions. Part 1: Continuum thermoplastic models. *international journal for numerical methods in engineering*, 56:2069–2100, 2003.
- H. Askes. *Advanced spatial discretisation strategies for localised failure: mesh adaptivity and meshless methods*. PhD thesis, Delft University of Technology, 2000.
- H. Askes, L. Bodé, and L. J. Sluys. ALE analyses of localization in wave propagation problems. *Mechanics of Cohesive-Frictional Materials*, 3:105–125, 1998.
- S. N. Atluri and T. Zhu. A new meshless local Petrov-Galerkin (MLPG) approach in computational mechanics. *Computational Mechanics*, 22:117–127, 1998.
- S. N. Atluri, Z. D. Han, and A. M. Rajendran. A New Implementation of the Meshless Finite Volume Method, Through the MLPG “Mixed” Approach. *CMES: Computer Modeling in Engineering & Sciences*, 6(6):491–513, 2004.
- S. N. Atluri, H. T. Liu, and Z. D. Han. Meshless local petrov-galerkin (MLPG)

- mixed collocation method for elasticity problems. *CMES: Computer Modeling in Engineering & Sciences*, 14(3):141–152, 2006.
- S.N. Atluri and S. Shen. The meshless local Petrov-Galerkin (MLPG) method: A simple & less-costly alternative to the finite element and the boundary element methods. *CMES: Computer Modeling in Engineering & Sciences*, 3: 11–51, 2002.
- I. Babuška and I. Melenk. The partition of unity method. *International Journal for Numerical Methods in Engineering*, 40(4):727–758, 1997.
- I. Babuška, U. Banerjee, and J. E. Osborn. Superconvergence in the generalized finite element method. *Numer. Math.*, 107:353—395, 2007.
- I. Babuška, V. Nistor, and N. Tarfulea. Generalized finite element method for second-order elliptic operator with dirichlet boundary conditions. *Journal of computaional and applied mathematics*, 2008. in press.
- Y. Bai and B. Dodd. *Adiabatic Shear Localization*. Pergamon Press, 1992.
- J. P. Bardet. Analytical solutions for the plane strain bifurcation of compressible solids. *Journal of Applied Mechanics*, 58:651–657, 1991.
- R. C. Batra and H. K. Ching. Analysis of elastodynamic deformations near a crack/notch tip by the meshless local Petrov-Galerkin (MLPG) method. *CMES: Computer Modeling in Engineering & Sciences*, 3:717–730, 2002.
- R. C. Batra and C. H. Kim. Effect of thermal conductivity on the initiation, growth and bandwidth of adiabatic shear bands. *International Journal of Engineering Science*, 29:949–960, 1991.
- R. C. Batra and G. M. Zhang. Analysis of adiabatic shear bands in elasto-thermo-viscoplastic materials by Modified Smooth-Particle Hydrodynamics (SPH) method. *Journal of Computational Physics*, 201:172–190, 2004.
- B.J.C. Baxter. Preconditioned conjugate gradient, radial basis functions, and toeplitz matrices. *Compu. Math. Appl.*, 43:305–318, 2002.

- A. Bayliss, T. Belytschko, M. Kulkarni, and D. A. Lott-Crumpler. On the dynamics and the role of imperfections for localization in thermo-viscoplastic materials. *Modelling and Simulation in Materials Science and Engineering*, 2:941–964, 1994.
- Z. P. Bazant and T. Belytschko. Wave propagation in a strain softening bar: exact solution. *Journal of Engineering Mechanics (ASCE)*, 111:381–398, 1985.
- Z. P. Bazant, T. Belytschko, and T. P. Chang. Continuum theory for strain-softening. *Journal of Engineering Mechanics (ASCE)*, 110:1666–1691, 1984.
- A. Beballal, A. S. Botta, and W. S. Venturini. On the description of localization and failure phenomena by the boundary element method. *Computer methods in applied mechanics and engineering*, 195:5833–5856, 2006.
- T. Belytschko and T. Black. Elastic crack growth in finite elements with minimal remeshing. *International Journal for Numerical Methods in Engineering*, 45:601–620, 1999.
- T. Belytschko, Y. Y. Lu, and L. Gu. Element-free Galerkin methods. *International Journal for Numerical Methods in Engineering*, 37:229–256, 1994.
- T. Belytschko, Y. Y. Lu, and L. Gu. Crack propagation by element-free Galerkin methods. *Engineering Fracture Mechanics*, 51:295–315, 1995a.
- T. Belytschko, D. Organ, and Y. Krongauz. A couple finite element-element free galerkin method. *Computational Mechanics*, 17(3):186–195, 1995b.
- T. Belytschko, Y. Krongauz, M. Fleming, D. Organ, and W.K. Liu. Smoothing and accelerated computations in the element-free Galerkin method. *J. Comput. Appl. Math*, 74:111–126, 1996a.
- T. Belytschko, Y. Krongauz., D. Organ, M. Flemming, and P. Krysl. Meshless method: an overview and recent developments. *Computer Methods in Applied Mechanics and Engineering*, 139:3–47, 1996b.

- T. Belytschko, D. Organ, and C. Gerlach. Element-free Galerkin methods for dynamic fracture in concrete. *Computer Methods in Applied Mechanics and Engineering*, 187:385–399, 2000.
- T. Belytschko, H. Chen, J. Xu, and G. Zi. Dynamic crack propagation based on loss of hyperbolicity and a new discontinuous enrichment. *International Journal for Numerical Methods in Engineering*, 58:1873–1905, 2003a.
- T. Belytschko, W. K. Liu, and B. Moran. *Nonlinear Finite Elements for Continua and Structures*. John Wiley & Sons, LTD - ISBN:0-471-98774-3, 2003b.
- S. Bordas, P. V. Nguyen, C. Dunant, H. Nguyen-Dang, and A. Guidoum. An extended finite element library. *International Journal for Numerical Methods in Engineering*, 2:1–33, 2006.
- S. Bordas, M. Duflot, and P. Le. A simple error estimator for extended finite elements. *Communications In Numerical Methods In Engineering*, 24:961–971, 2008a.
- S. Bordas, T. Rabczuk, H. Nguyen-Xuan, V.P. Nguyen, S. Natarajan, T. Bog, Do Minh Quan, and V.H Nguyen. Strain smoothing in fem and xfem. *Computers and Structures*, page doi:10.1016/j.compstruc.2008.07.006, 2008b.
- S. Bordas, T. Rabczuk, and G. Zi. Three-dimensional crack initiation, propagation, branching and junction in non-linear materials by an extended meshfree method without asymptotic enrichment. *Engineering Fracture Mechanics*, 75(5):943–960, 2008c.
- D. Brown, L. Ling, E.J. Kansa, and J. Levesley. On approximate cardinal preconditioning methods for solving pdes with radial basis functions. *Engineering Analysis with Boundary Elements*, 29:343–353, 2005.
- E. Budyn. *Multiple Crack Growth by the eXtended Finite Element Method*. PhD thesis, Northwestern University, June 2004.

- E. Budyn, G. Zi, N. Moës, and T. Belytschko. A method for multiple crack growth in brittle materials without remeshing. *International Journal for Numerical Methods in Engineering*, 61:1741–1770, 2004.
- Z. Cai and G. Starke. First order system least-squares for stress-displacement formulation linear elasticity. *SIAM J. Numer. Anal.*, 41:715–730, 2003.
- Z. Cai, R. D. Lazarov, T. Manteuffel, and S. McCormick. First order system least-square for second-order partial differential equations: Part 1. *SIAM J. Numer. Anal.*, 31:1785–1799, 1994.
- Z. Cai, T. Manteuffel, and S. McCormick. First order system least-squares for stokes equations with application to linear elasticity. *SIAM J. Numer. Anal.*, 34:1727–1741, 1997a.
- Z. Cai, T. Manteuffel, and S. McCormick. First order system least-squares for second-order partial differential equations: Part 2. *SIAM J. Numer. Anal.*, 34:425–454, 1997b.
- Z. Cai, T. Manteuffel, S. McCormick, and S. Parter. First order system least-squares (FOSLS) for planar linear elasticity: pure traction problem. *SIAM J. Numer. Anal.*, 35:320–335, 1998.
- Z. Cai, C.-O. Lee, T. Manteuffel, and S. McCormick. First order system least-squares for linear elasticity: numerical results. *SIAM J. SCI. COMPUT.*, 21:1706–1727, 2000.
- G. T. Camacho and M. Ortiz. Computational modelling of impact damage in brittle materials. *International Journal of Solids and Structures*, 33:2899–2938, 1996.
- J.S. Chen, HP. Wang, S. Yoon, and Y. You. An improve reproducing kernel particle methods for nearly incompressible finite elasticity. *Comp. Meth. Appl. Mech. Eng.*, 181:117–145, 2000.

- J.S. Chen, W. Hu, and H.Y. Hu. Reproducing kernel enhanced radial basis collocation method. *International Journal for Numerical Methods in Engineering*, 75:600–627, 2008a.
- J.S. Chen, W. Hu, and H.Y. Hu. Reproducing kernel enhanced local radial basis collocation method. *International Journal for Numerical Methods in Engineering*, 75:600–627, 2008b.
- A.H.D Cheng, M.A. Golberg, E. J. Kansa, and G. Zamitto. Exponential convergence and h-c multiquadric collocation method for partial differential equations. *Numerical Methods for Partial Differential Equations*, 19:571–594, 2003.
- J. Chessa, H. Wang, and T. Belytschko. On the construction of blending elements for local partition of unity enriched finite elements. *International Journal of Numerical Methods in Engineering*, 57:1015–1038, 2003.
- Jack Chessa. *The Extended Finite Element Method for Free Surface and Two Phase Flow Problems*. PhD thesis, Northwestern University, December 2002.
- E. Cueto, N. Sukumar, B. Calvo, M. A. Matínez, and M. Doblaré. Overview and recent advances in natural neighbour galerkin methods. *Archives of Computational Methods in Engineering*, 10:307–384, 2003.
- R. de Borst. Fracture in quasi-brittle materials: a review of continuum damage-based approaches. *Engineering Fracture Mechanics*, 69:95–112, 2002.
- J. Dolbow and T. Belytschko. Volumetric locking in the element-free Galerkin method. *International Journal for Numerical Methods in Engineering*, 46:925–942, 1999.
- J. E. Dolbow. *An Extended Finite Element Method with Discontinuous Enrichment for Applied Mechanics*. PhD thesis, Northwestern University, July 1999.

- T. A. Driscoll and A. R. H. Heryudono. Adaptive residual subsampling methods for radial basis functions interpolation and collocation problems. *Computers & Mathematics with Applications*, 53:927–939, 2007.
- C. A. Duarte and I. Babuška. Mesh-independent p-orthotropic enrichment using the generalized finite element method. *International Journal for Numerical Methods in Engineering*, 55:1477–1492, 2002.
- C. A. Duarte and D. J. Kim. Analysis and application of a generalized finite element method with global-local enrichment functions. *Computer Methods in Applied Mechanics and Engineering*, 197:487–504, 2008.
- C. A. Duarte, I. Babuška, and J. T. Oden. The generalized finite element methods for three dimensional structural mechanics problems. *Computer & Structures*, 77:215–232, 2000.
- C. A. Duarte, O. N. Hamzeh, T. J. Liszka, and W. W. Tworzydło. A generalized finite element method for the simulation of three-dimensional dynamic crack propagation. *Computer Methods in Applied Mechanics and Engineering*, 190:2227–2262, 2001.
- C. A. Duarte, D. J. Kim, and D. M. Quaresma. Arbitrary smooth generalized finite element approximations. *Computer Methods in Applied Mechanics and Engineering*, 196:33–56, 2006.
- C. A. Duarte, D. J. Kim, and I. Babuška. *Advances in meshfree techniques*, chapter A global-local approach for the construction of enrichment functions for the generalized FEM and its application to three-dimensional cracks, pages 1–26. ISBN 978-1-4020-6094-6. Springer, 2007.
- M. Dufflot. A meshless method with enriched weight functions for three-dimensional crack propagation. *International Journal for Numerical Methods in Engineering*, 65:1970–2006, 2006.
- M. Dufflot. A study of the representation of crack with level sets. *International Journal for Numerical Methods in Engineering*, 2008. In press.

- M. Duflot and H. Nguyen-Dang. A truly meshless Galerkin method based on a moving least square quadrature. *Communications in Numerical Methods in Engineering*, 18:441–449, 2002a.
- M. Duflot and H. Nguyen-Dang. Dual analysis by a meshless method. *Communications in Numerical Methods in Engineering*, 18:621–631, 2002b.
- M. Duflot and H. Nguyen-Dang. A meshless method with enriched weight functions for fatigue crack growth. *International Journal for Numerical Methods in Engineering*, 59:1945–1961, 2004.
- M. Elices, G. V. Guinea, J. Gómez, and J. Planas. The cohesive zone model: advantages, limitation and challenges. *Engineering Fracture Mechanics*, 69:137–163, 2002.
- M. L. Falk, A. Needleman, and J. R. Rice. A critical evaluation of cohesive zone models of dynamics fracture. *Journal of Physics IV 11(PR5)*, pages 43–50, 2001.
- R. Fan and J. Fish. The rs-method for material failure simulations. *International Journal for Numerical Methods in Engineering*, 73:1607–1623, 2008.
- G.E. Fasshauer. Solving partial differential equations by collocation with radial basis functions. In A. Le Méhauté, C. Rabut, and L.L. Schumaker, editors, *Surface Fitting and Multiresolution Methods*, pages 131–138. Vanderbilt University Press, 1997.
- S. Fernández-Mández and A. Huerta. Imposing essential boundary conditions in mesh-free methods. *Computer Methods in Applied Mechanics and Engineering*, 193:1257–1275, 2004.
- M. Fleming, Y. A. Chu, B. Moran, and T. Belytschko. Enriched element-free Galerkin methods for crack tip fields. *International Journal for Numerical Methods in Engineering*, 40:1483–1504, 1997.

- S.C. Forth and W.D. Keat. Three-dimensional nonplanar fracture model using the surface integral method. *International Journal of Fracture*, 77:243–262, 1996.
- T. P. Fries and T. Belytschko. The intrinsic XFEM: a method for arbitrary discontinuities without additional unknowns. *International Journal for Numerical Methods in Engineering*, 68:1358–1385, 2006.
- T. P. Fries and H.G. Matthies. Classification and overview of meshfree methods. Technical report, Informatikbericht-Nr. 2003-03, Technical University Braunschweig, Brunswick, Germany, July 2004a. <http://opus.tu-bs.de/opus/volltexte/2003/418><http://opus.tu-bs.de/opus/volltexte/2003/418>.
- T. P. Fries and H.G. Matthies. A review of petrov-galerkin stabilization approaches and an extension to meshfree methods. Technical report, Informatikbericht-Nr. 2004-01, Technical University Braunschweig, Brunswick, Germany, July 2004b. <http://www.digibib.tu-bs.de/?docid=00001549><http://www.digibib.tu-bs.de/?docid=00001549>.
- T.P. Fries. A corrected x fem approximation without problems in blending elements. *International Journal for Numerical Methods in Engineering*, 75: 503–532, 2008.
- L. Gao, K. Liu, and Y. Liu. Application of MLPG method in dynamic fracture problems. *CMES: Computer Modeling in Engineering & Sciences*, 12:181–195, 2006.
- F. García-Sánchez, A. Sáez, and J. Domínguez. Two-dimensional time-harmonic BEM for cracked anisotropic solids. *Engineering Analysis with Boundary Elements*, 30:88–99, 2006.
- A. Gravouil, N. Moës, and T. Belytschko. Non-planar 3d crack growth by the extended finite element and level sets. part II: level set update. *International Journal for Numerical Methods in Engineering*, 53:2569–2586, 2002.

- L. Gu. Moving kriging interpolation and element-free galerkin method. *International Journal for Numerical Methods in Engineering*, 56:1–11, 2003.
- Y. T. Gu and G. R. Liu. A meshfree Weak-Strong (MWS) form method for time dependent problems. *Computational Mechanics*, 35:134–145, 2005.
- E. Hairer and G. Wanner. *Solving Ordinary Differential Equations II. Stiff and Differential-Algebraic Problems*. Springer-Verlag, 1996.
- E. Hairer, S.P. Norsett, and G. Wanner. *Solving Ordinary Differential Equations I. Nonstiff Problems*. Springer-Verlag, 1987.
- Z. D. Han and S. N. Atluri. Truly Meshless Local Petrov-Galerkin (MLPG) Solutions of Traction & Displacement BIEs. *CMES: Computer Modeling in Engineering & Sciences*, 4(6):665–678, 2003.
- Z. D. Han, A. M. Rajendran, and S. N. Atluri. Meshless Local Petrov-Galerkin (MLPG) Approaches for Solving Nonlinear Problems with Large Deformations and Rotations. *CMES: Computer Modeling in Engineering & Sciences*, 10(1):1–12, 2005.
- Z. D. Han, H. T. Liu, A. M. Rajendran, and S. N. Atluri. The Applications of Meshless Local Petrov-Galerkin (MLPG) Approaches in High-Speed Impact, Penetration and Perforation Problems. *CMES: Computer Modeling in Engineering & Sciences*, 14(2):119–128, 2006.
- Z.D. Han and S.N. Atluri. A meshless local Petrov-Galerkin (MLPG) approach for 3-dimensional elasto-dynamics. *CMC*, 1:129–140, 2004.
- Z. Hehua, L. Wenjun, C. Yongchang, and M. Yuanbin. A meshless local natural neighbor interpolation method for two-dimensional incompressible large deformation analysis. *Engineering Analysis with Boundary Elements*, 31:865–862, 2007.
- R. Hill. Acceleration waves in solids. *J. Mech. Phys. Solids*, 10:1–16, 1962.

- H.Y. Hu, J.S. Chen, and W. Hu. Weighted radial basis collocation method for boundary value problems. *International Journal for Numerical Methods in Engineering*, 69:2736–2755, 2006.
- S. G. Idelsohn, E. Onate, N. Calvo, and F. D. Pin. The meshless finite element method. *International Journal for Numerical Methods in Engineering*, 58: 893–912, 2003.
- B. Jiang and J. Wu. The least-squares finite element method in elasticity-part 1: Plane stress with drilling degrees of freedom. *International Journal for Numerical Methods in Engineering*, 53:621–636, 2002.
- M. Jirásek. Comparative study on finite elements with embedded discontinuities. *Computer Methods in Applied Mechanics and Engineering*, 188:307–330, 2000.
- J. H. Jung. A note on the Gibbs phenomenon with multiquadratic radial basis functions. *Applied Numerical Mathematics*, 57:213–229, 2007.
- L. Kaiyuan, L. Shuyao, and L. Guangyao. A simple and less-costly meshless local petrov-galerkin (mlpg) method for the dynamic fracture problem. *Engineering Analysis with Boundary Elements*, 30:72–76, 2006.
- J. Kaljevic and S. Saigal. An improved element free galerkin formulation. *International Journal for Numerical Methods in Engineering*, 40:2953–2974, 1997.
- E. J. Kansa. Multiquadrics – a scattered data approximation scheme with applications to computational fluid dynamics – II. Solutions to parabolic, hyperbolic and elliptic partial differential equations. *Computers & Mathematics with Applications*, 19:147–161, 1990.
- E. J. Kansa, H. Power, G. E. Fasshauer, and L. Ling. A volumetric integral radial basis function method for time-dependent partial differential equations: I formulation. *Engineering Analysis with Boundary Elements*, 28:1191–1206, 2004.

- E.J. Kansa and Y.C. Hon. circumventing the ill-conditioning problem with multiquadric radial basis functions: application to elliptic partial differential equations. *Compu. Math. Appl.*, 39:123–137, 2000.
- B. L. Karihaloo and Q. Z. Xiao. Modelling stationary and growing cracks in FE framework without remeshing: a state-of-art review. *Computers & Structures*, 81:119–129, 2003.
- D. W. Kim, W. K. Liu, Y. C. Yoon, T. Belytschko, and S. H. Lee. Meshfree collocation method with intrinsic enrichment for interface problems. *Computational Mechanics*, 40:1037–1052, 2007a.
- D. W. Kim, Y. C. Yoon, W. K. Liu, and T. Belytschko. Extrinsic mesh-free approximation using asymptotic expansion for interfacial discontinuity of derivative. *Journal of Computational Physics*, 221:370–394, 2007b.
- R. Kouhia. Stabilized form of orthogonal residual and constant incremental work control path following methods. *Computer methods in applied mechanics and engineering*, 197:1389–1396, 2008.
- S. Krenk. An orthogonal residual procedure for non-linear finite element equations. *International Journal for Numerical Methods in Engineering*, 38:823–839, 1995.
- S. Krenk. *Non-linear modeling and analysis of solids and structures*. Cambridge University Press, 2009.
- S. Krenk and O. Hededal. A dual orthogonal residual procedure for non-linear finite element equations. *Computer methods in applied mechanics and engineering*, 123:95–107, 1995.
- Y. Krongauz and T. Belytschko. EFG approximation with discontinuous derivatives. *International Journal for Numerical Methods in Engineering*, 41:1215–1233, 1998.

- P. Krysl and T. Belytschko. The element-free Galerkin method for dynamic propagation of arbitrary 3-d cracks. *International Journal for Numerical Methods in Engineering*, 44:767–800, 1999.
- D. V. Kubair and P. H. Geubelle. Comparative analysis of extrinsic and intrinsic cohesive models of dynamic fracture. *International Journal of Solids and Structures*, 40:3853–3868, 2003.
- K. Kwon, S. Park, B. Jiang, and S. Youn. The least-squares meshfree method for solving linear elastic problems. *Computational Mechanics*, 30:196–211, 2003.
- P. Laborde, J. Pommier, Y. Renard, and M. Salaun. High-order extended finite element method for crack domains. *International Journal for Numerical Methods in Engineering*, 64:354–381, 2005.
- P. Le, N. Mai-Duy, T. Tran-Cong, and G. Baker. A meshless IRBF-based numerical simulation of adiabatic shear band formation in one dimension. In Nguyen Quoc Son and Nguyen Dung, editors, *Conference on Nonlinear Analysis & Engineering Mechanics Today*, HoChiMinh City, Vietnam, December 2006. CD paper No 28 (10 pages).
- P. Le, N. Mai-Duy, T. Tran-Cong, and G. Baker. A numerical study of strain localization in elasto-thermo-viscoplastic materials using radial basis function networks. *CMC: Computers, Materials & Continua*, 5:129–150, 2007a.
- P. Le, N. Mai-Duy, T. Tran-Cong, and G. Baker. Meshless IRBF-based numerical simulation of dynamic strain localization in quasi-brittle materials. In *9th U.S. National Congress on Computational Mechanics*, San Francisco, USA, July 2007b. CD page 63.
- P. Le, N. Mai-Duy, T. Tran-Cong, and G. Baker. A meshless modeling of dynamic strain localization in quasi-brittle materials using radial basis function networks. *CMES: Computer Modeling in Engineering & Sciences*, 25(1): 43–66, 2008a.

- P. Le, N. Mai-Duy, T. Tran-Cong, and G. Baker. An IRBFN cartesian grid method based on displacement-stress formulation for 2D elasticity problems. In *8th World Congress on Computational Mechanics (WCCM8)*, Venice, Italy, June-July 2008b.
- P. Le, N. Mai-Duy, T. Tran-Cong, and G. Baker. A Cartesian-grid Collocation Technique with Integrated Radial Basis Functions for mixed boundary value problems. *International Journal for Numerical Methods in Engineering*, 82(4):435–463, 2010a.
- P. Le, T. Rabczuk, N. Mai-Duy, and T. Tran-Cong. A moving RBFN-based galerkin meshless method. *CMES: Computer Modeling in Engineering & Sciences*, 2010b. Under review.
- P. Le, T. Rabczuk, N. Mai-Duy, and T. Tran-Cong. A moving RBFN-based integration-free meshless method. *CMES: Computer Modeling in Engineering & Sciences*, 2010c. Under review.
- P. Le, T. Rabczuk, N. Mai-Duy, T. Tran-Cong, and S. Bordas. An extended moving RBFN-based meshless method for elasto-static crack analysis. *International Journal for Numerical Methods in Engineering*, 2010d. Special issue of XFEM, under review.
- B. Lee. First order system least-squares for elliptic problems with Robin boundary conditions. *SIAM J. Numer. Anal.*, 37:70–104, 1999.
- S. H. Lee and Y. C. Yoon. Meshfree collocation method for elasticity and crack problems. *International Journal for Numerical Methods in Engineering*, 61:22–48, 2004a.
- S.H. Lee and Y.C. Yoon. Meshfree point collocation method for elasticity and crack problems. *International Journal for Numerical Methods in Engineering*, 61:22–48, 2004b.
- H. Li, T. Y. Ng, J. Q. Cheng, and K. Y. Lam. Hermite -cloud: a novel true meshless method. *Computational Mechancis*, 33:30–41, 2003.

- S. Li and W. C. Liu. Numerical simulation of Strain localization in inelastic solids using mesh-free method. *International Journal for Numerical Methods in Engineering*, 48:1285–1309, 2000.
- S. Li and W. C. Liu. Meshfree particle methods and their applications. *Applied Mechannics Reviews*, 55:1–34, 2002.
- S. Li and W. C. Liu. *Meshfree particle method*. Springer-Verlag Berlin Heidelberg, Germany, 2004.
- S. Li, W. Hao, and W. C. Liu. Meshfree simulations of shear banding in large deformation. *International Journal of Solids and Structures*, 37:7815–7206, 2000.
- X. Li, M. S. Shephard, and M. W. Beall. 3d anisotropic mesh adaptation by mesh modification. *Computer Methods in Applied Mechanics and Engineering*, 194:4915–4950, 2005.
- R. Y. K. Liang and Y. N. Li. simulation of nonlinear fracture process zone in cementitious matereial-a boundary element approach. *Computatonal Mechanics*, 7:413–427, 1991.
- N. A. Libre, A. Emdadi, E. J. Kansa, M. Rahimian, and M. Shekarchi. A stabilized RBF collocation scheme for Neumann type boundary value problems. *CMES: Computer Modeling in Engineering & Sciences*, 24:63–82, 2008.
- C. Linder and F. Armero. Finite elements with embedded strong discontinuities for the modelling of failure in solids. *International Journal for Numerical Methods in Engineering*, 72:1391–1433, 2007.
- L. Ling and E.J. Kansa. Preconditioning for radial basis functions with domain decomposition methods. *Mathematical and Computer Modelling*, 40:1413–1427, 2004.
- Leevan Ling and Manfred R. Trummer. Multiquadratic collocation method with

- integral formulation for boundary layer problems. *Computers & Mathematics with Applications*, 48:927–941, 2004.
- Leevan Ling and Manfred R. Trummer. Adaptive multiquadratic collocation for boundary layer problems. *Journal of Computational and Applied Mathematics*, 188:265–282, 2006.
- G. R. Liu. *Meshfree methods: moving beyond the finite element method*. CRC Press, USA, 2003.
- G. R. Liu and Y. T. Gu. A meshfree method: Weak-Strong (MWS) form method, for 2D solids. *Computational Mechanics*, 33:2–14, 2003.
- G. R. Liu and Y. T. Gu. *An introduction to Meshfree methods and their programming*. Springer, The Netherlands, 2005.
- G. R. Liu and G. Y. Zhang. Edge-Based Smooth Point Interpolation Methods. *International Journal of Computational Methods*, 5(4):621–646, 2008.
- G.R. Liu, G.Y. Zhang, and Y.T. Gu. A meshfree radial point interpolation method (RPIM) for three-dimensional solids. *Computational Mechanics*, 36(6):421–430, 2005a.
- G.R. Liu, J. Zhang, H. Li, K.Y. Lam, and B. Kee. Radial point interpolation based finite difference method for mechanics problems. *International Journal for Numerical Methods in Engineering*, 68:728–754, 2006.
- X. Liu, G.R. Liu, and K. Tai. Radial point interpolation collocation method (RPICM) for partial differential equations. *Computers & Mathematics With Applications*, 50(8–9):1425–1442, 2005b.
- B. Loret and J. H. Prevost. Dynamic strain localization in elasto-(visco-) plastic solid. Part 1. General formulation and one-dimensional examples. *Computer Methods in Applied Mechanics and Engineering*, 83:247–273, 1990a.

- B. Loret and J. H. Prevost. Dynamic strain localization in elasto-(visco-) plastic solid. Part 2. Plane strain examples. *Computer Methods in Applied Mechanics and Engineering*, 83:275–294, 1990b.
- J. Mackerle. Object-oriented techniques in fem and bem, a bibliography (1996-1999). *Finite Elements in Analysis and Design*, 36:189–196, 2000.
- W. R. Madych and S. A. Nelson. Multivariate interpolation and conditionally positive definite functions, II. *Mathematics of Computation*, 54:211–230, 1990.
- W.R. Madych. Miscellaneous error bounds for multiquadric and related interpolators. *Compu. Math. Appl.*, 24:121–138, 1992.
- L. Mai-Cao and T. Tran-Cong. A meshless IRBFN-based method for transient problems. *CMES: Computer Modeling in Engineering & Sciences*, 7:149–171, 2005.
- N. Mai-Duy. Solving high order ordinary differential equations with radial basis function networks. *International Journal for Numerical Methods in Engineering*, 62:824–852, 2005.
- N. Mai-Duy and R. I. Tanner. Solving high order partial differential equations with indirect radial basis function networks. *International Journal for Numerical Methods in Engineering*, 63:1636–1654, 2005.
- N. Mai-Duy and T. Tran-Cong. Numerical solution of differential equations using multiquadric radial basic function networks. *Neural Networks*, 14:185–199, 2001.
- N. Mai-Duy and T. Tran-Cong. Approximation of function and its derivatives using radial basis function networks. *Applied Mathematical Modeling*, 27:197–220, 2003.
- N. Mai-Duy and T. Tran-Cong. An efficient indirect RBFN-based method for

- numerical solution of PDEs. *Numerical Methods for Partial Differential Equations*, 21:770–790, 2005.
- N. Mai-Duy and T. Tran-Cong. Solving biharmonic problems with scattered-point discretization using indirect radial-basis-function networks. *Engineering Analysis with Boundary Elements*, 30:77–87, 2006.
- N. Mai-Duy and T. Tran-Cong. A cartesian-grid collocation method based on radial-basis-function networks for solving PDEs in irregular domains. *Numerical Methods for Partial Differential Equations*, 23:1192–1210, 2007.
- J. M. Melenk and I. Babuška. The partition of unity finite element method: Basic theory and applications. *Computer Methods in Applied Mechanics and Engineering*, 139:289–314, 1996.
- N. Moës, J. Dolbow, and T. Belytschko. A finite element method for crack growth without remeshing. *International Journal for Numerical Methods in Engineering*, 46:131–150, 1999a.
- N. Moës, J. Dolbow, and T. Belytschko. A finite element method for crack growth without remeshing. *International Journal for Numerical Methods in Engineering*, 46:131–150, 1999b.
- N. Moës, A. Gravouil, and T. Belytschko. Non-planar 3d crack growth by the extended finite element and level sets. part I: Mechanical model. *International Journal for Numerical Methods in Engineering*, 53:2549–2568, 2002.
- A. Molinari and R. J. Clifton. Analytical characterization of shear localization in thermoviscoplastic materials. *Journal of Applied Mechanics*, 54:806–812, 1987.
- J. F. Molinari, G. Gazonas, R. Raghupathy, and F. Zhou. The cohesive element approach to dynamics fragmentation: the question of energy convergence. *International Journal for Numerical Methods in Engineering*, 69:484–503, 2006.

- B. Moran and C. F. Shih. Crack tip and associated domain integrals from momentum and energy balance. *Engineering Fracture Mechanics*, 127:615–642, 1987.
- A. Nagarajan and S. Mukherjee. A mapping method for numerical evaluation of two-dimensional integrals with $1/r$ singularity. *Computational mechanics*, 12:19–26, 1993.
- P. V. Nguyen, T. Rabczuk, S. Bordas, and M. Duflot. Meshless method: a review and computer implementation aspects. *Mathematics and Computers in Simulation*, 2008a. in press.
- V.P. Nguyen, T. Rabczuk, S. Bordas, and M. Duflot. Meshfree method: A review and computer implementation aspects. *Mathematics and Computers in Simulation*, 2008b. In press.
- G. P. Nikishkov and S. N. Atluri. Calculation of fracture mechanics parameters for an arbitrary three-dimensional crack by the ‘equivalent domain integral’ method. *International Journ Numer Meth. Engng*, 24:851–867, 1987.
- Y. Ohtake, A. Belyaev, and H.P. Seidel. Sparse surface reconstruction with adaptive partition of unity and radial basis functions. *Graphical Models*, 68:15–24, 2006.
- J. Oliver. Modelling strong discontinuities in solid mechanics via strain softening constitutive equations. Part 1: Fundamentals. *International Journal for Numerical Methods in Engineering*, 39:3575–3600, 1996a.
- J. Oliver. Modelling strong discontinuities in solid mechanics via strain softening constitutive equations. Part 2: Numerical simulation. *International Journal for Numerical Methods in Engineering*, 39:3575–3600, 1996b.
- J. Oliver and A.E. Huespe. Theoretical and computational issues in modelling material failure in strong discontinuities scenarios. *Computer Methods in Applied Mechanics and Engineering*, 193:2987–3014, 2004a.

- J. Oliver and A.E. Huespe. Continuum approach to material failure in strong discontinuity settings. *Computer Methods in Applied Mechanics and Engineering*, 193:3195–3220, 2004b.
- J. Oliver, A.E. Huespe, and E. Samaniego. A study on finite elements for capturing strong discontinuities. *International Journal for Numerical Methods in Engineering*, 56:2135–2161, 2003.
- J. Oliver, A.E. Huespe, S. Blanco, and D.L. Linero. Stability and robustness issues in numerical modeling of material failure with the strong discontinuity approach. *Computer Methods in Applied Mechanics and Engineering*, 195:7093–7114, 2006a.
- J. Oliver, A.E. Huespe, and P.J. Sánchez. A comparative study on finite elements for capturing strong discontinuities: E-FEM vs X-FEM. *Computer Methods in Applied Mechanics and Engineering*, 195:4732–4752, 2006b.
- J. Oliver, D.L. Linero, A.E. Huespe, and O.L. Manzoli. Two-dimensional modeling of material failure in reinforced concrete by mean of a continuum strong discontinuity approach. *Computer Methods in Applied Mechanics and Engineering*, 197:332–348, 2008.
- E. Onate, F. Perazzo, and J. Miquel. A finite point method for elasticity problem. *Computers & Structures*, 79:2151–2163, 2001.
- M.J.L. Orr. Local smoothing of radial basis function networks. In *International Symposium on Artificial Neural Networks*, Hsinchu, Taiwan, 1995a.
- M.J.L. Orr. Regularisation in the selection of Radial Basis Function Centres. *Neural computation*, 7:606–623, 1995b.
- M.J.L. Orr. Introduction to radial basis function networks. *Technical report*, Centre for Cognitive Science, University of Edinburgh, Edinburgh EH8 9LW, Scotland, 1996.

- M. Ortiz and A. Pandoli. Finite-deformation irreversible cohesive elements for three-dimensional crack propagation analysis. *International Journal for Numerical Methods in Engineering*, 44:1267–1282, 1999.
- X. F. Pan, X. Zhang, and M. W. Lu. Meshless Galerkin least-squares method. *Computational Mechanics*, 35:182–189, 2005.
- K. Park, J. Pereira, C. A. Duarte, and G. H. Paulino. Integration of singular enrichment functions in the generalized/extended finite element method for three-dimensional problems. *International Journal for Numerical Methods in Engineering*, 78:1220–1257, 2009.
- S. Park and S. Youn. The least-squares meshfree method. *International Journal for Numerical Methods in Engineering*, 52:997–1012, 2001.
- M. Pastor, J. Peraire, and O. C. Zienkiewicz. Adaptive remeshing for shear band localization problems. *Archive of Applied Mechanics*, 61:30–39, 1991.
- B. Patzák and M. Jirásek. Process zone resolution by extended finite elements. *Engineering Fracture Mechanics*, 70:957–977, 2003.
- B. Patzák and M. Jirásek. Adaptive resolution of localized damage in quasi-brittle materials. *Journal of Engineering Mechanics*, 130:720–732, 2004.
- J. P. Pereira and C. A. Duarte. Extraction of stress intensity factors from generalized finite element solutions. *Engineering Analysis with Boundary Elements*, 29:397–413, 2005.
- D.O. Potyondy, P.A. Wawrzynek, and A.R. Ingraffea. An algorithm to generate quadrilateral or triangular element surface meshes in arbitrary domains with applications to crack propagation. *International Journal for Numerical Methods in Engineering*, 38:2677–2701, 1995.
- T. Rabczuk and P. Areias. A meshfree thin shell for arbitrary evolving cracks based on an external enrichment. *Computer Modeling in Engineering and Sciences*, 16(2):115–130, 2006.

- T. Rabczuk and T. Belytschko. Adaptivity for structured meshfree particle methods in 2D and 3D. *International Journal for Numerical Methods in Engineering*, 63(11):1559–1582, 2005a.
- T. Rabczuk and T. Belytschko. Cracking particles: A simplified meshfree method for arbitrary evolving cracks. *International Journal for Numerical Methods in Engineering*, 61(13):2316–2343, 2004a.
- T. Rabczuk and T. Belytschko. A three dimensional large deformation meshfree method for arbitrary evolving cracks. *Computer Methods in Applied Mechanics and Engineering*, 196(29–30):2777–2799, 2007a.
- T. Rabczuk and T. Belytschko. Cracking particles: a simplified meshfree method for arbitrary evolving cracks. *International Journal for Numerical Methods in Engineering*, 61:2316–2343, 2004b.
- T. Rabczuk and T. Belytschko. Adaptive for structured meshfree particle methods in 2d and 3d. *International Journal for Numerical Methods in Engineering*, 63:1559–1582, 2005b.
- T. Rabczuk and T. Belytschko. A three-dimensional large deformation meshfree method for arbitrary evolving cracks. *Computer Methods in Applied Mechanics and Engineering*, 196:2777–2799, 2007b.
- T. Rabczuk and E. Samaniego. Discontinuous modelling of shear bands using meshfree methods. *Computer Methods in Applied Mechanics and Engineering*, 197:641–658, 2008.
- T. Rabczuk and G. Zi. A meshfree method based on the local partition of unity for cohesive cracks. *Computational Mechanics*, 39:743–760, 2007.
- T. Rabczuk, T. Belytschko, and S.P. Xiao. Stable particle methods based on lagrangian kernels. *Computer Methods in Applied Mechanics and Engineering*, 193:1035–1063, 2004.

- T. Rabczuk, S.P. Xiao, and M. Sauer. Coupling of meshfree methods with finite elements: Basic concepts and test results. *Communications in Numerical Methods in Engineering*, 22(10):1031–1065, 2006.
- T. Rabczuk, P. M. A. Areias, and T. Belytschko. A simplified meshfree method for shear bands with cohesive surfaces. *International Journal for Numerical Methods in Engineering*, 69:993–1021, 2007a.
- T. Rabczuk, P.M.A. Areias, and T. Belytschko. A meshfree thin shell method for non-linear dynamic fracture. *International Journal for Numerical Methods in Engineering*, 72(5):524–548, 2007b.
- T. Rabczuk, S. Bordas, and G. Zi. A three dimensional meshfree method for static and dynamic multiple crack nucleation/propagation with crack path continuity. *Computational Mechanics*, 40(3):473–495, 2007c.
- T. Rabczuk, S. Bordas, and G. Zi. A three-dimensional meshfree method for continuous multiple-crack initiation, propagation and junction in statics and dynamics. *Computational Mechanics*, 40:473–495, 2007d.
- T. Rabczuk, S. Bordas, and G. Zi. On three-dimensional crack growth. *Computers & Structures*, 2008a. Submitted.
- T. Rabczuk, G. Zi, S. Bordas, and H. Nguyen-Xuan. A three-dimensional cohesive crack method for reinforced concrete structures. *Engineering Fracture Mechanics*, 2008b. Submitted.
- B. N. Rao and S. Rahman. An enriched meshless method for non-linear fracture mechanics. *International Journal for Numerical Methods in Engineering*, 59:197–223, 2004.
- B. N. Rao and S. Rahman. An efficient meshless method for fracture analysis of cracks. *Computational Mechanics*, 26:398–408, 2000.
- J. R. Rice. A path independent integral and the approximate analysis of strain

- concentration by notches and cracks. *Journal of Applied Mechanics*, pages 379–386, 1968.
- J. R. Rice and J. W. Rudnicki. A note on some features of the theory of localization of deformation. *International Journal for Solids Structures*, 16: 597–605, 1980.
- P. J. Roache. *Computational Fluid Dynamics*. Hermosa Publisher, 1980.
- J. W. Rudnicki and J. R. Rice. Conditions for the strain localization of deformation in pressure-sensitive dilatant materials. *J. Mech. Phys. Solids*, 23: 371–394, 1975.
- A. W. Rüegg. Implementation of generalized finite element methods for homogenization problems. *Journal of Scientific Computing*, 17:671–681, 2002.
- J. Rungamornrat. Analysis of 3d cracks in anisotropic multi-material domain with weakly singular SGBEM. *Engineering Analysis with Boundary Elements*, 30:834–846, 2006.
- R. J. Schilling, J. J. Carroll, and A. F. Al-Ajlouni. Approximation of nonlinear system with radial basis function neural networks. *IEEE Transaction on Neural Networks*, 12:1–15, 2001.
- M. Schollmann, M. Fulland, and H. A. Richard. Development of a new software for adaptive crack growth simulations in 3d structures. *Engineering Fracture Mechanics*, 70:249–268, 2003.
- J. A. Sethian. *Level Set Methods & Fast Marching Methods: Evolving Interfaces in Computational Geometry, Fluid Mechanics, Computer Vision, and Materials Science*. Cambridge University Press, Cambridge, UK, 1999.
- R. A. Sherif and T. G. Shawki. The role of heat conduction during the post-localization regime in dynamic viscoplasticity. *Plastic flow and Creep, ASME, AMD-Vol. 135/MD-Vol. 31:159–173*, 1992.

- C. F. Shih, B. Moran, and T. Nakamura. Energy release rate along a three-dimensional crack front in a thermally stressed body. *International Journal of Fracture*, 30:79–102, 1986.
- C. Shu and Y.L. Wu. integrated radial basis functions based differential quadrature method and its performance. *International Journal for Numerical Methods in Fluid*, 53:969–984, 2007.
- C. Shu, H. Ding, and K.S. Yeo. Local radial basis functions based differential quadrature method and its application to solve two-dimensional incompressible Navier-Stoke equations. *Computer Methods in Applied Mechanics and Engineering*, 192:941–954, 2003.
- N. P. P. Silveira, S. Guimaraes, and J. C. F. Telles. On the description of localization and failure phenomena by the boundary element method. *Engineering Analysis with Boundary Elements*, 29:978–985, 2005.
- J. C. Simo and T.J.R. Huges. *Computational Inelasticity*. Springer-Verlag New York, Inc, 1998.
- J. Sladek, V. Sladek, and A. N. Atluri. Meshless local Petrov-Galerkin (MLPG) method in anisotropic elasticity. *CMES: Computer Modeling in Engineering & Sciences*, 6:477–489, 2004.
- J. Sladek, V. Sladek, P. Solek, and L. Starek. Fracture analyses in continuously nonhomogeneous piezoelectric Solids by the MLPG. *CMES: Computer Modeling in Engineering & Sciences*, 19:247–262, 2006.
- J. Sladek, V. Sladek, and S. N. Atluri. Local boundary integral equation (lbie) method for solving problems of elasticity with nonhomogeneous material properties. *Computational Mechanics*, 24(6):456—462, Jan 2000.
- L. J. Sluys. *Wave propagation, localisation and dispersion in softening solids*. PhD thesis, Delft University of Technology, 1992.

- J. H. Song, H. Wang, and T. Belytschko. A comparative study on finite element methods for dynamic fracture. *Computational Mechanics*, 2008. in press.
- B.W. Spencer and P.B. Shing. Rigid-plastic interface for an embedded crack. *International Journal for Numerical Methods in Engineering*, 56:2163–2182, 2003.
- F. L. Stazi, E. Budyn, J. Chessa, and T. Belytschko. An extended finite element method with higher-order elements for curved cracks. *Computational mechanics*, 31:38–48, 2003.
- T. Strouboulis, I. Babuška, and K. Copps. The design and analysis of the generalized finite element method. *Computer Methods in Applied Mechanics and Engineering*, 181:43–71, 2000a.
- T. Strouboulis, K. Copps, and I. Babuška. The generalized finite element method: an example of its implementation and illustration of its performance. *International Journal for Numerical Methods in Engineering*, 47(8): 1401–1417, 2000b.
- T. Strouboulis, L. Zhang, and I. Babuška. Assessment of the cost and accuracy of the generalized FEM. *International Journal for Numerical Methods in Engineering*, 69:250–283, 2007.
- N. Sukumar, B. Moran, T. Black, and T. Belytschko. An element-free Galerkin method for three-dimensional fracture mechanics. *Computational Mechanics*, 20:170–175, 1997.
- N. Sukumar, B. Moran., and T. Belytschko. Natural neighbour element method in solid mechanics. *International Journal for Numerical Methods in Engineering*, 43:839–887, 1998.
- N. Sukumar, B. Moran., A. Y. Semenov, and V. V. Belikov. Natural neighbour Galerkin methods. *International Journal for Numerical Methods in Engineering*, 50:1–27, 2001.

- H. Tada, P. C. Paris, and G. R. Irwin. *Analysis of crack handbook*. The American Society of Mechanical Engineers, New York, USA, third edition, 2000.
- A. Tan, S. Hirose, and C. Zhang. A time-domain collocation-galerkin bem for transient dynamic crack analysis in anisotropic solids. *Engineering Analysis with Boundary Elements*, 29:1025–1038, 2005.
- Tao Tang and Manfred R. Trummer. Boundary layer resolving pseudospectral methods for singular perturbation problems. *SIAM Journal of Scientific Computing*, 17:430–438, 1996.
- R. Tian, G. Yagawa, and H. Terasaka. Linear dependence problems of partition of unity-based generalized FEMs. *Computer Methods in Applied Mechanics and Engineering*, 195:4768–4782, 2006.
- S. Timoshenko and J.N. Goodier. *Theory of elasticity*. McGraw-Hill, New York, USA, 3rd edition, 1970.
- I. Tobor, P. Reuter, and C. Schlick. Efficient reconstruction of large scattered geometric datasets using the partition of unity and radial basis functions. *journal of WSCG*, 12(1–3), 2004. ISSN-1213-6972.
- I. Tobor, P. Reuter, and C. Schlick. Reconstructing multi-scale variational partition of unity implicit surfaces with attributes. *Graphical Models*, 68: 25–41, 2006.
- G. Ventura, J. X. Xu, and T. Belytschko. A vector level set method and new discontinuity approximations for crack growth by EFG. *International Journal for Numerical Methods in Engineering*, 54:923–944, 2002.
- G. Ventura, R. Gracie, and T. Belytschko. Fast integration and weight function blending in the extended finite element method. *International Journal for Numerical Methods in Engineering*, 77:1–29, 2009.
- B. Šaler and R. Vertnik. Meshfree local radial basis function collocation for diffusion problems. *Compu. Math. Appl.*, 51:1269–1282, 2006.

- J. W. Walter. Numerical experiments on adiabatic shear band formation in one dimension. *International Journal of Plasticity*, 8:657–693, 1992.
- J. G. Wang and G. R. Liu. A point interpolation meshless method based on radial basis functions. *International Journal for Numerical Methods in Engineering*, 54:1623–1648, 2002.
- W. M. Wang, L. J. Sluys, and R. de Borst. Viscoplasticity for instabilities due to strain softening and strain-rate softening. *International Journal for Numerical Methods in Engineering*, 40:3839–3864, 1997.
- G. J. Wanger and W. K. Liu. Applied of essential boundary conditions in mesh-free methods: a corrected collocation method. *International Journal for Numerical Methods in Engineering*, 47:1367–1379, 1999.
- G. N. Wells and L. J. Sluys. Application of embedded discontinuities for softening solid. *International Journal for Numerical Methods in Engineering*, 65:263–281, 2000.
- H. Wendland. Piecewise polynomial, positive definite and compactly supported radial basis functions of minimal degree. *Advances in Computational Mathematics*, 4:389–396, 1995.
- H. Wendland. Fast evaluation of radial basis functions: Method based on partition of unity. In C.K. Chui, L.L. Schumaker, and J. Stöckler, editors, *Approximation theory X: Abstract and classical Analysis*, pages 473–483. Vanderbilt University Press, 2002.
- J. Wertz, E.J. Kansa, and L. Ling. The role of the multiquadric shape parameters in solving elliptic partial differential equations. *Computers and Mathematics with Applications*, 51:1335–1348, 2006.
- G.B. Wright and B. Fornberg. Scattered node compact finite difference-type formulas generated from radial basis functions. *Journal of Computational Physics*, 212:99–123, 2006.

- T. W. Wright. Adiabatic shear bands. *Journal of Applied Mechanics*, 43:S196–S200, 1990.
- T. W. Wright. *The physics and mathematics of adiabatic shear bands*. Cambridge University Press, 2002.
- T. W. Wright and J. W. Walter. On stress collapse in adiabatic shear bands. *Journal of Mechanics and Physics of Solids*, 35:701–720, 1987.
- T. W. Wu and M. Stern. Boundary element analysis of ductile crack growth using the traction-free fundamental solution. *Computational Mechanics*, 5:293–304, 1989.
- Q. Z. Xiao and B. L. Karihaloo. Recent developments of the extended/generalized FEM and a comparison with the FEM. *In Development and Applications of Solid Mechanics , University of Science and Technology of China Press, Hefei, China, ISBN 7-312-01842-4:303–324,, 2005.*
- X. Xin and Z. Chen. An analytical solution with local elastoplastic models for the evolution of dynamic softening. *international journal of Solids and Structures*, 37:5855–5872, 2000.
- X.-P. Xu and A. Needleman. Numerical simulations of fast crack growth in brittle solids. *J. Mech. Phys. Solids*, 42:1397–1434, 1994.
- A. M. Yan and H. Nguyen-Dang. Multiple-crackd fatigue crack growth by BEM. *Computational Mechanics*, 16:273–280, 1995.
- Q. Yang, A. Mota, and M. Ortiz. A class of variational strain localization finite elements. *International Journal for Numerical Methods in Engineering*, 62:1013–1037, 2005.
- Y. C. Yoon, S. H. Lee, and T. Belytschko. Enriched meshfree collocation method with diffuse derivatives for elastic fracture. *Computers & Mathematics*, 51:1349–1366, 2006.

- X. Zhang, K. Z. Song, M. W. Lu, and X. Liu. Meshless method based on collocation with radial basis functions. *Computational Mechancis*, 26:333–343, 2000.
- X. Zhang, X. H. Liu, K. Z. Song, and M. W. Lu. Least-squares collocation meshless method. *International Journal for Numerical Methods in Engineering*, 51:1089–1100, 2001.
- F. Zhou and J. F. Molinari. Dynamic crack propagation with cohesive elements: a methodolgy to address mesh dependency. *International Journal for Numerical Methods in Engineering*, 59:1–24, 2004.
- T. Zhu and S.N. Atluri. A modified collocation method and a penalty formulation for enforcing the essential condition in the element free garlerkin method. *Computational Mechanics*, 21(3):211–222, 1998.
- G. Zi, T. Rabczuk, and W. Wall. Extended meshfree methods without branch enrichment for cohesive cracks. *Computational Mechanics*, 40:367–382, 2007.